

UNIVERSITY *of the* WESTERN CAPE



Sustainable synthesis of BEA zeolite from fly ash-based amorphous silica

By

Emmanuel Alechine Ameh

BSc Chemistry (honours) – University of Jos

MSc Chemical Science – University of the Western Cape

**A thesis submitted in fulfilment of the requirements for the degree of
Doctor of Philosophy in Chemistry, Faculty of Natural Sciences, University of the
Western Cape.**

Supervisor: Prof. Leslie F. Petrik

Co-supervisor: Dr Nicholas M. Musyoka

September 2019

<http://etd.uwc.ac.za/>

Abstract

Power generation in South Africa depends majorly on the combustion of coal and the increasing demand for energy due to industrialisation and population growth signifies the continuous consumption of coal. During this process, a by-product known as coal fly ash (CFA) is generated which poses several environmental issues. The common management of the waste involves the disposal of CFA in landfills or the direct disposal to open uncultured lands, thus contaminating water bodies by the leaching of constituent CFA metals and salts that render arable land uncultivable. The transformation of CFA into a value added zeolitic product is a potential way to manage and reduce the negative environmental impact of the waste. Since the chemical components of CFA are mostly SiO_2 and Al_2O_3 , they are thus similar to the TO_4 (Si-O-Al) tetrahedral building units of zeolite framework structures. This is indicative that CFA is a suitable alternative feedstock material for the synthesis of zeolites but the Si/Al ratio of the waste material is low for the production of high silica zeolites. Thus, an external addition of Si or Al source is required for the high silica zeolitisation via indirect hydrothermal process. This research describes a novel design and formulations for the synthesis of BEA zeolite from South Africa CFA via indirect hydrothermal process without the addition of an external silica or aluminium source.

In the synthesis process of BEA zeolite, a multi-step approach involving: fusion of CFA, precipitation process, oxalic acid reflux process, and hydrothermal treatment was used. After the fusion and precipitation process, the recovered solid extract was further treated with 1.3, 1.5 and 1.7 M concentration of oxalic acid under reflux to obtain the silica extract. Herein, the Si/Al ratio of the silica extract significantly increased to 48, 61 and 53 elucidating that the major component of the extract is 92% silica, with a high percentage purity of 94% while Al and Na are the other components with significant amount (1-2% and Na 6-7%, respectively). Three molar regimes were formulated based on the different Si/Al ratios of the silica extract. A pure phase BEA zeolite was obtained after the hydrothermal crystallisation of the synthesis precursor with Si/Al ratio of 53 and 61 at 140 °C for 72 h.

The influence of sodium, aluminium and hydrothermal time was investigated based on the baseline molar regime: 1 Si: 0.017 Al : 0.241 Na : 0.399 TEAOH : 8.980 H_2O (Si1.5) for the synthesis of BEA zeolite. The variation in molar fraction of Na content affected the morphology of the synthesised BEA zeolite forming spheroidal-shaped structure at low molar fraction Na of ≤ 0.241 to large cuboidal-shaped crystals with increased Na fraction ≥ 0.317 . With further increase to 0.552 molar Na fraction, the phase purity was compromised (amorphous + BEA zeolite) and when the molar Na fraction is 0.734, a complete phase

transformation of BEA crystal to natrite phase was found. On the other hand, with increased molar fraction of Al a spheroidal-shape morphology was maintained and the crystallinity of BEA zeolite gradually increased with increased molar Al content. Although, at higher molar Al fraction of 0.172 a significant reduction of structural crystallinity to 55% was observed. The optimised molar regimes: 1 Si : 0.017 Al : 0.241 Na : 0.399 TEAOH : 8.980 H₂O (BEA4) or 1 Si : 0.060 Al : 0.241 Na : 0.399 TEAOH : 8.980 H₂O (BEAA1) was used to study the effect of hydrothermal time (12, 24, 48 and 72 h) at 140°C. It was found that the BEA4 molar regime enhanced fast nucleation rate and crystal growth within short hydrothermal time of 24 h compared to the slow crystal growth achieved after 48 h by the hydrothermal crystallisation of BEAA1 molar regime. To achieve a shorter hydrothermal time the molar water fraction of 1 Si : 0.017 Al : 0.241 Na : 0.399 TEAOH : x H₂O was varied. To this end, high molar water fraction hindered the complete formation of pure phase BEA zeolite within a short synthesis time due to the lowered concentration of TEA⁺ species, thus reducing the supersaturation of the molar regime. Upon reducing the molar water fraction, a rapid growth of BEA zeolite crystals within hydrothermal time of 8, 10 and 12 h was observed. The HBEA zeolites produced possessed fine micro-size with high thermal framework stability, high surface area, suitable pore volume, well-defined pore size distribution, and maintained both framework and extra framework Al and weak-stronger acid sites. Hence, this study eliminated the need for an external addition of silica or aluminium source to the synthesis mixture and developed suitable molar regime for the synthesis of HBEA zeolite from CFA via an indirect hydrothermal process.

In the present research, the behaviour of the synthesised HBEA zeolite in hot liquid reaction was investigated. After prolonged exposure time and high temperature, the crystalline structure reduced significantly by 30%. The structural degradation of the treated zeolite depended on reduced crystallinity and framework Si/Al ratio, the degree of desilication, and the presence of silanol defects under prolonged exposure time and high temperature in hot liquid. Moreover, the textural properties were decreased and changes in surface area and micropore volume induced gradual expansion of the framework structure thereby compromising the quality of the BEA zeolite. The hot liquid process enhanced framework desilication by the hydrolysis of Si-O-Si bonds which then formed terminal Si-OH species. Thus, the structural integrity of the zeolite was significantly compromised by the formation of structural defects at elevated treatment time and temperature, however, no phase transformation was observed.

The catalytic activity of the synthesised HBEA zeolite was tested in the acylation of anisole with benzoyl chloride. The reaction time, molar ratio of the reactant, surface area, mesoporous area, hierarchical pore structure and acid sites influenced the catalytic performance of the zeolite. Also, the combination of high framework Al content and large peak area of Q⁴ Si(0Al) species correlated with better catalytic activity. Over 85% of anisole was predominantly converted to selective *p*-position of 4-methoxyacetophenone while less than 10% include products such as 2-methoxyacetophenone and phenyl benzoate. Herein, the highest conversion rate of anisole was 99% with a selectivity of 98% and percentage yield of 97%. The synthesised BEA zeolite from CFA via indirect hydrothermal synthesis thus demonstrated high catalytic performance in acylation of anisole with benzoyl chloride ratio.



Keywords

Coal fly ash

Alkaline fusion

Acid precipitation

Silica extract

Hydrothermal treatment

Tetraethylammonium hydroxide

BEA zeolite

Framework stability

Hot liquid

Acylation of anisole

Conversion of anisole



UNIVERSITY *of the*
WESTERN CAPE

Declaration

I declare that '**Sustainable synthesis of BEA zeolite from fly ash-based amorphous silica**' is my own work, that it has not been submitted for any degree or examination in any other university, and that all the resources I have used or quoted have been indicated and acknowledged by means of complete references.

Emmanuel Alechine Ameh

September 2019

Signed:



UNIVERSITY *of the*
WESTERN CAPE

Acknowledgements

My sincere appreciation goes to my supervisor, Prof. Leslie Petrik for your mentorship. You have been a support system through tireless commitment, discussion, guidance and encouragement. Your enormous contribution has modelled me into a researcher with suitable knowledge to succeed in human development, scientific/academic research and industrial research. Thank you so much, this is a memorable journey that will stand the test of time “Prof I throway salute”.

I am grateful to my Co-supervisor, Dr Musyoka Nicholas for the many contributions made towards this thesis and for hosting me in the CSIR facility. I owe a debt of gratitude to Prof. Edith Antunes for her assistance with NMR analysis and data interpretations. I also appreciate Dr O. Fatoba and Dr Chuks Paul Eze for proofreading some thesis chapters and having time to guide me in the right direction. Your enormous contribution yielded this success.

During this research work, there are people who shared ideas on the analysis of results who I feel obliged to sincerely appreciate. These include Dr Francious Cummings and Adrian Josephs (Electron Microscopy Unit, University of Western Cape); Ilse Wells, the ENS laboratory manager and ICP analyst; Mr Timothy Lesch, the laboratory manager chemistry department (UWC), Dr Cynthia Sanchez-Garrido and Riana Rossouw (ICP-MS analysis, University of Stellenbosch); Stuart Moir (XRF analysis, United Scientific) Dr Remy Bucher (XRD analysis Ithemba labs); Mr. Yunus Kippie (TGA); Ms. Winnie Monama and Dr Ebrahim Mohiuddin (BET and TPD analysis, UWC). Also Samuel Lucas and Geoffrey Busch of the technical department, UWC, for their technical support.

I would also like to thank my colleagues at the Environmental and Nano Sciences Research (ENS) group; Mama Vanessa Kellerman, Jean-Luc Mukhaba, Mero-Lee Cornelius, Dr Kassim Badmus, Dr Omoniyi Perea, Cosmas Uche, Dr Emile Massima, Emmanuel Omoniyi, Anthony Okotie, Mr and Mrs Abegunde, Deborah Kalume, Cecilia Sanusi, Dr Jimoh Tijani, to mention but a few. I really appreciate your kind support.

To my friends who shared in my emotional, psychological and physical phases in the cause of this journey; “no be small thing oooo” but you made it small. Thank you to Comfort

Tamanda Mtotha, Dr Daniel Adeniyi, Dr Lela Mukaruzima, Horyen Shaiyen, Dr Chris Ademola, Agnes Lutomiah, Abah Maria, Dr Roland and Family, Dr Olushola Adeniyi and family, Stephen, Mrs Moyin John-Aliu, Dipo David, Sally, Dr Ife, Marcus, Maria Odiba and Dr Richard. I cannot ignore the likes of Aunty Margaret, Bro John, family of Ogwuche, family of Dr Obutu, Martha, family of Abah, and to the RCF family (I love this family of God). My sincere thanks. My gratitude also goes out to those special individuals that time and space do not permit me to mention their names. Indeed, the journey of success which yields great delight, in the end, is not a solitary journey. I wish to say I appreciate you all.

This acknowledgement cannot be complete without the recognition of the love, care, prayers, support and many other significant roles of family members (nieces, nephews, Mr & Mrs Bello, Mr & Mrs Eriba, Mr & Mrs Ochigbo, Owoicho, Abraham and my lovely parents, David and Regina Ameh) towards my success. You are all wonderful people and my life is incomplete without you all. I love you all.

After “all’s been said and done, there is just one thing that matters” (song by Don Moen). All the Praise, all the Honour, all Adoration and my profound gratitude to the Almighty God - Who is, Who was and Who is to come. He fashioned this research from the beginning to the end out of mercy and grace. Lord, I am immensely grateful.

The logo of the University of the Western Cape, featuring a stylized classical building with columns and a pediment.

UNIVERSITY of the
WESTERN CAPE

Dedication

This thesis is dedicated to my:

Parents

MWO (rtd) Ameh David

Regina Ameh David

And

In lovely memory

of

Grace & Joy Ameh.



UNIVERSITY *of the*
WESTERN CAPE

Table of Contents

ABSTRACT	I
KEYWORDS	IV
DECLARATION	V
ACKNOWLEDGEMENTS	VI
DEDICATION	VIII
TABLE OF CONTENTS	IX
LIST OF FIGURES	XIII
LIST OF TABLES	XVI
LIST OF EQUATION	XVIII
LIST OF ABBREVIATIONS	XIX
RESEARCH OUTPUT	XXI
CHAPTER 1	1
1 INTRODUCTION	1
1.1 PROBLEM STATEMENT AND MOTIVATION OF THE STUDY	3
1.2 THESIS STATEMENT	4
1.3 RESEARCH QUESTIONS	4
1.4 AIMS AND OBJECTIVES	5
1.5 THESIS DELIMITATION	5
1.6 THESIS OVERVIEW	5
CHAPTER 2	7
LITERATURE REVIEW	7
CONVERSION OF COAL FLY ASH: A HEURISTIC APPROACH FOR THE SYNTHESIS OF HIGH SILICA ZEOLITE VIA INDIRECT HYDROTHERMAL PROCESS	7
HIGHLIGHTS	7
2 INTRODUCTION	7
2.1 COAL FLY ASH	9
2.1.1 Physicochemical properties of CFA	9
2.1.1.1 Morphology of CFA	9
2.1.1.2 Mineral composition of coal fly ash	10
2.1.1.3 Chemical composition of CFA	11
2.1.2 Environmental challenges of CFA	14
2.1.3 Potential use of CFA	15
2.2 ZEOLITE	17
2.2.1 Classification of zeolites	20

2.2.2	Principle components and their roles in the synthesis of zeolites	25
2.2.2.1	Silicon and aluminium sources.....	25
2.2.2.2	Mineralising agent.....	26
2.2.2.3	Structure directing agent	27
2.3	SYNTHESIS OF ZEOLITES FROM CFA	28
2.3.1	Presynthesis and mechanism of zeolite crystallisation.....	29
2.3.1.1	Dissolution-condensation stage.....	29
2.3.1.2	Nucleation-crystal growth stage.....	29
2.3.2	Direct synthesis process	31
2.3.3	Indirect synthesis process.....	32
2.3.4	Challenges with the conversion of CFA to high silica zeolite	35
2.3.5	Properties and applications of high silica zeolite	39
2.3.6	The investigated zeolite structure and properties in the present study: HBEA zeolite	40
2.4	CHAPTER SUMMARY.....	42

CHAPTER 3 **43**

MATERIALS AND METHODOLOGY **43**

3 INTRODUCTION..... **43**

3.1	MATERIALS	43
3.1.1	Sample location and sampling of feedstock material	43
3.1.2	Chemicals	44
3.2	METHODOLOGY.....	44
3.2.1	Alkaline fusion of FA.....	45
3.2.2	Extraction of silica from FFA	46
3.2.3	Synthesis of BEA zeolite from silica extract.....	46
3.2.4	Influence of reduced H ₂ O content to enhance fast crystallisation of BEA zeolite	49
3.2.5	Catalytic applications of BEA zeolite	50
3.2.5.1	Hot-liquid phase test.....	50
3.2.5.2	Friedel-Crafts acylation process.....	51
3.2.5.3	Regeneration process of the catalyst	53
3.3	CHARACTERISATION TECHNIQUES	53
3.3.1	pH.....	53
3.3.2	Inductively Coupled Plasma – Optical Emission Spectrometry.....	54
3.3.3	Laser Ablation Inductively Coupled Plasma-Mass Spectrometry.....	54
3.3.4	X-ray Fluorescence Spectroscopy analysis	54
3.3.5	Scanning Electron Microscopy (SEM)- Energy dispersive spectroscopic (EDX)	55
3.3.6	X-ray diffractometer (XRD).....	55
3.3.7	FT-IR analysis	56
3.3.8	Thermogravimetric analysis	56
3.3.9	Nuclear magnetic resonance (²⁷ Al- ²⁹ Si MAS NMR).....	56
3.3.10	Brunauer–Emmett–Teller (BET)	57
3.3.11	Temperature programmed desorption (TPD)	57
3.3.12	Gas chromatograph (GC)	58

CHAPTER 4	59
HYDROTHERMAL CONVERSION OF FLY ASH BASED AMORPHOUS-SILICA TO NANOCRYSTAL BEA ZEOLITE	59
GRAPHICAL ABSTRACT	59
HIGHLIGHTS	60
4 INTRODUCTION	61
4.1 CHARACTERISATION OF COAL FLY ASH (CFA)	61
4.2 EXTRACTION OF SILICA FROM FUSED FLY ASH.....	66
4.2.1 Effect of oxalic acid on the silica extract	66
4.3 SYNTHESIS OF BEA ZEOLITE FROM EXTRACTED FLY ASH BASED SILICA	73
4.4 SYNTHESIS AND CHARACTERISATION OF BEA ZEOLITE	75
4.4.1 Effect of water on the crystallisation of BEA zeolite	75
4.4.2 Effect of sodium and aluminium on the crystallisation of BEA zeolite	80
4.4.3 Effect of aluminium on the crystallisation of BEA zeolite	84
4.4.4 Comparison of the optimum conditions for the synthesis of fly ash based BEA zeolite	88
4.4.5 Effect of hydrothermal time of crystallisation upon BEA zeolite	92
4.4.5.1 Influence of synthesis time on thermal stability, framework structure and textural properties of BEA zeolite	97
4.5 CHAPTER SUMMARY.....	107
CHAPTER 5	109
STABILITY OF FLY ASH-BASED BEA-ZEOLITE IN HOT LIQUID PHASE	109
GRAPHICAL ABSTRACT	109
HIGHLIGHTS	109
ABSTRACT	110
5 INTRODUCTION	111
5.1 EXPERIMENTAL	112
5.1.1 Stability test.....	113
5.2 RESULTS AND DISCUSSION	114
5.2.1 Phase crystallinity of treated BEA zeolite in hot liquid	114
5.2.2 Structural probe of O-T-O bonds	120
5.2.3 Si-OH content within the BEA zeolite structure using thermogravimetric analysis ..	123
5.2.4 Framework changes of hot liquid treated BEA zeolite	126
5.2.5 Lifetime activity of fly ash based BEA zeolite in hot liquid phase.....	135
5.2.6 Textural properties of the fly ash BEA zeolite in hot liquid phase	136
5.3 CHAPTER SUMMARY.....	140
CHAPTER 6	142
ACYLATION OF ANISOLE WITH BENZOYL CHLORIDE OVER RAPIDLY SYNTHESISED H-BEA ZEOLITE CATALYST	142

HIGHLIGHTS.....	142
ABSTRACT.....	143
6 INTRODUCTION.....	144
6.1 EXPERIMENTAL	145
6.2 RESULTS AND DISCUSSION	146
6.2.1 Rapid synthesis of HBEA zeolite: effect of low water content on hydrothermal time 146	
6.2.2 Mineralogical, morphological and structural features.....	146
6.2.3 Characterisation of optimised HBEA zeolite products	159
6.2.3.1 Framework stability of HBEA zeolite structure.....	163
6.2.3.2 Textural and acidic properties of HBEA zeolites.....	169
6.2.4 Friedel-Crafts acylation of anisole with benzoyl chloride over HBEA zeolites	176
6.2.4.1 Activity of fly ash-based HBEA zeolite in acylation reaction	176
6.2.4.2 Influence of framework structure in the acylation reaction over HBEA zeolite	181
6.2.4.3 Influence of HBEA textural and acidic properties in the acylation reaction.....	184
6.2.4.4 Influence of anisole/benzoyl chloride ratio in acylation reaction.....	187
6.2.4.5 Reaction kinetics	191
6.2.4.6 Regeneration of HBEA zeolite in acylation reaction	193
6.3 CHAPTER SUMMARY.....	196
CHAPTER 7.....	197
CONCLUSIONS AND RECOMMENDATIONS.....	197
7 INTRODUCTION.....	197
7.1 RESEARCH FINDINGS	198
7.1.1 Attaining high molar Si/Al ratio of the feedstock	198
7.1.2 Optimisation of BEA zeolite process from CFA.....	198
7.1.3 Influence of molar water on the hydrothermal time.....	200
7.1.4 Stability of the synthesised BEA zeolite in hot liquid phase reaction.....	200
7.1.5 Physicochemical properties and catalytic performance of HBEA zeolite.....	201
7.1.6 Significance of the research findings	202
7.2 RECOMMENDATIONS FOR FUTURE STUDY.....	202
REFERENCES.....	204
APPENDIX.....	229

List of Figures

Figure 2.1: Global source of energy consumption	8
Figure 2.2: SEM micrograph of CFA morphology	10
Figure 2.3: Potential applications of CFA	16
Figure 2.4: Framework structure of zeolite showing the respective tetrahedral	19
Figure 2.5: Schematic for Brönsted acid hydroxyl	19
Figure 2.6: Secondary building units of zeolites framework.....	21
Figure 2.7: Example of framework structure	22
Figure 2.8: Example of pore opening of various zeolite framework structures	24
Figure 2.9: Pathway of silica and alumina source in the formation of primary and secondary building unit of zeolite structure	26
Figure 2.10: Schematic illustrating the four steps: a) dissolution, b) condensation, c) nucleation and d) crystal growth for the crystallisation of zeolites from CFA	28
Figure 2.11: Representation of the nucleation rate and the crystal growth of zeolite structure	30
Figure 2.12: One-step process for the synthesis of zeolite from CFA via hydrothermal process.	32
Figure 2.13: Two-step indirect hydrothermal process	33
Figure 2.14: SEM image of crystalline zeolite	37
Figure 2.15: Multi-step approach for the synthesis of high silica zeolite from CFA.....	38
Figure 2.16: Stacking sequences of the three distinctive BEA polymorphs	40
Figure 3.1: Locations of coal power plants in South Africa	43
Figure 3.2: Experimental design for the synthesis of BEA zeolite from fly ash based silica extract	45
Figure 4.1: SEM micrograph of the South African class F Arnot CFA.....	62
Figure 4.2: XRD pattern of coal fly ash (CFA) and fused fly ash (FFA).....	63
Figure 4.3: FT-IR spectra for the structural analysis of Arnot CFA and FFA	65
Figure 4.4: XRD patterns of the extracted silica	67
Figure 4.5: SEM images of extracted silica.....	68
Figure 4.6: FT-IR spectra of fly ash based silica samples.....	69
Figure 4.7: XRD patterns of the BEA zeolites synthesised from treated FFAE.....	74
Figure 4.8: XRD patterns of the BEA zeolites synthesised from four different molar composition	77
Figure 4.9: SEM images of the BEA zeolites synthesised from four different molar composition	79
Figure 4.10: XRD patterns showing the effect of NaOH on the phase formation of BEA zeolites	81
Figure 4.11: SEM morphology showing the effect of NaOH on the phase formation of BEA zeolites	83
Figure 4.12: XRD patterns showing the effect of aluminium on the phase formation of BEA zeolites	85
Figure 4.13: SEM morphology showing the effect of aluminium on the phase formation of BEA zeolites	87
Figure 4.14: Ternary plot of the molar composition.	89

Figure 4.15: XRD patterns of the HBEA zeolite synthesised at different hydrothermal crystallisation times	93
Figure 4.16: SEM morphology of HBEA zeolite synthesised at different hydrothermal crystallisation time	94
Figure 4.17: Graphical presentation of crystallinity over time for the synthesis of BEA zeolite	95
Figure 4.18: Thermal profiles of HBEA zeolite synthesised at different hydrothermal times from the molar compositions	98
Figure 4.19: ²⁷ Al MAS NMR of HBEA zeolite synthesised at different hydrothermal time from the molar composition	99
Figure 4.20: ²⁹ Si MAS NMR of HBEA zeolite synthesised at different hydrothermal times from the molar composition	101
Figure 4.21: N ₂ adsorption-desorption isotherms of BEA zeolite prepared from synthesis composition with different Si/Al ratio.....	105
Figure 5.1: XRD patterns of the parent and treated NaBEA zeolite in hot liquid phase reaction	114
Figure 5.2: XRD patterns of parent and treated AIBEA zeolite in hot liquid phase reaction	115
Figure 5.3: Percentage crystallinity of the parent BEA.....	116
Figure 5.4: pH behaviour of NaBEA zeolite in the interactive environment of hot liquid reaction	118
Figure 5.5: pH behaviour of AIBEA zeolite in the interactive environment of hot liquid reaction	118
Figure 5.6: FT-IR spectra of parent and hot liquid treated NaBEA zeolites at different temperature.....	120
Figure 5.7: FT-IR spectra of parent and hot liquid treated AIBEA zeolites at different temperature.....	121
Figure 5.8: TGA of the untreated (NaBEA) and treated zeolite in hot liquid phase reaction	123
Figure 5.9: TGA of the untreated (AIBEA) and treated zeolite in hot liquid phase reaction	124
Figure 5.10: ²⁹ Si MAS NMR of the parent and treated NaBEA zeolite.....	126
Figure 5.11: ²⁹ Si MAS NMR of the parent and treated AIBEA zeolite	127
Figure 5.12: Relationship between the relative crystallinity and the ²⁹ Si MAS NMR peak intensity and peak area of the parent and treated NaBEA zeolite.	130
Figure 5.13: Relationship between the relative crystallinity and the ²⁹ Si MAS NMR peak intensity and peak area of the parent and treated AIBEA zeolite.....	130
Figure 5.14: ²⁷ Al MAS NMR analyses of parent and treated NaBEA zeolite.	131
Figure 5.15: ²⁷ Al MAS NMR analyses of the parent and treated AIBEA zeolite.....	132
Figure 5.16: Lifetime activity of parent BEA zeolites treated in hot liquid phase.....	135
Figure 5.17: N ₂ adsorption-desorption isotherms of the parent and treated BEA zeolite .	137
Figure 5.18: DFT pore size distribution plot of the parent and treated NaBEA zeolite....	139
Figure 6.1: XRD patterns showing the effect of molar fraction of water on the crystallisation of BEA zeolites.	147
Figure 6.2: FTIR patterns showing the effect of molar fraction of water on the BEA zeolites structure.....	148

Figure 6.3: SEM morphology showing the effect of molar fraction of water on the crystallisation of BEA zeolites over 12 h.	150
Figure 6.4: Relationship between crystallinity, crystal size and percentage yield of the synthesised products at 140 °C for 12 h.	151
Figure 6.5: XRD patterns showing the effect of molar fraction of water on the crystallisation of BEA zeolites.	153
Figure 6.6: FTIR patterns showing the effect of molar fraction water on the crystallisation of BEA zeolites.	155
Figure 6.7: SEM morphology showing the effect of molar fraction of water on the crystallisation of BEA zeolites.	157
Figure 6.8: XRD patterns of the synthesised HBEA zeolite produced from the molar composition	159
Figure 6.9: SEM micrographs of the synthesised HBEA zeolite produced from the molar composition	161
Figure 6.10: TGA analysis of the synthesised HBEA zeolite produced from the molar composition	163
Figure 6.11: ²⁷ Al MAS NMR analyses of the synthesised HBEA zeolite produced from the molar composition.	165
Figure 6.12: ²⁹ Si MAS NMR analyses of the synthesised HBEA zeolite produced from the molar composition	168
Figure 6.13: N ₂ adsorption-desorption isotherms of HBEA zeolite prepared at short crystallisation time.	170
Figure 6.14: Mesopore size distributions of the synthesised HBEA zeolite produced from the molar composition	172
Figure 6.15: Mesopore size distributions of the synthesised HBEA zeolite produced from the molar composition.	173
Figure 6.16: TPD profiles of the synthesised HBEA zeolite produced from the molar composition.	174
Figure 6.17: Anisole conversion over HBEA zeolites.	177
Figure 6.18: Selectivity of P _{4Me} over HBEA zeolites.	178
Figure 6.19: Percentage yield of P _{4Me} over HBEA zeolites	180
Figure 6.20: Influence of zeolite framework and extra-framework Al HBEA on the yield of P _{4Me}	181
Figure 6.21: Influence of the area, Q4 Si(0Al) HBEA on the yield of P _{4Me}	183
Figure 6.22: Conversion of anisole as a function of mesoporosity of HBEA zeolite	186
Figure 6.23: Anisole conversion and selectivity of P _{4Me} over HBEA2 and HBEA24 zeolites.	188
Figure 6.24: Anisole conversion and selectivity of P _{4Me} over HBEA2 and HBEA24 zeolites.	188
Figure 6.25: Regression plot illustrate the pseudo-first-order reaction.	192
Figure 6.26: Conversion of anisole and percentage yield of P _{4Me} over recycled HBEA2	194
Figure 6.27: Conversion of anisole and percentage yield of P _{4Me} over recycled HBEA24.	194
Figure 6.28: XRD spectra of the recycled catalyst.	195

List of Tables

Table 2.1: Chemical constituent of burnt CFA from anthracite, bituminous, sub-bituminous and lignite coal.....	12
Table 2.2: ASTM standard classification of CFA.	12
Table 2.3: Elemental composition of CFA sourced from different power plants in South Africa.	13
Table 2.4: Trace elemental composition of CFA sourced from different power plants in South Africa.....	14
Table 2.5: Examples of different zeolites illustrating their shape, SBU and framework density.....	24
Table 2.6: Type of zeolite based on the Si/Al ratio produced from CFA.....	35
Table 3.1: List, source and purity of chemicals used.	44
Table 3.2: Conditions for the extraction of silica from FFAE.....	46
Table 3.3: Preliminary synthesis conditions for the synthesis of BEA zeolite from silica extract.	47
Table 3.4: Conditions for the synthesis of BEA zeolite from Si1.5 silica extract.....	48
Table 3.5: The effect of water content in relation to synthesis time for BEA zeolite formation.	49
Table 3.6: Experimental conditions for hot-liquid test of NaBEA and AlBEA zeolite.	50
Table 3.7: Acylation reaction of anisole with benzoyl chloride over HBAE zeolite.	51
Table 4.1: XRF analysis of the major elemental composition of CFA	61
Table 4.2: Comparison of the extracted fly ash based silica and pure fumed silica.....	70
Table 4.3: Elemental composition of the various silica extracts from CFA.....	71
Table 4.4: Percentage purity and yield of the extracted fly ash based silica.	73
Table 4.5: Comparison of crystallinity, crystal size and yield of products prepared from different molar fraction of NaOH.	82
Table 4.6: Comparison of crystallinity, crystal size and yield of products prepared from different molar fraction of aluminium.	86
Table 4.7: Comparison of the Si/Al ratio, crystal size, crystallinity and yield of the BEA zeolite synthesised at different times.	96
Table 4.8: Detailed ²⁷ Al MAS NMR spectra depicting the integration of FAI and EFAI in the HBEA zeolite synthesised at different hydrothermal times.	100
Table 4.9: Chemical shift, peak width, peak area and Si/Al _{FW} ratio of deconvoluted Q ³ /Q ⁴ environments.	103
Table 4.10: Textural properties of the synthesised BEA zeolite at different time and Si/Al ratio of the synthesis mixtures.	106
Table 5.1: Experimental conditions for hot-liquid test of NaBEA and AlBEA zeolite. ...	113
Table 5.2: Relation between adsorbed surface water, bonded framework water and silanol content.	125
Table 5.3: Comparison of chemical shift, Si/Al ratio, intensity and area of deconvoluted Q ³ and Q ⁴ peak.....	128
Table 5.4: Detailed ²⁷ Al MAS NMR spectra after integration of FAI and EFAI in the parent and hot liquid treated NaBEA and AlBEA zeolite.	133
Table 5.5: Textural properties of parent and hot liquid treated NaBEA zeolite under different temperature and time.	138

Table 6.1: Comparison of the crystallinity, crystal size and yield of the synthesised products.	148
Table 6.2: Elemental composition and Si/Al ratio of the synthesised products using SEM-EDS.....	151
Table 6.3: Comparison of the crystallinity, crystal size and yield of the synthesised products.	154
Table 6.4: Elemental composition and crystal size of the synthesised products using SEM-EDS.....	158
Table 6.5: Elemental composition and crystal size of the HBEA zeolite using SEM-EDS.	162
Table 6.6: The adsorbed surface water (surface moisture content), bonded framework water (dehydroxylation) and total weight loss.	164
Table 6.7: Detailed ²⁷ Al MAS NMR spectra after deconvolution FAI and EFAI in the synthesised HBEA zeolite samples.	166
Table 6.8: Chemical shift, Si/Al ratio, intensity and area of deconvoluted Q ³ and Q ⁴ peak.	169
Table 6.9: Textural properties of the synthesised HBEA zeolite at different hydrothermal time.	171
Table 6.10: Acidity of the synthesised HBEA zeolites.	175
Table 6.11: Correlation of the catalytic performance to the textural and acid sites properties of HBEA zeolites.....	184
Table 6.12: Selectivity and yield of P _{2Me} , P _{4Me} and phenyl benzoate (P _{Bz}) over HBEA2 and HBEA24 zeolite in a reaction mix of anisole/BzCl ratio	189
Table 6.13: Selectivity and yield of P _{2Me} , P _{4Me} and phenyl benzoate (P _{Bz}) over HBEA2 and HBEA24 zeolite in a reaction mix of anisole/BzCl ratio	190
Table 6.14: Kinetics showing the rate of reaction of anisole with BzCl over HBEA zeolite.	193

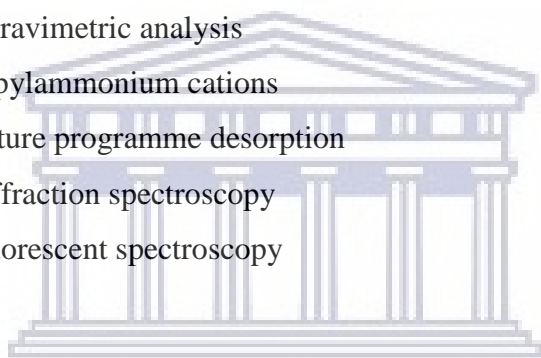
List of Equation

$Mxnxn + AlO42_xSiO42_y \cdot mH2O$	Equation 2.1	18
$SiO2s + 2NaOHs \rightarrow Na2SiO3s + H2O$	Equation 2.2	34
$Al2O3 + 2NaOH \rightarrow 2NaAlO2s + H2O$	Equation 2.3	34
% anisole conversion = $\frac{P2Me + P4Me + PPHBP2Me + P4Me + PPHB + PBzCl}{100} \times$	Equation 3.1	52
% Si = $\frac{P2Me \text{ or } P4Me \text{ or } PPHBP2Me + P4Me + PPHB}{100} \times 100$	Equation 3.2	53
% Yield _i = conversion \times selectivity	Equation 3.3	53
$SiO2 + 2NaOH \rightarrow Na2SiO3 + H2O$	Equation 4.1	72
$Na2SiO3 + H2SO4 \rightarrow SiO2 + X2SO4 + H2O$	Equation 4.2	72
$P \% = 1 - i = 1mi\%$	Equation 4.3	72
Yield % = $\frac{mextract}{mextract + mCFA} \times 100$	Equation 4.4	72
Relative crystallinity = $\frac{PPO}{100} \times 100$	Equation 4.5	76
Yield % = $\frac{mproduct}{mbulk} \times 100$	Equation 4.6	80
$SiAl(^{29}Si) = 2.IQ22Al + 3.IQ31Al + 4.IQ40AlIQ31Al$	Equation 4.7	102
$pH = -\log H3O + \quad pOH = -\log OH -$	Equation 5.1	117
$H2O \leftrightarrow H3O + +OH -$	Equation 5.2	119
$H - OH + \equiv Si - O - Si \equiv \leftrightarrow \equiv Si - OH + OH - Si \equiv$	Equation 5.3	119
$NOH = 2W1 - W2MH2O \times 1000$	Equation 5.4	124
$-\ln(1 - X) = kt$	Equation 6.1	191

List of Abbreviations

AMR	Amorphous
ASTM	American Society for Testing Materials
ATR	Attenuated total reflectance
BET	Brunauer-Emmett-Teller
BzCl	Benzyl chloride
CFA	Coal fly ash
D4R	Double four member ring
DFT	Density functional theory
EaO	Metal oxides = group 1 or 2
EDS	Energy dispersive spectroscopic
EFAI	Extra framework aluminium
ENS	Environmental and Nano Sciences Research Group
FAI	Framework aluminium
FFA	Fused fly ash
FFAE	Fused fly ash extract
FGD	Flue gas desulfurization
FID	Flame ionization detector
FTIR	Fourier transform infrared spectroscopy
GC	Gas chromatography
HR-TEM	High resolution transmission electron microscopy
ICDD	International Centre for Diffraction Data
ICP-ME	Inductively coupled plasma – mass spectrometry
ICP-OES	Inductively coupled plasma – optical emission spectrometry
IE	Industrial ecology
IUPAC	International union of pure and applied chemistry
IZA	International Zeolite Association
JCPDA	Joint committee on powder diffraction standards
JCPDS	Joint committee on powder diffraction standards
LOI	Loss on ignition
MAS-NMR	Magic angle spinning nuclear magnetic resonance
nd	Not detected
NMR	Nuclear magnetic resonance

OSDAs	Organic structure directing agents
P _{2Me}	2-methoxyacetophenone
P _{4Me}	4-methoxyacetophenone
PBU	primary building units
P _{PHB}	Phenyl benzoate
SBU	Secondary building blocks
SDA	Structure directing agent
SEM	Scanning electron microscopy
SOD	Sodalite
T	Atoms = Si and Al (silicon and aluminium)
TEA ⁺	Tetraethylammonium cation
TEAOH	Tetraethylammonium hydroxide
TGA	Thermogravimetric analysis
TPA ⁺	Tetrapropylammonium cations
TPD	Temperature programme desorption
XRD	X-ray diffraction spectroscopy
XRF	X-ray fluorescent spectroscopy



UNIVERSITY *of the*
WESTERN CAPE

Research output

Patent filed

International Bureau of the World Intellectual Property Organization - Patent Application No. PCT/IB2017/053730, in the name of University of the Western Cape, Titled: Process for Production of High Silica Content Zeolite from Fly Ash (2017) (Department of [Business Innovation Centre](#), University of the Western Cape). [Petrik, L.F., Missengue-Na-Moutoula, R., **Ameh, A.E.** and Hlatywayo, T., University of the Western Cape, 2019. *Process for production of high silica content zeolite from fly ash*. U.S. Patent Application 16/312,553]

Publication

- **Alechine E. Ameh**, Chuks P. Eze, Edith Antunes, Mero-Lee U. Cornelius, Nicholas M. Musyoka and Leslie F. Petrik (2019). Stability of fly ash-based BEA-zeolite in hot liquid phase. *Catalysis Today*.

Drafted manuscripts

- **Alechine E. Ameh**, Mero-Lee U. and Leslie F. Petrik. Conversion of coal fly ash: a heuristic approach for the synthesis of high silica zeolite via indirect hydrothermal process.
- **Alechine E. Ameh**, Chuks P. Eze, Nicholas M. Musyoka and Leslie F. Petrik. Hydrothermal conversion of fly ash based amorphous-silica to nanocrystal BEA zeolite. *Hazardous Materials*
- **Alechine E. Ameh**, Fatoba, O. O, Nicholas M. Musyoka and Leslie F. Petrik. Acylation of anisole with benzoyl chloride over rapidly synthesised H-BEA zeolite catalyst. *Journal of Catalysis*

Presentations

- **Alechine E. Ameh**, Chuks P. Eze, Edith Antunes and Leslie F. Petrik (2018). Stability of fly ash-based Beta zeolite in hot liquid phase. Twelfth International Symposium on Heterogeneous Catalysis, 26-29 August 2018, Sofia, Bulgaria (Oral).
- Kassim Badmus, **Emmanuel Alechine Ameh** and Leslie Petrik (2018). Application of zeolite-Fe⁰ nanoparticles for the removal of toxic metals. Faraday Discussion, 16-18 May 2018, Burlington House, London, UK (Poster).

- **Alechine E. Ameh**, Roland Missengue-Na-Moutoula, Chuks P. Eze and Leslie F. Petrik (2017). Synthesis of high silica porous material from waste coal fly ash. Commonwealth Science Conference 2017, 13-16 June 2017, Singapore (Poster).



UNIVERSITY *of the*
WESTERN CAPE

Chapter 1

This chapter provides background information on porous materials with specific focus on zeolites. It is followed by a brief introduction on the effects of particulate waste such as fly ash on the ecosystem. Furthermore, the problem statement, the research statement, research questions, aims and objectives are highlighted. Thereafter, the research approach, delimitation and the thesis overview is described.

1.0 Introduction

Nanoporous materials are well-defined, porous network structures made from either organic or polymeric materials (Javaid, 2005). The classification of nanoporous materials according to the International Union of Pure and Applied Chemistry (IUPAC), into macroporous (>50 nm), mesoporous (between 2 and 50 nm) and microporous (<2 nm) depends on the pore opening of that particular material (IUPAC, 1996). The methods of synthetic design, modification, characterisation and application of both existing and novel porous materials have gained industrial and scientific attention globally (Allothman, 2012). This is due to their significant properties of high surface area, large pore openings, active acid sites and narrow and well-distributed pore size. More so, inorganic porous materials have also demonstrated good thermal and hydrothermal stability during structural modification and structural tailoring which allow further framework functionalisation (Wang et al., 2001; Yin et al., 2013). These unique characteristic lay the foundation for their extensive industrial advancements and application in different fields such as catalysis, as adsorbents, for separations, sensors, insulation, chromatography as well as host guest in drug delivery (Allothman, 2012). Among the numerous types of synthesised porous materials, research has been geared towards the synthesis and structural tailoring of zeolites with both microporous and mesoporous properties synthesised from pure chemical sources.

Zeolites are crystalline aluminosilicates with a three-dimensional framework of SiO_4 and AlO_4 that are tetrahedrally-connected based on corner-sharing oxygen atoms (Ramakrishna et al., 2011). The Angstrom pore size of the different zeolites gives these mineral phases their unique properties of size exclusion and shape selectivity in catalysis. Based on the different molar Si/Al ratios, zeolites can be grouped into low and high silica zeolites with weak or strong acid sites respectively. The usual methods used to prepare both the low and high silica zeolite is through the conventional hydrothermal process with pure chemicals. With this strategy, the synthesis of high silica zeolites involves three steps, namely: i) the

formation of organic inorganic species; ii) the polycondensation (also called the rearrangement process of the inorganic species matrix) and iii) the pyrolysis or calcination process. Consequently, the micellar species allow the silica source made from synthetic inorganic soluble silica to condense around the organic template and the template is thereafter removed by pyrolysis or calcination (Bukhari et al., 2015). The major challenge of these silicate precursors and templates is the cost of the raw materials, thereby resulting in the high cost of mass production (Misran et al., 2007). In order to overcome these limitations, an alternative and perhaps more effective source of silica needs to be developed. A number of studies have proposed the use of coal fly ash (CFA) as a recyclable, inexpensive and cheap feedstock material to produce the silica needed for the synthesis process of low and high silica zeolites (Halina et al., 2007; Chandrasekar et al., 2008).

CFA is a by-product produced during the combustion of coal in thermal plants for the generation of electricity. The recent global estimation indicates that 750 Mt of CFA is generated per annum (Yao et al., 2015). In 2011, Eskom, the main power provider in South Africa, consumed 124.7 Mt of coal per annum to generate electricity which in turn produced 36.2 Mt of CFA. However, only 5.5 % of South African CFA has been put to use while the rest (94.5 %) is disposed in dams and dumpsites (Eskom, 2011). As one of the most complex anthropogenic waste materials, if not put to more valuable use, it will constitute an environmental nuisance (Blissett and Rowson, 2012). Therefore, it is essential to develop a cost-effective technique that will utilise and transform the constituents of CFA into an eco-friendly end-product. Thus, the utilisation of CFA as feedstock for preparing heterogeneous catalysts such as zeolites could be an effective method for the reuse and recycling of part of this waste. CFA constituents are mainly inorganic minerals of their metal oxides such as SiO_2 , Al_2O_3 and Fe_2O_3 (60-70 wt%) expressed as $\text{SiO}_2 - \text{Al}_2\text{O}_3 - \text{Fe}_2\text{O}_3 - \text{EaO}$, where EaO are metal oxides of group 1, Na_2O and K_2O , metal oxides of group 2, CaO and MgO , and transition metal oxides such as MnO , ZnO , TiO_2 (Musyoka et al., 2011a; Boycheva et al., 2013; Ameh et al., 2016). Taking advantage of the silica and aluminium content in the CFA, it is of significant benefit to recover these elements. It is proposed that fly ash based amorphous silica materials can be used as feedstock for the synthesis of high silica zeolites such as BEA zeolite.

1.1 Problem statement and motivation of the study

The generation of fly ash through the burning of coal for energy production in South Africa has economic and environmental implications. Inherently, the consequence of direct disposal and storage of generated fly ash in ash dams is of great concern due to the contamination of ground water by the ash through leaching of toxic elements (Akinyemi et al., 2011). Besides, there is the problem of air pollution with the particulate matter from CFA, reduction in useable land areas and high cost of ash disposal (Eary et al., 1990). Despite all these environmental challenges, the demand for energy keeps increasing as a consequence of the high population growth and rapid industrial expansion. This increasing energy demand indirectly increases the burning of coal which in-turn raises the amount of generated coal fly ash. Environmental policy advocates the conservation of resources, which would require either safe disposal of coal fly ash or conversion into more useful materials. Hence, more valuable utilisation of residual fly ash waste via innovative approaches that will further enhance the existing remediation techniques is highly desired. This will reduce the negative impacts of coal fly ash in the environment and create alternative recycling process of the waste material.

In view of the above, a number of studies have reported the conversion of CFA to low silica zeolite (such as SOD, Na-A, Na-X and Na-Y) using both the direct and indirect hydrothermal crystallisation method (Musyoka et al., 2011a; Musyoka et al., 2011b; Ameh et al., 2017). The indirect route has become the conventional method mostly used for the synthesis of high silica zeolite such as ZSM-5 from CFA (Missengue et al., 2018). However, the problem associated with these methods is the i) existence of a large amount of unwanted and toxic elements incorporated into the framework structure of the high silica zeolite, and ii) the further addition of external silica or alumina into the solution during the dissolution of the CFA due to its low molar Si/Al ratio (2 to 6). The synthesis of BEA zeolite using a proposed three step process: fusion-extraction followed by indirect hydrothermal crystallisation to the best of our knowledge has not been reported. The extraction process following fusion allows the direct adjustment of the silica concentration (amount) in solution which in turn may increase the Si/Al ratio to the ratio needed for the synthesis of high silica zeolites. It is proposed that these steps will thereby eliminate the requirement for external addition of Si or Al to the synthesis solution, and so maximise the phase purity, improve the morphological structure and enhanced the textural properties of the CFA based BEA zeolite.

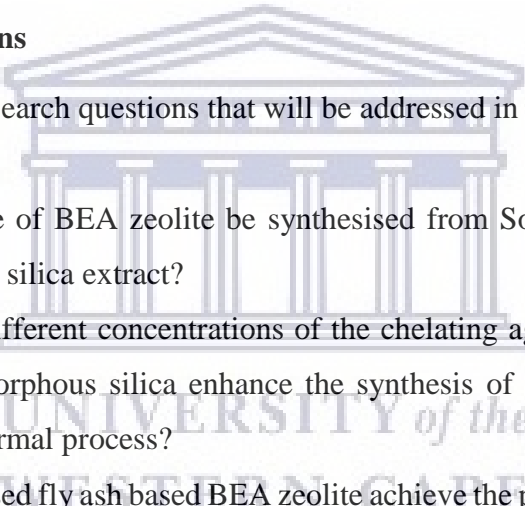
Hence, the efficient recycling of CFA as feedstock material to recover silica would be important for the production of high silica zeolites. This will not only reduce the pollution problems caused by fly ash but will ultimately enhance environmental sustainability through the production of value added porous products such as BEA zeolite and their application as green catalyst for hydrocarbon conversion.

1.2 Thesis statement

High molar Si/Al ratio feedstock for zeolite synthesis can be obtained from coal fly ash-based extract. The extracted, amorphous silica-rich feedstock can be used to design a sustainable condition for the synthesis of high purity, high silica BEA zeolite which will be catalytically active in liquid phase reaction.

1.3 Research Questions

The following are the research questions that will be addressed in this study:

- 
- Can a pure phase of BEA zeolite be synthesised from South African coal fly ash based amorphous silica extract?
 - Can the use of different concentrations of the chelating agent (oxalic acid) for the extraction of amorphous silica enhance the synthesis of BEA zeolite through the indirect hydrothermal process?
 - Will the synthesised fly ash based BEA zeolite achieve the phase purity, surface area, micro- and mesoporous structure, crystallinity and thermal stability similar to that of a typical commercial BEA zeolite?
 - What is the effect of the molar composition and synthesis time on the synthesis products?
 - Will the synthesised BEA zeolite maintain its stability when expose to hot liquid phase reaction?
 - Will the catalytic performance of the fly ash-based BEA zeolite in Friedel-Crafts acylation reaction be similar to a conventional BEA zeolite?
 - Can the BEA zeolite be regenerated after use in the acylation reaction and still retain the catalytic properties

1.4 Aims and Objectives

The aims of the study are i) to synthesis BEA zeolite by indirect hydrothermal synthesis from South Africa CFA without the addition of an extra silica source, ii) to study the behaviour of the synthesised BEA zeolite in hot liquid and iii) to apply and study the performance of the synthesised BEA zeolite in Friedel-Crafts acylation. In order to achieve these aims, the following objectives were set:

- Attain a high molar Si/Al ratio of the feedstock by use of oxalic acid as the chelating agent for the extraction of silica from CFA
- Identify and optimise the synthesis conditions such as molar formulation and synthesis time for the production of BEA zeolite from the fly ash based extract using the indirect hydrothermal process.
- Determine the stability of the synthesised BEA zeolite in hot liquid phase reaction.
- Determine the physicochemical properties and catalytic performance of the synthesised BEA zeolite in acylation reaction.
- Determine the percentage conversion, selectivity and product yield in the acylation reaction.
- Study the regeneration of the BEA zeolite after each cycle of the acylation reaction

1.5 Thesis delimitation

Conventionally, coal fly ash has been converted to BEA zeolite using mainly the direct hydrothermal synthesis process, which is similar in some aspects to the indirect synthesis route. Among the two synthesis routes, only the indirect synthesis process was considered in this study based on the fact that the direct route allows the introduction of unwanted and toxic elements from CFA into the zeolite structure and thereby, compromises the phase purity of the BEA zeolite. In order to have an in-depth understanding of the physicochemical properties of the products, fly ash based-BEA zeolite was subsequently synthesised using only one structure directing agent.

1.6 Thesis overview

This thesis is divided into nine chapters including chapter 1 (the present chapter). Its organisation is as follows:

Chapter 2 provides an overview of relevant literature on coal, coal fly ash and some classification properties of the coal fly ash. Thereafter, a comparative study is made of the different methods used to synthesise high silica zeolites such as BEA zeolite from a pure chemical source or coal fly ash, with more insights on the extraction of silica and the mechanism of the synthesis of BEA zeolite based on CFA as the feedstock material.

Chapter 3 presents all the materials and methods used and gives the experimental details of the extraction process and the hydrothermal processes that were applied to synthesis BEA zeolite. Variables investigated that were aimed at optimising suitable synthesis conditions are set out. The molar regime and synthesis methods are described. The experimental details of the performance test of the catalyst for its hot-liquid stability is given followed by the procedures used for Friedel-Crafts acylation.

Chapter 4 focuses on the results of characterisation of the raw fly ash, the extracted silica and optimising the crystal morphologies of the various synthesised BEA zeolite. A comparison is also drawn between the crystal size, crystallinity, shape, structure, surface area and thermal stability of the synthesised BEA zeolites. The optimal molar regimes for the synthesis of high purity BEA zeolite are identified. The characterisation results of the zeolite products such as elemental, mineralogical, morphological and structural analysis are presented and discussed.

Chapter 5 gives a brief context and afterwards, describes the behaviour and stability of the synthesised BEA zeolite products in hot-liquid. These aspects are then related to the different liquid-phase reaction conditions in which the synthesised zeolite can be used in real life applications.

Chapter 6 features the Friedel-Crafts acylation of anisole with benzoyl chloride over fly ash-based BEA zeolite and its regeneration and reuse.

Chapter 7 gives a summary of the results obtained in the previous chapters (4-6) and highlights the important findings and the significance thereof which led to conclusions and recommendations for future work.

Chapter 2

Literature review

Conversion of coal fly ash: a heuristic approach for the synthesis of high silica zeolite via indirect hydrothermal process

The present review focuses on various CFA synthesis procedures for the production of zeolites via the direct and indirect hydrothermal process. Detailed literature of coal, coal combustion, coal fly ash (CFA) and its classification and physicochemical properties is presented. This review highlights the limitation associated with existing literature for the production of high silica zeolites from CFA. Furthermore, suggestions are provided for the possible development of novel synthesis route for the production of high silica zeolite from CFA. Afterwards, a chapter summary is presented.

Highlights

- The component of SiO_2 and Al_2O_3 in CFA is similar to the composition of the zeolite framework
- CFA is a cheap source of aluminosilicate for the synthesis of zeolite
- Synthesis of zeolite via direct and indirect hydrothermal process is possible
- There are challenges associated with the synthesis of high silica zeolite from CFA

2.0 Introduction

Coal is a combustible, solid carbonaceous material and is a natural deposit of a sedimentary rock. Coal is mainly composed of organic and inorganic matter and ranked according to the following classifications: anthracite, bituminous, sub-bituminous and lignite coal (Sheng and Li, 2008; Ahmaruzzaman, 2010). The classification of coal depends on the degree of maturation, the fraction of carbon content and the amount of heat energy produced by the coal (Ahmaruzzaman, 2010; Xia et al., 2017). For example, anthracite has the highest heat value with a carbon content between 86 to 97% while bituminous coal with carbon content of 45 to 86% is mostly used by power plants for the production of electricity. Sub-bituminous coal contains 35 to 45% carbon with a lower heating value. Whereas, lignite coal contains the lowest carbon value (25 to 35%) and heat content (Belviso, 2018).

Coal is one of the most abundant and extensively sourced fossil fuel used for the production of energy (Burnard and Bhattacharya, 2011; Asl et al., 2019). About 1000 billion tonnes of

the coal reserves and deposit are distributed worldwide. According to the BP statistical review of world energy 2017, coal (28%) is ranked the second highest source of energy supply among other contributors such as oil (33%), natural gas (24%), hydroelectric, nuclear and renewables (as illustrated in Figure 2.1). Due to its natural abundance and availability, the demand of coal for energy production has been projected to increase with pollution growth and industrial development particularly among developing countries (Bukhari et al., 2015; Asl et al., 2019).

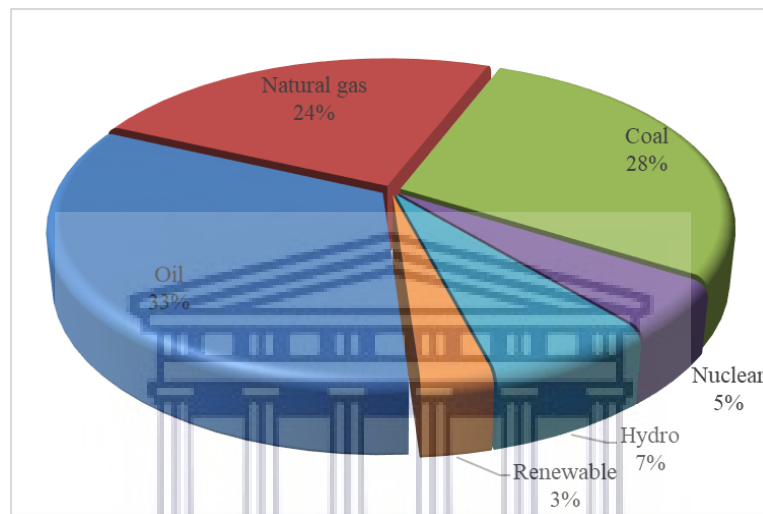


Figure 2.1: Global source of energy consumption (BP Statistical Review of World Energy 2017).

Globally, about 41 % of coal accounts for electricity production and the amount is expected to increase with 3% in the succeeding 10 years (Mehmood et al., 2012). Similarly, South Africa with an estimated reserves of 53 billion tonnes relies heavily on coal for energy sufficiency and currently the contribution of coal to the energy mix in South Africa amounts to 77%. More than 52% of South Africa electricity production depends on the continuous combustion of coal (Eskom, 2018). In 2012, South Africa was considered the second largest consumer of coal for the production of electricity, and the country's energy supply was mainly provided by coal to meet its electricity demand (WCA, 2013). Consequently, increasing energy demand indirectly increases the burning of coal which in-turn raises the amount of generated particulate CFA by-product. The combustion of coal in power plants produces a non-combustible residue of solid waste such as fine particles of CFA, bottom ash, and residual slag (Álvarez-Ayuso and Querol, 2008; Vinai et al., 2013). The world annual production rate of coal ash was estimated to be between 780 to 800 million tonnes (Mt) (Heidrich et al., 2013). The vast majority of the coal ash was made of 70-80 % CFA;

the rest of the 17-20 % burnt coal ash is composed of bottom ash, slag and/or flue gas desulphurisation (FGD) materials (Ahmaruzzaman, 2010). The continuous demand for coal subsequently leads to more CFA production.

2.1 Coal fly ash

CFA is a fine non-volatile and incombustible residue generated from the burning of pulverised coal in power plants at elevated temperature between 1200-1700 °C (Scheetz and Earle, 1998). The CFA is a powder, mainly comprised of micron size particles with a mixture of spherical particles of glassy appearance, mostly grey in colour which is mainly alkaline (Querol et al., 2002; Ahmaruzzaman, 2010). The dominant form of the coal combustion by-product of fine particles, CFA, is captured and removed by dust collectors before the release of the flue gases into the atmosphere (Saikia et al., 2006; Izquierdo, M., & Querol, 2012). The particle of a typical CFA differs in size in the micron range, with variation in colour indicating the different mineralogical composition of the CFA and the remaining unburnt coal residue (Scheetz and Earle 1998; Speight, 2005).

2.1.1 Physicochemical properties of CFA

The physicochemical properties of CAF such as morphology, chemical and mineralogical content depend on the mineralogical formation of the coal, the degree of pulverisation, type of collecting devices (emission control devices), type of furnace, the oxidation conditions and the process of storage and handling (Siddique et al., 2004; Jala and Goyal, 2006; Crelling et al., 2010). The composition and properties of the CFA is considered important because it indicates the possible applicability.

2.1.1.1 Morphology of CFA

The physical properties of CFA include different characteristics such as particle sizes, shape, colour and surface properties (Kutchko and Kim, 2006). CFA particles are predominantly micron sized, smooth, spherical shaped that may consist of hollow spheres (cenospheres) and irregular-amorphous particles or unburned carbon. The spherical shape of CFA particles can assume other morphologies including angular (lacy) opaque; non-opaque; crystals (pelospheres) non-opaque; solid spheres non-opaque; spheres of internal crystals non-opaque and rounded spheres (Fisher et al., 1976; Fisher et al., 1978; Ahmaruzzaman, 2010). Figure 2.2 presents the spherical morphology of cenospheres and magnetic sphere CFA

(Blissett et al., 2012). The smooth spherical outer surface of CFA particles are comprised of a glassy phase, consisting of an aluminosilicate matrix (Bhanarkar et al., 2008). The formation of the spheroidal shape CFA is greatly influenced first by the high combustion temperature of the coal in the economisers. The burnt, inorganic residue is gradually released into the flue gas and travels with it to the ash collection system. Upon the solidification of the inorganic fragments, the inorganic silica-rich residues experience a sudden cooling due to temperature difference which enable CFA to assume the spherical morphology (Adriano et al., 1980; Fatoba et al., 2010).

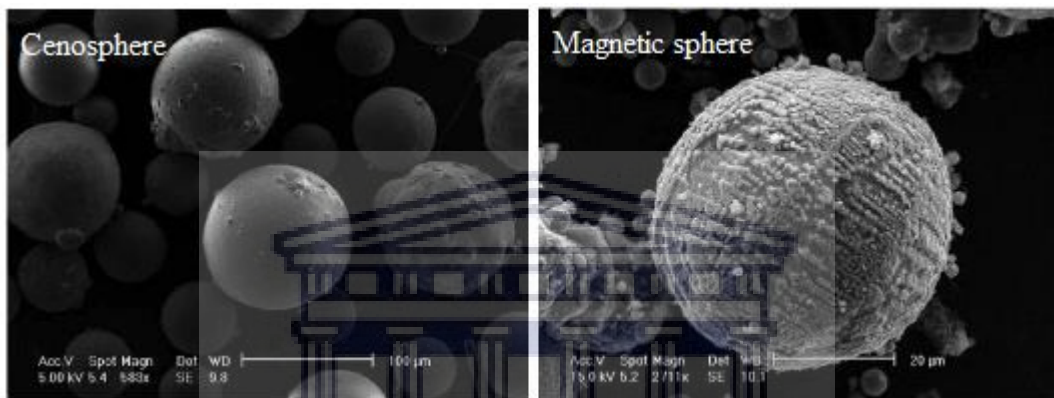


Figure 2.2: SEM micrograph of CFA morphology (Blissett et al., 2012).

The average diameter of a typical CFA varies in micrometres between 0.01 to 100 μm (Young, 1993; Cho et al., 2005). CFA generally has a surface with silt loam texture (Nyambura et al., 2011; Muriithi et al., 2013). The specific gravity of CFA varies from 2.1 to 2.9 g cm^{-3} and its bulk density is about 1.04 to 1.76 t/m^3 (El-Mogazi et al., 1988; EPRI, 2009). The appearance of CFA varies from tan to grey to brown to opaque (light grey), depending mainly on the percentage of carbon content and Fe_2O_3 in the CFA. Generally, the unburnt carbon content is responsible for the lighter grey or brown colour and as it becomes dark brown, this signifies the presence of Fe oxide (either Fe^{2+} or Fe^{3+}) in the CFA (Raclavska et al., 2009; Shaheen et al., 2014).

2.1.1.2 Mineral composition of coal fly ash

The complexity of coal fly ash is due to the different mineral phases that emanated from the mixture of the inorganic and organic content of the coal, the chemical composition of the coal as well as the processes involved during the coal combustion (such as the collection process of the coal and fly ash) (Vassilev and Vassileva, 2005; Blissett and Rowson, 2012).

Majorly, CFA contains a higher percentage of inorganic components (90–99%) and a lower organic component (>10 %). The inorganic component is made up of amorphous (non-crystalline) matter (34–80%) and crystalline matter (17–63%) (Vassilev and Vassileva, 2005) with a high amount of SiO₂ (15-60%) present in the amorphous glass phase (Tishmack and Buruns, 2004).

At present, about 316 individual mineral phases and 188 mineral groups have been identified as the major constituents of CFA (Blissett and Rowson, 2012). Examples of the mineral phases are: quartz (SiO₂), mullite (Al₆Si₂O₁₃), magnetite (Fe₃O₄), lime (CaO), calcite (CaCO₃), hematite (Fe₂O₃) and pyrite (FeS₂) as well as tricalcium aluminate (Ca₃Al₂O₆), melilite (Ca₂(Mg,Al)(Al,Si)₂O₇) and merwinite (Ca₃Mg(SiO₄)₂) among others (White and Case, 1990; Moreno et al., 2005). Among all the identified mineral phases present in the parent coal, only quartz remains in CFA after the thermal combustion (White and Case, 1990). In 2008, Fatoba et al. delineated that the major crystalline mineral phases in two South Africa coal fly ashes were quartz (SiO₂) and mullite (3Al₂O₃.2SiO₂). Lime and calcite mineral phases were noticed in low/small concentration. Musyoka et al., (2011a) showed similar trends after conducting a comparative study on three South Africa coal fly ash samples collected from different power plants. They found that the major mineral phases of South African coal fly ash are mainly quartz, mullite and hematite with a low amount of lime content.

2.1.1.3 Chemical composition of CFA

The chemistry and properties of the coal greatly influences the chemical composition of the CFA generated. Since coal is classified into anthracite, bituminous, sub-bituminous and lignite, it is evident that the inorganic chemical constituents of the coal are similar to the composition of the burnt CFA (Siddique, 2004; EPRI, 2009; Bukhari et al., 2015). CFA is composed mainly of major oxides of silica, alumina, iron and calcium as well as varying amounts of unburnt carbon (Crelling et al., 2010).

Table 2.1 shows the chemical composition of CFA that remains after the combustion of anthracite, bituminous, sub-bituminous and lignite coal.

Table 2.1: Chemical constituent of burnt CFA from anthracite, bituminous, sub-bituminous and lignite coal (Adriano et al., 1980; Ahmaruzzaman, 2010; Barnes, 2010).

Component (wt%)	Anthracite	Bituminous	Sub-bituminous	Lignite
SiO ₂	28–57	20–60	40–60	15–45
Al ₂ O ₃	18–36	5–35	20–30	10–25
Fe ₂ O ₃	3–16	10–40	4–10	4–15
CaO	1–27	1–12	5–30	15–40
MgO	1–4	0–5	1–6	3–10
SO ₃	0–9	0–4	0–2	0–10
Na ₂ O	0–1	0–4	0–2	0–6
K ₂ O	0–4	0–3	0–4	0–4
LOI	1–8	0–15	0–3	0–5

As summarised in Table 2.1, the Loss on Ignition (LOI) measures the amount of unburned carbon in CFA (Foner et al., 1999; Koukouzas et al., 2009). Other metal oxides such as magnesium and sulphur, K, Mg, Na, Ti and P alongside trace elements of Co, Cd, As, Se, Zn, Mo, Mn, Pb, B, Cu and Ni in parts per million (ppm) are embedded in the core matrix of CFA (Crelling et al., 2010). The variation in chemical composition of the burnt anthracite, sub-bituminous, lignite or bituminous coal is used as the threshold to classify CFA (Iyer and Scott, 2001). According to the American Society for Testing Materials standards (ASTM C618), CFA can be classified into Class F or C. This is based on the summation of total weight percentage (wt %) of Si, Al and Fe oxides and the amount of the CaO content is presented in Table 2.2.

Table 2.2: ASTM standard classification of CFA (ASTM C 618, 1993).

Properties	Class F	Class C
SiO ₂ + Al ₂ O ₃ + Fe ₂ O ₃ , max., %	70	50
CaO, max., %	≤8	≤35
SO ₃ , max., %	5	5
Moisture content, max., %	3	3
LOI, %	<12	<6
Available alkali (as Na ₂ O), max., %	1.5	1.5

Basically, the chemical composition of Class F CFA ash usually contains more than 70 wt% SiO₂, Al₂O₃, Fe₂O₃ but has a low percentage of lime (CaO) content (≤ 8%). Most of Class F CFA is usually the product of burnt bituminous and anthracite coal. Whereas, Class C CFA

are products derived from burnt lignite and sub-bituminous coal with a SiO_2 , Al_2O_3 , Fe_2O_3 content in the range of 50 – 70 wt% and a significantly higher CaO content, between 10 to 35%. Furthermore, the amount of unburned carbon is low in Class C CFA compared to Class F CFA (see Table 2.2) (Vassilev and Vassileva, 2007; Ameh et al., 2017; Belviso, 2018). Apart from the classification based on the difference in the Si, Al, Fe and Ca oxide content, Vassilev and Vassileva (2007) suggested that CFA can also be classified into four groups with respect to the $\text{SiO}_2/\text{Al}_2\text{O}_3$ ratio and the content of Ca oxide. The first group is referred to as the silico-aluminate rich CFA with $\text{SiO}_2/\text{Al}_2\text{O}_3$ ratio ≥ 2 , while the second group is alumina-silicate rich CFA with $\text{SiO}_2/\text{Al}_2\text{O}_3 < 2$ and $\text{SO}_3 < 3\%$; both groups have CaO content less than 15%. Group 3 is lime sulphate CFA with CaO content greater than 15% and SO_3 less than 3% while the fourth group is the basic CFA with CaO content greater than 15% and SO_3 less than 3%.

South Africa CFA has a relatively high concentration of SiO_2 , and Al_2O_3 (Somerset et al., 2004). Comparing three different South Africa CFA from three power plants, Musyoka et al. (2012b) shows that >70 wt% of the CFA components are $\text{SiO}_2 + \text{Al}_2\text{O}_3 + \text{Fe}_2\text{O}_3$ which belong to a typical Class F. They further indicated that the elemental composition varies according to handling process and origin of the coal and location of the power stations.

Table 2.3: Elemental composition of CFA sourced from different power plants in South Africa.

Major oxide	Mass, wt%				
	Musyoka et al. (2012a)	Doucet et al. (2016)	Ojumu et al. (2016)	Ameh et al. (2017)	Madzivire et al. (2019)
SiO_2	49.8-50.9	49.3	55.4	56.2	51.1
Al_2O_3	27.3-30.9	34.0	31.5	26.8	29.2
Fe_2O_3	3.12-4.8	5.8	4.9	5.3	3.2
CaO	3.7-6.2	5.1	3.8	4.7	7.5
MnO	0.02-0.1	-	0.03	0.05	0.04
MgO	1.0-1.48	1.0	1.2	1.4	2.2
Na_2O	0.07-0.1	-	0.04	-	0.5
K_2O	0.6-0.7	0.9	0.5	0.7	0.7
P_2O_5	0.6-0.7	0.6	0.3	0.4	0.9
TiO_2	0.3-1.7	2.0	1.1	1.7	1.7
SO_3	0.2-1.7	0.2	0.1	-	0.6
LOI	3.9-6.6	0.5	1.2	3.6	-
$\text{SiO}_2/\text{Al}_2\text{O}_3$	1.5-2.0	1.5	1.8	2.1	1.8

Table 2.3 present the variation in the elemental composition of different South Africa coal fly ash. South Africa CFA thus consists mainly of Si, Al, and Fe oxides content, greater than 75% of the total oxides composition. It is evident that the CaO content is below 8% assigning the CFA into Class F with SiO₂/Al₂O₃ ratio of about 2. Moreso, CFA is characterised by the chemical composition of other minor oxides which include Mg, K, P, Mn, Ti and S which constitute about 4.2% of CFA (Musyoka et al., 2012a; Doucet et al., 2016; Ojumu et al., 2016; Ameh et al., 2017; Madzivire et al., 2019). The presence of trace elements such as Co, Cu, Nb, Ni, Pb, Rb, Y, V, and Zn were found in the matrix of CFA in low concentrations and this might classify the material as toxic (Jegadeesan et al., 2008; Pandey et al., 2011). Presented in Table 2.4 are examples of trace elements in various South Africa coal fly ash.

Table 2.4: Trace elemental composition of CFA sourced from different power plants in South Africa.

Trace element	Concentrations (ppm)		
	Musyoka et al. (2012a)	Ojumu et al. (2016)	Ameh et al. (2017)
Ba	-	486	389.9
Ce	-	254	228.23
Co	12.55-33.32	30	-
Cr	-	-	235.68
Cu	50.88-51.15	110	100.79
Mo	-	-	2.23
Nb	38.54-44.96	37	40.86
Ni	58.12-72.29	125	111.87
Pb	65.37-82.61	90	83.32
Rb	28.45-42.14	56	60.63
Sr	957.41-1194.85	989	1363.11
Th	-	-	43.36
U	-	-	35.53
V	85.11-125.55	79	76.68
Y	15.31-76.71	94	92.09
Zn	45.01-118.28	135	88.73
Zr	403.98-527.84	-	637.99

2.1.2 Environmental challenges of CFA

The burning of coal contributes significantly to the emission of gaseous and particulate pollutants. Aside from the gaseous pollutants of CO₂, SO_x, NO_x, CFCs and trace gases, the release of particulate pollutants such as CFA has been viewed as a possible hazard to human health and the environment (Nelson et al. 2010). This is because CFA contains substantial amount of several trace elements contained in fine micro size which are environmentally

sensitive (Saikia et al., 2006; Yao et al., 2015). The toxicity of CFA due to the organic and inorganic constituents pose severe environmental challenges such as: i) contamination of ground water and soil through the leaching of toxic elements such as Se, Cr, B and Ba, ii) carcinogen effects, iii), iv) exposure to background radiation since CFA contains radioactive elements such as U and Th (Borm, 1997; Ahmaruzzaman, 2010), v) air pollution because of its fine particles and vi) render large arable land areas unusable (Eary et al., 1990). Furthermore, Akinyemi et al. (2011) noticed that the impoundments of toxic elements in CFA resulted in the accumulation of toxic metals which contaminate ground water. Also, the soluble species build-up as salts and alkalinity in the fly ash dump thereby altering pH and when leached by weathering, would affect the permeability of sediments.

CFA is one of the most abundant residual by-products among other particulate sources of industrial wastes in the world (Jankowski et al., 2006). However, only a small part (20-30 %) of the generated CFA is employed and utilised while the rest (45-50 %) of CFA is being disposed in landfills (Álvarez-Ayuso and Querol, 2008), or disposed in ash dams and dumps as landfills (Eskom, 2011). In South Africa, only 1.2 million tons of the available 25 million tons generated CFA are used for brickmaking, dam building and as an extender for cement manufacturing (Eskom, 2016). The industrial ecology (IE) has been advocating the conservation and reuse of the generated waste by-product. The efficiency of any sustainable waste management is when the by-product generated by a particular industry becomes a feedstock material of value for other industry. With this, it reduces the negative environmental impact and economic cost of managing the by-product disposal (Quijorna et al., 2011). Therefore, the reuse of CFA can have a direct positive impact on the environment and upon socio-economic development. Consequently, considerable effort for the effective beneficiation and/or utilisation of CFA continues through research, thus process development is highly needed (Wang and Wu, 2006; Zacco et al., 2014). Hence, the main focus of this study is the transformation of CFA into value added products beneficial to the economy.

2.1.3 Potential use of CFA

CFA is predominantly classified as a hazardous material, however, it has the potential to be employed as a value-added material for other industrial applications. Research has demonstrated the importance of the development of sustainable techniques to source and recover useful components from CFA as a feedstock material for various industrial uses

(Blissett and Rowson, 2012). Moreover, the potential applications of CFA as a prized material is based on their physicochemical properties (Boycheva et al., 2013). A number of uses for CFA have been reported as summarised in Figure 2.3.

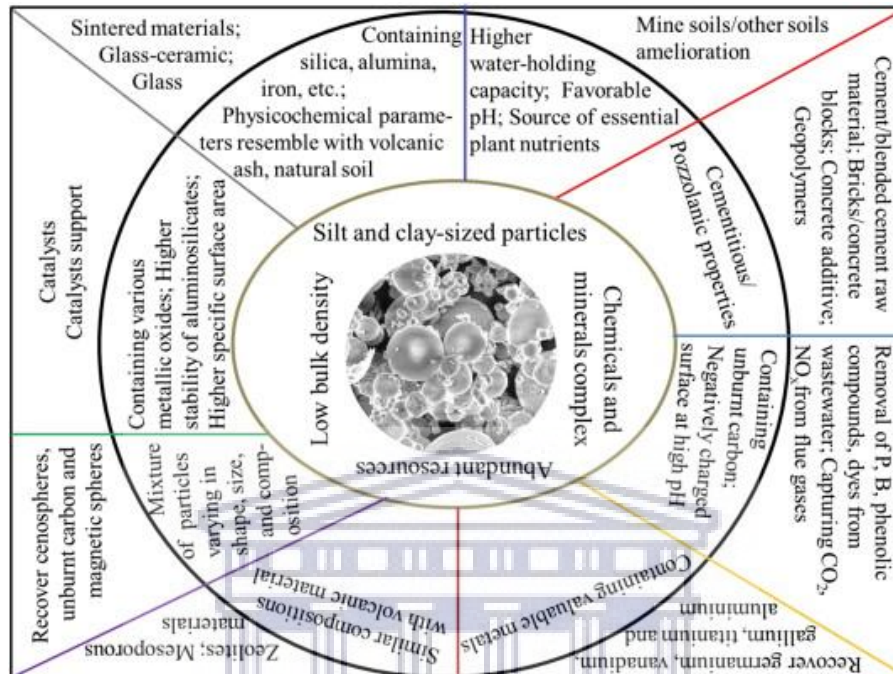


Figure 2.3: Potential applications of CFA (Yao et al., 2015).

The physicochemical property of CFA such as water holding capacity and surface area enhance its application as adsorbent of molecules and particles of different sizes (Ahmaruzzaman, 2010). Pathan et al., (2003) reported that CFA can be used to increase the soil water-holding capacity which in turn increases the soil's cation exchange capacity (CEC). Furthermore, Madzivire et al., (2010) demonstrated the removal of sulphates and heavy metals from wastewater using CFA as the adsorbent. This is because the alkaline nature of the CFA serves as the neutralising agent thereby favouring the adsorption of most metals in form of hydrous oxide by adjusting the pH of the wastewater (Petrik et al., 2005). Furthermore, CFA has been widely utilised in construction materials such as additive in cement and other building materials (concrete), and structural filling materials as well as in small scale production of geopolymer materials and zeolite crystals (Álvarez-Ayuso and Querol, 2008; Yao et al., 2015). Moreover, the geochemical properties such as thermal behaviour, specific gravity, permeability and internal angular friction of CFA have enable CFA to function as additive in road construction (Ahmaruzzaman, 2010). Activation of CFA with alkaline solution under low temperature allows for the production of cementitious

materials also known as geopolymers (Rattanasak and Chindaprasirt, 2009). Geopolymers are mineral polymers that are formed from the geopolymerisation of the alumina-silica chain. Due to the properties of geopolymers such as high resistance to fire, durability and high mechanical stability, geopolymers have been used as ceramics, in cement production and as fire-resistant materials (Cioffi et al., 2003; Yao et al., 2015).

Alternative the reutilisation of CFA have been reported as a value-added feedstock material in the synthesis of zeolites. The framework structure of zeolite is a network of silica and alumina precipitated from aluminosilicate precursor or gel under hydrothermal treatment (Boycheva et al., 2013). Generally aluminate and silicate compounds are commercially sold in pure form such as aluminum isopropoxide, aluminum hydroxide, alumina trihydrate, sodium aluminate, sodium silicate, silica sol, which are used as the Al and Si source for the synthesis of zeolites (Andaç et al., 2005; Bukhari et al., 2015). However, CFA contains amorphous and/or crystalline inorganic minerals, mainly elemental oxides of SiO_2 and Al_2O_3 as well as other metal oxides such as K_2O , CaO and MgO . Consequently, the elemental composition of Si and Al in CFA can be used as a source of aluminosilicate for the synthesis of zeolites (Boycheva et al., 2013). Inada et al., (2005), Tanaka et al., (2006) and Musyoka et al., (2012b) have applied the direct and indirect hydrothermal synthesis methods to synthesise low silica zeolite such as Na-P1, X and A form CFA respectively. The production of high silica zeolite from CFA offers another route to use the waste by-product to form a valuable material.

2.2 Zeolite

Zeolites are crystalline aluminosilicates with a three-dimensional framework of SiO_4 and AlO_4 . The tetrahedral unit of the TO_4 , where the T atom can be Si or Al, are connected through bridge corner-sharing oxygen atoms, thus generating a 3D microporous structure (Ramakrishna et al., 2011; Li and Yu, 2014). Natural zeolites are found abundantly in nature mostly in deposits of volcanic rocks (Byrappa and Yoshimura, 2001; Querol et al., 2002; Andrade et al., 2008). Minerals such as analcime, chabazite, erionite, ferrierite, heulandite, laumontite, mordenite and phillipsite are zeolitic and are named after the geologists who discovered those (Wang et al., 2008). Zeolites can also be synthesised using different combinations of inorganic chemical sources of Si, Al and mineralising agent of alkaline or alkaline-earth metals and may have the addition of structure-directing-agents (SDA).

Numerous synthetic zeolites have been successfully made through hydrothermal processes, this includes: A (Na, Ca, K), zeolite X (Na, K, Ba), zeolite Y (Na, Ca, NH₄), zeolite L (Na, H), zeolite MOR (H, Na), ZSM-5 (Li et al., 2018) and BEA (Vaudry et al., 1997).

To date, the International Zeolite Association (IZA) nomenclature assigned a given three-letter code to about 176 distinctive zeolite framework (Baerlocher et al., 2007; Bukhari et al., 2015), however, more than 235 framework have been documented by IZA (<http://www.iza-online.org/>). The framework structure of a typical zeolites consist of oxygen and silicon primary building units with aluminium replacing some of the silicon to form aluminosilicate blocks which are arranged into the tetrahedral geometry of the secondary building units (Martinez Sanchez and Pérez Pariente, 2011). The crystallographic unit cell of the structure of the zeolite are represented by equation 2.2:



Where M is an exchangeable, charge balancing alkali or alkaline earth ion, m the number of water molecules per unit cell, n is the number of valence of the cation and x and y is the sum of tetrahedra per unit cell. The $[(AlO_{4/2})_x (SiO_{4/2})_y]$ represents the framework composition and these species are joined tetrahedrally according to Löwenstein's rule where the value of y/x must be equal or greater than one. Generally, the charge of the tetrahedral SiO₄ units is neutral, thus with the replacement of Si⁴⁺ by Al³⁺, a negative charge is generated in the framework. To this end, an inorganic cations of alkali or alkaline earth metal such as Li⁺, Na⁺, and K⁺ or organic cation such as tetramethylammonium, tetraethylammonium, and tetrapropylammonium are used to counter balance the negative charge of the zeolite framework (Jiang et al., 2001; Sun et al., 2009; Guo et al., 2017). Figure 2.4 present the tetrahedral [SiO₄]⁴⁻ with the substituted [AlO₄]⁵⁻ and the charge balance cation (negative ions) of a typical zeolite framework structure.

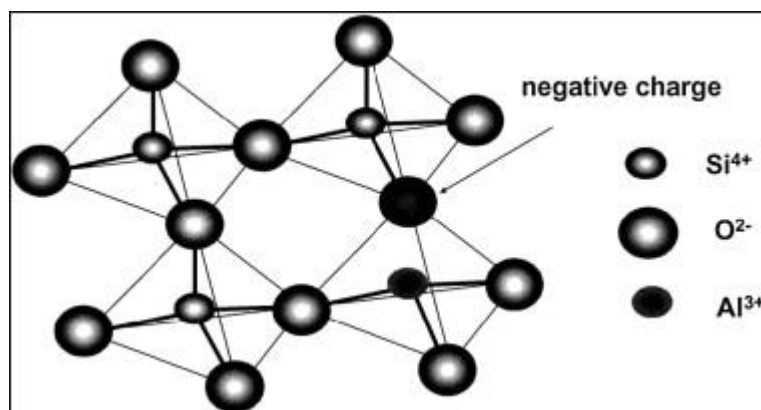


Figure 2.4: Framework structure of zeolite showing the respective tetrahedral $[\text{SiO}_4]^{4-}$ and substitution $[\text{AlO}_4]^{5-}$ with the negative charge cations (Querol et al., 2002).

The substitution of Al^{3+} in the Si^{4+} tetrahedra results in an overall negative charge that forms Brönsted acid sites in the structure located within the square brackets in the equation (2.1) above. This Brönsted acid site is compensated by the presence of positively charged alkali or alkaline cations of Na^+ and K^+ that reside in the pores as charge balancing entities, thereby making the zeolites structure neutral (Martínez and Pérez-Pariente, 2011). Thus, each negatively charged Al atom is compensated by a positive cation and when the cations are substituted with hydrogen ions by ion-exchange a strong acid site is created. Furthermore, this site can be converted to a Lewis acid site through dehydroxylation (Na and Somorjai, 2015). Figure 2.5 illustrates the Brönsted acid hydroxyl and Lewis acid site (Barzetti et al., 1996).

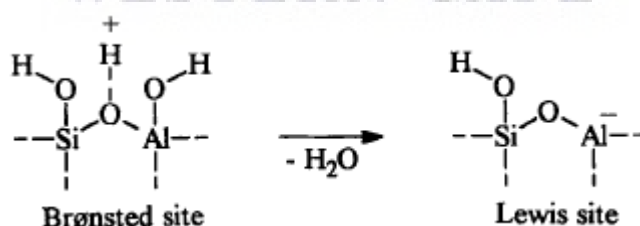


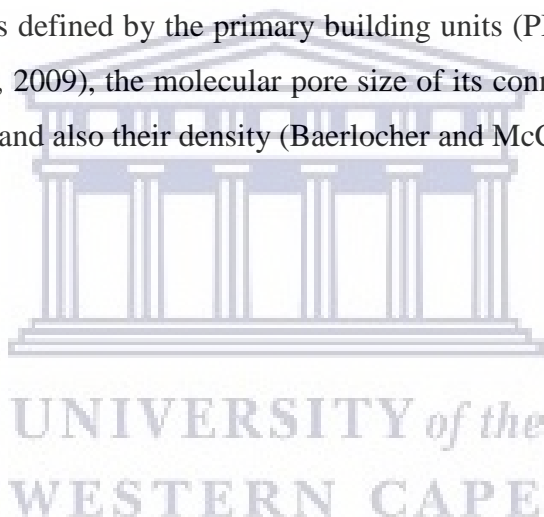
Figure 2.5: Schematic for Brönsted acid hydroxyl (Barzetti et al., 1996).

The arrangement of silica, aluminium and oxygen (Si-O-Al-O-Si) within the lattice framework of zeolites follows an observation expressed by Lowenstein's rule which states that two neighbouring Al-O-Al linkages cannot connect via an oxygen bond in the zeolite structure because of the electrostatic repulsions associated with the negative charge of AlO_4^- (Zhao et al., 1997; Weitkamp, 2000). The configuration of the siloxane bond can be modified

by replacing tetrahedral AlO_4^- with elements having a valence of three or four, mostly found in group III and IV of the periodic table. Furthermore the extra-framework cation of a monovalent or multivalent element (mostly with charge of +1, +2 and +3) sitting in the zeolite voids and cavities can be ion-exchanged with organic, inorganic metals or rare earth metals in an aqueous or solid phase which give rise to high ion-exchange capacity of zeolite (Chester and Derouane, 2009; Wright and Lozinska, 2011). Other unique properties defined by the regular voids or open spaces in the matrix of the zeolite include porosity, size-shape selectivity (molecular sieve nature), and reversible hydration (Nagy et al., 1998). These properties elucidate the differences between various framework structures of zeolites.

2.2.1 Classification of zeolites

The framework structure of zeolite structures are mainly built from primary and secondary building units. Zeolite is defined by the primary building units (PBU), secondary building units (SBU) (Carr et al., 2009), the molecular pore size of its connecting cage, aperture of the cavities or channels and also their density (Baerlocher and McCusker, 2007).



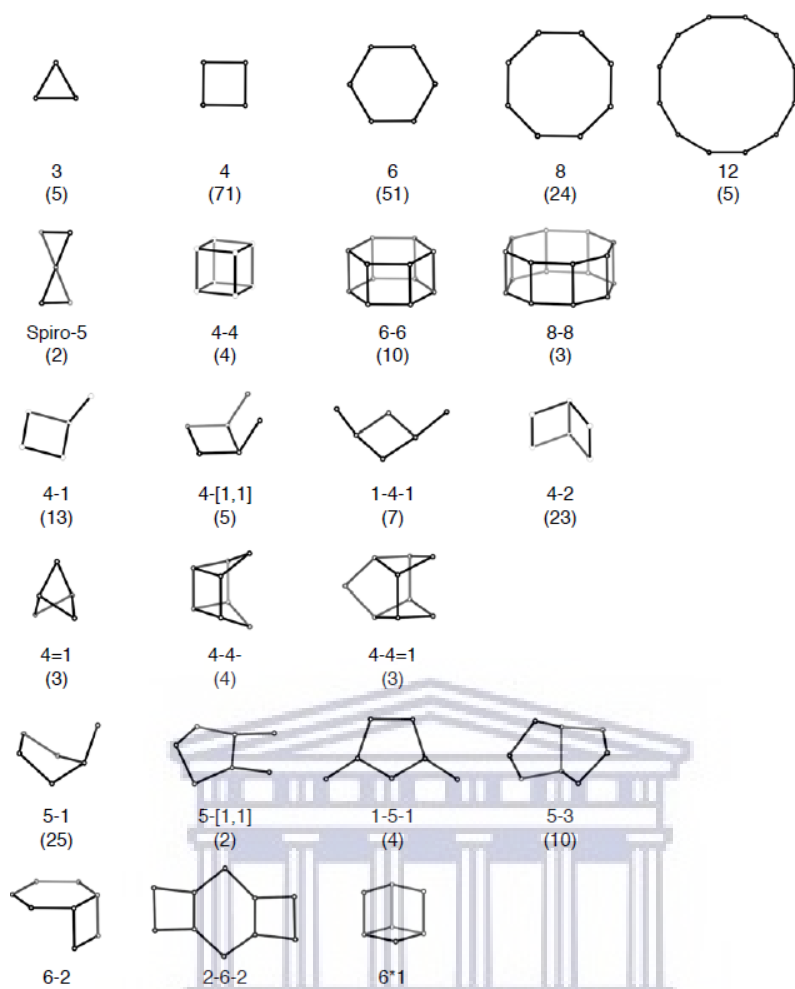


Figure 2.6: Secondary building units of zeolites framework (Baerlocher et al., 2007).

The primary tetrahedral building unit is the tetrahedron of TO_4 , where T is central tetrahedrally bonded atom to either Si or Al atom by corner-sharing oxygen atoms. This makes up the three-dimensional network containing pores and cages that are mainly occupied by cations of group I and II, and H_2O (Querol et al., 2002). By linking the tetrahedra of the T atoms in geometric array of periodic squares, pentagons, hexagons or octagons patterns the secondary building units (SBU) are developed. The combination of repeated unit of several tetrahedral units define the zeolite framework structure (Morris, 2005; Wright and Lozinska, 2011) (see Figure 2.6).

The combination of the T-atoms (primary units) elucidate the connection of the SBUs cage in a manner of T-O-T linkage (by sharing of their square faces). These units build the interconnected TO_4 tetrahedra structure but due to the different arrangement of the lattices by specific number of connected units divers zeolite framework are produced (Weitkamp,

2000; Li and Yu, 2014). Different tetrahedral atoms connectivity showing various topologies of zeolite framework structure are presented in Figure 2.7.

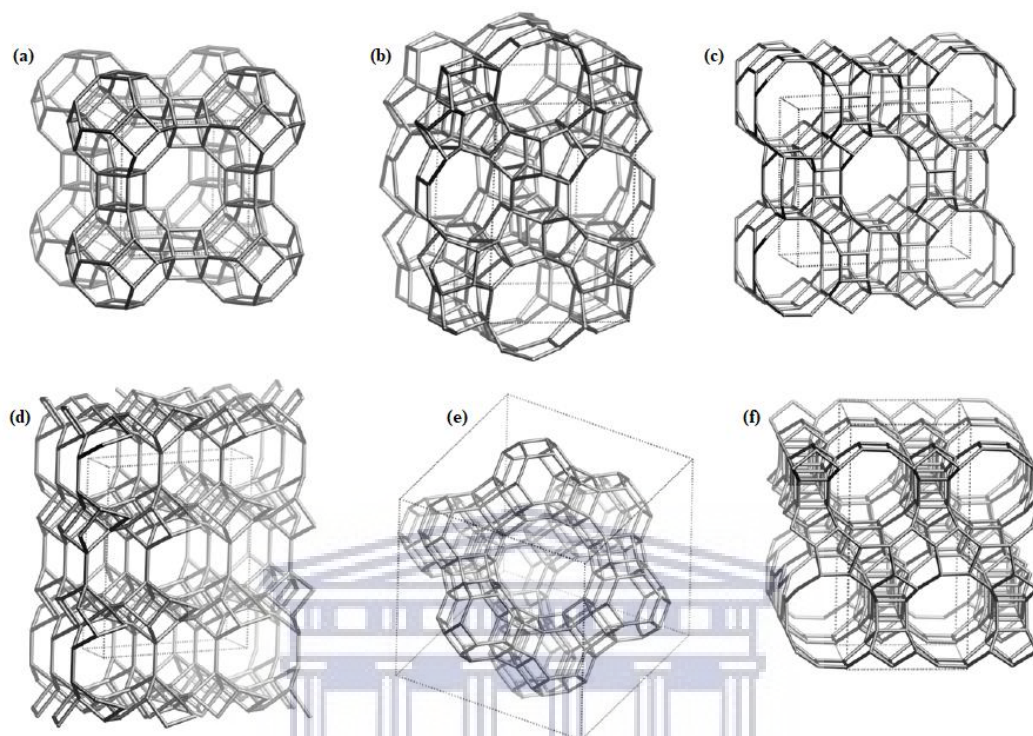


Figure 2.7: Example of framework structure of a) LTA, b) MFI, c) HEU, d) MOR, e) FAU and f) BEA zeolites (Baerlocher et al., 2007).

Each of the framework structures as documented in the Atlas of Zeolite Framework Types were given a three-letter nomenclature code such as LTA (Linde type A), SOD (sodalite), CHA (chabazite), MFI (ZSM-5), HEU (heulandite), MOR (mordenite), FAU (faujasite), GIS (gismondine) and BEA (beta) (Baerlocher et al., 2007; Gross et al., 2007). Among the documented zeolite structures most research and industrial applications have been focused on the following MOR, FAU, BEA, FER and MFI (Yilmaz et al., 2012).

Zeolite frameworks are also defined based on their pore size and shape, which are described in terms of the designated numbers (n) and arrangement of T atoms (T = Si or Al) in the n-ring (shape), and the interconnectivity of the cage or channels (Frost and Sullivan, 2010). It is, moreover, seen that the pores are bonded by oxygen atoms of connected n-rings consisting of different structural features such as four, six, eight, ten, or twelve membered rings according to the subunit summation of the secondary building blocks (Pophale et al., 2011). These structural features have shown ring-like pore-openings. For example, SOD

structure constitutes of six-membered-ring windows (4 rings SBU) of the β -cages which have the smallest pore size of 0.28 nm. However, connecting eight of the sodalite cages (α -cage) led to the formation of zeolite-A with an accessible pore size of 0.41 nm through octahedral six eight-membered-ring windows (4-4 SBU) formation. Through a prism hexagonal arrangement of sodalite cages, zeolite X and Y with channels of four 12-membered-ring window (6-6 SBU) was formed. A typical zeolite X or Y has a large pore opening of about 0.74 nm (Weitkamp, 2009).

The International Union of Pure and Applied Chemistry (IUPAC) has classified porous materials according to the pore size distribution namely: microporous (< 2 nm), mesoporous (≥ 2 but ≤ 50 nm) and macroporous (> 50 nm). The frameworks of zeolites can be categorised into rings of various sizes, which is associated with the pore opening and channels of zeolites. The pore opening of zeolites is defined on the basis of the number of TO_4 tetrahedra and the pores with more T atoms connected to oxygen atoms have a larger pore size. Thus, zeolites can be categorized into small pore (delimited by 8 TO_4), medium pore (10 TO_4), large pore (12 TO_4), and extra-large pore (more than 12 TO_4) (Li and Yu, 2017).

- i. Small-pore zeolites (≤ 8 -ring): include those pore opening structures made of six, eight or nine-member oxygen rings such as Na-A zeolite.
- ii. Medium-pore zeolites (10-ring): have a pore opening structure of 10-member-rings such as offretite, ferrierite, ZSM-5 and silicalite.
- iii. Large-pore zeolites: have 12-member-ring window such as zeolite X and Y (faujasite) and mordenite (MOR) (Matsukata et al., 2011). To differentiate between X and Y, zeolite X has a Si/Al ratio of 1-1.5, while zeolite Y lies within 1.5-3 Si/Al ratio (Masoudian et al., 2013).
- iv. Extra-large pore zeolites have more than 12-member-ring window such as BEA zeolite

Examples of the zeolite pore size and channels illustrating the oxygen model is presented in Figure 2.8.

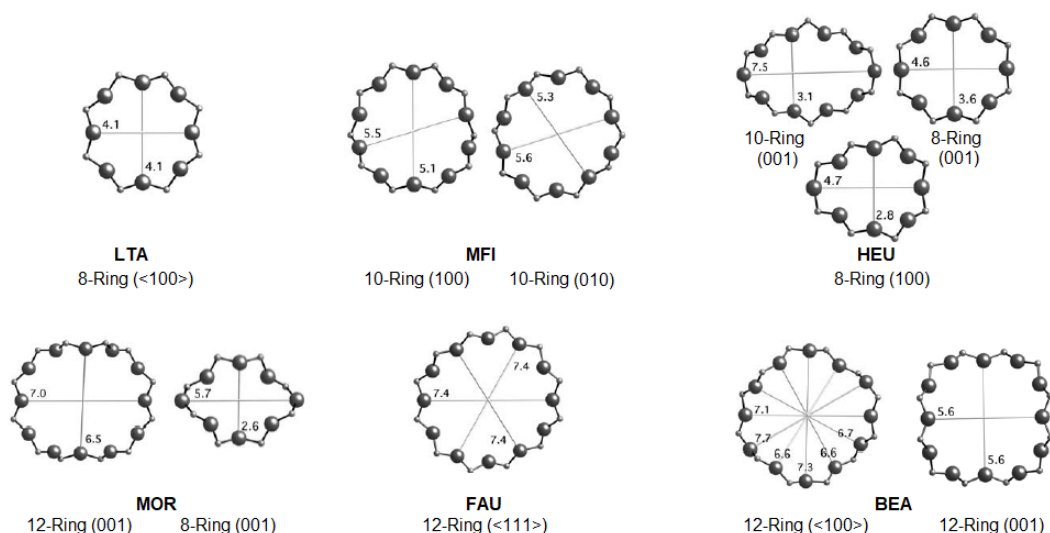


Figure 2.8: Example of pore opening of various zeolite framework structures (Baerlocher et al., 2007).

The pore diameter of the 8-membered ring zeolites range from 0.3 to 0.45 nm whereas the medium pore zeolites of 10-membered ring possesses a larger pore diameter with a size between 0.45 to 0.6 nm. The 12-membered ring zeolites have the largest window (pore) diameter greater than 0.6 nm to 8 nm (Ramesh and Reddy, 2011; Wright and Lozinska, 2011). The pore space is usually embedded into the cages of zeolite called cavities which lie within the polyhedral units of the zeolite framework (Baerlocher et al., 2007). Baerlocher et al., (2007) reported that the maximum density for the zeolite framework is where T-atom ranges from 12 to 21 T-atom per 1000 \AA^3 compared to the non-zeolitic framework which ranges from 20 to 21 T-atom per 1000 \AA^3 . Thus, the framework density reflects the pore volume within a zeolite structure, this distinguishes different zeolite types and any other dense tetrahedral framework structure such as AlPO_4 as seen in Table 2.5 (Xu et al., 2007).

Table 2.5: Examples of different zeolites illustrating their shape, SBU and framework density.

Zeolite type	Shape	Ring number	SBU	Framework density (Tatom/nm^3)
LTA	Cubic	8 ring	8, 4-4, 6-2, 6, 1-4-1 or 4	12.9
MFI	Orthorhombic	10-10 ring	5-1,	17.9
HEU	Monoclinic	10-8-8 ring	4-4,	17.1
MOR	Orthorhombic	12-8 ring	5-1,	17.2
FAU	Cubic	12 ring	6-6, 6-2, 6, 4-2, 1-4-1 or 4	12.7
BEA	Tetragonal	12-12 ring	4-4, 4 or mtw	15.1

The pore diameter of the zeolite structure is greatly influenced by the size of the tetrahedral ring of the secondary building units (SBU) (Jia et al., 2018).

2.2.2 Principle components and their roles in the synthesis of zeolites

Zeolite are generally produced by the hydrothermal conversion of a sol-gel solution containing silica, alumina, mineralising agent (hydroxide cation or fluoride anions) and/or structure-directing agent and a solvent. The aqueous solution is subjected to other physical conditions such as autogenous pressure, reaction time and elevated temperatures for the crystallisation of zeolites (Hould et al., 2009; Grand et al., 2016). The inorganic and organic components influence the induction, nucleation and crystal growth mechanism of zeolite formation (Derouane et al., 1992). Generally, both the inorganic and organic species make up the precursor for the synthesis of zeolites. These components are usually expressed as the molar ratios of the reactive oxides: $\text{SiO}_2 : \text{Al}_2\text{O}_3 : \text{M}_2\text{O} : \text{R} : \text{TO}_2 : \text{H}_2\text{O}$, where M is the alkali metal atoms of Na, K or Li among others, R is the organic structure directing agent (OSDA) and H_2O is solvent for the synthesis mixture. Water is mostly used as the solvent nevertheless it is possible to use alcohols, diols and ammonia as solvent for the synthesis process (Grand et al., 2016). Each of the determinate factors that can impact on the formation of zeolite is further discussed in the subsequent sub-sections.

2.2.2.1 Silicon and aluminium sources

The precursor composition for the synthesis of zeolites is a mixture of silica and alumina in an alkaline condition. This aqueous gel initiates the formation of nonhomogeneous amorphous precursors by creating an exchangeable interphase between the undissolved solids and alkaline solution, thereby promoting the dissolution of the reactive species. Interestingly, with exposure to prolonged hydrothermal treatment, the dissolved species crystallise into microporous structures as illustrated in Figure 2.9 (Cundy and Cox, 2005; Li et al., 2018). In this case, the dissolution of silica can only be achieved when the solid/liquid interphase is at equilibrium.

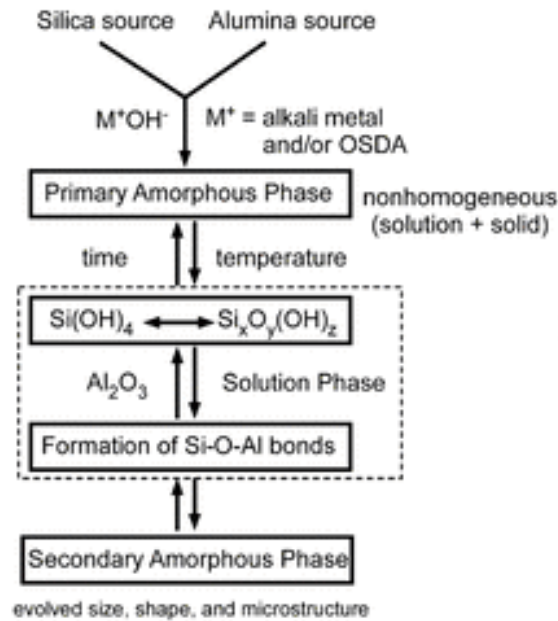


Figure 2.9: Pathway of silica and alumina source in the formation of primary and secondary building unit of zeolite structure (adopted with modification from Cundy and Cox, 2005).

Consequently, the role of silica source can be related to their degree of polymerisation which influence the monomeric or polymeric species whereas undissolved silica is cross-linked within the alumina matrix during the condensation process of aluminosilicate species (Lai et al., 2000; Kumar et al., 2016; Li et al., 2018). Hence, the source, purity and reactivity of the silica and alumina is important because it can influence the phase purity and catalytic performance of the synthesised zeolites (Robson, 2001; Losch et al., 2016). Different types of silica source such as colloidal silica, fumed silica, and alkali silicate have been reported for the successful synthesis of zeolites (Kumar et al., 2016). According to Georgiev et al. (2009), the production cost of different source of silica and alumina are expensive. In this regard, the present study focus on the use of coal fly ash as a cheap source of silica and alumina needed for the synthesis of high silica zeolite.

2.2.2.2 Mineralising agent

The mineralising agent is an important factor in the crystallisation process of zeolite because it enhances the dissolution and precipitation of the silicate and aluminosilicate source in the synthesis solution. During the zeolitisation process, the mineralising agent depolymerise or hydrolyse the aluminosilicate species in the synthesis mixture. The chemical species of the mineralising agent are consumed during the dissolution and rearrangement process but they are recovered during the condensation of the nuclei and the crystal growth process

(Derouane et al., 1992; Guth et al., 1999; Moliner, 2011). The most common mineralisation agents are the hydroxide anion (OH^-) or the fluoride anion (F^-). They both function effectively in a favourable pH condition during the hydrothermal synthesis (Yang and Navrotsky, 20002). Interestingly, the hydroxide anion (OH^-) increases the solubility of TO_4 (where T = silicon and aluminium source) by direct interaction, thus creating a silicate and aluminate ion ($[\text{Si}(\text{OH})_{4-n}\text{O}_n^{n-}]$ and $[\text{Al}(\text{OH})_4^-]$) of their respective species. At a pH of about 12 the hydroxyl anion favours the formation of aluminium rich zeolites in the absence of organic structure directing agents (OSDAs), hence pH is an important factor in the synthesis process. The presence of OSDA and OH^- in the synthesis mixtures favours the formation of high silica zeolites by increasing the molar Si/Al ratio, filling of the zeolite cavities with organic molecules, whilst lowering the incorporation of positive charges in the framework structure of the zeolite by reduced framework and extra-framework aluminium atoms (Moliner, 2011).

In the case of fluoride anions as a mineralising agent the hydrothermal synthesis of the mixture can be performed at pH near-neutral media (pH near 7) and the presences of the F^- anion increase the stability of the OSDA by preventing the degradation of the structure directing agent (Serrano et al., 2001; Moliner, 2011).

2.2.2.3 *Structure directing agent*

The structure directing agent (SDA) serves as a template to direct the microporous growth of a well-defined zeolite framework. Interestingly, the most common SDA is used for the production of zeolites include amines and quaternary ammonium cation. The templates usually have a positive charge which interacts with the negatively charged building units of the monomers by electrostatic forces (Moliner, 2011; Moliner et al., 2013). These tetrahedral assembled building units condense into various nuclei which crystallise into interconnected polyhedra (secondary building units) under high hydrothermal treatment. The polyhedra define the connected infinite units unique to the pore structure of a specific zeolite framework. Since the quaternary ammonium such as tetraethylammonium (TEA^+) and tetrapropylammonium (TPA^+) cations are bulky by nature, they only occupy or remain in the zeolite void space, thus reducing the density of the negative charge and lowering the amount of aluminium in the framework structure (Wright and Lozinska, 2011).

Various types of inorganic cations such as Na^+ , K^+ , Ca^+ , Mg^{2+} among others, have been used as structure directing agents for the purpose of synthesising high aluminium zeolites. The positively charged cations compensate the negative charge associated with AlO_4^- which create exchangeable cationic sites within the framework structure (Wright and Lozinska, 2011; Moliner et al., 2013). However, the use of inorganic cations is limited to the synthesis of low silica zeolites such as Na-A (Musyoka et al., 2012b; Ameh et al., 2017), Na-X (Shigemoto et al., 1993; Musyoka et al., 2012b), Na-P, cancrinite (Musyoka et al., 2012a; Mainganye et al., 2013), Na-L and sodalite (Belviso et al., 2010; Musyoka et al., 2011b).

2.3 Synthesis of zeolites from CFA

Zeolite can be produced using various natural and waste by-products such as clay (Ma et al., 2014; Maia et al., 2015), siliceous minerals (Liu et al., 2015), biomass of plant waste fly ash (Belviso, 2018), electronic waste (Mallapur and Oubagaranadin, 2017) and CFA. The suitability of CFA over other feedstock materials is due to the negligible cost, availability and the sufficient content of Si and Al that allows the application of the reaction condition for the production of zeolites (Wdowin et al., 2014). The conversion of the CFA aluminosilicate content into the crystalline structure of zeolites is generally performed via alkali hydrothermal conditions in a closed reactor vessel under high temperature between 45 and 200 °C for a specified period of time. In addition, this type of reaction occurs in the presence of organic and/or inorganic cations as well as mineralising agent (Belviso et al., 2009; Moliner, 2011; Belviso, 2018).

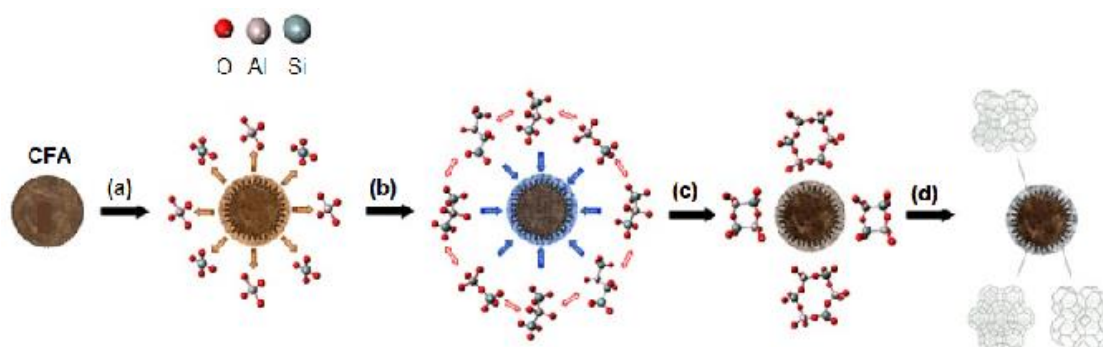


Figure 2.10: Schematic illustrating the four steps: a) dissolution, b) condensation, c) nucleation and d) crystal growth for the crystallisation of zeolites from CFA (Bukhari et al., 2015).

In the synthesis process of zeolite, the CFA aluminate and silicate content dissolve and condense to produce a supersaturated solution which is then subjected to a spontaneous

nucleation and crystal growth under the hydrothermal treatment (Querol et al., 2001; Querol et al., 2002; Bukhari et al., 2015). Figure 2.10 illustrates the four step mechanism for the production of zeolites from CFA, this includes: dissolution, condensation, nucleation and crystallisation (Bukhari et al., 2015).

2.3.1 Presynthesis and mechanism of zeolite crystallisation

2.3.1.1 Dissolution-condensation stage

The dissolution stage involves the monomerisation of Si and Al content of CFA into the solution to produce a homogeneous mixture with well distributed components. To this end, the synthesis mixture contain colloidal amorphous aluminosilicates, coagulated silica and alumina which was then condensed and rearranged into various monomers, dimers and trimers (Cubillas and Anderson, 2010; Bukhari et al., 2015; Grand et al., 2016). Under this stage, most of the reactant species possess the ability to properly dissolve in alkaline mixtures and thereafter, the appearance of the resultant synthesis mixture becomes a visible gel or clear suspension (Grand et al., 2016). The dissolution and condensation of the reactants in the synthesis mixture determine the rate of nucleation and crystallisation. This stage also affect the formation of a particular type of zeolite, the crystal size and the morphology of the zeolite (Drzaj et al., 1985; Grand et al., 2016). The dissolution of the reactants is influenced by various physical factors such as the order of mixing, agitation and curing (Grand et al., 2016).

The role of curing: During curing, the surface bonds of the reactive species breaks in the presence of the solvent and thus leads to the formation of soluble species (dissolving solid) (Rodríguez et al., 2013). As a result, the concentration of silica and alumina species in the synthesis mixture increased by the complete dissolution of the amorphous solid phase. The transformation of the solid phase into oligomers initiates the arrangement of the polymerised hydrogel between the silicate and aluminate phase (Yan et al., 2012).

2.3.1.2 Nucleation-crystal growth stage

The synthesis mixture for the crystallisation of zeolite contains dense aluminosilicate solution with amorphous materials of large monomers, dimers and trimers. The different types of nuclei in the super-saturated solution redissolve through depolymerisation and appear again. As a result, the nuclei undergo a spontaneous nucleation into clusters of the zeolitic nuclei phase and then grows into crystalline zeolitic materials (Byrappa and

Yoshimura, 2001; Cubillas and Anderson, 2010; Bukhari et al., 2015). Figure 2.11 illustrates the nucleation and crystal growth of zeolite.

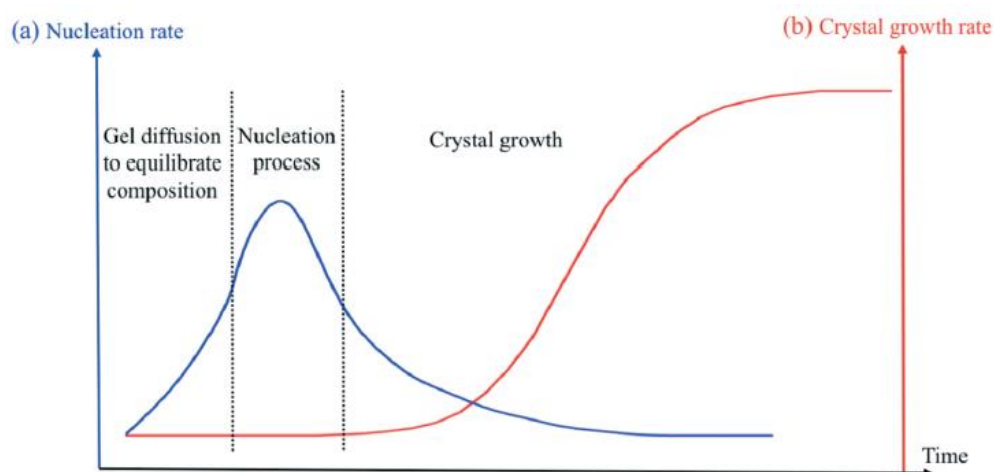


Figure 2.11: Representation of the nucleation rate and the crystal growth of zeolite structure (Grand et al., 2016).

It is evident in Figure 2.11 that after breakthrough maximum nucleation, a sharp decline was noticed because at that point the crystal growth initiation consumes the reactant species, thus limiting their viability for nucleation process (Firouzi et al., 1997; Kirschhock et al., 2008). The S-shaped curve shows the transformation of the related amorphous aluminosilicate into crystalline zeolite structure. The nucleation process of the supersaturated solution can result in either uniform homogeneous mixture or non-uniform heterogeneous mixture. The uniform homogeneous nucleation is induced by the presence of impurities or external particles in the synthesis mixture while the heterogeneous mixture ensures a spontaneous formation of small nuclei into linkage of zeolitic phase compositions and eventually grows into zeolite crystals. The heterogeneous nucleation enhanced structural and chemical rearrangement of the reactant in the synthesis mixture in order to promote nuclei formation and crystal growth of a well-defined zeolite structure (Kirschhock et al., 2008; Grand et al., 2016).

The formation of zeolite is a complex process due to the diverse chemical reaction, equilibria and varying solubility (variations) (Byrappa and Yoshimura, 2001). The conversion process of CFA to zeolite is mostly achieved by the direct and indirect synthesis process assisted by the following heat treatment methods; conventional hydrothermal, fusion hydrothermal, microwave or ultrasonication process. Hence, this review further investigates the advantages

and limitations associated with the synthesis of zeolites with a focus on high silica zeolites from CFA via the direct and indirect hydrothermal process.

2.3.2 Direct synthesis process

The direct hydrothermal process usually involves: first the dissolution at ambient conditions (room temperature or slightly elevated temperature) of CFA silicate and aluminate contents in an alkaline medium of NaOH or KOH solution. Second, the applicable molar regime in the synthesis mixture is then treated hydrothermally under pressure and elevated temperature for the crystallisation of zeolite products. During the presynthesis dissolution step, the molar Si/Al ratio can be adjusted to the targeted zeolite typology by the direct addition of silicate or aluminate compounds. Figure 2.12 illustrates the production of zeolites from CFA via the direct synthesis process. Generally, the process relies on various synthesis conditions such as: the concentration of alkaline or acidic solutions used in the pre-treatment of CFA, molar Si/Al ratio (Mondragon et al., 1990), alkalinity, pH, aging process and incorporation of zeolite crystals (seeding process) (Zhao et al., 1997), CFA/alkaline ratio (Querol, 1995), hydrothermal temperature (Lin and Hsi, 1995), hydrothermal time, reactor pressure (Bukhari et al., 2015).

In the set of experiments conducted by Murayama et al. (2002), the effect of single and double alkaline solutions of NaOH, Na₂CO₃, KOH, NaOH/Na₂CO₃, NaOH/KOH and Na₂CO₃/KOH as well as the ratio of CFA and alkaline solution on the production of Na-P zeolite and chabazite from CFA was investigated. The slurry of the CFA and different alkaline solution (mass/volume ratio = 1:400) was prepared and treated hydrothermally at 100 °C in a reactor vessel under agitation. It was observed that the recovered Na-P zeolite and chabazite grew together with the crystalline phase of quartz and mullite originally contained in CFA by the direct hydrothermal process. To enhance the synthesis process, Querol et al. (1997) studied the influence of crystal growth via direct alkaline activation of the CFA. They concluded that the crystal growth under such condition occurs either by short hydrothermal activation under low temperature or long hydrothermal activation under high temperature. Among the multifarious mineral phases in the CFA, the short hydrothermal activation allowed only for the complete dissolution of the aluminosilicate glass phase whereas the long activation process dissolution of recalcitrant mineral phases such as quartz, mullite and aluminosilicate glass phase. Both processes showed the residual remains of one

or two of the CFA mineral phases among the zeolitic crystals and the co-crystallisation of two zeolitic phases.

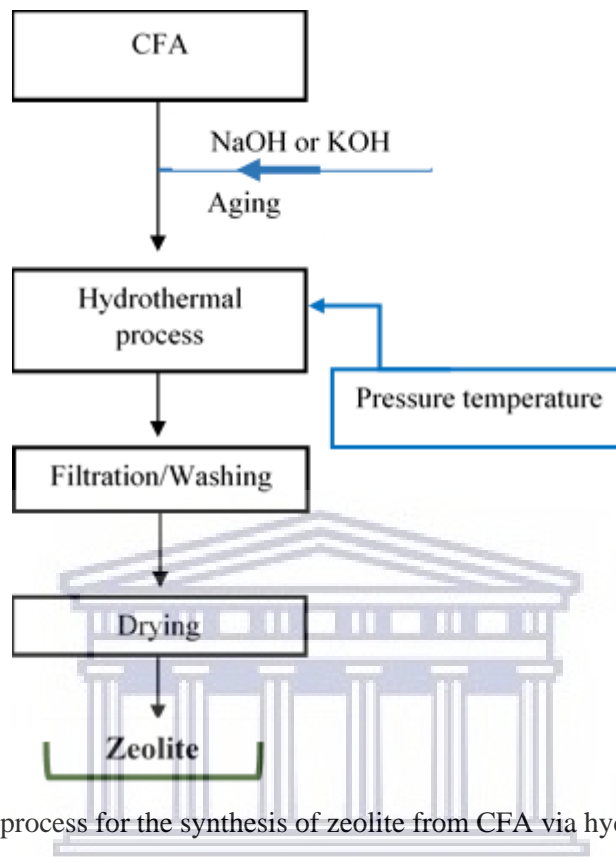


Figure 2.12: One-step process for the synthesis of zeolite from CFA via hydrothermal process.

In similar research, Zhao et al. (1997) investigated the influence of ageing and seeding prior to the hydrothermal synthesis of CFA based zeolites. The research findings indicate that the ageing step induced dissolution of Si and Al content in the CFA into the alkaline solution which promoted the production of zeolites. They further suggested that the introduction of a particular type of zeolite seed into the precursor solution reduced both the induction and nucleation steps but enhanced the crystal growth of the targeted zeolite. Examples of the zeolite produced from the direct hydrothermal process are mostly mixed phases of low silica zeolites such as Na-P, Na-A, Na-X (Sakthivel et al., 2013), sodalite, analcime or chabazite (Bukhari et al., 2015).

2.3.3 Indirect synthesis process

An indirect hydrothermal process was developed to improve the zeolitisation process via a two-step method that involved the alkaline fusion of CFA with NaOH at high temperature of about 550 °C prior to hydrothermal treatment (Shigemoto et al., 1993). First, a specific

dry mass ratio of CFA and alkaline salt were fused to completely destroy and transform the SiO_2 (quartz) and $3\text{Al}_2\text{O}_3 \cdot \text{SiO}_2$ (mullite and aluminosilicate glass) into their respective Na_2SiO_3 and Na_2AlO_2 species (sodium aluminates and sodium silicate). Afterwards, the fused solid was brought into solution for the dissolution of Si and Al by aging for a period of time and then followed by adjusting the molar Si/Al ratio using an external aluminium source (Musyoka et al., 2012b; Ameh et al., 2017). Thereafter hydrothermal conditions were applied for complete crystallisation of zeolite. Figure 2.13 illustrates the two-step indirect hydrothermal process of a) batch slurry mixture and b) clear solution extract.

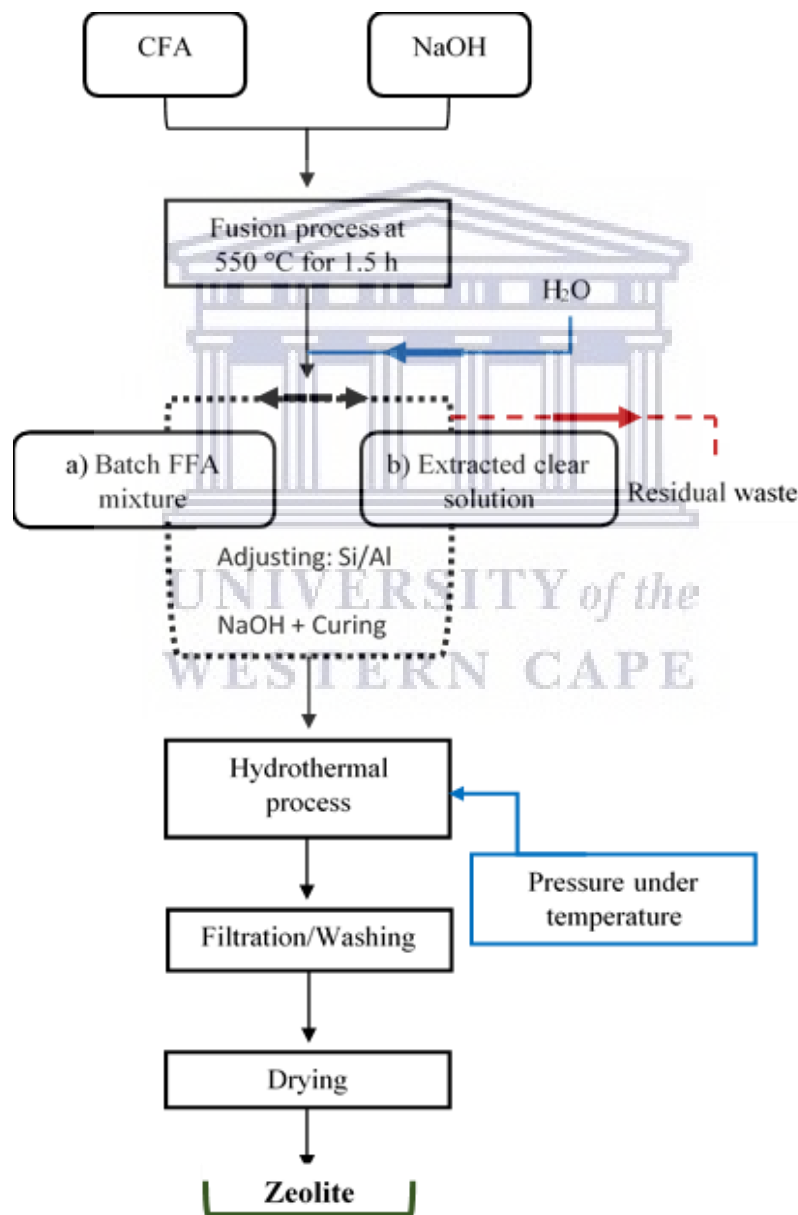
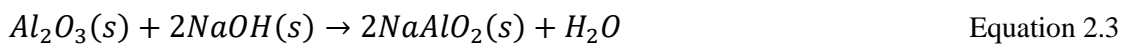
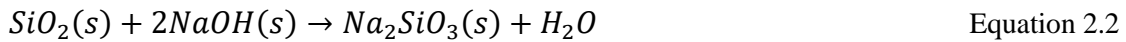


Figure 2.13: Two-step indirect hydrothermal process of a) batch slurry mixture and b) clear solution extract.

The indirect hydrothermal process via the two-step approach have validated the following: i) the conversion of CFA mineral content (quartz and, mullite and aluminosilicate glass) into sodium silicate, sodium aluminates or aluminosilicate during the alkaline fusion of CFA according to equation 2.2 and 2.3, ii) allowing spontaneous and easy dissolution of active Si and Al species into solution, and iii) improving crystal growth of a particle zeolite type (Chang and Shih, 1998; Bukhari et al., 2015; Lee et al., 2017).



Lee et al. (2017) reported that the complete transformation of CFA into the respective sodium silicate and sodium aluminate by the fusion process depends mainly on the NaOH/CFA ratio. They indicate that the purity of zeolite produced with NaOH/CFA ratio ≤ 0.8 will be compromised but a pure zeolite crystal is achievable when NaOH/CFA ratio ≥ 1.0 to 1.2. Kazemian et al. (2010) use the batch slurry mixture for the hydrothermal crystallisation of Na-P1 zeolite from CFA. During the process, sufficient amount of CFA was mixed with NaOH in a weight ratio of 1/1.2 (CFA/NaOH) and the obtained mixture was then subjected to fusion process set at 550 °C for 1 h. Afterwards, the resultant fused fly ash was milled to fine powder which was then dissolved in 0.2 M NaOH solution to generate the batch slurry mixture. The batch slurry mixture was agitated vigorously for several hours at 70 °C and the Si/Al ratio was adjusted by adding sodium aluminate solution. To this end, the batch slurry mixture was transferred into the reactor vessel for hydrothermal treatment at different temperature of 100 or 120 °C for 4 h (Kazemian et al., 2010). On the other hand, during the indirect hydrothermal process via clear extraction mixture, the fused fly ash slurry is filtered to obtain a clear solution for the hydrothermal crystallisation of zeolite.

In a comparative study conducted by Musyoka et al. (2012b) three different South African CFA were transformation into zeolite Na-A, Na-X and Na-P using the alkaline fusion process. It was demonstrated that a NaOH/CFA ratio of 1.2 and adjustment of molar Si/Al ratio of the clear extracted solution though the addition of sodium aluminate during the aging stage is sufficient for zeolitisation and hence promotes the formation of zeolite Na-A and Na-X. The indirect hydrothermal process significantly increased the dissolution of

aluminosilicate into the synthesis solution, thereby promoting the yield of the zeolite production, purity and crystallinity, improved cation exchange capacity and increased the surface area (Molina and Poole, 2004; Sakthivel et al., 2013; Soe et al., 2016). However, Chang and Shih (2000) reported the necessities of external addition of aluminium hydroxide to the extracted solution from the alkaline fused CFA. Thus, confirming the hindrance and challenge of dissolved Al in the extracted CFA solution. They further showed that the Al species were not sufficient for the conversion of the fused CFA extracted solution into high value zeolites. Besides the conventional hydrothermal and alkaline fusion hydrothermal process, the heating process of the direct and indirect methods can be assisted with different process such as: molten-salt, microwave and ultra-sonication (Ojumu et al., 2016; Belviso, 2018).

2.3.4 Challenges with the conversion of CFA to high silica zeolite

The synthesis of CFA based zeolite were successful through the direct and indirect crystallisation process among others. The difference between each method depends on several factors such as the nature of the alkaline solution, alkalinity (pH), reaction time, source of heat, reaction temperature, reaction pressure, molar Si/Al ratio, solution/solid ratio and type of aging process (Belviso et al., 2009) as well as the presence of seeds and type of SDA.

Table 2.6: Type of zeolite based on the Si/Al ratio produced from CFA.

Type of zeolite	Si/Al ratio	Examples	Silica source
Low silica	1-1.5	Na-A, Na-P, Na-X, sodalite, analcime, cancrinite	CFA or CFA + T (T = Si or Al or both)
Intermediate silica	2-5	Na-L, Na-Y	
High silica	≥ 10	ZSM-5, BEA	CFA + Fumed silica or/and alumina

Table 2.6 summaries the class of zeolites that have been synthesised from CFA by direct and indirect hydrothermal processes. The synthesised zeolite from CFA can be classified into: low silica, intermediate silica and high silica zeolite based on their respective Si/Al ratio of the products (Jha and Singh, 2011). Over the past decades, many studies on the

synthesis of zeolite from CFA have shown improved development in both laboratory and pilot plant scale. This has translated into industrial scale with the interest of commercialising the process of converting CFA to zeolite (Moriyama et al., 2005; Wdowin et al., 2014). Yet there are considerable limitations associated with the direct and indirect crystallisation process for the production of high silica zeolites. The production of zeolites using the hydrothermal process from CFA has been reported mostly for condensed structure of low silica zeolites (Querol et al., 2002; Elliot and Zhang et al., 2005) such as zeolite A (Musyoka et al., 2012b; Ameh et al., 2017), zeolite X (Shigemoto et al., 1993; Musyoka et al., 2012b), zeolite P, cancrinite (Musyoka et al., 2012a; Mainganye et al., 2013), zeolite L, Sodalite (Belviso et al., 2010; Musyoka et al., 2011b) and analcime (Kotova et al., 2016; Vereshchagina et al., 2018).

The direct hydrothermal process also known as the one-step process requires high temperatures and long treatment times to facilitate the dissolution of the predominant CFA mineral phases of mullite and quartz into aluminate and silicate species under alkaline conditions. However, only a small fraction of Al and Si dissolves from the bulk of CFA leaving the remainder locked in the bulk of the CFA. Moreover, the dissolution of Al from the mullite phase of the CFA is low compared to that of Si species. Due to incomplete dissolution, the minerals phases still remain inert, thereby hindering the transformation of CFA into pure zeolitic phase. Consequently, compromising the quality of the resultant products with a mixture of zeolite, mullite and quartz crystalline phases emanating (Belviso et al., 2010; Belviso, 2018). Hence, the zeolite structure forms around the spherical morphology of the CFA core which can be described as a coating covering the CFA core as illustrated in Figure 2.14. Also, this method incurs a low conversion, thereby reducing the percentage yield, the transformation efficiency of the zeolite and incorporating significant amount of CFA into the product (Querol et al., 2002; Yao et al., 2015; Missengue et al., 2017).

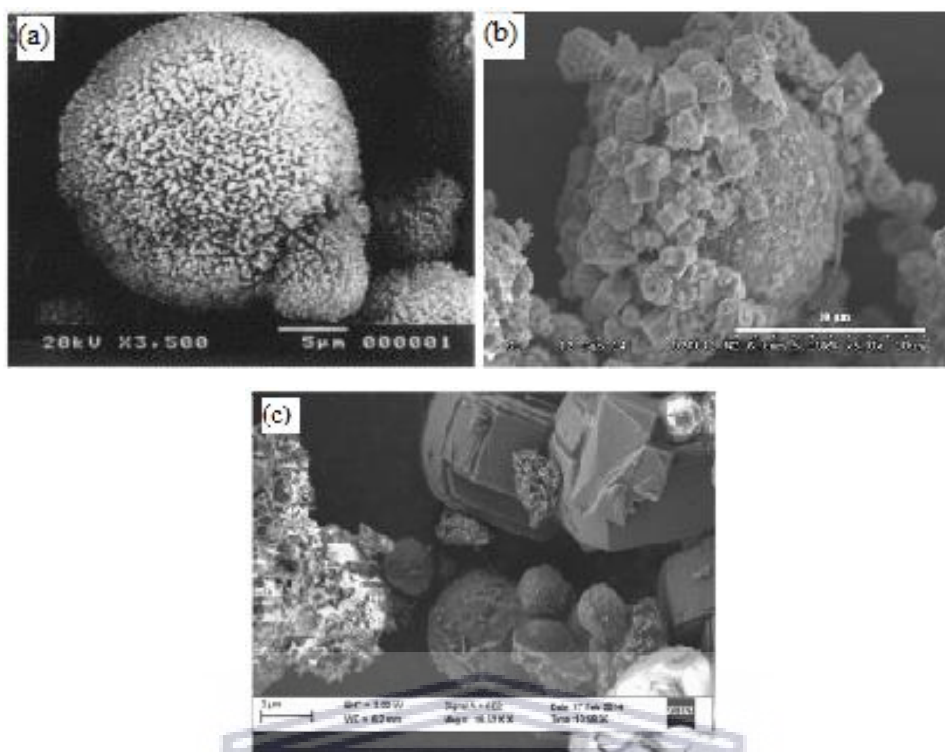


Figure 2.14: SEM image of crystalline zeolite a) Na-P (Murayama et al., 2002), b) Na-A (Bukhari et al., 2014) and c) ZSM-5 (Missengue et al., 2017) over CFA core.

The presence of other CFA elemental components of group I and II metal oxides such as CaO, MgO, Na₂O and K₂O, alongside some trace metal oxide of TiO₂ and MnO, appear to enhance nucleation and crystal growth (Rayalu et al., 2001). However, these cations and anions selectivity promote a particular type of zeolite such as low silica zeolite over high silica zeolite. To enhance the zeolitisation process using CFA feedstock materials, Hollman et al. (1999) proposed and developed a two-step process by adopting the indirect hydrothermal process via alkaline pre-treatment at 90 °C for 6 h and a treatment period of 90 °C for 48 h. This process enhanced the dissolution of Si and Al content into solution thereby increasing their concentration (Bukhari et al., 2015). This subsequently generated varying molar Si/Al ratios that might be sufficient for the hydrothermal production (Zhao et al., 1997). Consequently, the deficient Si or Al was adjusted by addition of external chemical constituents appropriate to generate the right molar Si/Al ratio for the production of low and high silica zeolite. The Si/Al ratio is one of the most important factor affecting the type of zeolite produced during zeolitisation process. Also, the composition of the synthesised zeolites is generally close to the molar Si/Al ratio of the synthesis mixture used for the hydrothermal crystallisation (Panagiotopoulou et al., 2015).

Significant success was demonstrated for the synthesis of low silica zeolite from CFA using the indirect hydrothermal process. Recently, Muniz et al. (2010) and Missengue et al. (2017) experienced challenges using the two-step hydrothermal process for the production of high silica BEA and ZSM-5. These challenges included: i) the process required the addition of a large amount of external fumed silica and ii) the phase purity of the crystalline zeolite was compromised with a blend of mullite, quartz, haematite or amorphous materials. Hence, to eliminate these limitations the potential for the recovery of greater Si or Al contents from CFA is eminently important for the recycling of CFA for high silica zeolite production. This is in order to: i) enhance the reactivity of the aluminosilicate species during the dissolution stage, ii) allow the control of the molar Si/Al ratio that promotes the synthesis of high silica zeolite without needing external added chemical sourced silica or alumina and iii) improve the crystal purity, framework stability, textural properties, structural activity of the high silica zeolites.

More recently, Petrik et al. (2017) and Missengue et al. (2018) proposed a multi-step process assisted by hydrothermal treatment for the production ZSM-5. The multi-step process is sub-grouped into four namely: i) alkaline fusion, ii) precipitation of amorphous aluminosilicate, iii) extraction of silicate and, iv) hydrothermal treatment as illustrated in Figure 2.15.

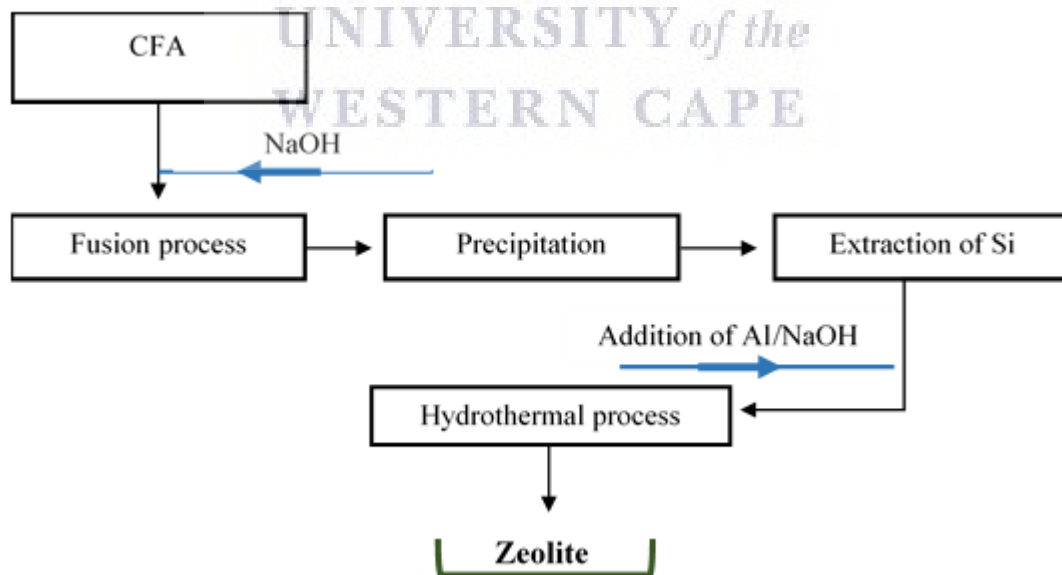


Figure 2.15: Multi-step approach for the synthesis of high silica zeolite from CFA.

Figure 2.15 shows that the precipitation process enhanced the extraction of amorphous silica which apparently, improved the phase purity, the crystalline structure and performance of the CFA based ZSM-5. An external amount of aluminium was required to adjust the molar Si/Al ratio suitable for the conversion of CFA into high silica ZSM-5 zeolite. Hence, this study proposes to design and develop a novel step for the production of high silica BEA zeolite without addition Al. The focus of the present study includes the formulation of the appropriate synthesis conditions and molar composition without the addition of external Si or Al sources as well as the evaluation of the active properties of the CFA based BEA zeolite.

2.3.5 Properties and applications of high silica zeolite

Zeolites are uniform crystalline microporous materials with well-ordered framework structures that have gained attention due to their unique properties which allows multifarious applications. The crystalline framework properties of zeolite impact on their high thermal and mechanical stability, thus allowing the direct application under harsh reaction environment. Also, the multitude of tetrahedra interconnected voids provide the different zeolite frameworks with their distinctive structural typology, porosity and channel dimensionality (Baerlocher et al., 2007; Wei et al., 2015). The ion exchange capacity, larger surface area and pore volume and intrinsic acid sites of the zeolites have enable their high transformation capacity and adsorption efficiency when applied as adsorbents, catalysts, or in fine chemicals production (Tanabe and Hölderich, 1999; Farrusseng and Tuel, 2016).

This ion-exchange property gives zeolite framework the useful advantage in different application such the detergent production and water treatment as water softener (Jha and Singh, 2011), uptake of metal (Somerset et al., 2008) and the treatment of radioactive waste (Eisler, 2012). Moreover, the framework structure of zeolite can be tailored either by ion-exchange or by incorporation of some metals such as Ti, V, Fe and Cr in the framework thereby activating the strong acid sites (Brönsted acid sites or Lewis acid sites) towards the selectivity of certain products in the area of host-guest chemistry (Nagy et al., 1998; Zhu et al., 2008; Gascon et al., 2012; Kamimura et al., 2012). Interestingly, the presence of acidic centres within the zeolites framework structure can be used as an heterogeneous catalysis particularly in various petrochemical and fine chemistry reactions such as alkylation, acylation (Mu et al., 2015; Wang et al., 2017, aldol condensation, isomerisation and cracking process (Hahn et al., 2013; Primo and Garcia, 2014; Xiong et al., 2014).

The pores connectivity of zeolites void space (micro-mesoporous openings) allows selective passage of guest molecules of different dimension, shape, and polarity possible through the zeolite pores (Vogt and Weckhuysen, 2015). This behaviour of zeolite is known as molecular sieving which influences various catalytic reactions (Davidson, 2009; Wei et al., 2015; Hartmann et al., 2016). Shape selectivity of molecules depend on the type framework structure either small, medium, large or extra-large pore zeolite (Perez-Ramirez et al., 2008). Considering the need for improved catalytic performance of zeolites two design approaches were proposed: i) to downsize the micro-size to nano dimension to enable decreased diffusion paths in the microporous area and promotes products recovery through increased external surface area (Ding et al., 2009; Al-Eid et al., 2019) and ii) enhancing the micro- and mesoporous pore size distribution into hierarchical structure (Zhang and Ostraat, 2016; Al-Eid et al., 2019). Due to the characteristic properties such as larger pore sizes and well defined channel for zeolites such as ZSM-5, MOR and BEA, these zeolites have gained attraction in the diffusion of larger molecules through selective sorption within its pore structure.

2.3.6 The investigated zeolite structure and properties in the present study: HBEA zeolite

BEA zeolite is an open three-dimensional framework with a 12 membered-ring and intersectional channels that are linear (0.67×0.76 nm) or non-linear channels (0.56×0.65 nm) that are tetragonal in nature.

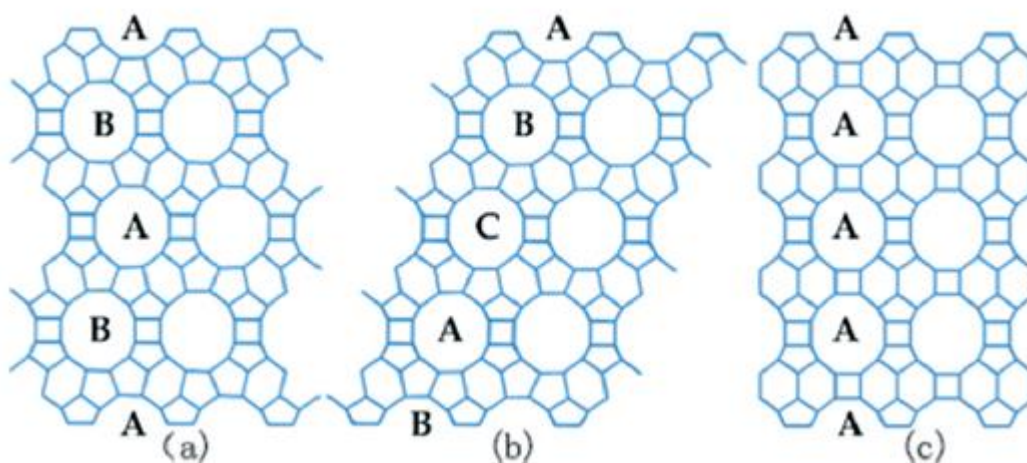


Figure 2.16: Stacking sequences of the three distinctive BEA polymorphs. a) ABAB b) ABCABC and c) AA, respectively (Tong et al., 2016).

The framework of BEA zeolite possesses a hybrid structure of three different polymorphs A, B or C or an intergrowth of two combined polymorphs (see Figure 2.16). Each polymorph is distinct with an identical centrosymmetric arrangement using different stacking sequence of the atoms in the unit cell (Costa and Capaz, 2015). This stacking disorder causes high framework defects that create both weak and strong acid sites within the BEA zeolite structure (Simon-Masseron et al., 2007).

Despite the first synthesis of BEA zeolite by Wadlinger et al. in 1975, extensively research in the preparation methods involving the use of cheap feedstock material, easy and fast synthesis processes and modification of the framework structure as well as their potential application have gained industrial interest (Mintova et al., 2003; Zhu et al., 2017). Due to its large microporous area, high external area (van Bekkum and Kouwenhoven, 2009), good thermal and hydrothermal stability and intrinsic acidity (Cambor et al., 1998; Al-Eid et al., 2019), HBEA has been widely used in various catalytic process such as: catalytic cracking, isomerisation (Lima et al., 2011), alkylation and acylation reaction (Bellussi et al., 1995), aromatic alkylation (Wu et al., 2012), esterification (Kirumakki et al., 2006) and etherification (Hu et al., 2006).

BEA zeolites are usually synthesised in an alkaline media or with fluoride anions containing structure directing agents such as tetraethylammonium ions (TEA^+) followed by the addition of pure source of silica and aluminium in the synthesis precursor mixture and then treated hydrothermally for a period of time (Cambor et al., 1998; Chen et al., 2006; Prasetyoko et al., 2006; Kong et al., 2009). Before the crystallisation process, the molar Si/Al ratio of the precursor is adjusted within the required range of 12 to 200 needed for the production of BEA zeolite (Larlus et al., 2011). It is known that different types of silica sources such as tetraethylorthosilicate (Cambor et al., 1998), amorphous aluminosilicate, silica sol, colloidal silica, precipitated silica and fumed silica (Kong et al., 2009) have been reported for the successful synthesis BEA zeolite. According to Georgiev et al. (2009), the cost of different sources of silica and alumina are high. Therefore, this present study focused on the use of coal fly ash as a feedstock material to formulate and design the synthesis protocol for BEA zeolite via an indirect hydrothermal treatment without the addition of external silica or aluminium sources.

2.4 Chapter summary

Power generation in South Africa relies heavily on the combustion of coal. The demand for energy is on the increase due to industrialisation and population increase. However, in the process of coal combustion for power production, a waste material known as coal fly ash is generated. The problem associated with CFA is that the direct disposal on land or dumpsites poses an environmental hazard, impacts upon land and contaminates water bodies, both underground and surface water. Less than 10% of South Africa CFA has been used in the construction industry or for research purposes. Interestingly, taking account the chemical composition of CFA (Si, Al and Ca) this waste material can be seen as a value-added feedstock for the synthesis of zeolite.

In the past 10 years, extensive research focus has been on the synthesis of various types of low silica zeolites such as Na-A, Na-P, SOD, Na-X, and cancrinite from CFA via the direct and indirect hydrothermal process. This grade of zeolite can be classified as low silica zeolites which are promising in various applications. However, there are challenges during the synthesis of high silica zeolite which compromise the structural and performance integrity. The limitations include: the low CFA Si/Al molar ratio, the synthesis requirement for external addition of Si and Al source and the retention of the CFA mineral phase in the synthesised zeolite product. Hence, this study focused on the utilization of CFA for the synthesis of high silica zeolite (BEA zeolite) without the addition of external Si or Al sources. New routes to reuse of fly ash through method development and design of necessary formulation needed for the production of BEA zeolite from CFA via indirect hydrothermal process are envisaged.

The next chapter gives detailed experimental and analytical methods used for preparing and characterizing of BEA zeolite. Also, the protocol involved in the study of the behaviour of BEA zeolite in hot liquid phase and acylation reactions are given.

Chapter 3

Materials and Methodology

3.0 Introduction

This chapter highlights the materials (sample location and sampling of feedstock material) and chemicals used in this study. Detailed descriptions of the step-by-step experimental procedure used in actualising the research aims and objectives are presented. The analytical techniques employed in the characterisation of the feedstock materials, synthesised products and the reactants are also described.

3.1 Materials

In this section the source, location and the description of the feedstock materials (CFA) used in this study are presented. Also, this section lists the various chemicals used in the research experiments.

3.1.1 Sample location and sampling of feedstock material

Coal fly ash (CFA) was collected at Arnot power station in Mpumalanga Province as indicated in the map (Figure 3.1).

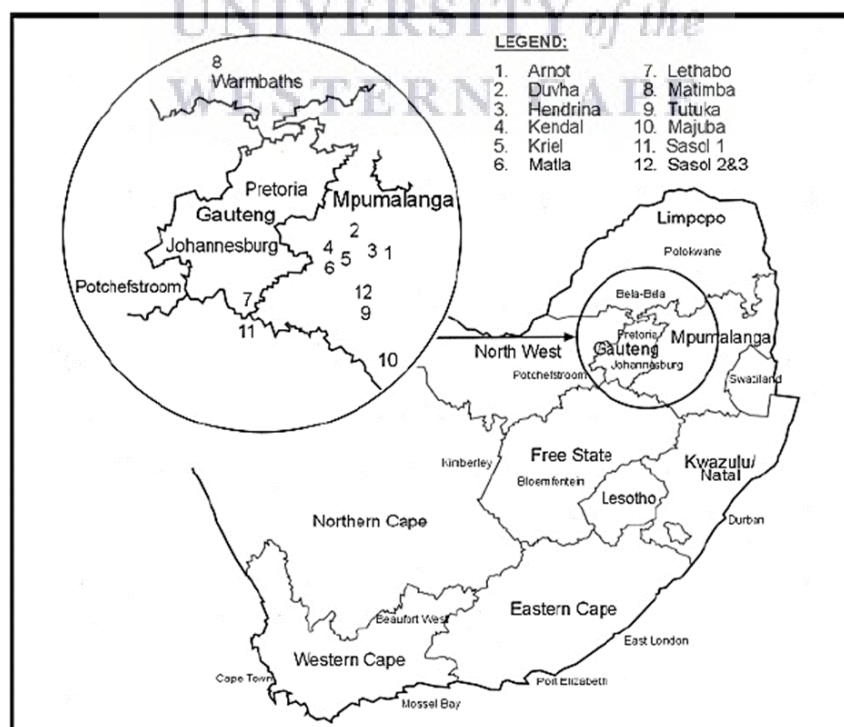


Figure 3.1: Locations of coal power plants in South Africa (Krüger, 2003).

Fresh fly ash (CFA) samples were collected at different points directly from the precipitators (an air pollution particulate control device) within the power station. Afterwards, the collected FA was mixed together to achieve homogeneity of the sample. Thereafter, the CFA sample was kept in airtight plastic containers to prevent ingress of CO₂ which may alter the alkalinity of the sample. The collected FA sample was stored away from light to preserve the initial mineral composition contained in the FA (Sonqishe, 2008).

3.1.2 Chemicals

This section presents the list of chemicals used in the present study as shown in Table 3.1.

Table 3.1: List, source and purity of chemicals used.

Chemical	Source	Purity
Oxalic acid	Kimix Chemicals	99 %
Tetraethylammonium hydroxide	Sigma-Aldrich	40 %
Sodium hydroxide	Kimix Chemicals	97 %
4-methoxybenzophenone	Sigma-Aldrich	97 %
2-methoxybenzophenone	Sigma-Aldrich	-
Phenyl benzoate	Sigma-Aldrich	99 %
Benzoyl chloride	Sigma-Aldrich	99 %
Nitrobenzene	Sigma-Aldrich	99 %
Anisole	Sigma-Aldrich	99.7 %
Sulphuric acid	Sigma-Aldrich	95-99 %
Hydrochloric acid	Sigma-Aldrich	-
Hydrofluoric acid	Sigma-Aldrich	48 %
Nitric acid	Sigma-Aldrich	65 %
Rhodamine 6G	Sigma-Aldrich	95 %
Ammonium nitrate	Sigma-Aldrich	-
Dichloromethane	Sigma-Aldrich	≥99.8 %

3.2 Methodology

The experimental design for the synthesis of BEA zeolite from CFA followed a sequential step-by-step process which is systematically divided into three steps: alkaline fusion of CFA, extraction of silicate and hydrothermal crystallisation of the extracted silica. The subsections

below describe the step-by-step approach of the aforementioned processes. The overview of the experimental design is summarised in Figure 3.2.

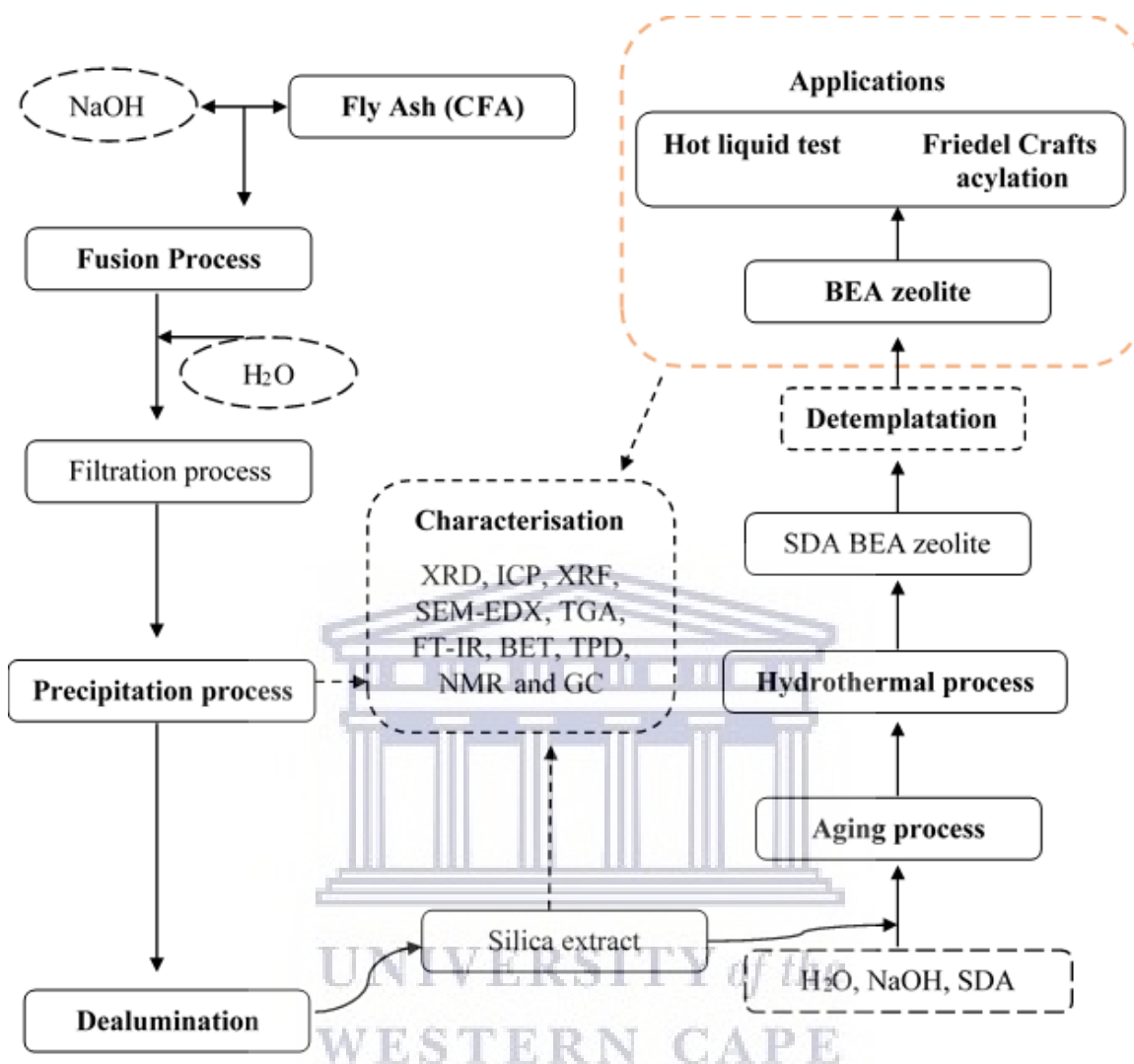


Figure 3.2: Experimental design for the synthesis of BEA zeolite from fly ash based silica extract (SDA: structure directing agent).

3.2.1 Alkaline fusion of FA

In the present study, a specific amount of CFA and NaOH pellets in a mass ratio of 1:1.2 was mixed vigorously for a few minutes. Then, the obtained homogenous mixture (FA-NaOH pellets) was poured into a porcelain crucible and transferred to a muffle furnace set at 550 °C for 1.5 h. After the high temperature alkaline fusion process, the fused material was subsequently cooled to room temperature. Thereafter, the sintered granules of fused fly ash (FFA) were ground into a fine powder using a laboratory scale ball mill grinder and stored until needed for the extraction process.

3.2.2 Extraction of silica from FFA

This process follows a chronological order involving two steps: precipitation and chelating process as illustrated in Figure 3.2:

Precipitation process: After the fusion step, the crushed FFA was mixed with deionised water in a solid/liquid ratio of 1:5 and then stirred for 2 h at room temperature and filtered to separate the solid residue from the filtrate. Next, the resultant filtrate was treated with concentrated sulphuric acid (95-99%) in a dropwise manner while stirring until a white precipitate was formed as suggested by Baldyga et al., (2012). The white precipitate with an assigned code name FFAE was dried at 70 °C overnight. The FFAE was then treated with different concentrations of oxalic acid (chelating process), as presented in Table 3.2.

Table 3.2: Conditions for the extraction of silica from FFAE.

Code names	Oxalic acid (M)	Constant parameters
FFAE	-	Reflux condition Liquid (acid)/solid ratio: 10:1 Temperature: 80 °C Time: 6 h
Si1.3	1.3	
Si1.5	1.5	
Si1.7	1.7	

Chelating process: A specific solid/liquid (1:10) ratio of the precipitated FFAE and different concentrated oxalic acid solutions was mixed (see Table 3.2). Subsequently, the mixture was subjected to reflux at 80 °C for 6 h. The silica extract was recovered by hot-filtration and the solid fraction was then dried overnight at 70 °C in an oven. Afterwards, the extracted silica was tightly sealed in a sample bottle and stored until needed for the synthesis of BEA zeolite. The obtained samples were labelled with codes (see Table 3.2).

3.2.3 Synthesis of BEA zeolite from silica extract

This section presents a detailed description of the synthesis of BEA zeolite from fly ash based silica extract (Si1.3, Si1.5 and Si1.7). The experimental design followed a one-step-at-a-time synthesis protocol as described in Table 3.3 and 3.4. Different synthesis mixtures were prepared by adding 1.9051 g of the dried silica extract to a given amount of NaOH or Al(OH)₃, tetraethylammonium hydroxide (TEAOH), and H₂O as presented in Table 3.3 and Table 3.4. The resulting reaction mixture was aged for 30 min at room temperature and then transferred into a 100 mL capacity Teflon lined stainless steel autoclave. Afterwards, the

reaction vessel was treated hydrothermally at a set temperature of 140 °C for a period of 72 h under static conditions.

In the preliminary synthesis process, Si1.3, Si1.5 and Si1.7 silica extract were subjected to hydrothermal treatment for the crystallisation of BEA zeolite. The reaction vessel contains 1.9051 g silica extract, 0.1 g NaOH, 4.2361 g TEAOH and 4.661 g H₂O except FFAE which had no additional NaOH. The detailed experimental conditions and molar compositions are described in Table 3.3.

Table 3.3: Preliminary synthesis conditions for the synthesis of BEA zeolite from silica extract.

Code name	Molar Composition				
FFAE	1 Si	0.095 Al	2.425 Na	0.853 TEAOH	19.212 H ₂ O
Si1.3	1 Si	0.022 Al	0.218 Na	0.396 TEAOH	8.906 H ₂ O
Si1.5	1 Si	0.017 Al	0.241 Na	0.399 TEAOH	8.980 H ₂ O
Si1.7	1 Si	0.020 Al	0.217 Na	0.396 TEAOH	8.900 H ₂ O

Note: synthesis temperature = 140 °C and synthesis time = 72 h.

After the synthesis time allocated, the reaction vessel was allowed to cool down and then the recovered solid particles were repeatedly washed with deionised water and filtered. The resultant mass of the synthesised products was determined after drying the solid products overnight at 70 °C. Thereafter, the products were detemplated, at a ramping rate of 2 °C/min for 2 h at 120 °C and then at 550 °C for 3 h in air with a ramping rate of 3 °C/min to remove the organic template (TEAOH).

Similarly, on the basis of the best preliminary synthesis conditions (Si1.5 silica extract), further studies such as the effect of Na and effect of Al were conducted as described in Table 3.4. Details of the various amounts of NaOH, Al(OH)₃, and TEAOH, as well as the varying physical conditions such as time, are presented in Table 3.4.

Table 3.4: Conditions for the synthesis of BEA zeolite from Si1.5 silica extract.

Variables	Code name	Molar composition					Physical parameters	
Effect of H₂O	BEA4	1 Si	0.017 Al	0.241 Na	8.980 H ₂ O	0.399 TEAOH	Synthesis Time: 72 h	
	BEA6	1 Si	0.017 Al	0.241 Na	12.828 H ₂ O	0.399 TEAOH		
	BEA9	1 Si	0.017 Al	0.241 Na	17.958 H ₂ O	0.399 TEAOH		
	BEA14	1 Si	0.017 Al	0.241 Na	26.937 H ₂ O	0.399 TEAOH		
Effect of Na	BEAN1	1 Si	0.017 Al	0.317 Na	8.980 H ₂ O	0.399 TEAOH		
	BEAN3	1 Si	0.017 Al	0.461 Na	8.980 H ₂ O	0.399 TEAOH		
	BEAN4	1 Si	0.017 Al	0.506 Na	8.980 H ₂ O	0.399 TEAOH		
	BEAN5	1 Si	0.017 Al	0.552 Na	8.980 H ₂ O	0.399 TEAOH		
	BEAN6	1 Si	0.017 Al	0.734 Na	8.980 H ₂ O	0.399 TEAOH		
Effect of Al	BEAA1	1 Si	0.060 Al	0.241 Na	8.980 H ₂ O	0.399 TEAOH		
	BEAA2	1 Si	0.098 Al	0.241 Na	8.980 H ₂ O	0.399 TEAOH		
	BEAA3	1 Si	0.172 Al	0.241 Na	8.980 H ₂ O	0.399 TEAOH		
Effect of time	BEA4	1 Si	0.017 Al	0.241 Na	8.980 H ₂ O	0.399 TEAOH		Synthesis Time (h): 12, 24, 48 and 72
	BEAA1	1 Si	0.060 Al	0.241 Na	8.980 H ₂ O	0.399 TEAOH		

*Additional Na = NaOH and synthesis temperature was 140 °C.

To obtain the H-BEA zeolite, the detemplated Na-BEA zeolite (calcined using a heating rate of 2 °C/min and held for 2 h at 120 °C and then at 550 °C for 3 h in air with a ramping rate of 3 °C/min) was treated with 1 M ammonium nitrate (NH₄NO₃) solution in a mass/volume ratio 1 g:50 mL (zeolite/NH₄NO₃) at 80 °C for 2 h under stirring conditions. The suspension was then centrifuged, and the solids were redispersed in a fresh aliquot of NH₄NO₃ solution. This procedure was repeated twice in order to completely exchange the Na⁺ ion present in the zeolite (Manrique et al., 2016). Upon completion, the recovered BEA zeolite was oven dried at 80 °C overnight and thereafter, calcined in air at 200 °C for 2 h and then set at 500 °C for 4 h with a ramping rate of 10 °C/min to remove NH₃ and produce the H-BEA zeolite form.

3.2.4 Influence of reduced H₂O content to enhance fast crystallisation of BEA zeolite

The synthesis of BEA zeolite follows the description presented in section 3.2.3. The aim of this section was to draw a correlation between the amount of water in the synthesis mixture and the shortest synthesis time required for the formation of BEA zeolite. Herein, the molar composition of BEA4 (see Table 3.4) with the synthesis time of 12 h at 140 °C was selected and Table 3.5 shows the synthesis conditions for the crystallisation of BEA zeolite with reduced water content in the synthesis mixtures and synthesis time. Each of the synthesised BEA products were denoted/labelled with different code names as presented in Table 3.5.

Table 3.5: The effect of water content in relation to synthesis time for BEA zeolite formation.

Code name	Molar composition					Physical parameters
	Si	Al	Na	TEAOH	H ₂ O	
NaBEA44	1	0.017	0.241	0.399	5.986	Time: 12 h
NaBEA2	1	0.017	0.241	0.399	3.991	
NaBEA1	1	0.017	0.241	0.399	2.661	
NaBEA0	1	0.017	0.241	0.399	1.776	Time: 10 h
NaBEA12	1	0.017	0.241	0.399	3.991	
NaBEA11	1	0.017	0.241	0.399	2.661	
NaBEA10	1	0.017	0.241	0.399	1.776	Time: 8 h
NaBEA84	1	0.017	0.241	0.399	3.991	
NaBEA82	1	0.017	0.241	0.399	2.661	
NaBEA80	1	0.017	0.241	0.399	1.776	

Note: synthesis temperature was 72 °C

Each of the synthesised products was detemplated in air to remove TEAOH and then ion-exchanged and calcined to prepare the H-form (as described in section 3.2.3 of this chapter).

3.2.5 Catalytic applications of BEA zeolite

The catalytic performance of the optimised BEA zeolite is described in this section. The catalytic application and performance tests included: hot-liquid phase test and Friedel-Crafts acylation. The following subsection describes each of the aforementioned.

3.2.5.1 Hot-liquid phase test

Stability tests were carried out on the synthesised BEA-zeolite (BEA4 and BEA1) in hot liquid phase environment in a similar way as described by Zhang et al. (2015). In each run, 0.5 g of the zeolite and 100 mL of deionised water were added in a 200 mL Teflon container that was then placed inside an autoclave pressure reactor. Thereafter, the mixture inside the Teflon in the pressure reactor was stirred vigorously at 550 rpm under different temperature and time as presented in Table 3.6. The parent (BEA4 and BEA1), as well as the treated BEA zeolites, were assigned different code names of NaBEA and AlBEA, respectively as shown in Table 3.6.

Table 3.6: Experimental conditions for hot-liquid test of NaBEA and AlBEA zeolite.

Variables	-1 (Low)	0	1 (High)
Reaction time (h)	6	12	24
Temperature (°C)	150	-	200
Sample Code	Runs	A	B
NaBEA16	1	-1	-1
NaBEA112	2	-1	1
NaBEA124	3	0	-1
NaBEA26	4	0	1
NaBEA212	5	1	-1
NaBEA224	6	1	1
AlBEA16	7	-1	-1
AlBEA112	8	-1	1
AlBEA124	9	0	-1
AlBEA26	10	0	1
AlBEA212	11	1	-1
AlBEA224	12	1	1

After a specific reaction cycle, the autoclave was allowed to cool to room temperature and the treated BEA zeolites were filtered and dried at 80 °C overnight for further characterisation.

3.2.5.2 *Friedel-Crafts acylation process*

Friedel-Crafts acylation of anisole with benzoyl chloride in this study was adapted from Berrichi et al., (2007). The liquid-phase acylation reaction was carried out in a pressure tube, held in an oil bath and purged with nitrogen gas to remove air before use. 1.365 g (50 mmol) of anisole was quickly introduced into the reaction vessel and allowed to stir. Anisole acted as a solvent as well in the reaction process. Thereafter, 0.068 g of the freshly calcined HBEA zeolite was added with continuous stirring at 650 rpm until a temperature of 120 °C was reached. Afterwards, 1.365 g (50 mmol) of benzoyl chloride (acylating reagent) was then added to the reacting mixture contained in the pressure tube.

The experimental design for the acylation reaction was based on the following conditions in Table 3.7, which present the chemical and physical parameters in the reaction process.

Table 3.7: Acylation reaction of anisole with benzoyl chloride over HBAE zeolite.

Chemical parameters		
Anisole (mmol)	Benzoyl chloride (mmol)	Ratio
-	50	Control
50	50	1:1
50	20	2.5:1
50	10	5:1
50	5.26	9.5:1
Physical parameters		
❖ Temperature (°C): 120		
❖ Reaction time (min): 0-1440		
❖ Stirring speed (rpm): 650		
❖ Mass of catalyst (g): 0.068		

Note: the ratio represents the mixture of anisole: benzoyl chloride (acylating agent)

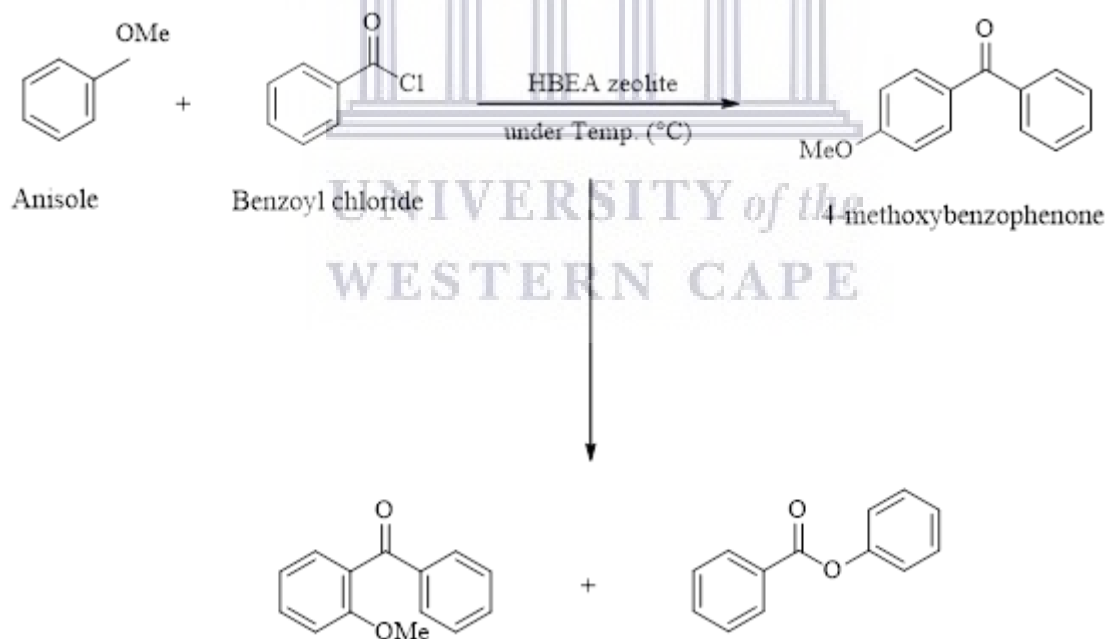
After mixing each of the reactants in the pressure tube (as described in the preliminary stage and synthesis conditions presented in Table 3.7), at the end of a specific period of time, the

reaction was stopped using a fast cooling method by running water over the pressure tube. The collected samples were quickly filtered and both the liquid and solid product was kept for further analysis. The liquid products were identified and quantified by GC (as described in section 3.3.12) in order to establish the best conditions based on time and temperature needed for the next reaction stage. The influence of reaction time and anisole/acylating molar ratio were investigated as described in Table 3.7. Also, the effect of the zeolite crystal size, morphology, Al content and textural properties of HBEA zeolite on the acylation reaction were explored.

Calculations:

The percentage conversion, selectivity and product yield were determined considering the amount of reactant and products at the end of each reaction run. The obtained HBEA zeolites were used for the acylation of anisole with benzoyl chloride as illustrated in Scheme 3.1.

Scheme 3.1: The Friedel-Crafts acylation of anisole with benzoyl chloride:



The conversion of anisole were calculated using equation 3.1 (Wang et al., 2017):

$$\% \text{ anisole conversion} = \left[\frac{P_{2\text{Me}} + P_{4\text{Me}} + P_{\text{PHB}}}{P_{2\text{Me}} + P_{4\text{Me}} + P_{\text{PHB}} + P_{\text{BzCl}}} \right] \times 100 \quad \text{Equation 3.1}$$

Selectivity of 2- and 4-methoxyacetophenone and other side products such as phenyl benzoate were calculated as given in equation 3.2:

$$\% S_i = \left[\frac{P_{2Me} \text{ or } P_{4Me} \text{ or } P_{PHB}}{P_{2Me} + P_{4Me} + P_{PHB}} \right] \times 100 \quad \text{Equation 3.2}$$

where S_i is selectivity and P_{2Me} , P_{4Me} and P_{PHB} were the peak area of the products (2-methoxybenzophenone, 4-methoxybenzophenone and phenyl benzoate, respectively) at specific time and P_{BzCl} was the peak area of benzoyl chloride. Percentage yield of the products was calculated using the following equation:

$$\% \text{Yield}_i = \left[\frac{\text{conversion} \times \text{selectivity}}{100} \right] \quad \text{Equation 3.3}$$

3.2.5.3 Regeneration process of the catalyst

The recyclability of the zeolite catalyst was investigated. At the end of each reaction run, the aliquots were filtered-off and the catalyst was washed with dichloromethane several times. The solid zeolite catalyst was then dried overnight at 100 °C before reuse. In addition, the synthesised catalyst and the recycled catalyst were analysed using different analytical techniques such as XRD and solid-liquid state NMR.

3.3 Characterisation techniques

The characterisation of the FA, silica extract and the synthesised BEA zeolite was carried out using different analytical techniques needed to provide detailed sample information. In this section, various techniques were used to determine the elemental, mineralogical composition, thermal stability, framework stability and textural properties of the samples. The following subsection present and discusses the respective analytical techniques used in this study.

3.3.1 pH

The degree of acidity or alkalinity of the supernatant obtained after the hot test reaction were measured using a pH meter (Hanna HI 991 301 pH meter with portable pH/EC/TDS/Temperature probe). The pH meter was calibrated before use with buffer

solutions of pH 4.0 and 7.0, thereafter, the probe was rinsed with deionised water. Each sample supernatant was measured in replicate at room temperature.

3.3.2 Inductively Coupled Plasma – Optical Emission Spectrometry

The concentration of minor and trace elements in the synthesised HBEA zeolites was measured using Varian Liberty II inductively coupled plasma-optical emission spectrometry (ICP-OES). The samples, which are liquid, were filtered using a micro-membrane filter of 0.45 μm to remove suspended particles and then diluted to 10, 100 and 1000 times with the addition of a few drops of 2% nitric acid, with data corrected for each dilution factor. An ICP-OES instrument was calibrated before analysis and standards were used to correct for matrix effects. Analysed samples were done in triplicate.

3.3.3 Laser Ablation Inductively Coupled Plasma-Mass Spectrometry

The laser ablation ICP-MS was generally used for the quantitative elemental analysis of trace elements in FA and solid silica extracts. The sample was first coarsely crushed and then fused into a disc chip by fluxing the sample into a pellet by the use of an automatic Claisse M4 Gas Fusion instrument and ultrapure Claisse Flux. The chip was mounted in a round resin disk of 2.4 cm and was then polished. To analyse for trace elements, the ablated polished chip was exposed to a flow of He gas in a 213 nm laser ablation system which was then mixed with Ar gas after coming out of the ablation cell. The sample was then introduced into the laser ablation ICP-MS unit by passing through a mixing chamber that was connected to the 213 nm laser ablation system.

Before the collection of results, the trace elements were quantified using NIST 612 as a calibration method and ^{29}Si as internal standard which was run at the beginning of the analysis. Also, a fusion control standard (reference material BCR-2, from USGS) was analysed to verify ablation on the fused material at the beginning. Elemental analysis of trace elements was conducted for the FA and solid silica extract samples in triplicate and data was processed using Glitter software.

3.3.4 X-ray Fluorescence Spectroscopy analysis

The X-ray fluorescence spectroscopy (XRF) analysis was carried out to quantify the elemental composition of both the FA and solid silica extracts. Each sample was prepared by mixing 2 g of 10% C-wax binder and 90% EMU powder with 10 g of FA and silica

extract (powder). The mixture was thoroughly blended, poured into the mould and then pelletised for 1 minute under a pressure of 15 tons using a Dickie and Stockler manual pelletiser to form powder briquettes. By also placing a portion of each of the samples into a furnace at 900 °C for at least 45 minutes the loss on ignition (LOI) was measured. XRF analysis was done on a Philips PW 1480 X-ray fluorescence spectrometer, the spectrometer is fitted with a chromium tube. Gas-flow proportional counter and a scintillation detector combination made up the five analysing crystals namely LIF 200, LIF 220, GE, PE and PX and the detectors. The gas flow proportional counter uses P 10 gas, which is made of 90% argon and 10% methane mixture. In order to measure the amount of the major and trace elements in each sample, the samples were moulded into pellets. Major elements were analysed on the pellet at 40 kV and 50 mA tube operating conditions and trace elements were analysed on the powder briquettes at 50 kV and 40 mA tube operating conditions. Three replicate measurements were made for each sample and the matrix effects in the samples were corrected for by applying theoretical alpha factors and measured line overlap factors to the raw intensities measured with the SuperQ Philips software.

3.3.5 Scanning Electron Microscopy (SEM)- Energy dispersive spectroscopic (EDS)

The structural morphology of FA, silica extract and BEA zeolite was analysed by Zeiss Gemini Auriga high resolution scanning electron micro-analyser (HR-SEM) equipped with a CDU-lead detector at 25 kV and a tungsten filament. A fine, dried, powdery sample was dusted on a carbon adhesive tape attached onto an aluminium stub disc and then coated with carbon for 6 sec in an Emitech K950X Carbon Evaporator to make the sample conductive. The morphology of each conductive sample at a given spot was observed under a powerful microscope and images focused at different magnification were taken. The current and illumination was set at 5 kV and 0.1 mrad, respectively while the magnification, resolution and working distance was captured on each sample micrograph. At each focus spot, Energy dispersive spectroscopic (EDS) analysis was done for qualitative elemental composition of a given sample.

3.3.6 X-ray diffraction (XRD)

Phase purity and crystal structure of the fly ash, fused fly ash, silica extract and Na or H form of BEA zeolite were determined by X-ray diffraction (XRD) patterns. XRD was carried out on a Philips X-pert pro MPD X-ray diffractometer using Cu-K radiation, operated at 40 kV and 40 mA to analyse and collect spectra data. Zeolite powder sample preparation was

done by grinding samples into a fine powder and then the powder was pressed onto a rectangular polypropylene sample holder which was then clipped into the XRD instrument. The powdered zeolite samples were scanned over a range of 4° to 60° 2θ with a step size of $0.02^\circ/\text{s}$. The crystalline mineral phases were identified by performing a match search and comparing the diffraction spectra with the database of standard peaks patterns provided by International Centre for Diffraction Data (ICDD) assisted with Highscore Xpert software.

3.3.7 FT-IR analysis

Fourier Transform Infrared spectroscopy (FT-IR) was carried out on the silica extract samples in order to understand the functional groups found within the silica extract and BEA zeolites. Approximately 13 mg of the samples (FA, FFA, silica extract and Na or H form of BEA zeolite) was placed on the Attenuated Total Reflectance (ATR) metal disc samples holder of Perkin Elmer spectrum 100 FT-IR spectrometer. Gentle force was applied to the sample and IR spectra were collected within a range of $4000\text{--}400\text{ cm}^{-1}$ to identify structural configuration. Before data collection baselines were corrected for background noise which was subtracted from spectra.

3.3.8 Thermogravimetric analysis

The thermogravimetric analysis evaluated the thermal stability and volatile content by measuring the weight loss in progression with a change in temperature. The changes in the physical and chemical composition of silica extract and H-BEA zeolites was carried out using Setaram Setsys Evolution 16 TGA-DTA-DSC. Typically, 20 mg of each sample (FA, silica extract and BEA zeolite) was placed into a crucible supported on an analytical balance. The heating ramp of the furnace was adjusted to $5\text{ }^\circ\text{C min}^{-1}$ under airflow of 50 mL min^{-1} at $25\text{ }^\circ\text{C}$ until a maximum set temperature of $900\text{ }^\circ\text{C}$ was reached. The H-BEA zeolites powder was then analysed using Q500 thermo-gravimetric analyser (TGA).

3.3.9 Nuclear magnetic resonance (^{27}Al - ^{29}Si MAS NMR) spectroscopy

The nuclear magnetic resonance spectroscopy was used to elucidate the framework structure of the synthesised H-BEA zeolite and the hot liquid treated BEA samples. ^{27}Al single pulse MAS NMR experiments were performed at a magnetic field of 11.4 T on a spectrometer with the corresponding Larmor frequencies of 130.3 (^{27}Al) and 99.3 (^{29}Si) MHz. All single pulse spectra were acquired using a single pulse at 90 degrees with a recovery delay of 0.5 s (^{27}Al) or 25 s (^{29}Si). The spectra were accumulated from 1200 scans (^{27}Al) or 300 scans

(²⁹Si) using a 4 mm BBO probe at a spinning rate of 14 kHz (²⁷Al) and 8 kHz (²⁹Si) for all experiments. The samples (BEA zeolites) were packed into standard zirconia 4 mm rotors (Bruker). The ²⁷Al 3QMAS NMR spectra were acquired using the z-filter 3QMAS pulse sequence using a 4 mm probe with sample spinning rate at 14 kHz. The optimised pulse widths were p1 = 4.8 us, p2 = 1.69 us and p3 = 20 us. In the MQMAS experiment, 60 transients with a 0.5 s recycle delay and 512 evolution increments were used. Spectral widths for the F2 (acquisition) and F1 (evolution) dimension were 50 and 14 kHz, respectively. All spectra were externally referenced (i.e. the 0 ppm position) to a 0.1 M Al(NO₃)₃ and TMS (neat) solution.

3.3.10 Brunauer–Emmett–Teller (BET)

The textural properties of the synthesised H-BEA zeolites involving the BET surface area was performed with a Micromeritics ASAP 2020 HD analyser at 77 K. The N₂ adsorption/desorption isotherms was evaluated by subjecting the samples to a degassed down to 10⁻⁷ bar at 200 °C for 8 h in order to remove moisture and/or other volatile residue. The microporous and mesoporous surface area and the pore volume of the samples was calculated by Brunauer-Emmett-Teller (BET) model as well as the t-plot measurements used to differentiate between external surface area and microporous area. Density functional theory (DFT) model was used in obtaining the pore size distributions whereas the total pore volume was determined using the Horvath–Kawazoe (*HK*) model at P/P_o ~0.99.

3.3.11 Temperature programmed desorption (TPD) analysis

Ammonia temperature-programmed desorption (NH₃-TPD) was carried out using Micromeritics Autochem II 2920. Approximately, 30 to 50 mg of the HBEA zeolites were pretreated at 550 °C (heating ramp: 10 °C/min) in 10 mL/min helium for 1 h in order to desorb any moisture. Afterwards, the zeolite samples was then cooled to 50 °C, and ammonia was adsorbed for 30 min using 20 mL/min of 10 vol% NH₃ in helium. Each of the zeolites samples was then purged under flowing helium for 30 min and the NH₃ desorption was recorded by heating the zeolite to 700 °C using a 10 °C/min ramp. The obtained curves were normalised according to the mass of the samples and the peak areas analysed using Gauss line shape in OriginPro 8.5 software.

3.3.12 Gas chromatograph (GC) analysis

Gas chromatography was used to analyse, identify and quantify final and intermediate products of the acylation reaction. Each of the components was separated in a GC II 5890 Hewlett Packard equipped with a capillary column oven programmed for a 2 min hold period at 70 °C followed by heating (15 °C/min H gas) to 250 °C, after which temperature was held constant for 14 min. The injector temperature was 250 °C, and the injector split ratio was set to 100:1. (100 mL/min He gas). The GC was equipped with a flame ionisation detector (FID).

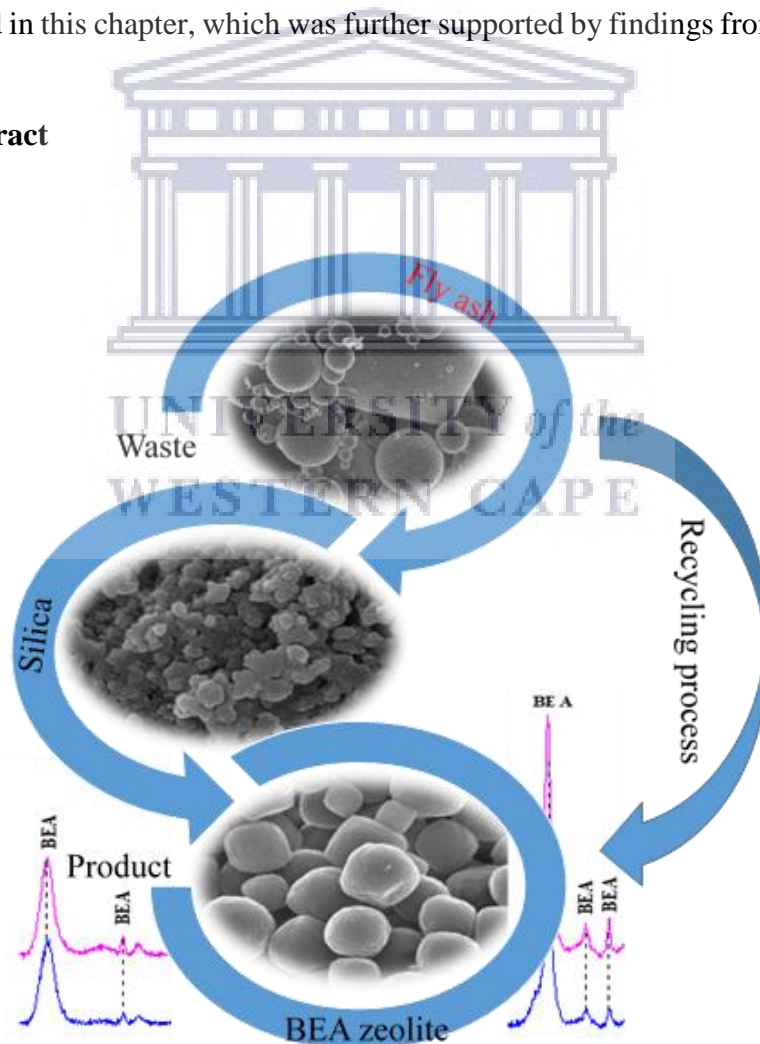


Chapter 4

Hydrothermal conversion of fly ash based amorphous-silica to nanocrystal BEA zeolite

This chapter presents the mineralogical composition, morphological formation, structural and elemental composition of coal fly ash (feedstock material). The detailed description of the resultant silica extract from the fused fly ash through the reflux and precipitation method is given in this chapter. The hydrothermal crystallisation of the silica extract into BEA zeolite using different synthesis mixtures at varying synthesis temperature and time are discussed in detail. Afterwards, a correlation of the synthesised BEA zeolite quality in relation to water content of the synthesis mixture, the synthesis temperature and time is drawn and further discussed. Different analytical techniques are used to validate each of the results presented in this chapter, which was further supported by findings from the literature.

Graphical abstract



Highlights

- Fly ash based silica and aluminium extract was converted to HBEA zeolite by indirect hydrothermal processes
- The spherical morphology of HBEA zeolite changes to a cuboidal-shape as the Si/Na ratio of the synthesis mixture reduces.
- Alteration in the Si/Al ratio influences crystallinity and crystal size of HBEA zeolite
- High Si/Al ratio induced short crystallisation time and promoted the framework structure of HBEA zeolite
- HBEA demonstrated framework stability with high surface area and pore volume



4.0 Introduction

This chapter's main focus as discussed in chapter 1 was to synthesis BEA zeolite from South Africa CFA without the addition of an extra silica source using the indirect hydrothermal process. Also, the optimisation process which included suitable molar compositions, Si/Na ratio, Si/Al ratio, synthesis time and effect of water content on the synthesis process was a major outlook in this chapter. The detailed experimental protocol was presented in section 3.2.3, chapter 3 with all synthesis conditions. Different analytical techniques such as XRD, SEM, FTIR, BET, TGA and Si and Al NMR were used in order to ensure the characteristic properties of the extracted and synthesis zeolite materials (section 3.3).

4.1 Characterisation of coal fly ash (CFA)

CFA as the feedstock material for the synthesis of BEA zeolite was characterised using the following analytical tools: SEM, XRD, FT-IR and XRF with in-depth discussion. The chemical composition of South Africa CFA was analysed using X-ray fluorescence (XRF) as described in Section 3.3.4. Table 4.1 shows the major elemental content in the CFA with each of the analysis carried out in triplicate (n = 3) of the same sample on dry bases.

Table 4.1: XRF analysis of the major elemental composition of CFA (n = 3).

Major oxides	Coal fly ash samples (%)			
	CFA1	CFA2	CFA3	Average (%)
SiO ₂	56.54	56.51	56.51	56.52±0.02
Al ₂ O ₃	27.54	27.43	27.39	27.45±0.08
Fe ₂ O ₃	5.90	5.97	5.97	5.95±0.04
CaO	5.58	5.59	5.60	5.59±0.01
TiO ₂	1.69	1.70	1.71	1.70±0.01
MgO	1.67	1.70	1.72	1.70±0.03
K ₂ O	0.59	0.60	0.61	0.60±0.01
P ₂ O ₅	0.39	0.39	0.38	0.39±0.01
MnO	0.05	0.05	0.06	0.05±0.01
Cr ₂ O ₃	0.02	0.03	0.03	0.03±0.01
V ₂ O ₅	0.02	0.02	0.02	0.02
Na ₂ O	0.01	Nd	Nd	0.01±0.01
Total	100.00	100.00	100.00	100.01
SiO ₂ /Al ₂ O ₃	2.05	2.06	2.06	2.06

*Nd = not detected.

Table 4.1 summarised the amount of major elements present in CFA as determined by XRF. The CFA is predominantly composed of two metal oxides, Si and Al ($\text{SiO}_2 > \text{Al}_2\text{O}_3$) with a sum total of 82.08% as confirmed in Figure 4.2 (XRD analysis). Other metal oxides constitute less than 20% of the total elemental content with a minor amount of divalent elements such as Ca, Ti, Mg and Mn as well as monovalent elements of Fe, P, Na. The CFA can then be classified as class F since the weight percentage oxides of Si, Al and Fe, in accordance with the American Society for Testing and Materials (ASTM) is greater than 70% (ASTM C168-1993). Since the silica and alumina are the major components found in CFA, similarly, when both elements are tetrahedrally bonded to oxygen there is a possibility that transformation into zeolitic phase can occur.

The chemical composition of CFA as presented in Table 4.1 shows that the $\text{SiO}_2/\text{Al}_2\text{O}_3$ of South Africa CFA (class F) was 2.06. According to Cao and Shah (2007), the mechanism of zeolite formation from CFA depends on the $\text{SiO}_2/\text{Al}_2\text{O}_3$ ratio. The $\text{SiO}_2/\text{Al}_2\text{O}_3$ ratio as suggested by Majchrzak-Kucęba (2013), should fall within the range of 2-2.4. Musyoka et al., (2012a) reported that in order to synthesis a low silica zeolite such as A, P, and X from the CFA, the amount of $\text{SiO}_2/\text{Al}_2\text{O}_3$ in South Africa coal fly ash should be > 1.65 . Thus, the low $\text{SiO}_2/\text{Al}_2\text{O}_3$ ratio is an indication that the direct use of CFA is not suitable for the synthesis of high silica zeolites such as BEA since the required synthesis molar ratio is above 10.

The morphological composition of the CFA was determined using SEM analysis as described in chapter 3 (section 3.3.5). The micrograph in Figure 4.1, presents the morphology of the CFA.

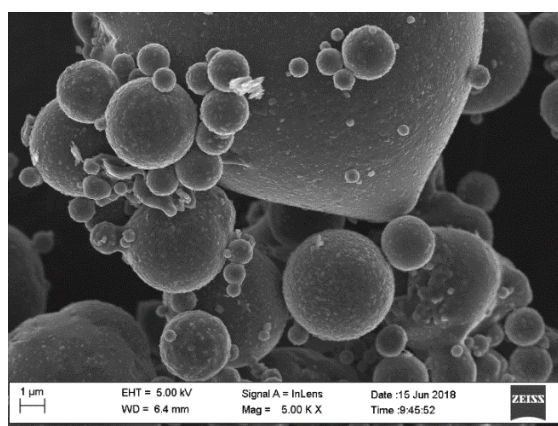


Figure 4.1: SEM micrograph of the South African class F Arnot CFA.

The resultant SEM micrograph in Figure 4.1, reveals that the particles of CFA were predominantly spherical in shape with a smooth surface while the oval spherical particles are related to the amorphous glass phases of the CFA. Ahmaruzzaman, (2010) also related the smooth and spherical shape as a characteristic phenomena observed in FA. In the same way, Inada et al., (2005) attributed the amorphous glassy phase coverage to be responsible for the smooth surface appearance of CFA as shown in Figure 4.1. The amorphous glassy phase can only be related to the mineral content in the CFA.

The mineralogical phase composition of CFA was determined using XRD analysis in accordance with the experimental procedure highlighted in Section 3.3.6. FFA is the code name assigned to the fused fly ash obtained after the fusion of FA + NaOH at 550 °C for 1.5 h in a furnace as described in Section 3.2.1. Figure 4.2 presents the various mineral phases in the CFA and FFA.

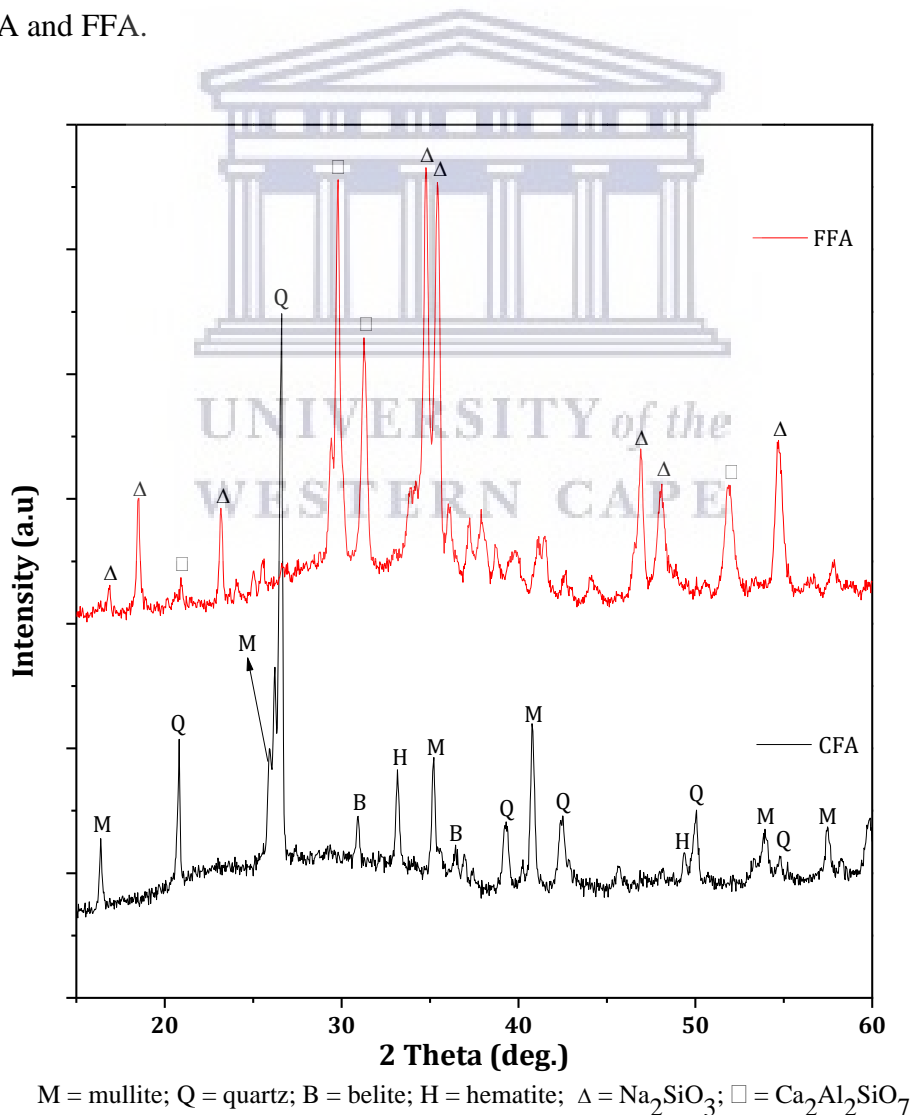


Figure 4.2: XRD pattern of coal fly ash (CFA) and fused fly ash (FFA).

The obtained XRD spectra of the CFA as presented in Figure 4.2, constituted glassy amorphous phases between the range of 20 and 40° 2θ in the CFA. Two major crystalline phases also were observed in the CFA, this included mullite and quartz, while the other mineral phases embedded within the matrix of the CFA particles are hematite and magnetite. Since the mineral phases were predominantly composed of aluminosilicate glass (3Al₂O₃.SiO₂) and crystalline quartz (SiO₂) or mullite, this accounted for the rich SiO₂ and Al₂O₃ content in CFA. Similarly, the quantitative X-ray diffraction conducted by Aldahri et al. (2016) substantiated that 88% of the CFA was amorphous aluminosilicate, 8% quartz (SiO₂), 3% mullite (3Al₂O₃.SiO₂) and 1% other mineral phases. Ríos and William (2008) and Musyoka et al., (2011b), reported that mullite, quartz, hematite, and magnetite are the major mineral phases found in CFA.

The interaction of CFA with NaOH in Figure 4.2 (FFA) shows that the identified mineral phases of mullite, quartz, and hematite were converted to other mineral phases after the alkali activation of the CFA via fusion. The absence of the CFA mineral phases in FFA indicates the complete transformation of the primary components into Na₂SiO₃ and Na₂AlO₂ (aluminates and silicate of sodium, respectively) in the presence of NaOH during the fusion process at 550 °C for 2 h (see Figure 4.2-FFA). The hump observed at lower diffraction angle between 20-34° 2θ indicated that both CFA and FFA contained amorphous glassy materials. Similarly, Ojha et al., (2004) found that in the process of the solid-state reaction of CFA with NaOH under high temperature, the existing mineral phase transformed into two mineral phases of aluminate and silicate of sodium. The transformation of the aforementioned mineral phases suggest the elimination of the embedded mineral phases in the CFA, thus the silicon and aluminium in the FFA can easily be released into solution to enhance the zeolitization process.

The structural configuration of various elements in the CFA and FFA can be associated with different vibrational and stretching bonds. The FT-IR spectroscopy in Figure 4.3 represents the structural characterisation of CFA and FFA, these spectra were collected following the detailed procedure described in Section 3.3.7. Figure 4.3 describes the major characteristic bands associated with CFA which include the bending, symmetric stretching and asymmetric stretching vibrations. Furthermore, the three wide bands related to the internal

vibrations of TO_4 (where T = Al or Si) were identified and are discussed in this section (Figure 4.3).

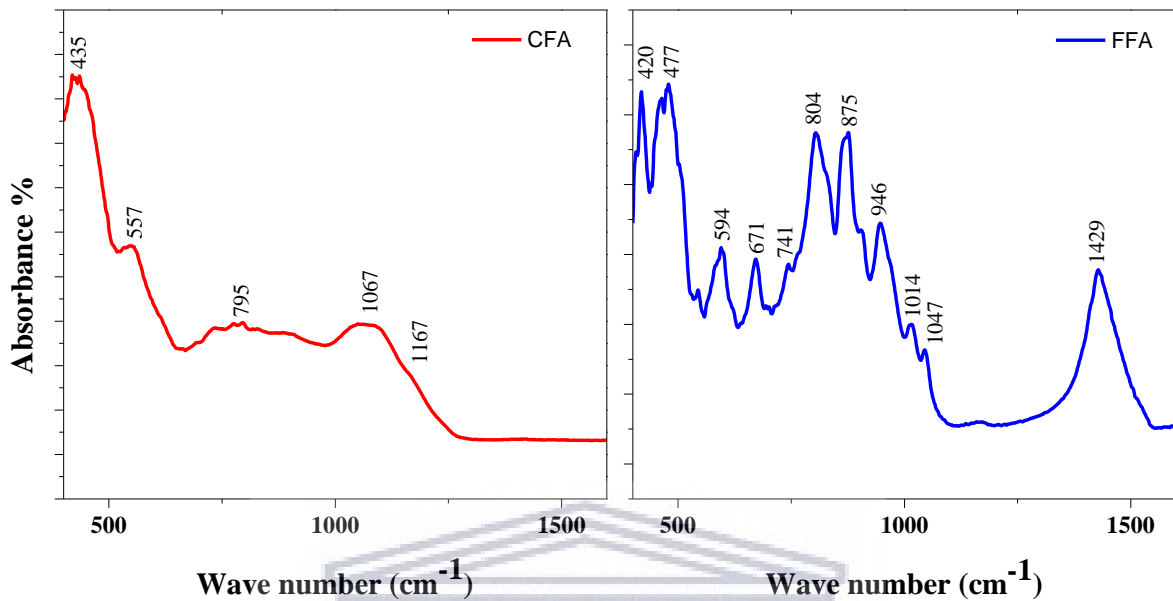


Figure 4.3: FT-IR spectra for the structural analysis of Arnot CFA and FFA

The FT-IR spectra of CFA is shown in Figure 4.3. The bands at 435, 795 and 900 cm^{-1} were assigned to the asymmetric bending vibration or stretching vibration bonds. At 435 cm^{-1} the band was attributed to Si-O-Si symmetric bending vibrations (Fernández-Jiménez and Palomo, 2005). The octahedral aluminium that is present in the mullite phase was associated with the band located at 557 cm^{-1} (Criado et al., 2007). The bands appearing at about 795 cm^{-1} and 900 cm^{-1} are associated with symmetric T-O (T = Al, Si) stretching vibration of the quartz phase in the CFA. The broad and intense bands at 1067 cm^{-1} could be assigned to the asymmetric stretch associated with Si-O (T = Al, Si) for mullite, glass and quartz phase. Also, the symmetrical stretching vibration and asymmetrical vibration associated with Al-O-Si can be responsible for the spectral bands appearing at 1167 cm^{-1} (Colthup et al., 1990; Rida and Harb, 2014).

Interestingly, during the fusion process, the peaks associated with quartz (at 795 cm^{-1}) were depolymerized into small monomeric silicate and oligomer bands between (671 and 946 cm^{-1}). Whilst, the peaks between 594 cm^{-1} and 875 cm^{-1} are associated with external asymmetric vibrations and could relate to the presence of silicates and aluminosilicate species that are linked tetrahedrally to oxygen atoms (AlO_4 and SiO_4) (Criado et al., 2007). Moreso, Bass

and Turner (1997) suggested that the peaks between 875 cm^{-1} and 1047 cm^{-1} can be associated with sodium silicate while the peaks below 875 cm^{-1} were assigned to glassy sodium silicate. It was found that the peaks at 874 cm^{-1} and 946 cm^{-1} can be attributed to T-O asymmetric stretching vibration of orthosilicate which can be used to elucidate the degrees of crystallinity. Tanaka et al. (2002) observed that the formation of T-O bending vibrations can be confirmed with the presence of the peak spectra between 420 cm^{-1} and 477 cm^{-1} . Whereas, Álvarez-Ayuso and Querol (2008), found that the band centred at 1429 cm^{-1} corresponds to the carbonate asymmetric stretching of sodium carbonate which resulted from the reaction of alkali metal hydroxide with atmospheric CO_2 . Overall, the formation of monomers and oligomers in FFA clearly indicates the formation of soluble silicates and aluminosilicate species as confirmed by XRD (see Figure 4.2).

4.2 Extraction of silica from fused fly ash

In Chapter 3 (see section 3.2.2), the extraction of silica from fused fly ash solution was elucidated. The silica extract was prepared in a two-step process, namely: precipitation and reflux process. The first step involved the acid treatment (sulphuric acid 95%) of fused fly ash solution. During the dropwise addition of the acid, a white precipitate was formed which was then separated and dried. The obtained powder precipitate (FFAE) was further treated under reflux with different concentrations of oxalic acid. This section addresses the effect of oxalic acid as a chelating agent for the extraction of silica with high Si/Al ratio from CFA.

4.2.1 Effect of oxalic acid on the silica extract

The reflux process involved a mixture of FFAE and various molar concentration of oxalic acid in ratio 1g: 10 mL treated at $80\text{ }^\circ\text{C}$ for 6 has set out in Section 3.2.2. The FFAE was treated using different concentrations of either 1.3, 1.5 or 1.7 M oxalic acid. Subsequently, the resultant silica extract was dried overnight at $70\text{ }^\circ\text{C}$ then code names: Si1.3, Si1.5 and Si1.7 were assigned to the obtained solid Si extract according to the concentration of oxalic acid used. This section presents discusses and compares the results of the various oxalic acid extracted FFAE obtained using the following analytical techniques XRD, SEM, FTIR and XRF analysis. Figure 4.4 compares the XRD pattern of the extracted silica from FFA.

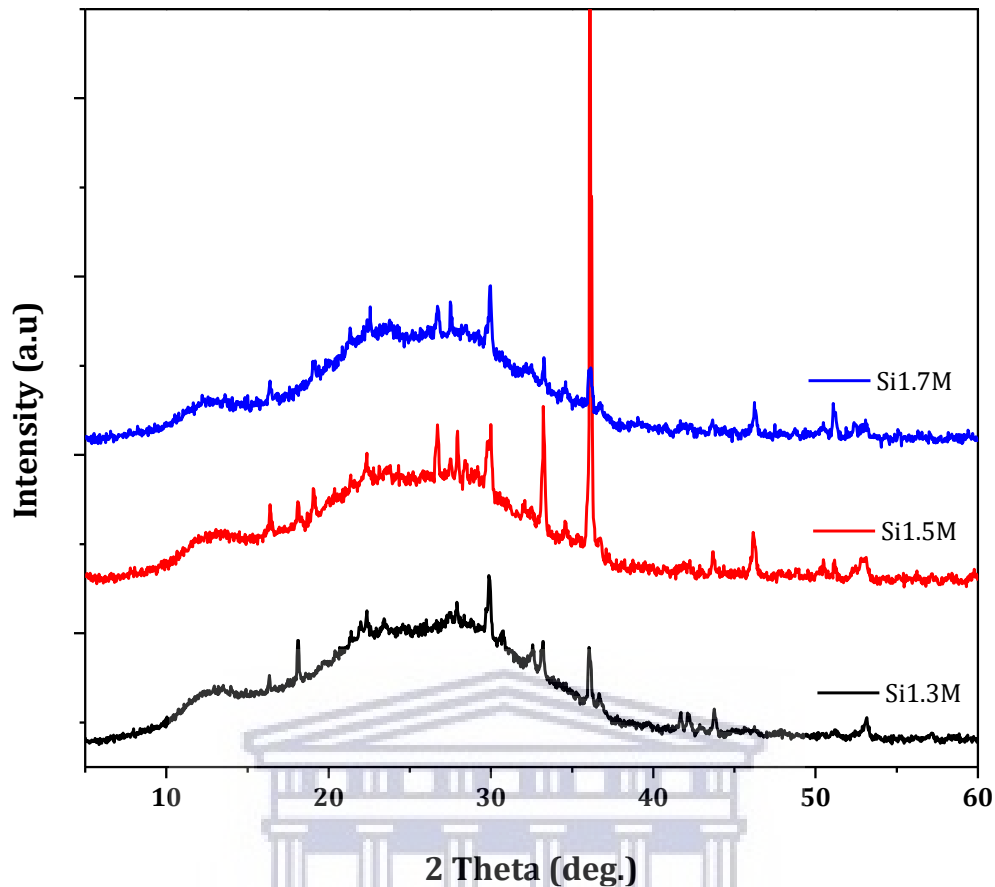


Figure 4.4: XRD patterns of the extracted silica obtained using 1.3, 1.5 and 1.7 M oxalic acid (Si1.3, Si1.5 and Si1.7, respectively) under reflux condition of 80 °C for 6h.

The XRD patterns of the oxalic acid refluxed FFAE using different concentrations are shown in Figure 4.4. The XRD spectra show that the products constitute mainly of an amorphous phase that exhibited a broad hump between 15 and 37° 2 θ . The peak intensity of Si1.5 at 36° 2 θ increased significantly compared to Si1.3 and Si1.7. It can be speculated that the presence of the sharps peaks indicate an induced crystalline phase. Yuvakkumar et al. (2014) reported that the observed sharp peaks in the XRD spectra is an evident of a crystalline nano silica phase. The observed hump typically characterises amorphous silica, which is in agreement with Gao et al. (2017) and Suttipat et al. (2018) who attributed the hump at 2 θ in the range of 15 to 35° to amorphous nano silica. These spectra indicate that the mineral phases of quartz, mullite and other mineral phases in fly ash were completely transformed into amorphous silica as shown in Figure 4.4.

Since the characteristic shape of CFA is mostly spherical, the morphology of the extracted amorphous silica was studied with SEM. Figure 4.5 presents the SEM micrographs showing the morphology of Si1.3, Si1.5 and Si1.7 extracted silica.

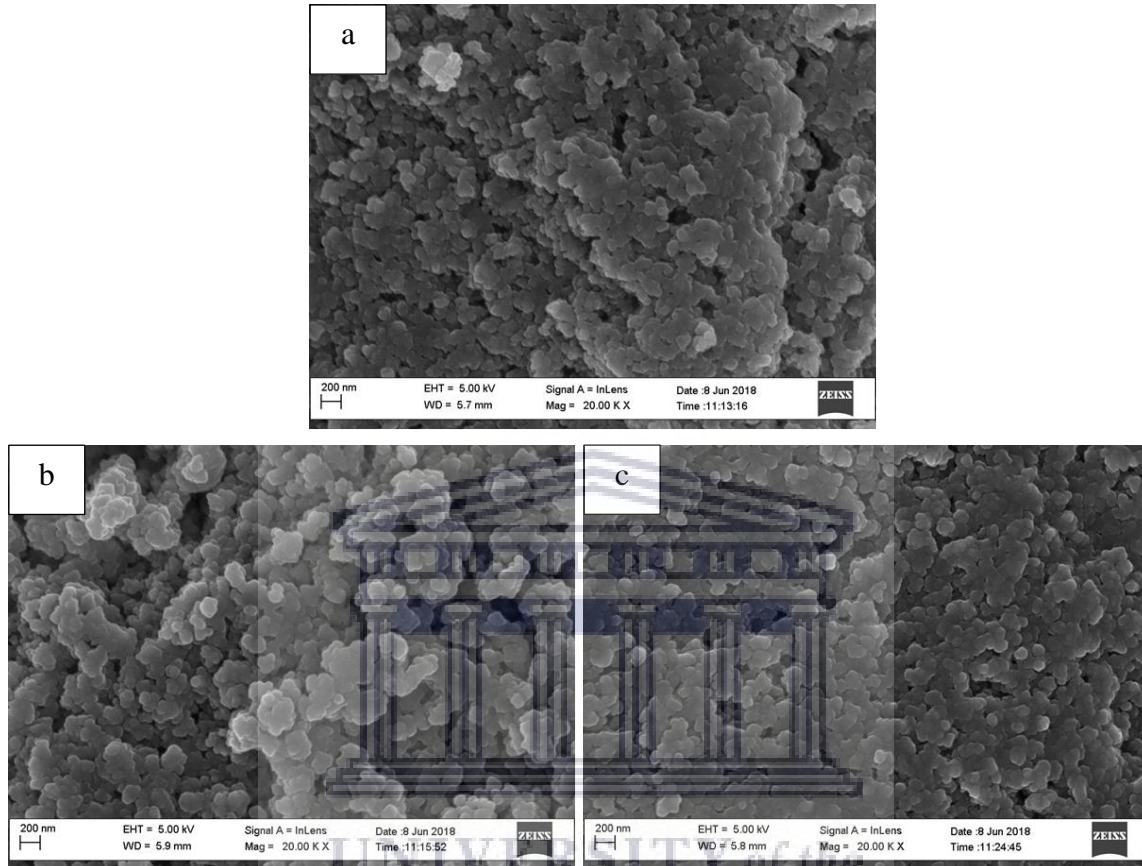


Figure 4.5: SEM images of extracted silica obtained from the treatment of FFAE using different concentrations of oxalic acid of a) 1.3M (Si1.3) b) 1.5M (Si1.5) and c) 1.7M (Si1.7).

The morphology of the amorphous silica extracts (Si1.3, Si1.5 and Si1.7) was characterised by SEM analysis as shown in Figure 4.5. It was observed that the spherical particles of the respective mineral phases in the CFA (see Figure 4.1) were totally transformed into agglomerated spheroid nanoparticles of amorphous silica generally smaller than 200 nm (see Figure 4.5). Mor et al. (2017) described such morphology obtained from agricultural waste as spheroid nano silica particles. These results show that the appearance of the amorphous nano-sized particles of silica (Si1.3, Si1.5 and Si1.7) were different to the CFA morphology. To further investigate the characteristics of silica from FA, the structural analysis was conducted by FT-IR as described in Section 3.3.7.

Figure 4.6 presents the structural analysis of the samples obtained when FFAE was treated with different concentrations of oxalic acid (1.3, 1.5 and 1.7M) using FT-IR analysis as highlighted in Section 3.3.7.

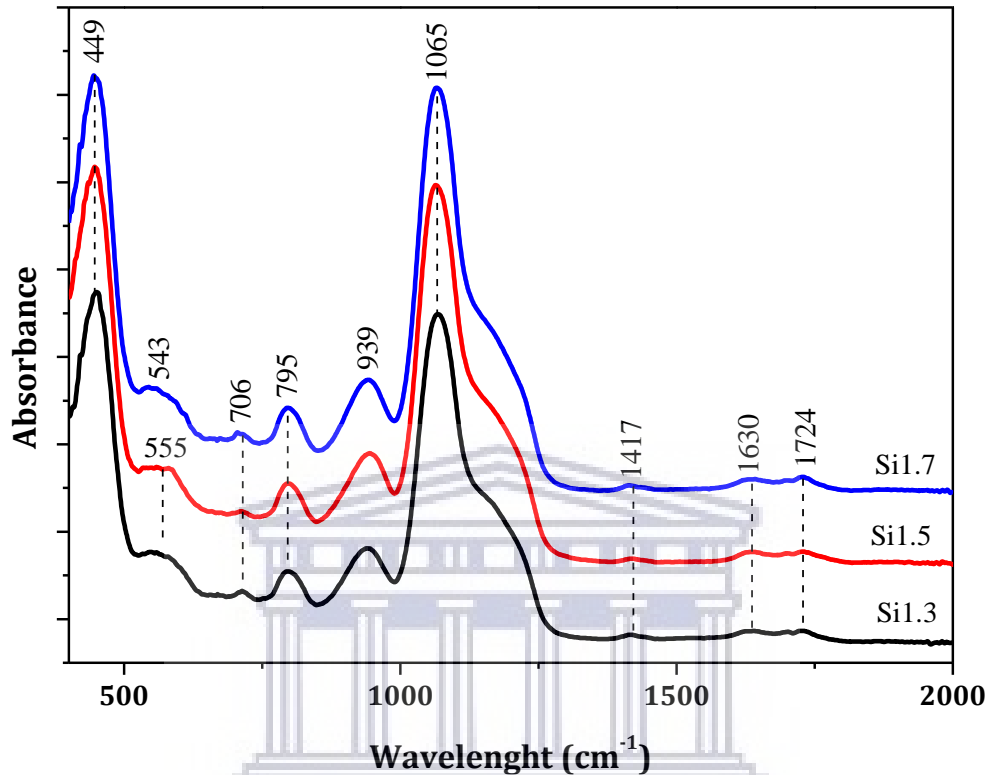


Figure 4.6: FT-IR spectra of fly ash based silica samples extracted at different oxalic acid treatment concentrations of 1.3, 1.5 and 1.7M (Si1.3, Si1.5 and Si1.7 respectively).

The FT-IR spectra in Figure 4.6 illustrate the characteristic peaks of samples obtained from FFAE using different concentrations of oxalic acid (Si1.3, Si1.5 and Si1.7). In Figure 4.6, the peaks at 455, 795 and 1065 cm^{-1} were linked to Si-O-Si bonds, which can be attributed to bending vibration, symmetrical stretch and asymmetrical stretching vibrations of the siloxane structure respectively (Mor et al., 2017; Yan et al., 2017). It was observed that the intensity of the assigned bending and stretching vibrations increased as the treatment concentration with oxalic acid increased (Si1.3<Si1.5<Si1.7). While the small shoulder at 555 cm^{-1} (Si1.3 and Si1.5), which corresponded to the four-member rings $[\text{Si-O}]_4$ (Yan et al., 2017) gradually shifted to a lower position at 543 cm^{-1} (Si1.7) as the oxalic acid concentration increased. The adsorption band around 939 cm^{-1} could be related to the monomeric or dimeric SiO^- network structure of Si-OH vibrations as reported by Li et al. (2014). Costa and Paranhos (2018) attributed the bending vibration at 1630 cm^{-1} to the water

molecule (H-O-H) adsorbed upon the framework structure of the extracted silica. Furthermore, the other absorption bands at 706 and 1417 cm^{-1} could be assigned to the Si-C group and C-N stretching vibration respectively, as suggested by Li et al. (2014), which might be contrary to the case of the fly ash based extracted silica. However, Saikia and Parthasarathy (2010), related the band at 1417 cm^{-1} to a carbonate band of Na, Ca or K cation.

Herein, it was observed that the spectra of the FFA (see Figure 4.3) either shifted, disappeared or formed new bands after treatment with oxalic acid. This shows that the leaching of metallic ions such as Na^+ and Al^{3+} by the oxalic acid from the sodium silicate and alumina silicate aided the amorphous form of silica formation. In order to corroborate the aforementioned results, Table 4.2 compares the band formed in the fly ash based extracted silica with commercial fumed silica as reported by Li et al. (2014).

Table 4.2: Comparison of the extracted fly ash based silica and pure fumed silica.

Bands	Type of silica band (cm^{-1})		Assignment
	Fumed silica (Li et al., 2014)	FFAE based silica (This work)	
Si-O-T (T=Al or Si)	468 802	455 795	Bending vibration Symmetric stretching
Si-O	969	939	Asymmetric stretching
Si-O-T	1087	1065	
CO_3	-	1417	Carbonate of Na, Ca or K
H-O-H	1628	1630	H_2O adsorbed

Table 4.2 shows that the identified functional group of the relative bending vibrations, symmetric and asymmetric stretching bands are comparable to that of a typical fumed silica. The adsorption wavelength of the identified Si-O-T and Si-OH bending and stretching bands (Figure 4.6 and Table 4.2) in the extracted fly ash based silica were similar to the bands present in commercial fumed silica as presented by Li et al. (2014) (Table 4.2). This clearly validated the fact that the mineral phases of the CFA (Figure 4.3) are completely transformed into suitable SiO_2 and aluminosilicate species as supported by XRD and SEM in Figure 4.4 and 4.5, respectively. Moreso, this is an indication that the extracted silica could be suitable

for the zeolitisation process of BEA zeolite since both XRD and FT-IR confirm the presence of amorphous silica. Therefore, it is necessary to establish that the Si/Al ratio of the silica extract would be suitable for the synthesis of BEA zeolite.

Table 4.3 presents the elemental composition, Si/Na and Si/Al ratio of the Si1.3, Si1.5 and Si1.7 extracted silica. The elements in the extracted fly ash was determined by XRF analysis in triplicate as described in Section 3.3.4.

Table 4.3: Elemental composition of the various silica extracts from CFA.

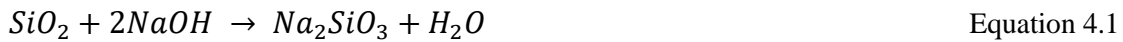
Major oxides	FFAE (wt%)	Extracted fly ash based silica (wt%)		
		Si1.3	Si1.5	Si1.7
SiO ₂	42.53±0.17	91.74±0.930	90.98±1.835	91.80±0.232
Al ₂ O ₃	3.42±0.205	1.69±0.078	1.31±0.005	1.53±0.005
Fe ₂ O ₃	0.21±0.027	0.07±0.017	0.05±0.001	0.08±0.017
CaO	0.01±0.002	Nd	Nd	Nd
TiO ₂	0.01±0.001	0.01	0.02±0.005	0.01
MgO	0.03±0.003	0.03±0.012	0.05±0.006	0.05±0.012
K ₂ O	0.49±0.043	0.07±0.011	0.15±0.082	0.14±0.07
P ₂ O ₅	0.10±0.003	0.04	0.06±0.012	0.04
MnO	Nd	Nd	Nd	Nd
Cr ₂ O ₃	Nd	Nd	Nd	Nd
V ₂ O ₅	Nd	Nd	Nd	Nd
Na ₂ O	53.20±0.157	6.35±0.260	7.38±0.918	6.35±0.027
Total	100	100	100	100
Si/Na	0.50	9.1	7.76	9.11
Si/Al	10.98	47.88	61.14	53.04

*Note: Nd – not detected

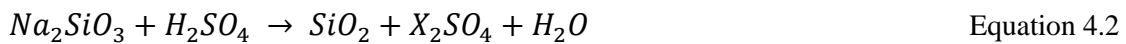
It should be recalled that CFA was fused with NaOH prior to sulphuric acid treatment, because of this, the obtained FFAE was than treated with 1.3, 1.5, and 1.7 M oxalic acid (Si1.3, Si1.5 and Si1.7) respectively. The composition of the extracted fly ash based silica describes the elemental content in their oxide form as presented in Table 4.3. After the treatment of CFA solution with sulphuric acid, the oxide of Na in the precipitated FFAE showed a great increase of about 48.44% compared to the feedstock CFA (see Table 4.1). This is due to the addition of NaOH during the fusion process of CFA as described in Section

3.2.1. The major oxides of Na>Si>Al comprised 90.45% of the total chemical composition in FFAE which had a Si/Al ratio of 10.98. However, the high amount of Na oxide and low Si/Na ratio (0.50) in FFAE (Table 4.3) might be a limitation for the zeolitisation process of BEA zeolite. Awizar et al. (2013) illustrated the extraction of silica with the following equations (4.1 and 4.2).

Fusion process



Precipitation process



where X can be Na or Ca or other alkaline metals.

A high percentage removal of Na from FFAE (53.20%) to 6.35, 7.38 and 6.35 of Si1.3, Si1.5 and Si1.7 respectively was obtained with the oxalic acid treatment with a gradual decrease of Al content from 3.42% to <1.70% in these samples. Other metals that might be a source of impurities such as Ca, Fe, Ti, Mg, K and P were reduced to less than 0.9%. Hence, the oxalic acid leaching was able to remove unwanted components apart from SiO₂. Accordingly, the Si/Al ratio of Si1.3, Si1.5 and Si1.7 increased to 47.88, 61.14 and 53.04 respectively as the treatment concentration increased (oxalic acid). These results confirmed the characteristics of Si-O-Si and Si-OH identified by XRD and FT-IR analysis as the major component in the samples of silica (Si1.3, Si1.5 and Si1.7). Also, the efficient removal of Na, Al as well as Fe components from FFAE, resulted in a silica extract with little or no impurities. The percentage purity (%) and yield (%) of Si1.3, Si1.5 and Si1.7 was calculated using equations 4.3 and 4.4 respectively.

$$P (\%) = 1 - \sum_{i=1} m_i \% \quad \text{Equation 4.3}$$

$$Yield (\%) = \frac{m_{extract}}{m_{extract} + m_{CFA}} \% \quad \text{Equation 4.4}$$

where m_i , is the mass of the components in the extracted silica expect SiO_2 , m_{extract} is the and m_{CFA} is the mass of the elemental components in the silica extract and CFA, respectively. Table 4.4 compares the percentage purity and yield of untreated and treated FFAE leached with different concentrations of oxalic acid (Si1.3, Si1.5 and Si1.7).

Table 4.4: Percentage purity and yield of the extracted fly ash based silica.

Conc. of oxalic acid (M)	Percentage		Code name
	% Purity	% Yield	
Untreated	57.95	50.77	FFAE
1.3	94.20	44.77	Si1.3
1.5	93.58	44.92	Si1.5
1.7	94.21	44.79	Si1.7

The purity of the extracted fly ash based samples as shown in Table 4.4, indicate that the percentage purity increased significantly from 57.95% to approximately 94 % when FFAE was treated with oxalic acid (Si1.3, Si1.5 and Si1.7). These results further confirmed that the main component of the oxalic acid treated FFAE extract is predominately silica. However, the percentage yield decreased as the FFAE was treated with different concentration of oxalic acid in the following order: FFAE>Si1.5>Si1.7>Si1.3. The reduction in product yield clearly suggest that i) most of the Al, Fe and Ca component and about 14.01% Si are still in the solid residual waste obtained after the separation of FFA and H_2O (see Table 4.1 and 4.3 and section 3.2.1-3.2.2) and ii) during the treatment of FFAE with oxalic acid. Cations such as Na, K, Mg, Ca, Fe were chelated into their respectively soluble metal ions as illustrated in equation 4.1 and 4.2. Nevertheless, it is noteworthy, that the pure silica extracted from CFA offers an advantage as a feedstock material for the synthesis of high silica BEA zeolite without the addition of other silica sources. Also, the Si/Al ratio of the products were within the range needed for the synthesis of BEA zeolite as suggested by Cao et al. (2011).

4.3 Synthesis of BEA zeolite from extracted fly ash based silica

After the treatment of the precipitated FFAE with oxalic acid, three silica products were obtained namely: Si1.3, Si1.5 and Si1.7 as presented and discussed in the previous section of this chapter. The silica extracts (Si1.3, Si1.5 and Si1.7) with different resultant Si/Al ratios

of 47.88, 61.14 or 53.04 respectively were mixed with specific amount of NaOH, Al(OH)₃, H₂O and TEAOH to form the synthesis mixtures with the respective molar compositions:

- 1 Si : 0.022 Al : 0.218 Na : 0.396 TEAOH : 8.906 H₂O (Si1.3)
- 1 Si : 0.017 Al : 0.241 Na : 0.399 TEAOH : 8.980 H₂O (Si1.5)
- 1 Si : 0.020 Al : 0.217 Na : 0.396 TEAOH : 8.90 H₂O (Si1.7)

(See Table 3.3, section 3.2.3 for detailed description).

determined, the synthesis mixtures were subjected to hydrothermal crystallisation at 140 °C for 72 h and the recovered crystals were oven-dried overnight. Figure 4.7 present the XRD spectra elucidating the effect of Si1.3, Si1.5 or Si1.7 silica extract on the synthesised products.

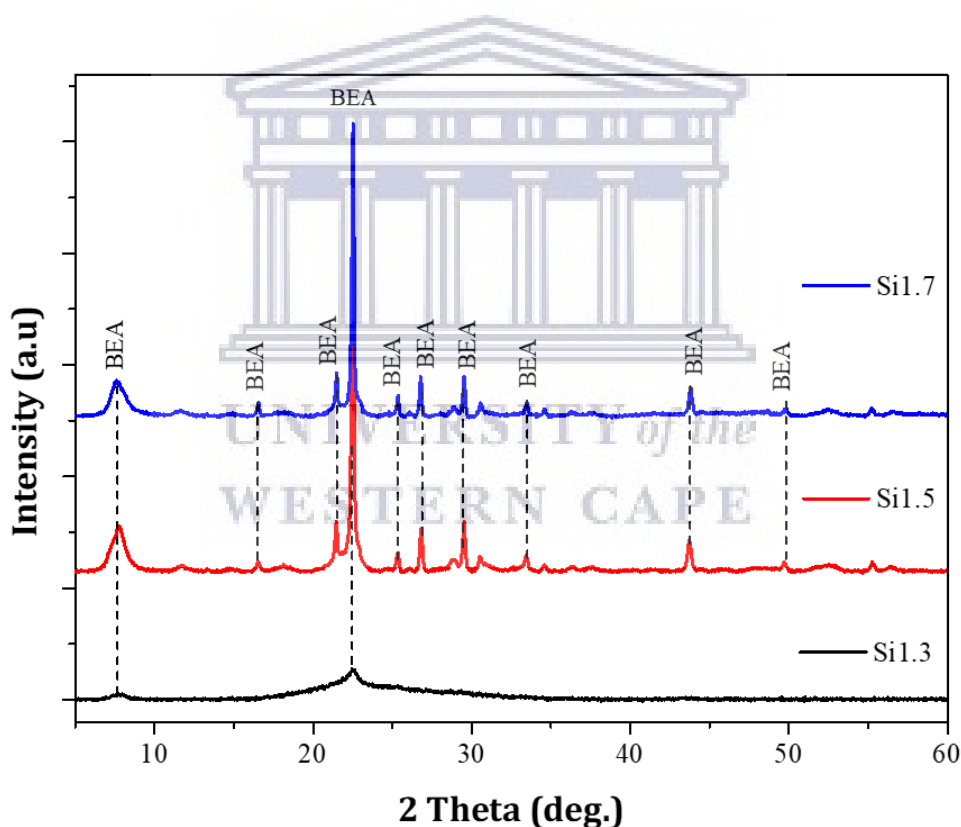


Figure 4.7: XRD patterns of the BEA zeolites synthesised from treated FFAE with different concentrations (1.3, 1.5M and 1.7 M) of oxalic acid (Si1.3, Si1.5 and Si1.7, respectively) at 140 °C for 72 h.

Figure 4.7 compared the XRD patterns of BEA zeolite samples synthesised with different silica extracts obtained from the treatment of precipitated FFAE with 1.3, 1.5 and 1.7 M oxalic acid. It is found that the major diffraction peaks at 7.7 and 22.5 2θ which are assigned

to be BEA zeolite phase was observed in all the synthesised products. However, Si1.3 silica extract contained mainly amorphous phase. With increased concentration of oxalic (Si1.5 and Si1.7 silica extras), the intensity of the diffraction peaks increased with the appearance of other relevant peaks of BEA zeolite and no impurities. This clearly indicated that fly ash based silica extracts with Si/Al ratio ≥ 53 were completely converted to the BEA zeolite mineral phase (Joint Committee on Powder Diffraction Standards (JCPDS)). The fly ash based extracted silica (Si1.5) was sufficient for the synthesis of pure phase BEA zeolite which condition was set as the best for further study in the subsequent subsections. These results validate that the purity of the fly ash base silica extract allowed the complete solubility and dissolution of the new silica source in the synthesis mixtures which promoted the successful synthesis of BEA zeolite. Hence, the synthesis of BEA zeolite from fly ash based silica extracts presents an effective alternative strategy to produce high quality high silica zeolite.

4.4 Synthesis and characterisation of BEA zeolite

The synthesis of BEA zeolite as described in Chapter 3 (Section 3.2) involved four major steps: alkaline fusion, precipitation (sulphuric acid), reflux (oxalic acid treatment) and hydrothermal crystallisation. These experiments were performed to identify the optimum conditions for the crystallisation of BEA zeolite from South Africa CFA (using Si 1.5 silica extract). The characteristic of phase purity and crystallinity (XRD), morphological formation (SEM), framework structure (NMR), textural properties (BET) and thermal stability (TGA) were used to identify the optimum synthesis conditions in this section. Herein, the effect of the following parameters such as water content, sodium content, aluminium content and synthesis time during hydrothermal treatment of the synthesis mixture at 140 °C are presented and discussed in detail in the following subsections.

4.4.1 Effect of water on the crystallisation of BEA zeolite

In this sub-section, four molar composition was formulated from the optimal silica extract of 1.5Si extract. The effect of water was investigated based on the following molar composition:

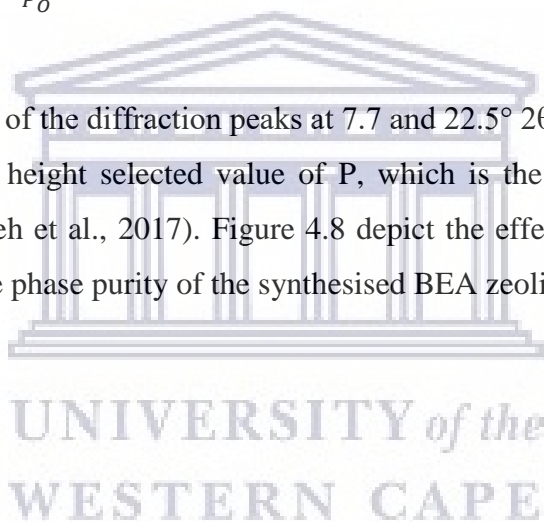
- 1 Si : 0.017 Al : 0.241 Na : 0.399 TEAOH : x H₂O

where $x = 8.980, 12.828, 17.958$ and 26.937 represent the varying water content (see Table 3.4, section 3.2.3).

Each of the molar composition was subjected to hydrothermal crystallisation at $140\text{ }^{\circ}\text{C}$ for 72 h. The following code names BEA4, BEA6, BEA9 and BEA14 were assigned to the different molar compositions in the order of increasing water content ($x = 8.980, 12.828, 17.958$ and 26.937), respectively (see Table 3.3). The recovered products were characterised using XRD and SEM analysis. The relative crystallinity was estimated by analysing the areas under the two main peaks in the diffraction spectra (at $2\theta = 7.7$ and 22.5°) using the following equation 4.5:

$$\text{Relative crystallinity} = \frac{P}{P_o} \times 100 \quad \text{Equation 4.5}$$

where P is the total area of the diffraction peaks at 7.7 and $22.5^{\circ} 2\theta$ and P_o is the equivalent area in the case of the height selected value of P , which is the corresponding standard assigned as 100% (Ameh et al., 2017). Figure 4.8 depict the effect of added water to the synthesis mixture on the phase purity of the synthesised BEA zeolites.



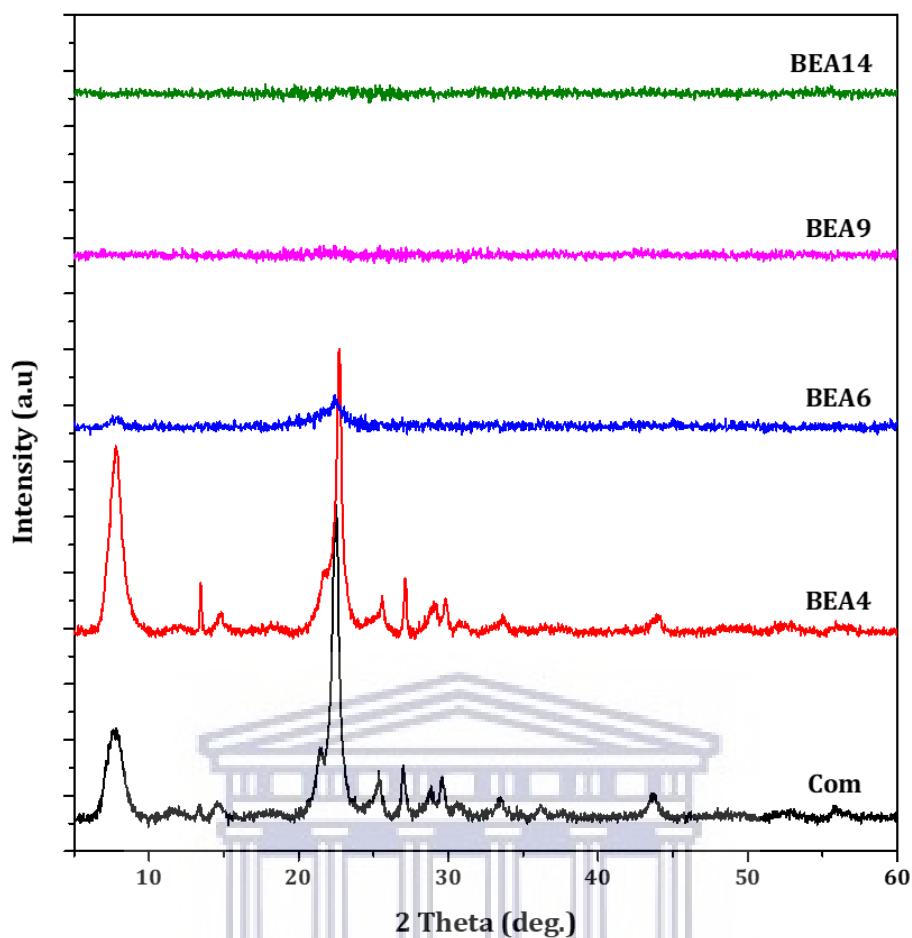


Figure 4.8: XRD patterns of the BEA zeolites synthesised from four different molar composition with varying water contents (BEA4, BEA6, BEA9 and BEA14 = 8.980, 12.828, 17.958 and 26.937, respectively) at 140 °C for 72 h.

The XRD patterns presented in Figure 4.8 shows the diffractogram of the different BEA zeolite synthesised by varying the molar fraction of water in the synthesis mixture. It was observed that the diffractogram of the BEA4 sample perfectly matched the associated peaks of reference BEA zeolite (Com) (see Figure 4.8). When further compared with the diffraction pattern as reported in the Database of Zeolite Structure, the collected diffraction peak of the sample BEA4 indicate that a pure phase BEA zeolite was synthesised (<http://www.iza-structure.org/databases/>). With increased molar fraction of water, BEA6 =12.828 only the two major peaks at 7.7 and 22.4° was observed. This suggested that the synthesised BEA6 sample contained both BEA zeolite and amorphous material. On the other hand, the main diffraction peaks at 7.7, 13.4, 22.4, 27.1, 28.7, 29.6 and 43.4° of sample BEA4 gradually disappeared as the water content in the synthesis mixtures increased (BEA9 and BEA14 = 17.958 and 26.937, respectively) into amorphous material. This clearly elucidated that an increase in the molar fraction of water content from $x = 12.828$ to $x \geq$

17.958 shifted the BEA crystal phase to being amorphous. This is similar to the findings of Manrique et al. (2016) and Gabrienko et al. (2010), who showed that higher H₂O/SiO₂ ratio lead to the formation of amorphous materials rather than a pure phase BEA zeolite. As the water content is reduced within the synthesis mixture, the solution becomes super-saturated, thereby enhancing the nucleation process and increasing crystal growth. Whereas, an increase in water content dilutes the concentration of primary aluminium and silicon species and this might hinder the processes of induction and cause slow nucleation.

Interestingly, the peak area at 7.7 and 22.4° of BEA4 zeolite was found to be high compared to the commercial BEA zeolite (Com) (see Figure 4.8). This implied that the relative crystallinity of the synthesised BEA4 zeolite was 11% higher than the commercial BEA zeolite (Com = 82%). Although, with increased molar water fraction the relative crystallinity of the fly ash based BEA zeolite reduced to less than 7%. Thereby, confirming the zeolitic phase transformation to amorphous phase with increased molar water fraction ≥ 12.828 . To validate the obtained product, SEM analysis was further carried out as described in chapter 3 (section 3.3.5).

Figure 4.9 presents the SEM micrograph of the zeolite products synthesised by varying the molar fraction of water content in the synthesis mixture (BEA4, BEA6, BEA9 and BEA14 = 8.980, 12.828, 17.958 and 26.937, respectively). Each of the obtained SEM micrographs was put into ImageJ software to calculate the crystal sizes of the synthesized BEA zeolite.

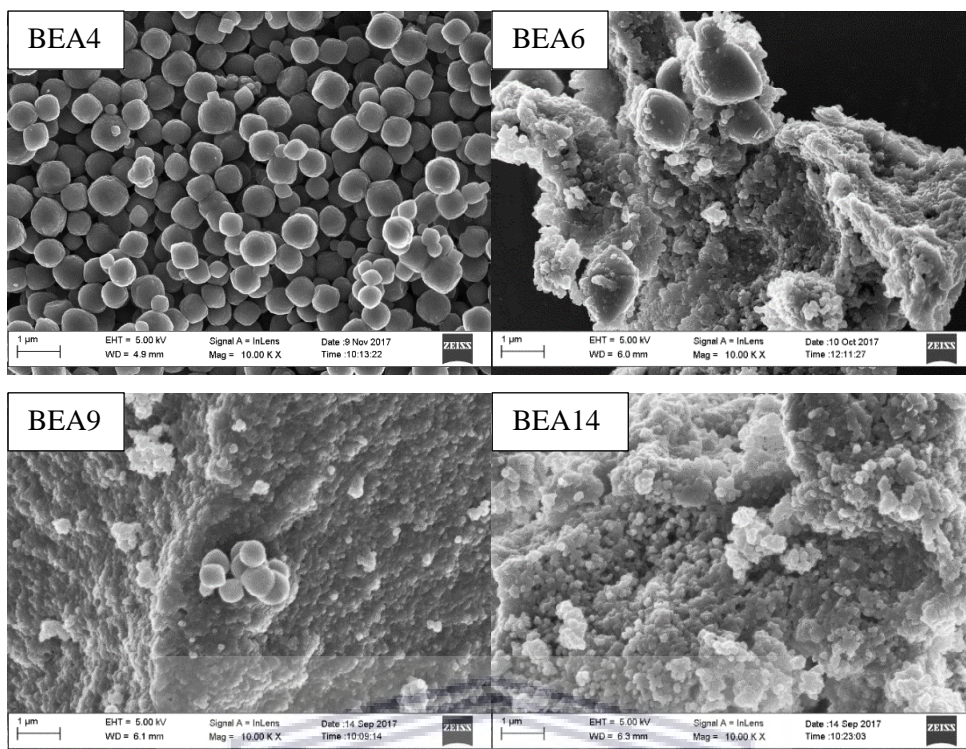


Figure 4.9: SEM images of the BEA zeolites synthesised from four different molar composition with varying water contents (BEA4, BEA6, BEA9 and BEA14 = 8.980, 12.828, 17.958 and 26.937, respectively) at 140 °C for 72 h.

The SEM micrographs in Figure 4.9 clearly illustrate the morphological features obtained from four set molar compositions with varying water content. The BEA4 and BEA6 micrographs showed the presence of spheroidal-shaped crystal structures (crystal size of 0.50 and 1.23 μm , respectively) however, the presence of nano-spherical agglomerates particles (85 to 90 nm) which were similar to the extracted silica (Figure 4.5b) was also observed in sample BEA6. Bregolato et al. (2007) described the crystal shape of a typical BEA zeolite to be spheroidal. The nanoparticle morphology seen in BEA6, BEA9 and BEA14 (see Figure 4.9) are due to lack of transformation of the silica precursor resulting from the high water content which prevented the formation of BEA zeolite under the applied conditions. It was also observed by Manrique et al. (2016) that a high molar fraction of water in the synthesis mixtures restricts the phase formation of the zeolite from the rearranged amorphous species of the precursor. The amorphous phase was further confirmed by lack of the diffraction peaks at 7.7, 13.4, 22.4, 27.1, 28.7, 29.6 and 43.4° as was presented by the XRD spectra in Figure 4.8 (BEA6, BEA9 and BEA14). This indicates that the dilution of the synthesis mixture prevented the nucleation and growth of the BEA zeolite. This is

because a supersaturated, concentrated synthesis mixture promotes the nucleation rate and enhance crystal growth (Vaudry et al., 1997).

After the characterisation of the synthesised samples, it was found from the aforementioned results that the best quality BEA zeolite with a pure phase and well-defined spheroidal morphology had a crystal size of 0.50 μm and was achieved with the molar formulation of 1 Si : 0.017 Al : 0.241 Na : 0.399 TEAOH : 8.980 H₂O (BEA4) under hydrothermal temperature of 140 °C for 72 h. Thus, the condition for the synthesis of BEA4 zeolite was set as the baseline to further study.

4.4.2 Effect of sodium and aluminium on the crystallisation of BEA zeolite

In this section, the effect of NaOH in the molar composition on the phase purity and morphology of BEA zeolite was investigated. The optimised molar composition (BEA4) from the previous section (4.3.2): 1 Si : 0.017 Al : 0.241 Na : 0.399 TEAOH : 8.980 H₂O was set as the baseline for this study. Presented herein is the generated molar composition:

- 1 Si : 0.017 Al : x Na : 0.399 TEAOH : 8.980 H₂O

where $x = 0.317, 0.461, 0.506, 0.552$ or 0.734 indicate the varying molar Na content due to the different amounts of NaOH added in the synthesis mixture (see Table 3.4, section 3.2.3).

Code names as described in Table 3.4 were assigned to each of the molar compositions: BEAN1, BEAN2, BEAN3, BEAN4, BEAN5 and BEAN6 following the amount of added NaOH (0.317, 0.461, 0.506, 0.552 and 0.734, respectively). Changing the molar Na content directly by use of NaOH affects the alkalinity of the molar composition which is regarded as one of the most important parameters in the hydrothermal production of zeolites (Lechert et al., 2011). The quality of the crystalline phase, the relative crystallinity (equation 4.5), crystal size and yield of the products was used to determine optimal conditions for the synthesis of BEA zeolite in this section. The percentage yield was determined from equation 4.6:

$$Yield (\%) = \frac{m_{product}}{m_{bulk}} \%$$

Equation 4.6

where, $m_{product}$ and m_{bulk} is the mass of the recovered product and bulk solid in the synthesis mixture (dry mass), respectively. Figure 4.10 and 4.11, show the mineral composition and morphological formation of the synthesised products after calcination. The mineralogical characterisation of the products was determined using XRD analysis (as described in section 3.3.6 giving the experimental procedure) and is presented in Figure 4.10.

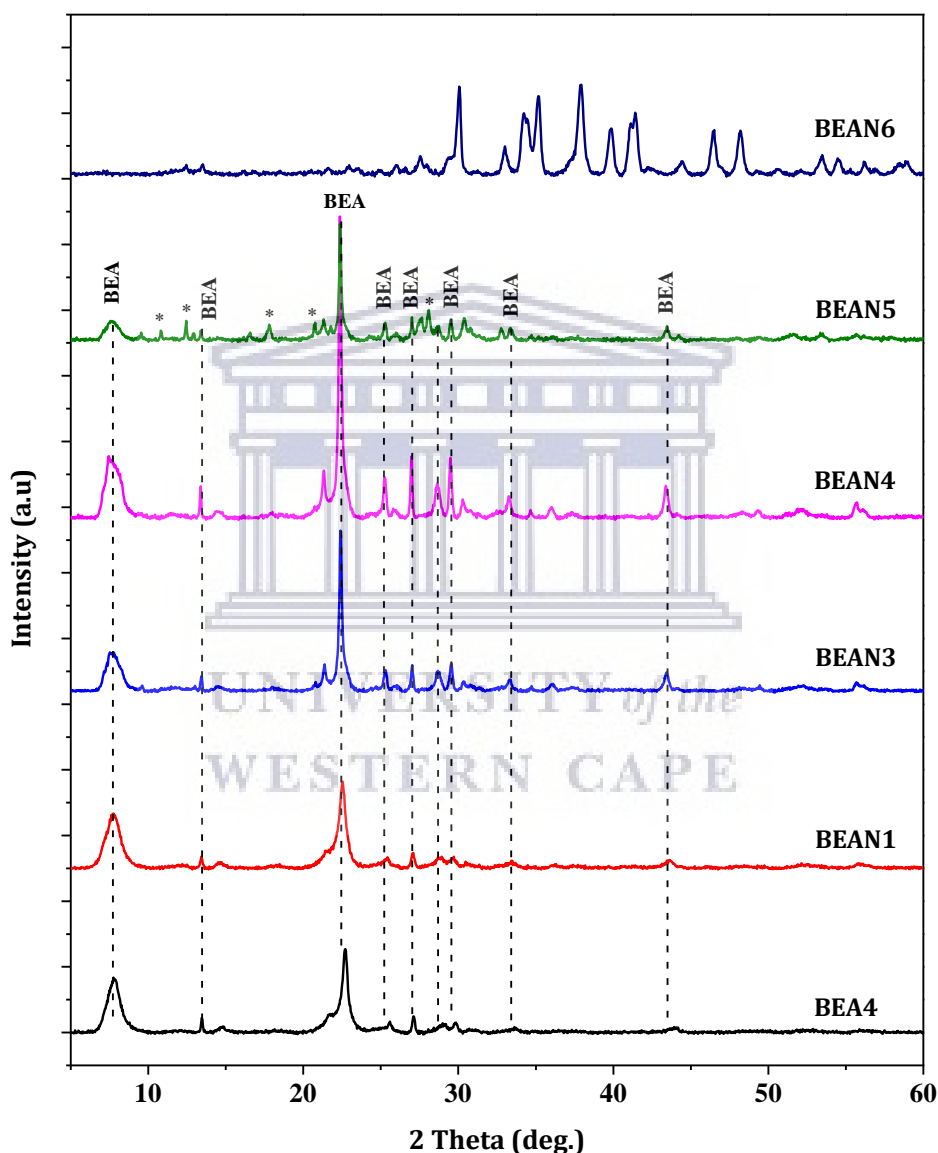


Figure 4.10: XRD patterns showing the effect of NaOH on the phase formation of BEA zeolites at 140 °C for 72 h. Different molar composition with varying molar Na contents (x) include: x = 0.241, 0.317, 0.461, 0.506, 0.552 and 0.734 (BEA4, BEAN2, BEAN3, BEAN4, BEAN5 and BEAN6, respectively).

Figure 4.10 shows the XRD patterns of BEA zeolite prepared from molar composition with different molar fraction of NaOH. For sample BEA4, BEAN1, BEAN3 and BEAN4 the associated diffraction peaks at 7.7, 13.4, 22.4, 27.1, 28.7, 29.6 and 43.4° of a typical BEA zeolite were observed (Joint Committee on Powder Diffraction Standards (JCPDS)). The broad peaks of samples BEA4 at 22.4° become narrow as the molar fraction of NaOH increased (BEAN1, BEAN3 and BEAN4, respectively). According to Yin et al. (2013), the narrowing of the main peaks can be associated with increased crystal size growth. To this end, Table 4.5 presents the comparable crystallinity, crystal size and percentage yield (see equation 4.6) of the various synthesised BEA zeolite. The crystal size was calculated from the SEM micrographs using ImageJ software.

Table 4.5: Comparison of crystallinity, crystal size and yield of products prepared from different molar fraction of NaOH.

Sample	Crystallinity (%)	Crystal size (µm)	Yield (%)
BEA4	70.7	0.50	25.7
BEAN1	80.8	0.62	14.6
BEAN3	57.0	0.86	9.0
BEAN4	100.0	1.95	9.9
BEAN5	27.2	1.75	5.3
BEAN6	NA	NA	19.8

When the molar fraction of NaOH in the molar composition increased from 0.241 (BEA4) to 0.317 (BEAN1), the growth in crystallinity and crystal size of BEAN1 increased with a noticeable decrease in the percentage yield of the product (see Table 4.5). As molar fraction of NaOH further increased from 0.317 (BEAN1) = 0.461 (BEAN3) and to 0.506 (BEAN4), the intensity of the characteristic diffraction peaks at 7.7 and 22.5° 2θ steadily increased (Figure 4.10) indicating the growth of the crystal size and crystallinity in the case of BEAN4 (Table 4.5). However, the percentage yield of BEAN3 and BEAN4 greatly decreased from 25.7% (BEA4) to ≤ 9.9 indicating that the recovery of the products reduced significantly compared to BEA4 zeolite with low molar fraction of NaOH (see Table 4.5). With further increase in the molar fraction of NaOH from 0.506 = 0.552 (BEAN5), other phases were introduced alongside the BEA zeolite, thereby compromising the purity and yield of the synthesised BEAN5 zeolite (Figure 4.10). A complete phase transformation was observed when the molar fraction of NaOH ≥ 0.734 (BEAN6). This indicates that a molar fraction ≤

0.506 NaOH content is required in the molar composition to form highly crystalline BEA zeolite. This, in turn, shows that the low Na content in the molar composition of BEA4 impacted directly in achieving sufficient crystallinity, yield and nano crystal size of the synthesised BEA zeolite as well as good yield.

The morphology of the BEA zeolite from synthesised molar compositions with different molar fractions of NaOH is presented in Figure 4.11.

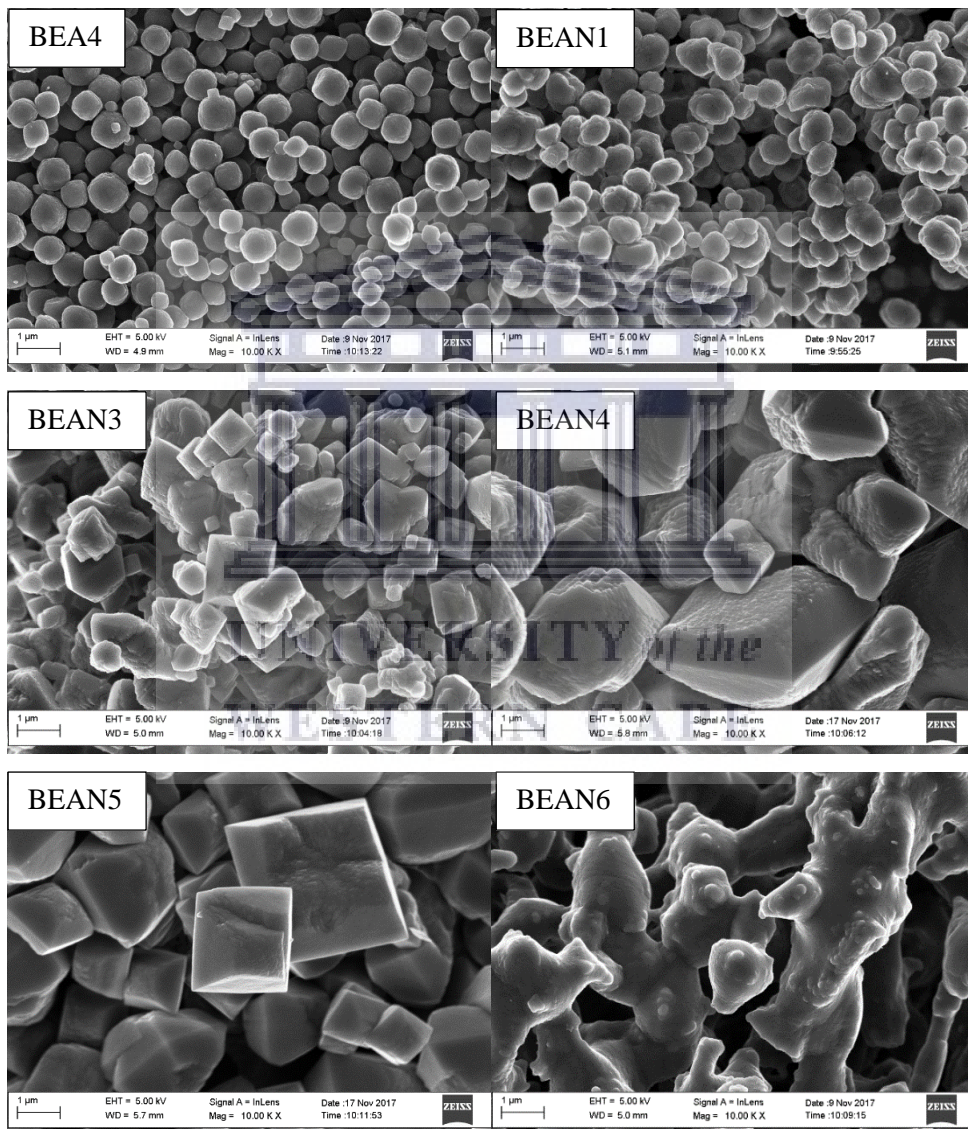


Figure 4.11: SEM morphology showing the effect of NaOH on the phase formation of BEA zeolites at 140 °C for 72 h. Different molar composition with varying molar Na contents (x) include: x = 0.241, 0.317, 0.461, 0.506, 0.552 and 0.734 (BEA4, BEAN2, BEAN3, BEAN4, BEAN5).

The morphology of the synthesised BEA zeolite crystals with varying molar fraction of NaOH in the molar composition is shown in Figure 4.11. Three distinctive morphologies were observed in the synthesised samples. BEA4 and BEAN1 sample exhibited a spheroidal-shaped structure with a crystal size of 0.50 and 0.63 μm , respectively (Table 4.5). As the molar fraction of NaOH content increased from 0.241 and 0.317 to 0.461, 0.506 and 0.552 (BEAN3, BEAN4 and BEAN5, respectively) the spherical crystal shape changed to a large cuboidal-shaped crystal structure. The spheroidal or cuboidal morphology have both been associated with BEA zeolite structure (Bregolato et al. (2007); Zhang et al. (2016)). Also, this follows a progressive crystal growth with respect to the increasing molar fraction of NaOH (BEAN2, BEAN3, BEAN4 and BEAN5, respectively) as measured from the SEM micrographs (see Table 4.5). This might be attributed to the crystal growth that occurred with the increased molar fraction of NaOH. These results further elucidate the fact that BEA zeolite with high crystallinity and small crystal size can be produced hydrothermally from a molar composition with NaOH content as low as 0.241 and as high as 0.461.

Notably, as the molar fraction of Na increased further to 0.734 (BEAN6), an irregular shaped crystal morphology was formed. These images alongside the XRD patterns (Figure 4.10) confirmed that the hydrothermal synthesis of the molar composition with NaOH content > 0.506 can shift the formation of BEA zeolite into other mineral phases. A high molar Si/Na ratio (3.15 to 4.15) of the synthesis mixture allowed the complete transformation of coal fly ash into pure phase crystalline BEA zeolite with small crystals and increased product yield. Thus BEA4 zeolite formulation (1 Si : 0.017 Al : 0.317 Na : 0.399 TEAOH : 8.980 H₂O) was considered to be the best due to its smaller crystal size (0.5 μm), good crystalline structure and high percentage yield and thus additional NaOH is not of benefit.

4.4.3 Effect of aluminium on the crystallisation of BEA zeolite

The framework aluminium atoms have been linked to the acid properties of zeolites. To this end, the effect of adding different molar fractions of aluminium (aluminium hydroxide) in the molar composition for the production of BEA zeolite was studied in this section. Table 3.4 (section 3.2.3) shows the amount of the aluminium contained in each of the molar compositions. With BEA4 (1 Si : 0.017 Al : 0.241 Na : 0.399 TEAOH : 8.980 H₂O) set as the baseline, the following molar composition were generated:

1 Si : x Al : 0.241 Na : 0.399 TEAOH : 8.980 H₂O

where x is 0.017, 0.060, 0.098 or 0.172, respectively (see Table 3.4, section 3.2.3).

Each of the generated molar composition were assigned code names BEA4, BEAA1, BEAA2 and BEAA3 (0.017, 0.060, 0.098 or 0.172, respectively) according to increasing aluminium content as described in section 3.2.3. The prepared products were characterised using XRD and SEM techniques.

Figure 4.12 presents the XRD patterns used to characterise the crystallinity of the different products using equation 4.5 whereas the crystal size was obtained from the SEM micrograph assisted with ImageJ software.

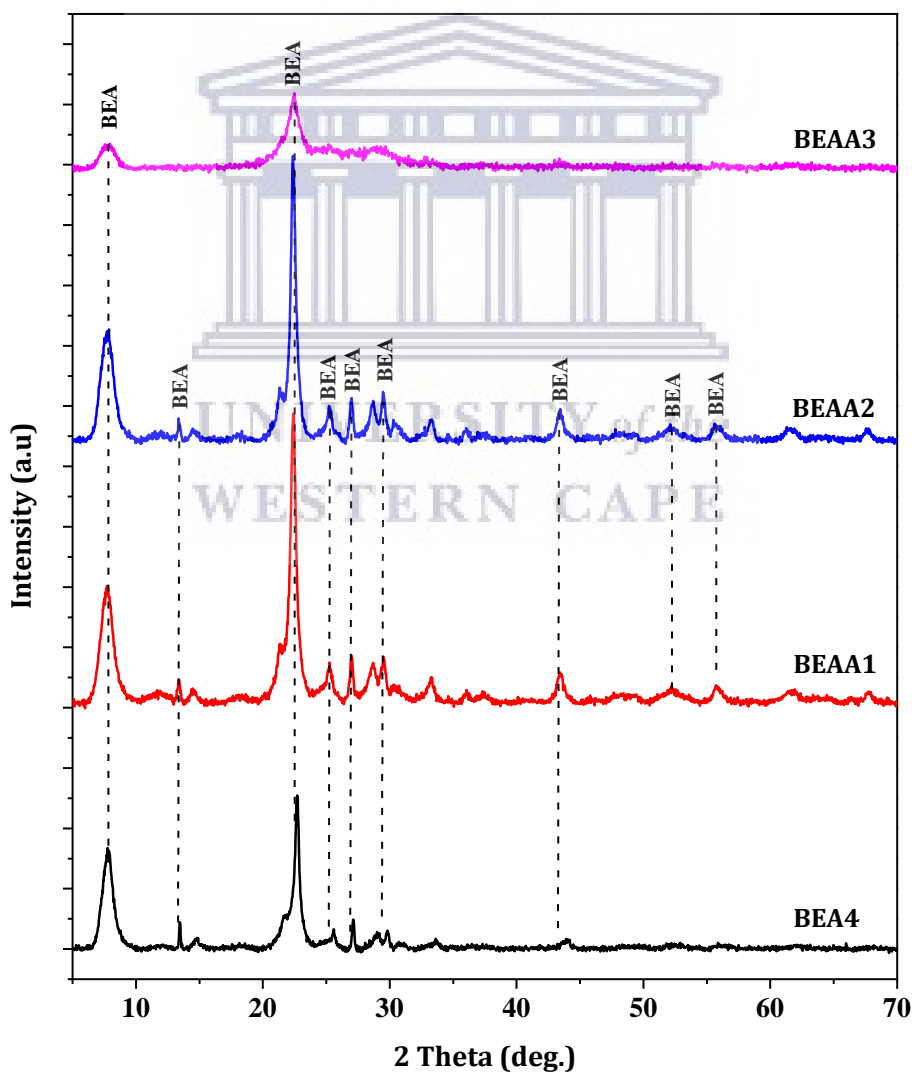


Figure 4.12: XRD patterns showing the effect of aluminium on the phase formation of BEA zeolites 140 °C for 72 h. Varying aluminium contents, $x = 0.017, 0.060, 0.098$ and 0.172 (BEA4, BEAA1, BEAA2 and BEAA3, respectively).

The XRD patterns presented in Figure 4.12 show the characteristic peaks of the prepared products obtained with different molar fractions of aluminium. The diffraction peaks of the baseline sample (BEA4) with molar fraction of aluminium (0.017) were relatively weak but the peaks at $2\theta = 7.7$ and 22.5° showed a significant increase in their intensity as the molar fraction of aluminium increased to 0.060 and 0.098 (BEAA1 and BEAA2). This indicated that the crystallinity changed (from 70.7% to 100 and 92.4% as presented in Table 4.6) with an increasing molar fraction of aluminium. All these samples were compared to BEAA1 which was set as the most crystalline sample.

Table 4.6: Comparison of crystallinity, crystal size and yield of products prepared from different molar fraction of aluminium.

Sample	Crystallinity (%)	Crystal size (μm)	Yield (%)
BEA4	70.7	0.50	25.7
BEAA1	100.0	0.60	30.1
BEAA2	92.4	0.57	32.7
BEAA3	45.7	1.75	48.9

It was found that the samples with high crystallinity have relatively low recovery yield as presented in Table 4.6 (BEAA2>BEAA1>BEA4) but the yield improved compared to when NaOH was adjusted previously. The product yield could be affected by the crystallisation of nano-crystal particles that may remain in the precursor solution after the recovery of the grown crystal > 100 nm. On the contrary, the sample BEAA3 with the highest molar fraction aluminium of 0.172, shows a significant reduction of the diffraction peak intensities (7.7 and 22.5°) with noticeably disappearance of other BEA zeolite peaks at 13.4 , 27.1 , 28.7 , 29.6 and 43.4° (Joint Committee on Powder Diffraction Standards (JCPDS)). This shows the incomplete conversion of amorphous material to BEA zeolite, in the case of BEAA3 thereby compromising the crystallinity and crystal phase of the zeolite (Figure 4.12 and Table 4.5). Thus, the inability to separate the amorphous phase from the crystals promoted the percentage yield of BEAA3. Overall, these results suggest that a molar fraction of aluminium between 0.017 and 0.098 is sufficient to synthesis high purity BEA zeolite with high crystallinity and reasonable percentage yield.

Moreso, to corroborate XRD results of the mineralogical formation of the BEA zeolite prepared in a formulation in which different molar fractions of aluminium were used was carried out by HRSEM (as described in section 3.2.6) and is presented in Figure 4.13.

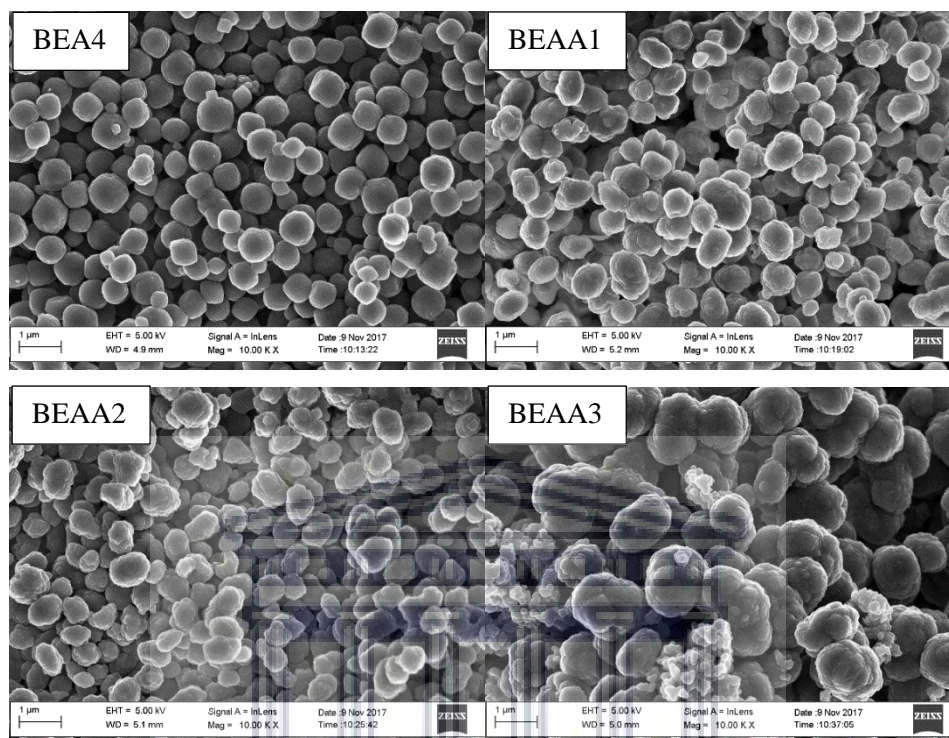


Figure 4.13: SEM morphology showing the effect of aluminium on the phase formation of BEA zeolites 140 °C for 72 h. Varying aluminium contents, $x = 0.017, 0.060, 0.098$ and 0.172 (BEA4, BEAA1, BEAA2 and BEAA3, respectively).

Figure 4.13 presents the morphology of the synthesised zeolites prepared using different molar fractions of aluminium. All the synthesised products maintained the spheroidal-shape of a typical BEA zeolite structure expect for samples BEAA3, which shows an agglomerated, irregular shape. Also, the increase in the molar fraction of aluminium ($0.017, 0.060, 0.098$) showed a gradual crystal size increase of 0.50 to $0.60 \approx 0.57 \mu\text{m}$, respectively as indicated in Table 4.6 and Figure 4.13. However, sample BEAA3 with the highest molar fraction aluminium (0.172) had crystal sizes of $1.75 \mu\text{m}$, this is ascribed to the presence of the irregular amorphous material within the nano scale. The SEM and XRD of sample BEAA3 support the fact that the molar fraction of aluminium ≥ 0.172 in the molar formulation applied during the hydrothermal synthesis will produce low crystallinity BEA zeolite, with amorphous material.

4.4.4 Comparison of the optimum conditions for the synthesis of fly ash based BEA zeolite

The parameters such as the effect of water and the effect of the molar fraction of sodium and aluminium content were investigated as discussed in section 4.3.2, 4.3.3 and 4.3.4, respectively. This section compares the outcome in each of the aforementioned sections, in order to show the best conditions (molar Si/Na and Si/Al ratio of the synthesis precursor) for the synthesis of BEA zeolite based on the investigated parameters.



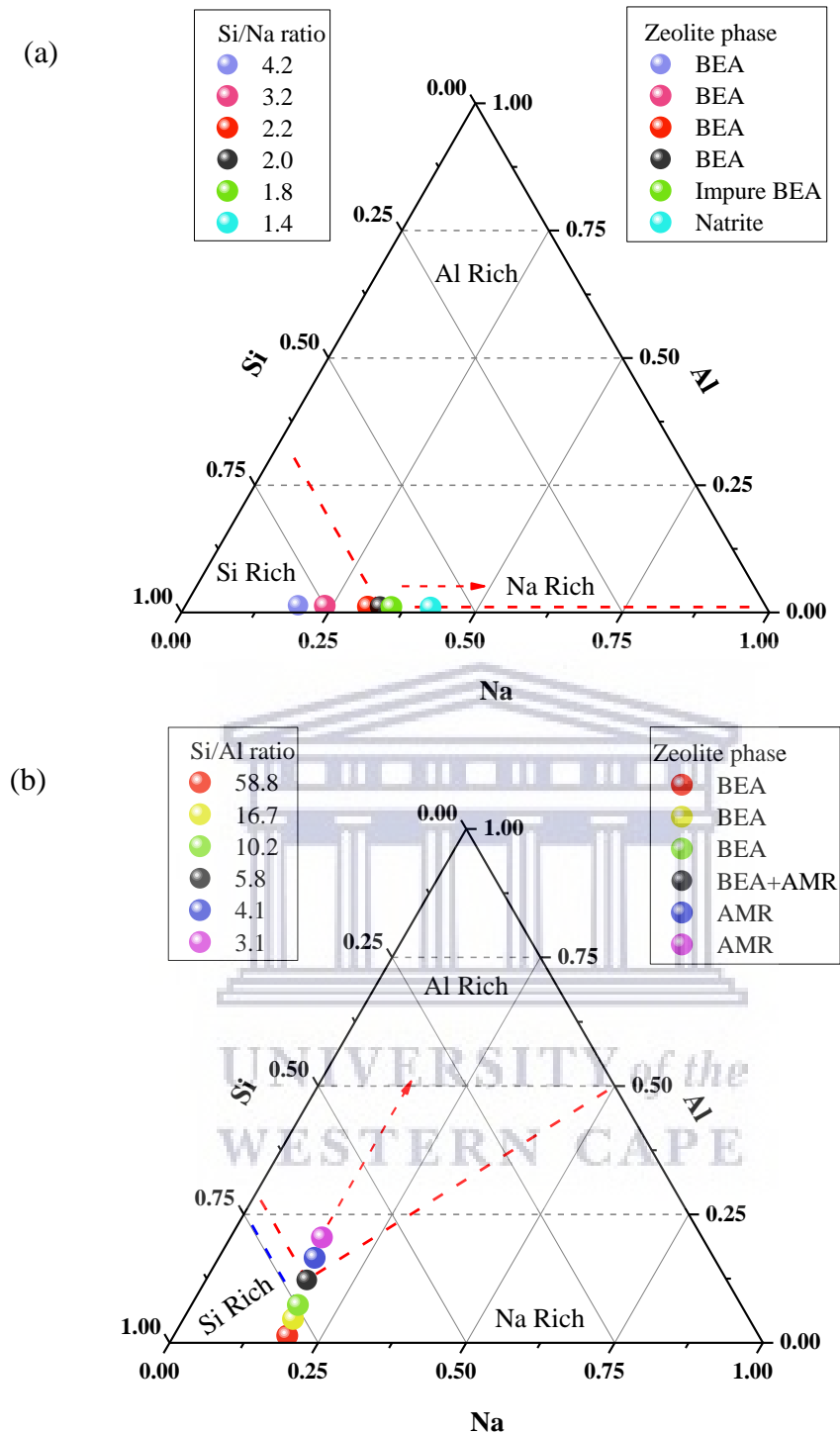


Figure 4.14: Ternary plot of the molar composition of Na, Si and Al with different amounts of a) NaOH and b) aluminium. *AMR = amorphous.

The ternary plots in Figure 4.14 (a-b) show the effect of altering the molar fraction of Si, Al and Na in the synthesis composition on the phase purity and morphology of the synthesised BEA zeolite. Herein, varying the amount of added NaOH in the synthesis mixture without changing any other parameters (see Table 3.4, section 3.2.3) influenced the molar Si/Na ratio

and the alkalinity of the synthesis precursor. When the sample was prepared with Si/Na = 4.2 the crystallinity of the BEA4 was 70.7%. As the synthesis, Si/Na ratio reduced to 3.2 and again to 2.0 the prepared BEAN1 and BEAN4 zeolite grew in crystallinity to 80.8 and 100%, respectively (see Figure 4.14a, .9 and Table 4.5). These results corroborate that the increasing amount of NaOH in the synthesis mixture promoted the molar Na fraction and alkalinity and thus, enhanced the relative crystallinity of the BEA zeolite, but the yield of the product reduced.

Under the investigated parameters, the decreasing Si/Na ratio showed a pronounced effect on the morphology of the product. The spheroidal shape (Si/Na = 4.2 or 3.2) gradually changed to a cuboidal crystal habit (Si/Na = 2.2 or 2.0) as the synthesis composition become richer in molar Na fraction (Figure 4.14a and 4.11). As the BEA4 and BEAN1 spheroidal morphology changes (crystal size = 0.5 and 0.62 μm , respectively), the formed cuboidal habit grew into a large crystal size of 0.86 and 1.95 μm (BEAN3 and BEAN4, respectively) (see Table 4.5). However, with a further decrease of the Si/Na ratio to 1.8 in the synthesis composition, an impure phase was incorporated into the prepared BEA products (Figure 4.14a) as supported by the XRD diffraction peaks in Figure 4.10. Moreover, the crystal size slightly decreased to 1.75 μm which can be attributed to the dissolution of the existing BEA zeolite crystal. With the continual decrease of molar Si/Na ratio to 1.4, a complete phase transformation from BEA zeolite to Natrite diffraction peaks were observed (see Figure 4.10). Furthermore, there is a significant reduction in the product yield as the molar Si/Na ratio of the synthesis composition decreased (see Table 4.5).

These results validate that the increase in Si/Na ratio (from 4.2 to 2.0) promoted crystallinity, crystal growth and affected the morphology of fly ash based BEA zeolite. Similarly, Zhang et al. (2016), noticed that the decrease in Si/Na ratio alongside an increase in alkalinity (pH) of the molar composition enhanced the crystallinity and crystal size of BEA zeolite. The low Si/Na ratio enabled strong alkalinity of the synthesis composition, this, in turn, improved the nucleation of the BEA zeolite crystals (Xiong et al., 2017). Although, with much lower molar Si/Na ratio (≤ 1.8) a competitive environment is created between the cation structure-directing agent of Na^+ and TEA^+ , in which the high molar fraction of alkali Na^+ cations direct the formation of another zeolitic phase such as Natrite (Möller et al., 2011; Zhang et al., 2016).

The sodium cations can either function as a promoter or hinder the nucleation rate of BEA zeolite depending on the amount of heteroatom within the reactive environment. This is because $[(\text{AlO}_2)^-\text{Na}^+]$ can be interchanged for $[(\text{AlO}_2)^-\text{TEA}^+]$ in order to retain smaller Na^+ cations to create the enabling T-atom environment of the precursor monomers and dimers close enough to that of BEA zeolite (Hould et al., 2011). Furthermore, this shows that the competition between Na^+ and TEA^+ cations to associate as $[(\text{AlO}_2)^-\text{Na}^+]$ or $[(\text{AlO}_2)^-\text{TEA}^+]$ clusters in the precursor monomers and dimers have a significant effect on the rate of nucleation of a typical BEA zeolite. Therefore the obtained results suggest that small molar Na fraction (Si/Na ratio between 2.0 and 4.2) provided the best environment for the preparation of highly crystalline BEA zeolite with crystal size between 0.50 and 1.95 μm and good product yield.

Successively, upon the optimum condition which was found to be Si/Na ratio of 4.2, the amount of aluminium in the molar composition was varied which then generated different Si/Al ratios as presented in Figure 4.14b. The hydrothermal crystallisation of the molar compositions with increasing Si/Al ratio from $10.2 < 16.7 < 58.8$ show that the products were highly crystalline with decreased crystal growth (see Figure 4.12 and Table 4.6). On the other hand, as the Si/Al ratio of the synthesis composition was further decreased to 5.8, the obtained BEA zeolite showed corresponding amorphous material with reduction in crystallinity and increased crystal size (see Table 4.6). This implied that low Si/Al ratio (5.8) of the molar composition is insufficient to crystalline a pure phase high silica BEA zeolite. This is ascribed to the high aluminium content in the synthesis mixture which slows the involvement of the silicate species in the formation of crystal nuclei (Pan et al., 2014). Therefore, the increase in Si/Al ratio of the molar composition promotes well-defined crystalline BEA structure (see Table 4.6). According to Cundy and Cox (2005), the high Si/Al ratio in the synthesis mixture allows easily dissolution of silicon and aluminium species thereby inducing the synthesis mixture to reach super-saturation which in turn induced the nucleation process and enabled crystal growth.

Thus the Si/Na = 4.2 provided sufficient Na^+ counter ions to charge balance AlO_4^- generated from the Si/Al ratio between 16.7 to 58.8 thereby improving the nucleation process which in turn benefited the crystallinity, crystal size and yield of prepared BEA zeolite. Interestingly, the decrease of Si/Al ratio resulted in the increase of the percentage yield of BEA zeolite. Therefore, based on the crystallinity, the crystal size and the yield, the

formulations used for BEA4 and BEAA1 were chosen for the optimum preparation of BEA zeolites.

4.4.5 Effect of hydrothermal time of crystallisation upon BEA zeolite

Considering the parameters investigated and the obtained results discussed in the aforementioned sections, the resultant products with high crystallinity, small crystal size and good percentage yield showed the best condition for the preparation of BEA zeolite. The set baseline include: BEA4 and BEAA1, with synthesis molar composition of:

- 1 Si : 0.017 Al : 0.241 Na : 0.399 TEAOH : 8.980 H₂O (BEA4)
- 1 Si : 0.017 Al : 0.060 Na : 0.399 TEAOH : 8.980 H₂O (BEAA1)

With Si/Al ratio of BEA4 and BEAA1 = 58.8 and 16.7, respectively. In the present section, the potentialities of these set baselines were explored to study the kinetics of the hydrothermal crystallisation of BEA zeolite in relation to the synthesis time. The two molar compositions were subjected to hydrothermal treatment of 140 °C at synthesis time x , where x can be 12, 24, 48 and 72 h, respectively (see section 3.2.3 for details). Code names were assigned based upon the molar composition, Si/Al ratio and synthesis time. The molar composition with Si/Al ratio = 58.8 was assigned HBEA12, HBEA24, HBEA48 and HBEA72 while the Si/Al ratio = 16.7 was given code names, HBEA_{Al}12, HBEA_{Al}24, HBEA_{Al}48 and HBEA_{Al}72 at synthesis time 12, 24, 48 and 74 h, respectively (see Table 3.5, section 3.2.4). Before characterising the synthesised products, further, XRD was used to identify Na-BEA zeolite samples which were then calcined and, afterwards changed to H-form (HBEA zeolite) as described in section 3.2.3. The following characterisation techniques were employed in this section: XRD, SEM, BET, TGA and Si/Al NMR, respectively.

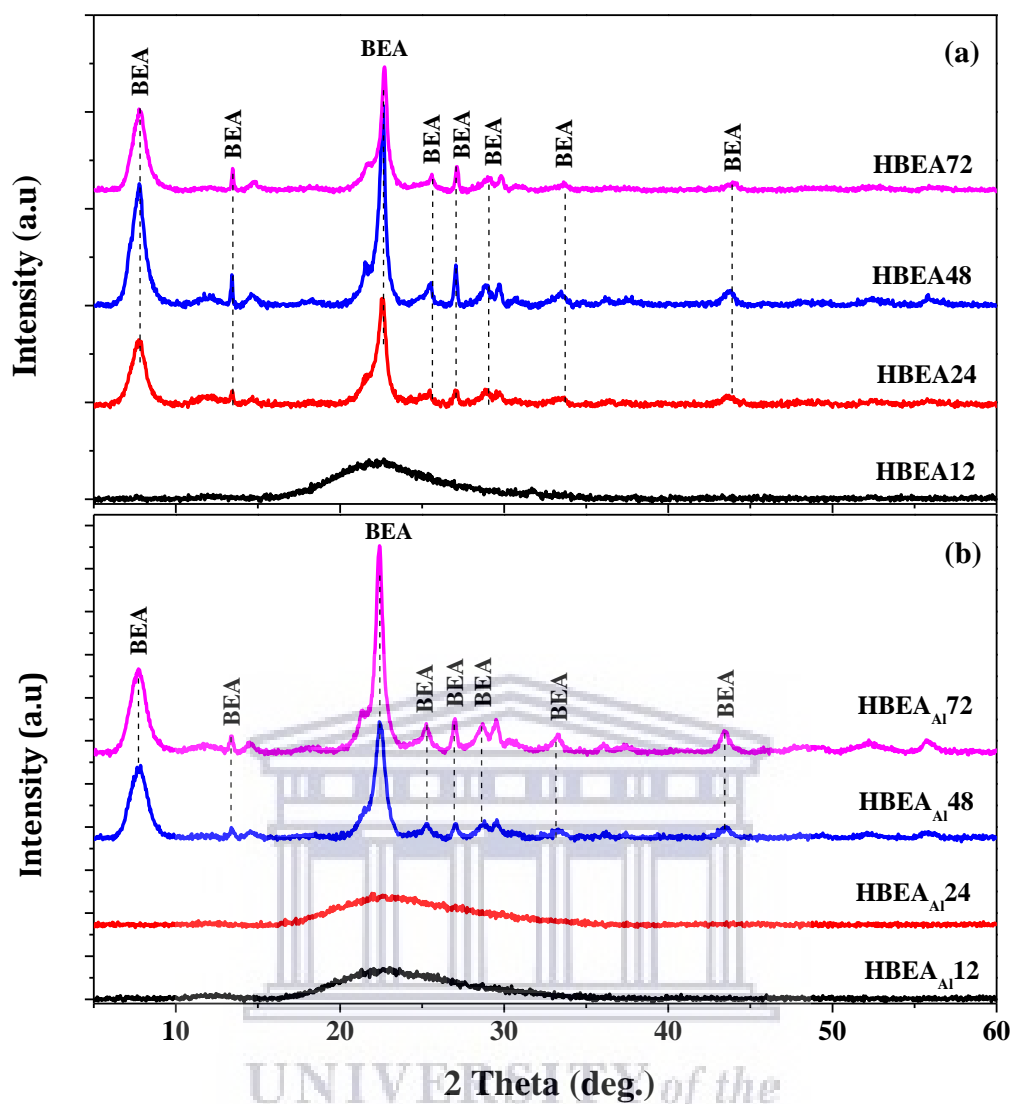


Figure 4.15: XRD patterns of the HBEA zeolite synthesised at different hydrothermal crystallisation times of 12, 24, 48 and 72 h at 140 °C using two molar composition of: a) 1 Si : 0.017 Al : 0.241 Na : 0.399 TEAOH : 8.980 H₂O (HBEA12, HBEA24, HBEA48 and HBEA71) or b) 1 Si : 0.060 Al : 0.241 Na : 0.399 TEAOH : 8.980 H₂O (HBEA_{Al}12, HBEA_{Al}24, HBEA_{Al}48 and HBEA_{Al}71), respectively.

Figure 4.15 presents the XRD diffraction patterns of the synthesised products at different hydrothermal times. When the hydrothermal treatment was performed for 12 h with Si/Al ratio of 13.3 (Figure 4.15a) and 8.1 (Figure 4.15b), a hump between 15 and 30° 2θ was observed which can be associated with the formation of X-ray amorphous precursor material. Prolonging the synthesis time to 24 h (Si/Al ratio = 58.8), resulted in significant diffraction peaks at 2θ = 7.7 and 22.5° related to typical BEA zeolite (HBEA24), unlike the synthesis mixture with Si/Al ratio of 16.7 which did not show the characteristic peaks of BEA zeolite but retained an amorphous phase at 24 h (HBEA_{Al}24) (Figure 4.15b) thus adding Al had a retarding effect on the crystallisation kinetics. As the synthesis time

increased to 48 h (HBEA_{Al}48), a pure phase BEA zeolite was formed with Si/Al ratio of 16.7, whereas the peak intensity of the zeolite (Si/Al ratio of 58.8) increased significantly in crystallinity and crystal size (HBEA48). The intensity of the peaks increased as the synthesis time was further prolonged to 72 h for sample BEA_{Al}72 while sample HBEA72 slightly reduced in peak intensity indicating reduction in crystallinity. SEM images in Figure 4.16 present the morphology and structure of the crystalline zeolites products.

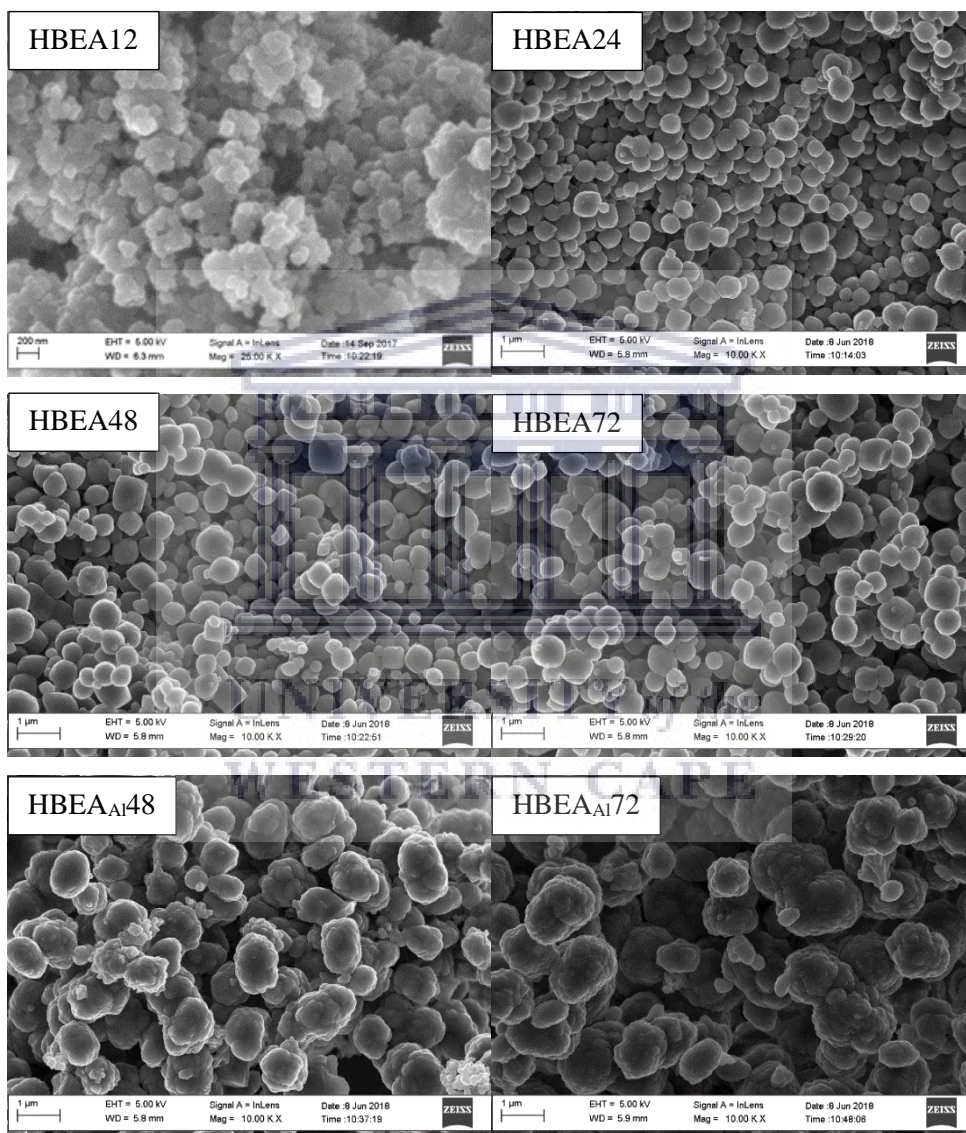


Figure 4.16: SEM morphology of HBEA zeolite synthesised at different hydrothermal crystallisation time of 12, 24, 48 and 72 h at 140 °C using two molar composition of: 1 Si : 0.017 Al : 0.241 Na : 0.399 TEAOH : 8.980 H₂O (HBEA12, HBEA24, HBEA48 and HBEA71) or 1 Si : 0.060 Al : 0.241 Na : 0.399 TEAOH : 8.980 H₂O (HBEA_{Al}48 and HBEA_{Al}71), respectively.

Figure 4.16 shows the morphological structures of the synthesised products at different hydrothermal times and Si/Al ratios. The SEM images in Figure 4.16 only present the

samples with pure phase BEA zeolite as identified by XRD in the case of HBEA_{Al}12 and HBEA_{Al}24. As presented in Figure 4.16-HBEA12, an irregular morphology was observed which corresponded to the X-ray amorphous precursor materials present in the synthesised products in the case of HEA12 and HBEA_{Al}12 (12 h synthesis time) as well as HBEA_{Al}24 (24 h synthesis time). With increasing synthesis time (24, 48 and 72 h), a uniform spheroidal-shaped crystalline phase was formed (HBEA24, HBEA48 and HBEA72). Under the same condition but different Si/Al ratio of the synthesis mixture, a similar spheroidal morphology was observed in sample HBEA_{Al}48 and HBEA_{Al}72, respectively. These suggest that with low Si/Al ratio the formation of BEA zeolite is attainable under the set conditions. The crystallisation of BEA zeolite with different levels of Al at 140 °C for 24, 48 and 72 h is presented in Figure 4.17.

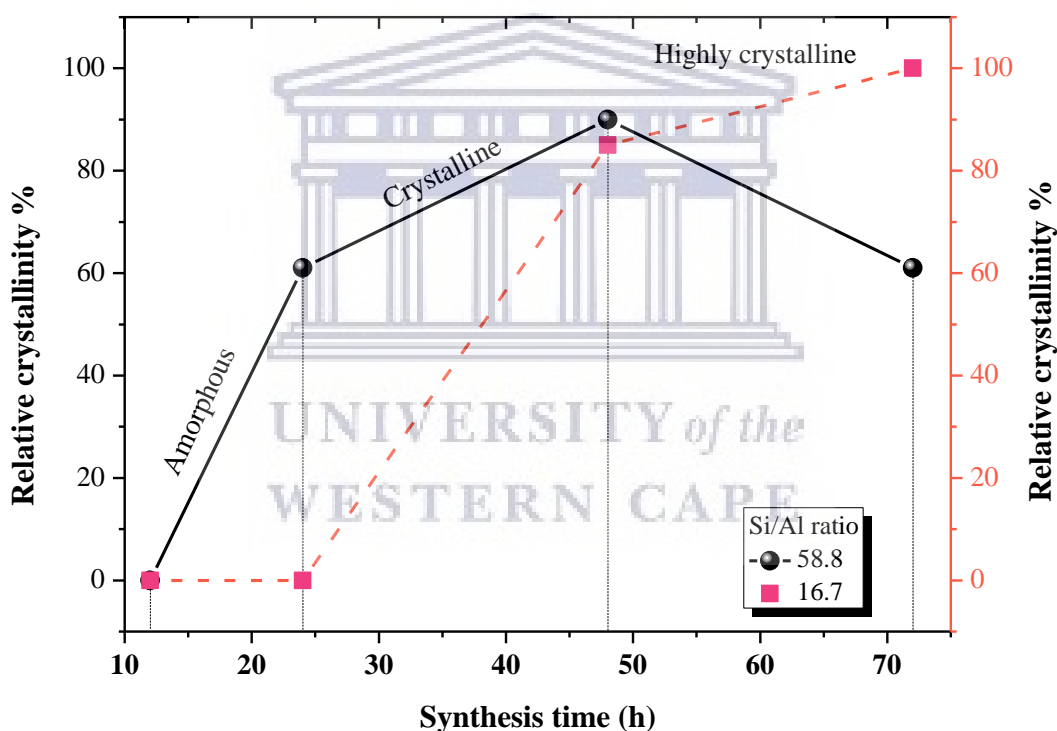


Figure 4.17: Graphical presentation of crystallinity over times (12, 24, 48 and 72 h) for the synthesis of BEA zeolite at Si/Al ratio of 58.8 or 16.7 at 140 °C.

The results shown in Figure 4.17 correlate the relative crystallinity, Si/Al ratio of the synthesis mixture and synthesis time of the sample products. In Figure 4.17, the level of crystal phase formation was grouped into three stages, this included: amorphous (induction period), crystal formation and stable crystal growth. At 12 h synthesis time, the assembled amorphous precursor species had formed but not transformed into crystalline material,

however, as synthesis time progresses to 24 h for sample HBEA24, the precursor species underwent transformation into a completely crystalline material of well-defined crystal structure except HBEA_{Al}24. Prolonging the synthesis time to 48 and 72 h allowed crystal growth (highly crystalline material). Principally, as the synthesis time increases crystallisation and crystal growth increased, indicating that BEA zeolite can be synthesised from coal fly ash within 24 h hydrothermal synthesis time in low Al environment. This is an indication that high molar Si/Al ratio of 58.8 induced high nucleation rate and accelerated crystal growth at shorter crystallisation synthesis time compared to low molar Si/Al ratio of 16.7. To this end, increased aluminium content (Si/Al ratio = 16.7) slowed the induction period, thereby hindering the nucleation process and fast rate of crystallisation. It has been reported by Cundy and Cox (2005) that an increase of the Si/Al ratio in the synthesis mixture enhanced the crystallisation of BEA zeolite. Similarly, Manrique et al. (2016) and Gabrienko et al. (2010) showed that high Si/Al ratio in the synthesis mixture reduced induction process and promoted crystal growth.

Table 4.7: Comparison of the Si/Al ratio, crystal size, crystallinity and yield of the BEA zeolite synthesised at different times.

Samples	Molar composition		BEA zeolite		
	Si/Al _{sy} ratio	Si/Al _{pro} Ratio	C _{y_{size}} (µm)	C _{y_{linity}} (%)	Yield (%)
HBEA24	58.8	28.07	0.39	61.06	21.93
HBEA48		27.51	0.41	90.09	26.71
HBEA72		27.88	0.45	60.79	25.39
HBEA48 _{Al}	16.7	9.31	0.78	85.21	49.09
HBEA72 _{Al}		11.57	1.07	100.00	59.30

Si/Al_{sy} and Na/Al_{sy} of synthesis mixture as determined by XRD; Si/Al_{pro}: synthesised BEA zeolite as determined by ICP; C_{y_{size}}: crystal size; C_{y_{linity}}: crystallinity, yield as calculated using equation 4.6.

Table 4.7 presents the influence of hydrothermal time upon the crystallinity and crystal size of the synthesised BEA zeolite. It can be seen that with the Si/Al ratio of 58.8 (synthesis mixture) the crystal size of the zeolite products was between 0.39 and 0.45 µm while Si/Al ratio of 16.7 produced BEA zeolite of 0.78 and 1.07 µm (Table 4.7). The crystal size of the synthesised BEA zeolites gradually increased as hydrothermal time increased (Table 4.7). With such steady growth in crystal structure, the dimension of the crystal enlarged as observed in Table 4.7 due to prolonged hydrothermal time. Similarly, Hould et al. (2009)

and Hould et al. (2011), related the crystal changes of BEA zeolite as a function of increased hydrothermal time, thereby inducing growth in crystallinity and crystal size of precursor species (6-50 nm) into micron sized crystals. Hence, the aggregation of small precursor at an early stage of synthesis induced the formation of the crystal and provided zeolitic structural features with high crystallinity at prolonged synthesis time.

A difference was noticed in the Si/Al ratio of the synthesis solution compared to the obtained zeolite products (Table 4.7). It was observed that the molar Si/Al ratio of the BEA products reduced compare to the precursor Si/Al molar ratio. The synthesised BEA zeolites from the precursor mixture of 58.8 Si/Al molar ratio maintained a Si/Al ratio of 28 after different hydrothermal synthesis of 24, 48 and 72 h (HBEA₂₄, HBEA₄₈ and HBEA₇₂). Whereas, in the case of the precursor solution of 16.7 Si/Al molar ratio, the BEA Si/Al molar ratio varies from 9 to 12. The difference between the Si/Al ratio of the synthesis mixture and the recovered products could be associated with the unreacted species which may have remained in solution. According to Chaves et al. (2015) and Mintova et al. (2006) the initial Si/Al ratio is different compared to the recovered solid zeolite, especially when Si/Al ratio of the synthesis mixture is high.

The influence of synthesis time on the percentage yield of the zeolite samples was also studied. It was observed that for the Si/Al_{sy} ratio of 58.8 after 24 h, the zeolite yield was 21.935% (HBEA₂₄) which increased to 26.71% (HBEA₄₈) and 49.09% (HBEA₄₈) after 48 h and slightly decreased to 25.39% (HBEA₇₂) after 72 h while sample HBEA₇₂ increased to 59.30% after 72 h synthesis (Table 4.7). Longer synthesis time thus promoted the product yield of the BEA zeolite. This is because at a shorter synthesis time most of the primary silica and alumina were unreacted and remain in the separated supernatant (Ding et al., 2006).

4.4.5.1 Influence of synthesis time on thermal stability, framework structure and textural properties of BEA zeolite

Comparison and discussion of stability, framework structure and textural properties of the synthesised pure phase BEA zeolite at different temperatures (24, 48 and 72 h) as identified by XRD as presented in section 4.3.5 is detailed in this section. The prepared BEA zeolite were obtained from two molar composition:

- 1 Si : 0.017 Al : 0.241 Na : 0.399 TEAOH : 8.980 H₂O (Si/Al_{sy} = 58.8)

- 1 Si : 0.060 Al : 0.241 Na : 0.399 TEAOH : 8.980 H₂O (Si/Al_{sy} = 16.7)

The prepared BEA from the synthesis Si/Al_{sy} ratio of 58.8 were assigned HBEA24, HBEA48 and HBEA72 while the products from Si/Al_{sy} ratio of 16.7 were coded with the following names: HBEA_{Al}48 and HBEA_{Al}72 according to hydrothermal temperature of 24, 48 and 72 h, respectively (see Table 3.5). Three characterisation techniques were used, this included: TGA, ²⁷Al/²⁹Si MAS NMR and BET analysis. The H-form of the zeolite was characterised considering that the HBEA zeolite will be used to test its catalytic activity. Figure 4.18 presents the weight loss as a function of temperature of the various synthesised BEA zeolites in their H-form.

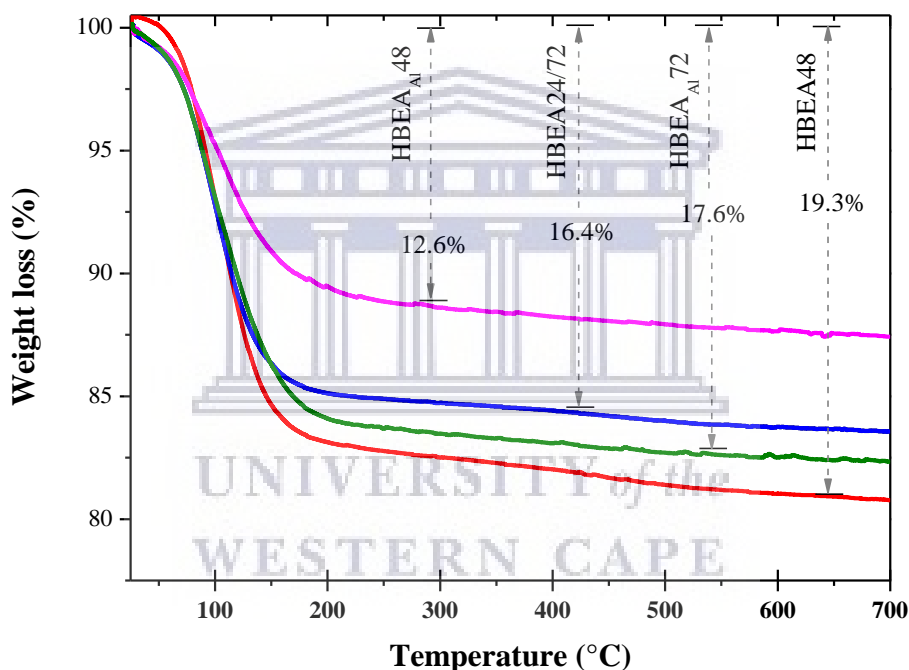


Figure 4.18: Thermal profiles of HBEA zeolite synthesised at different hydrothermal times from the molar compositions: 1 Si : 0.017 Al : 0.241 Na : 0.399 TEAOH : 8.980 H₂O (HBEA24, HBEA48 and HBEA72) or 1 Si : 0.060 Al : 0.241 Na : 0.399 TEAOH : 8.980 H₂O (HBEA_{Al}48 and HBEA_{Al}72) with Si/Al ratio of 58.8 and 16.7, respectively.

The thermogravimetric curves in Figure 4.18 show the temperature/weight loss profiles of HBEA zeolites samples prepared at different hydrothermal times. The HBEA zeolites showed a two-step weight loss at the lower temperature region between 25 and 150 °C and also at the high temperature region between 200 and 450 °C (all calculation made were at the same temperature). HBEA24 and HBEA72 exhibited a total weight loss of 16.4% while the total weight loss for sample HBEA48 was 19.3%. Also, the total weight loss of

HBEA_{Al}48 and HBEA_{Al}72 was 12.6 and 17.6%, respectively. The lower temperature weight loss is mainly caused by loss of the physisorbed moisture from air and hydrated water (Chen et al., 2015), while the higher temperature weight loss between 200 – 700 °C can be associated with dehydroxylation of the framework with ~Si-O-Si~ or ~Si-O-Al~ species leading to the formation of structural defects (Zhang et al., 2017). The changes in percentage of the total weight loss from 16.4% (HBEA24 and HBEA72) and 12.57% (HBEA_{Al}48) to approximately 19.3 and 17.6% (HBEA48 and HBEA_{Al}72) can be related to the porosity of the zeolite. This suggest that HBEA_{Al}48 could possess low porosity and high porosity might be found for HBEA48 sample. Hence, the moisture holding capacity (physisorbed moisture content) is indicative that the fly ash based HBEA zeolites are porous.

The slow mass loss after 200 °C might suggest the gradual dehydration of structural defects in the framework of the highly crystalline HBEA48 and HBEA_{Al}72 zeolite samples at prolonged heating. Furthermore, the framework stability of the prepared HBEA zeolites was studied using ²⁹Si and ²⁷Al MAS NMR analysed with 8 kHz spinning speed at a magnetic field strength of 11.4 T as described in section 3.10. Demonstrated in Figure 4.19a-b is the tetrahedral and octahedral aluminium environments analysed by ²⁷Al MAS NMR.

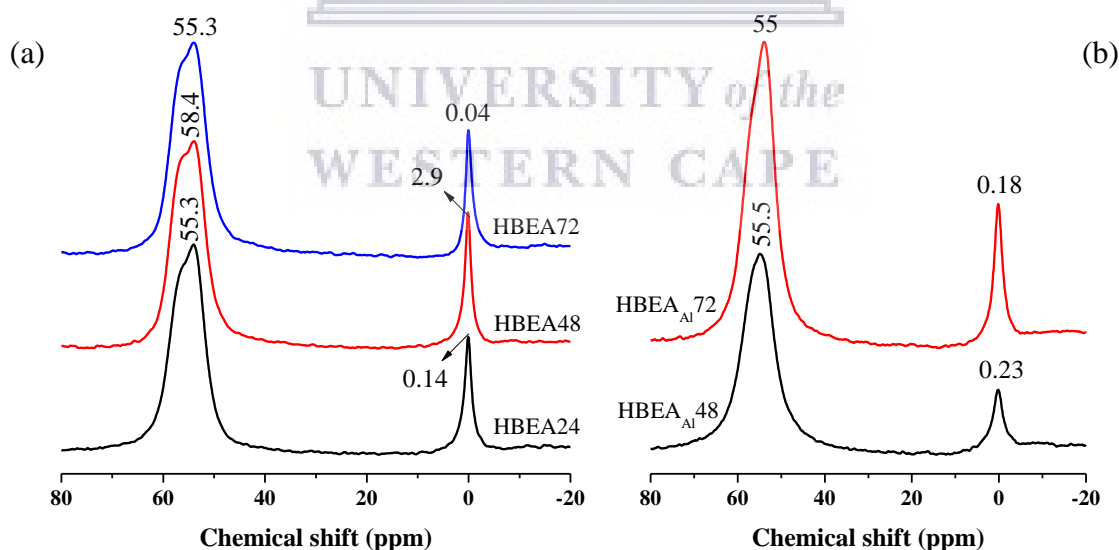


Figure 4.19: ²⁷Al MAS NMR of HBEA zeolite synthesised at different hydrothermal time from the molar composition: a) 1 Si : 0.017 Al : 0.241 Na : 0.399 TEAOH : 8.980 H₂O (HBEA24, HBEA48 and HBEA72) or 1 Si : 0.060 Al : 0.241 Na : 0.399 TEAOH : 8.980 H₂O (HBEA_{Al}48 and HBEA_{Al}72) with Si/Al ratio of 58.8 and 16.7, respectively.

The ²⁷Al MAS NMR spectra of HBEA zeolite samples prepared after different synthesis times using two molar composition are shown in Figure 4.19a-b. Two distinctive Al peaks

associated with tetrahedrally coordinated framework aluminium (FAI) or octahedrally coordinated extra framework aluminium (EFAl) located at $\delta = 55.3$ or 0.14 ppm (HBEA24), 58.4 or 2.9 ppm (HBEA48), 55.3 or 0.04 ppm (HBEA72) (see Figure 4.19a), 55.5 or 0.23 ppm (HBEA_{Al}48) and 55 or 0.18 ppm (HBEA_{Al}72) (see Figure 4.19b) were observed, respectively. Similarly, Manrique et al. (2016) observed the framework aluminium between 65 and 40 ppm and the extra framework aluminium between the region of 2.5 and 0 ppm.

The extra framework aluminium species of sample HBEA24 at $\delta = 0.14$ ppm experienced an up-field shift to $\delta = 2.9$ ppm (HBEA48) and then a downfield shift of $\delta = 0.04$ ppm (HBEA72) as the hydrothermal time increased to 48 and 72 h, respectively (Figure 4.19a). Similarly, as the hydrothermal synthesis time increased from 48 to 72 h, $\delta = 0.23$ ppm (HBEA_{Al}48) shifted to lower field $\delta = 0.18$ ppm (HBEA_{Al}72) (Figure 4.19b). Herein, the chemical shift is induced because of the sensitivity to Si-O-Al bonds and the downfield shift in peak position can be associated with distortions caused by the hydrolysis of Si-O-Si bands (Vjunov et al., 2015). Therefore, the gradually induced distortions can be caused by defects within the framework structure of highly crystalline HBEA48 and HBEA_{Al}72 zeolite and this could be associated with dehydroxylation as depicted by the TGA results (Figure 4.18). The percentage of the FAI and EFAl of the HBEA zeolite synthesised at different hydrothermal times was calculated from ^{27}Al MAS NMR peaks and presented in Table 4.8.

Table 4.8: Detailed ^{27}Al MAS NMR spectra depicting the integration of FAI and EFAl in the HBEA zeolite synthesised at different hydrothermal times.

Samples	Si/Al _{sy} ratio	FAI %	EFAl %
HBEA24		87.06	12.94
HBEA48	58.8	86.02	13.98
HBEA72		88.20	11.80
HBEA _{Al} 48		87.39	12.61
HBEA _{Al} 72	16.7	86.69	13.31

Si/Al_{sy} of the synthesis mixture

The percentage of FAI and EFAl peaks as derived from ^{27}Al MAS NMR is presented in Table 4.8. As crystallisation time increased, the percentage of framework aluminium (FAI) and extra aluminium framework (EFAl) synthesised at 24 h, 87.06 and 12.94% (HBEA24) changed to 86.02 and 13.98% (HBEA48) at 48 h. With prolonged crystallisation time of 72

h, the FAI of HBEA72 increased to 88.201 while the EFAl decreased to 11.80%. However, at 24 h crystallisation time, the synthesis mixture with Si/Al ratio of 16.7 shows only amorphous phase as confirmed by XRD (see Figure 4.15b and 4.19b, HBEA_{Al}24). As the crystallisation time increased to 48 h the percentage formation of FAI and EFAl (HBEA_{Al}48) was 87.39 and 12.61% which decreased to 86.69%, FAI as the EFAl increased to 13.31% (HBEA_{Al}72). Manrique et al. (2016) stated that the high thermal stability related to the framework Si/Al ratio might influence the increase in the framework aluminium (FAI) and decrease the extra framework aluminium (EFAl). This indicates that the changes of FAI and EFAl was due to the crystallisation time and the trend observed with decreased FAI and increased EFAl can be related to samples with high crystallinity (HBEA48 and HBEA_{Al}72). Generally, the aluminium species present in the HBEA zeolites are mainly located within the framework with a relating low amount of Al at extra framework sites.

Also, the framework Al atoms of tetrahedral coordination (FAI) and extra framework aluminium (EFAl) suggest that the fly ash based HBAE zeolite contained mainly Brønsted acid with some Lewis acid sites in the framework structure, respectively (Wang et al., 2017; Zhao et al., 2014). Figure 4.20 present the ²⁹Si MAS NMR of the HBEA zeolite prepared at different times (24, 48 and 72 h) and with Si/Al ratio of 58.8 or 16.7, respectively.

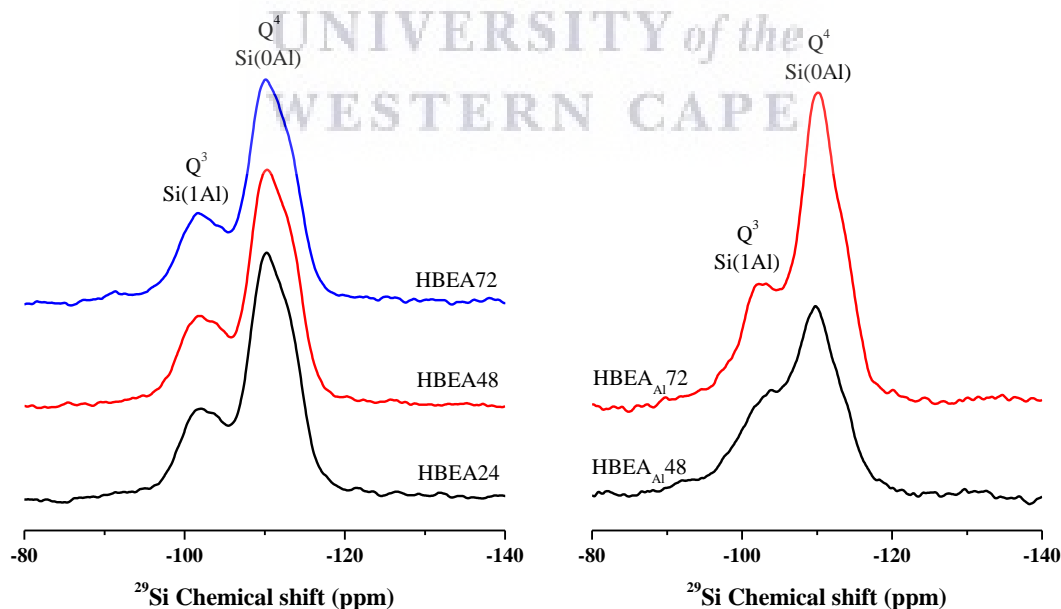
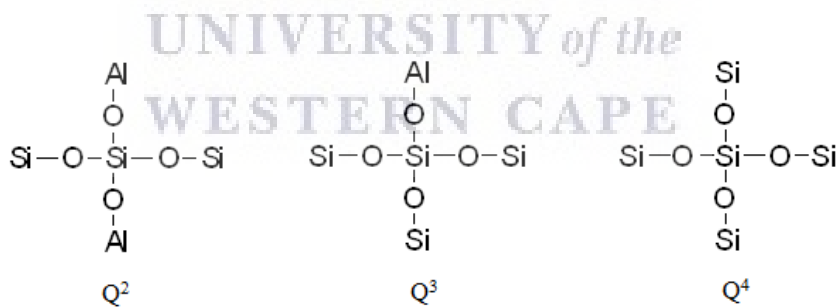


Figure 4.20: ²⁹Si MAS NMR of HBEA zeolite synthesised at different hydrothermal times from the molar composition: 1 Si : 0.017 Al : 0.241 Na : 0.399 TEAOH : 8.980 H₂O (HBEA24, HBEA48 and HBEA72) or 1 Si : 0.060 Al : 0.241 Na : 0.399 TEAOH : 8.980 H₂O (HBEA_{Al}48 and HBEA_{Al}72) with Si/Al ratio of 58.8 and 16.7, respectively.

Figure 4.20 shows ^{29}Si MAS NMR spectra of synthesised HBEA zeolite samples. The zeolite samples prepared from the molar composition with Si/Al ratio of 13.3 showed bands at around $\delta = -103$ and -110 ppm (HBEA24, HBEA48 and HBEA72) while samples HBEA_{Al}48 and HBEA_{Al}72 prepared from molar composition with low Si/Al ratio have bands around $\delta = -104$, -105 and -110 ppm. The bands at $\delta = -103$, -104 and -105 ppm correspond to Q^3 Si (1Al), and the bands at $\delta = -114$ are assigned to Q^4 Si (0Al) environment. A weak band at about $\delta = -112$ and -113 ppm, attributed to Q^4 Si (0Al) coordination was observed for all the synthesised HBEA zeolites. This is in agreement with the bands located in the structural framework of a typical BEA zeolite as reported by Zhang et al. (2013). Further study was conducted by deconvolution of the bands using mixed Lorentzian and Gaussian line shapes in order to calculate the band width, area and framework Si/Al ratio. The derived framework Si/Al ratio was calculated according to equation 4.7 (Holzinger et al., 2018).

$$\frac{\text{Si}}{\text{Al}}(^{29}\text{Si}) = \frac{2.I[\text{Q}^2\{2\text{Al}\}] + 3.I[\text{Q}^3\{1\text{Al}\}] + 4.I[\text{Q}^4\{0\text{Al}\}]}{I[\text{Q}^3\{1\text{Al}\}]} \quad \text{Equation 4.7}$$

where I is the peak intensity of Q^2 , Q^3 and Q^4 resonances identified by deconvolution of the ^{29}Si MAS NMR spectra. Scheme 4.1 illustrates Q^2 , Q^3 and Q^4 environments.



Scheme 4.1: The Q^2 , Q^3 and Q^4 resonances within the framework structure of the synthesised BEA zeolites.

However, only two major peaks, Q^3 and Q^4 were identified in the synthesised HBEA zeolite as shown in Figure 4.20. Table 4.9 shows the relationship between the deconvoluted Q^3 and Q^4 and their respective peak width and area to the framework Si/Al ratio.

Table 4.9: Chemical shift, peak width, peak area and Si/Al_{FW} ratio of deconvoluted Q³/Q⁴ environments.

Samples	Si/Al _{sy} ratio	Q ³ Si(1Al)		Q ⁴ Si(0Al)		Si/Al _{FW}	Si/Al _{BEA}
		δ _{decon} (ppm)	Width (ppm)	δ _{decon} (ppm)	Area %		
HBEA24		-103.32	6.26	-110.74	46.95	23.48	28.07
HBEA48	58.8	-103.27	7.20	-110.90	44.86	21.96	27.51
HBEA72		-103.14	6.55	-110.77	47.13	21.80	27.88
HBEA _{Al} 48	16.7	-105.60	9.75	-110.10	44.37	14.73	9.31
HBEA _{Al} 72		-104.53	12.37	-110.53	42.43	20.37	11.57

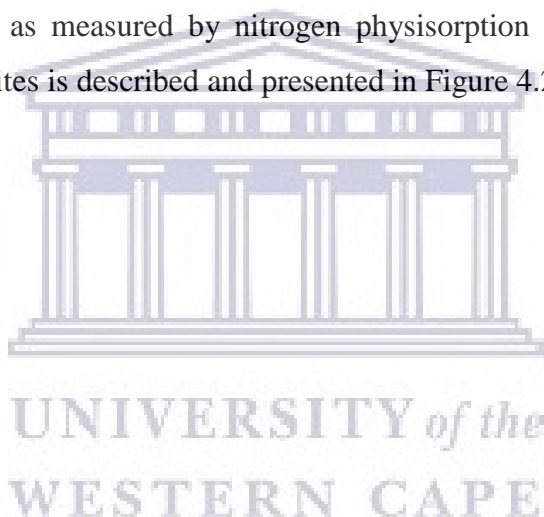
Note: δ_{decon} determine from NMR chemical shifts; calculated framework structure Si/Al_{FW} ratio by NMR; Si/Al_{sy} of the synthesis mixture and Si/Al_{BEA} ratio by ICP analysis.

The chemical shift, band width and area obtained by deconvolution of Q⁴ Si (0Al) and Q³ Si (1Al) species with the framework Si/Al ratio of the synthesised HBEA zeolite samples is presented in Table 4.9. Comparing the resultant zeolite products obtained from the two molar composition with Si/Al ratio of 58.8 (HBEA24, HBEA48 and HBEA72) or 16.7 (HBEA_{Al}48 and HBEA_{Al}72), the Q³ Si (1Al) species of samples HBEA24, HBEA48 and HBEA72 was maintained at δ = -103. However, under the same synthesis time of 48 and 72 h, the Q³ Si (1Al) environment of HBEA_{Al}48 and HBEA_{Al}72 samples experienced a significant chemical shift to δ = -105 and -104 as the Si/Al ratio of the molar composition was reduced to 16.7. The upward chemical shift is due to the direct impact of the increased aluminium content within the framework structure of the HBEA zeolites (Zhang et al., 2017). It is noteworthy, that HBEA_{Al}48 and HBEA_{Al}72 have the lowest framework Si/Al_{FW} ratio of 14.73 and 20.27, respectively (Table 4.9). This substantiated the fact that HBEA_{Al}48 and HBEA_{Al}72 contained more aluminium in the framework structure of the zeolite. This result complements the Si/Al ratio of the BEA product as measured by ICP (see Table 4.7 and 4.9).

A trend correlating the band width of Q³ Si (1Al) and area of Q⁴ Si (0Al) species to the relative crystallinity of the synthesised HBEA zeolites was observed (see Table 4.7 and 4.9). When the crystallinity was 61.06%, the band width and area was 6.26 ppm and 46.95% (HBEA24), respectively. With increased synthesis time (48 h) the crystallinity increased to

90.09% with a shift of the band position of Q³ Si (1Al) to 7.20 ppm with a decrease in band area of Q⁴ Si (0Al) to 44.86% (HBEA48). However, as the synthesis time reached 72 h, the crystallinity was reduced to 60.79% with a shift position of Q³ Si (1Al) to 6.55 ppm while the area of Q⁴ Si (0Al) increased to 47.13% (HBEA72). Interestingly, this suggested that as the band width of Q³ Si (1Al) increased and the area of Q⁴ Si (0Al) decreased the relative crystallinity of HBEA zeolite increased. Ameh et al. (2017) related that the reducing band area of Q⁴ Si (0Al) correlated with the relative crystal growth of the zeolite. Hence, the NMR signal of the synthesised fly ash based HBEA zeolites related mainly to Q³ Si (1Al) and Q⁴ Si (0Al) without the formation of terminal Si-OH group of structural defects. The results of TGA also validated that under the synthesis and post-synthesis conditions the framework structure of the synthesised HBEA zeolites was thermally stable.

The textural properties as measured by nitrogen physisorption comparing the different synthesised HBEA zeolites is described and presented in Figure 4.21.



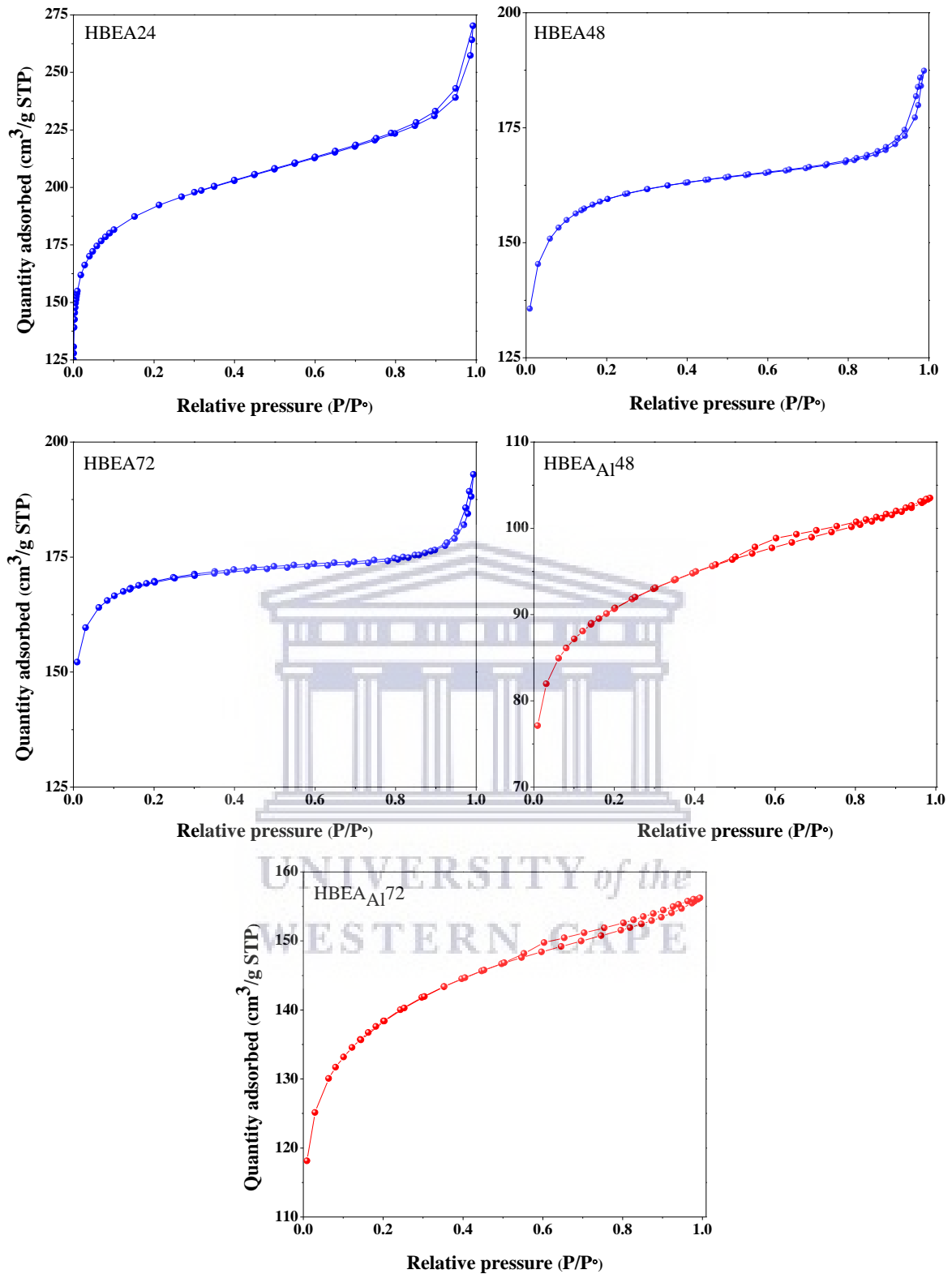


Figure 4.21: N₂ adsorption-desorption isotherms of BEA zeolite prepared from synthesis composition with different Si/Al ratio of 58.8 (HBEA24, HBEA48 and HBEA72) or 16.7 (HBEA_{Al}48 and HBEA_{Al}72) at 140 °C for 24, 48 and 72 hours, respectively.

The textural properties of the synthesised HBEA zeolites prepared at different hydrothermal times were characterised by N₂ adsorption-desorption and the relative isotherms of the samples are presented in Figure 4.21. Herein, the characteristic isotherm observed in HBEA24, HBEA48 and HBEA72 samples exhibited both type 1 and type IV while HBEA_{Al}48 and HBEA_{Al}72 displayed only type 1 isotherm (Thommes et al., 2015). The type 1 isotherms characterise the Langmuir adsorption due to the micropore filling in the region of $P/P_0 < 0.15$ whilst type IV isotherm is due to capillary condensation in the mesopores within the relative pressure of $0.2 < P/P_0 < 0.65$. Also, the hysteresis loop indicates the interconnected mesopores, which do not restrict capillary evaporation of adsorbed nitrogen. This shows that the HBEA zeolite samples have both micro and small mesoporous pore distribution. The textural properties of the various synthesised HBEA zeolites are summarised in Table 4.10.

Table 4.10: Textural properties of the synthesised BEA zeolite at different time and Si/Al ratio of the synthesis mixtures.

Zeolite	Si/Al _{sy} ratio	SBET [m ² /g]	S _{micro} [m ² /g]	S _{meso} [m ² /g]
HBEA24		722	512	210
HBEA48	58.8	538	439	99
HBEA72		670	543	127
HBEA _{Al} 48	16.7	307	230	77
HBEA _{Al} 72		468	361	107

Si/Al_{sy}: of the synthesis mixture; S_{BET}: BET surface area; S_{micro}: micropore surface area
S_{meso}: mesopore surface area

The textural properties of the obtained HBEA zeolites samples using two molar composition with Si/Al ratio of 58.8 or 16.7 at different hydrothermal time of 24, 48 and 72 h is presented in Table 4.10. The hydrothermal time during the formation of the framework structure had an impact on the surface area and mesopore surface area of the product. The BET and mesopore surface area of 722 (m²/g) and 210 (m²/g) was obtained after the hydrothermal time of 24 h (HBEA24) but after 48 h treatment time, the BET and mesopore surface area had reduced to 537 (m²/g) and 99 (m²/g) (HBEA48), respectively. With prolonged hydrothermal time (72 h), the surface area and mesopore area increased 670 (m²/g) and 127 (m²/g) (HBEA72), respectively. Following the observed trends, the decrease in surface area and mesopore area might be offset by the high relative crystalline structure of HBEA48

sample. Samples HBEA48 and HBEA_{Al}72 with high crystallinity (90 and 100%, respectively), high moisture capacity (19.3 and 17.6%) and slightly higher extra-framework Al were found to have reduced BET surface area of 538 and 468 (m²/g), respectively. However, HBEA24 and HBEA72 with relative crystallinity of 61 and 60%, moderate moisture capacity of 16.4% and reduced extra-framework Al showed higher BET surface area of 722 and 670 (m²/g), respectively (see Table 4.7-4.8 and Figure 4.11). According to Li et al. (2017) the crystalline structure can directly influence the mesopore nature and in turn, affect the surface area of BEA zeolites.

When comparing the textural properties of the synthesised products from the two molar composition with Si/Al ratio of 58.8 or 16.7 at 140 °C for hydrothermal time of 48 and 72 h, the molar composition with high Si/Al ratio of 58.8 resulted in HBEA24, HBEA48 and HBEA72 samples having the highest surface area of 722, 538 and 670 (m²/g), respectively. Whilst, the molar composition with low Si/Al ratio of 16.7 showed a reduction in surface area (307 and 468 m²/g) of the HBEA_{Al}48 and HBEA_{Al}72, respectively. The molar composition with lower Si/Al ratio promoted the incorporation of more aluminium into the framework structure of HBEA_{Al}48 and HBEA_{Al}72 which is in agreement with ²⁹Si MAS NMR spectra (as observed in Table 4.9). Also, the ICP results validate the presence of high aluminium content in HBEA_{Al}48 and HBEA_{Al}72 sample due to their low Si/Al ratio 9.31 and 11.57, respectively. Hence, the molar composition with low Si/Al ratio impacted upon the increased aluminium content within the framework structure of the synthesised HBEA zeolite, thereby reducing the microporous surface area and mesopore surface area of the zeolite. This might also induce poor catalytic performance of the HBEA_{Al}48 and HBEA_{Al}72 zeolite in different applications. Thus, it is possible to synthesis HBEA zeolite from coal fly ash with stable framework and high crystalline structure whilst also maintaining high microporosity and mesoporosity, which depended upon the Si/Al ratio and the hydrothermal synthesis time.

4.5 Chapter summary

The chapter demonstrated the possibility of preparing BEA zeolites from South African coal fly ash silica extract by indirect hydrothermal treatment. Extracted fly ash based silica contain Si, Al and Na with high Si/Al ratio which served as source of silica needed to synthesis BEA zeolite. Different conditions such as the effect of water, sodium (Si/Na ratio),

aluminium (Si/Al ratio) and the synthesis time of the molar composition was investigated. Increasing the amount of water in the synthesis mixture lowered the concentration of TEA⁺ and other species thus, reducing supersaturation and leading to the production of amorphous material. Both Si/Na and Si/Al molar ratio had a significant effect on the crystallinity, crystal size and percentage yield of the prepared BEA zeolites. Considering the aforementioned factors, two optimal molar regimes were selected: 1 Si : 0.017 Al : 0.241 Na : 0.399 TEAOH : 8.980 H₂O or 1 Si : 0.060 Al : 0.241 Na : 0.399 TEAOH : 8.980 H₂O, with Si/Al ratio of 58.8 or 16.7, respectively. The synthesised BEA zeolites from the above molar compositions had high crystallinity, small crystal size and improved yield. By subjecting the two molar composition to different synthesis times, it was found that the increase in synthesis time directly increased crystallinity, crystal size and percentage yield. Moreover, the study demonstrated that the molar composition of 1 Si : 0.017 Al : 0.241 Na : 0.399 TEAOH : 8.980 H₂O enhanced a fast nucleation rate and promoted crystallinity and crystal growth within the synthesis time of 24 h.

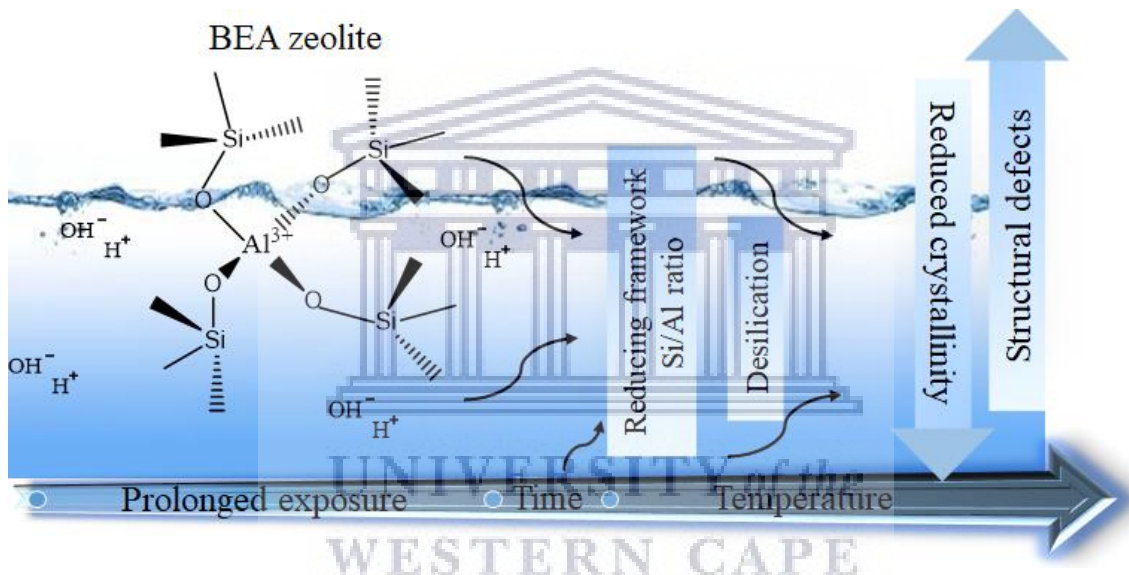
This study gave clearly designed synthesis protocols and formulated suitable molar regimes for the production of BEA zeolite from CFA silica extracts. Through this innovative process, the obtained HBEA zeolite products from CFA demonstrated high crystalline structure, suitable thermal stability, stable framework structure, high microporous area, large mesoporous area, well-distributed pore volume and weak/strong acid sites. These characteristic properties validated that the synthesised HBEA zeolite will be suitable for different catalytic applications. The focus of the subsequent chapter is the hot liquid test reaction of the synthesised BEA zeolite (Chapter 5) and acylation of anisole with benzoyl chloride over rapidly synthesised HBEA zeolite catalyst (Chapter 6).

Chapter 5

Stability of fly ash-based BEA-zeolite in hot liquid phase

Chapter 5 presents the background on the behaviour of zeolites in vapour and hot liquid reactions as well as the results of exposing fly ash based BEA zeolite in hot liquid phase. It also gives a detailed discussion of the phase and framework stability of the treated BEA zeolite by comparing the nucleating behaviour of Si and Al within the Si-O-Si and Si-O-Al environment. Afterwards, the summary of the chapter is presented.

Graphical abstract



Highlights

- Fly ash based silica extract was converted to BEA zeolite by hydrothermal processes
- Stability in hot liquid phase of the fly ash based BEA zeolite was demonstrated
- Stability was a function of relative crystallinity and the presence of defects
- Framework desilication and reduced Si/Al ratio caused reduced crystalline structure
- Desilication of framework showed little or no structural collapse or phase transformation

Abstract

South Africa coal fly ash (class F) was used as feedstock to extract silica for the indirect synthesis of BEA zeolite via a hydrothermal process. The extraction steps selectively retained major components of Si>Al>Na and eliminated the need for the addition of an extra silica source in the zeolite synthesis mixtures. The stability of BEA zeolite was studied in hot liquid phase at different exposure times (6, 12 and 24 h) and temperatures (150 and 200 °C). The structural changes in the framework of the treated zeolite was determined by X-ray diffraction, thermogravimetric analysis, N₂ adsorption-desorption and ²⁷Al and ²⁹Si magic-angle spinning nuclear magnetic resonance. Structural impacts on the treated zeolite depends on prolonged exposure time and high temperature and reduced crystallinity and framework Si/Al ratio, the degree of desilication, and the presence of silanol defects. The relative crystallinity and changes in framework Si/Al ratio were shown to depend on the exposure time and temperature in hot liquid phase. With prolong exposure time, the surface area and micropore volume decreased with an increase in the mesopore volume. The stability of BEA zeolite was influenced by the hydrolysis of Si-O-Si bonds (siloxane) through desilication which eventually caused the formation of structural defects at elevated treatment time and temperature, however, the crystal structure remained intact. Herein, the stability of fly ash based BEA zeolite in hot liquid shows its potential use as a catalyst for liquid phase reactions, considering the exposure time and temperature investigated.

Keywords: BEA zeolite, stability, crystallinity, framework, extraframework, desilication

5.0 Introduction

Heterogeneous catalysis in liquid phase reactions has been considered promising in the petrochemical and fine chemistry industry for alkylation, transalkylation, reforming, dehydration, deoxygenation, hydrolysis, aldol condensation reactions among others (Xiong et al., 2014; Hahn et al., 2013). The behaviour and performance of heterogeneous catalysts are determined by the shape selectivity induced by the framework structure, Si/Al ratio, acid density, tuneable tetrahedral coordination and the pore environment in the case of zeolite (Vjunov et al., 2015). Because of their unique catalytic properties, zeolites directly interact with a suitable solvent or feedstock in the vapour phase (gas) or in hot liquid environments for chemical conversion processes (Ennaert et al., 2016).

The behaviour of zeolites in the vapour or liquid phase environment is directly linked to the metastability of their framework (Prodinger et al., 2018). The tectosilicate structures of various zeolites are relatively stable in the vapour phase environment at reaction temperatures of about 350 to 500 °C. However, the exposure of zeolites in the liquid phase environment at elevated temperatures above 150 °C, causes the tectosilicates structure to gradually disintegrate resulting in pore distortion, structural collapse and/or phase transformation (amorphous or dense crystalline phase) (Ennaert et al., 2016; Zhang et al., 2016; Sun et al., 2015). The structural change is due to the attack of H⁺ and/or OH⁻ ions on the zeolite framework, thus reducing the catalytic functionality. Zeolite stability in traditional vapour-phase chemistry is determined by the OH⁻ hydrolytic attack at the Si-O-Al bonds which gradually leads to dealumination. The Si-O-Al bonds are typically resistant to water-induced degradation because the Al creates a negative charge within the tetrahedral environment, preventing terminal ~Si-O-Al~ from forming defective silanol-terminated lattice (Prodinger et al., 2016; Xiong et al., 2014). In contrast, the reactions in hot liquids with zeolites occur in an alkaline environment which exposes the Si-O-Si bonds in the zeolite framework to attack by the generated hydroxide ions, thereby exposing the tetrahedral framework to structural changes and framework transformation into different zeolite phases or structural collapse (Prodinger et al., 2016). Also, Zhang et al. (2015) related the poor stability of zeolites in hot liquid reactions to structural collapse due to factors such as hydrophilic moieties, domains of extraframework Al and cations, Si/Al ratio, Si-O-Si bonds, the nature of the zeolite structure and Si-OH defects.

Recently, Jamil et al. (2016) grouped the factors influencing the poor stability of ZSM-22 zeolite in hot liquid phase reactions into textural properties and physical parameters of the interactive environment. Such textural properties of the ZSM-22 zeolite include morphological type and shape, porosity, type of cation (Lutz et al., 2005), crystal size (Ding et al., 2007), Si/Al ratio (Lutz et al., 1994) and the existence of defects in the parent zeolite (Prodinger et al., 2016; Zhang et al., 2015). The physical parameters such as pH and temperature of the liquid phase direct the disintegration mechanism of the zeolite structure (Xiong et al., 2014). To this end, the response factors are measured by the loss in zeolite sorption capacity and loss in their relative crystallinity, which eventually results in structural collapse (Prodinger et al., 2016; Vjunov et al., 2015)

Understanding the behaviour, stability and possible structural disintegration of the BEA zeolite synthesised from waste coal fly ash in hot liquid phase is essential, since the fly ash feedstock material is readily available, cheap but contains other elements beside Si and Al. The integrity of coal fly ash-based BEA zeolite through assessment of its stability in hot liquid has not been reported. Therefore it is important to investigate the interaction and the characteristic response of the fly ash-based BEA zeolite in hot liquid phase. The determination of the structural and functional stability will further provide information on real-life utilisation of the fly ash-based BEA zeolite in aqueous phase reactions such as biomass conversion, acylation and alkylation. The aim of this study is to probe the stability of South African coal fly ash-based BEA zeolite in hot liquid phase reaction (objective 3 in chapter 1).

5.1 Experimental

The detailed experimental protocol for the synthesis and characterisation of BEA zeolite products from fly ash-based extracted silica was described and discussed in chapter 3 and 4 respectively. In chapter 4, the synthesis of BEA zeolite was achieved using different synthetic conditions and evaluation of the quality product was performed with various analytical techniques. Two of the zeolite products are further investigated in this chapter, namely: HBEA72 and HBEA_{Al}72 with different molar Si/Al ratios (58.8 and 16.7, respectively) in order to monitor the stability of the fly ash-based zeolite in hot liquid reaction. The zeolites were synthesised from the following molar regime: HBEA72 (1 Si : 0.017 Al : 0.241 Na : 8.980 H₂O : 0.396 TEAOH) and HBEA_{Al}72 (1 Si : 0.060 Al : 0.241

Na : 8.980 H₂O : 0.396 TEAOH) as described in Table 3.4. Each of the HBEA72 and HBEA_{Al}72 zeolite samples were in their respective H-form by ion exchange and calcination (see section 3.2.3) before use in the liquid phase reaction.

5.1.1 Stability test

Stability tests were carried out on the synthesised HBEA-zeolite (HBEA72 and HBEA_{Al}72) in hot liquid phase environment in a similar way as described by Zhang et al. (2015). In each run, 0.5 g of the zeolite and 100 mL of deionised water were added in a 200 mL Teflon container that was then placed inside an autoclave pressure reactor. Thereafter, the mixture inside the Teflon in the pressure reactor was stirred vigorously at 550 rpm at different temperatures and times as presented below (as described in section 5.2.1 and Table 5.1). Different code names are assigned to the treated zeolite as HBEA72 and HBEA_{Al}72 which can be related to NaBEA and AlBEA respectively.

Table 5.1: Experimental conditions for hot-liquid test of NaBEA and AlBEA zeolite.

Variables	-1 (Low)	0	1 (High)
Reaction time (h)	6	12	24
Temperature (°C)	150	-	200
Sample Code	Runs	A	B
NaBEA16	1	-1	-1
NaBEA112	2	-1	1
NaBEA124	3	0	-1
NaBEA26	4	0	1
NaBEA212	5	1	-1
NaBEA224	6	1	1
AlBEA16	7	-1	-1
AlBEA112	8	-1	1
AlBEA124	9	0	-1
AlBEA26	10	0	1
AlBEA212	11	1	-1
AlBEA224	12	1	1

After a specific reaction cycle, the autoclave was allowed to cool to room temperature and the treated BEA zeolites were filtered and dried at 80 °C overnight for further characterisation.

5.2 Results and discussion

The resulting structural changes were characterised by the following analytical techniques: XRD, SEM, TG-MS, FTIR and NMR as described in chapter 3, section 3.3. This section elucidated the behaviour of the synthesised NaBEA and AIBEA zeolite in hot liquid phase with detailed description and discussion of the results.

5.2.1 Phase crystallinity of treated BEA zeolite in hot liquid

The phase identification of the synthesised BEA zeolite after hot liquid test reaction was carried out using XRD analysis. This subsection describes and discusses the effect of hot liquid BEA zeolite phases (see Figure 5.1-5.2).

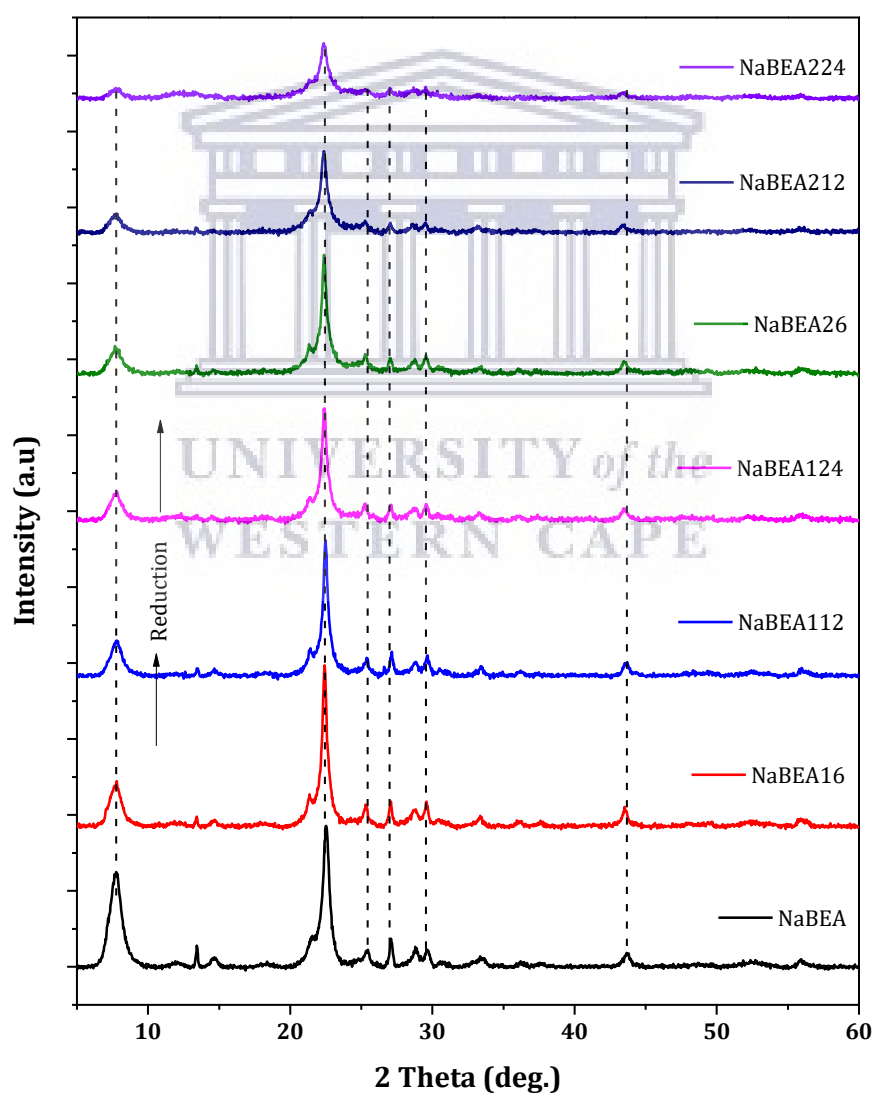


Figure 5.1: XRD patterns of the parent and treated NaBEA zeolite in hot liquid phase reaction at 150 °C for 6, 12 and 24 h (NaBEA16, NaBEA112 and NaBEA124) and 200 °C for 6, 12 and 24 h (NaBEA26, NaBEA212 and NaBEA224).

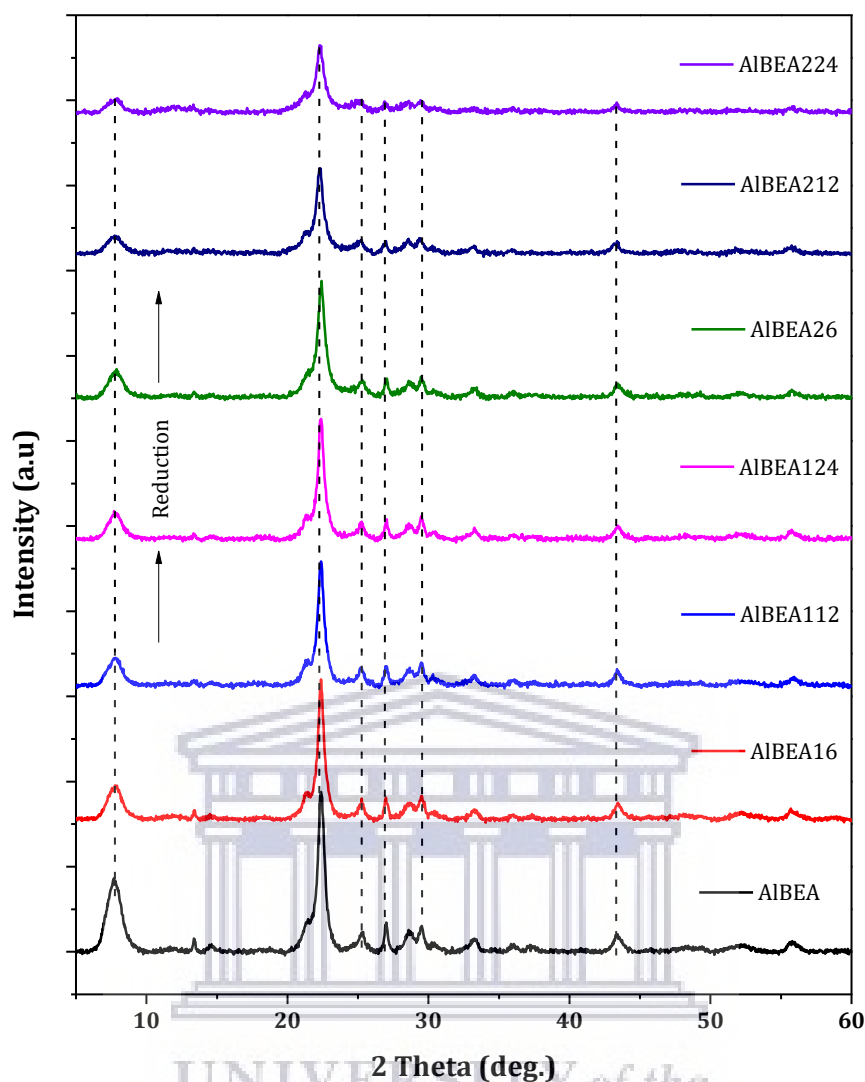


Figure 5.2: XRD patterns of parent and treated AIBEA zeolite in hot liquid phase reaction at 150 °C for 6, 12 and 24 h (AIBEA16, AIBEA112 and AIBEA124) and 200 °C for 6, 12 and 24 h (AIBEA26, AIBEA212 and AIBEA224).

The XRD diffractograms in Figure 5.1-5.2 shows the XRD patterns of the parent fly ash based NaBEA/AIBEA and hot liquid treated zeolite samples. The parent fly ash based NaBEA and AIBEA zeolite diffraction pattern was that of a typical crystalline BEA-zeolite with distinct and well-defined characteristic peaks located at 7.7 and 22.5° 2 θ . Upon hot liquid treatment at various times and temperatures, a notable reduction was observed in the intensity of the low angle peak at 7.7° 2 θ (as indicated by the arrows in Figure 5.1 and 5.2). The substantial loss in the intensity in this diffraction peak is correlated with the increased progression in treatment time (6>12>24 h) and temperature (150 to 200 °C). Similarly, the characteristic peak intensity at 22.5° 2 θ showed a slight decline, however, the structure of the hot liquid treated BEA zeolite retained the defined diffraction at 7.7 and 22.5 2 θ after

the extensive exposure to hot liquid phase with no phase impurity observed. Prodingler et al. (2016) indicated that the intensity loss is associated with the removal of atoms (Si or Al) and the generation of defects which induce the degradation of the 4- and 6-membered ring structure and the T-O-T bond arrangement in the crystal structure of BEA zeolite. Such disruptions have been linked to the increase or decrease in bond lengths of Al-O and Si-O species in the crystal structure which mostly affect the intensity of the characteristic peak at $2\theta = 7.7$ or 22.5° due to disorder in the lattice framework (Chaves et al., 2015).

The effect on the peak intensity of BEA zeolites suggest that the crystalline structure might be susceptible to degradation in hot liquid phase reactions. To determine the quality of the crystalline structure, the relative crystallinity of the parent and treated BEA zeolite was estimated by analysing the areas under the two main peaks in the diffraction spectra (at $2\theta = 7.7$ and 22.5°) using the following equation 4.5 (see section 4.3.3): In this case, P is the total area of the diffraction peaks at 7.7 and $22.5^\circ 2\theta$ for the treated samples and P_0 is the equivalent area in the case of the parent NaBEA and AlBEA zeolites, corresponding to the untreated sample. Figure 5.3 presents the relative crystallinity of the treated BEA zeolite in hot liquid in relation to the effect of the reaction temperature and time.

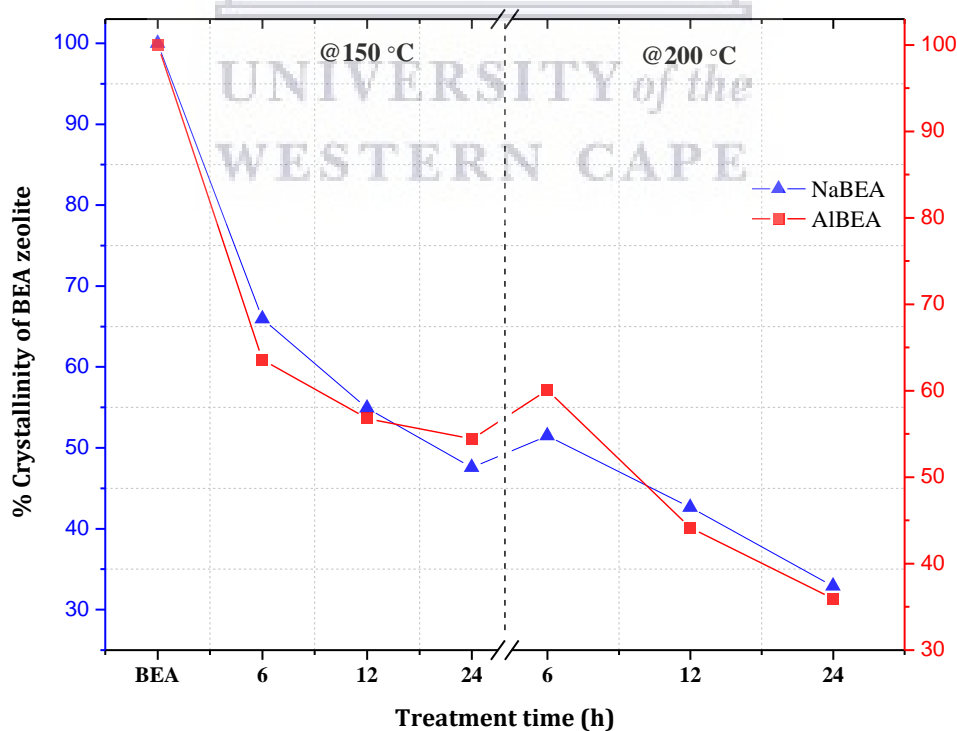


Figure 5.3: Percentage crystallinity of the parent BEA ((▲) NaBEA and (■) AlBEA) and hot liquid treated zeolite at 150 °C and 200 °C for 6, 12 and 24 h.

The crystallinity of the treated BEA zeolite presented in Figure 5.3 shows the behaviour of the crystal structure when exposed to hot liquid phase reaction. The relative crystallinity of the BEA zeolite before and after treatment decreased from 100 to 30%, which is a function of the treatment temperature and time. It was observed that the parent synthesised NaBEA and AlBEA samples were susceptible to hot liquid phase over time with a gradual decrease in relative crystallinity as a response factor to increasing treatment temperature and time. The treated samples lost about 35 to 67% of their original relative crystallinity after 6, 12 and 24 h at different thermal temperatures (150 and 200 °C). At 150 °C, the samples NaBEA16-AlBEA16, NaBEA112-AlBEA112, and NaBEA124-AlBEA124 exhibited less decrease in crystallinity (66-64 > 55-57 > 48-54 respectively) with an increase in reaction time (6 > 12 > 24). With an increase in treatment temperature (200 °C), about 40 to 58% (NaBEA26 and AlBEA26) of the crystallinity was lost within 6 h reaction time. After 24 h exposure to hot liquid, the samples lost 67 and 64% of the relative crystallinity (NaBEA224 and AlBEA224, respectively) suggesting that the crystallinity can be compromised upon increasing treatment time and temperature in hot liquid reaction media.

The reduction in the relative crystallinity is evidence of the gradual formation of amorphous phases or defects in the crystal structure of the treated zeolite. Furthermore, the significant reduction in peak intensity at $7.7^\circ 2\theta$ directly affects the 4- and 6-member rings that interconnect the large pores of BEA zeolite (Vjunov et al., 2015). These compromise the interconnected member rings which was indicated by a loss in relative crystallinity that may lead to the formation of different monomers and dimers of impure zeolitic or amorphous phases and, finally, a gradual structural collapse.

In addition, the interactive environment with H₂O may induce the response of the lower relative crystallinity of BEA zeolite in the hot liquid. Figures 5.4 and 5.5 present the effect of hot liquid upon the structure of the synthesised NaBEA and AlBEA zeolite measured by equation 5.1.

$$pH = -\log[H_3O^+] \qquad pOH = -\log[OH^-] \qquad \text{Equation 5.1}$$

The pH of the recovered solution after hot liquid treatment of the zeolite was measured in triplicate (n=3).

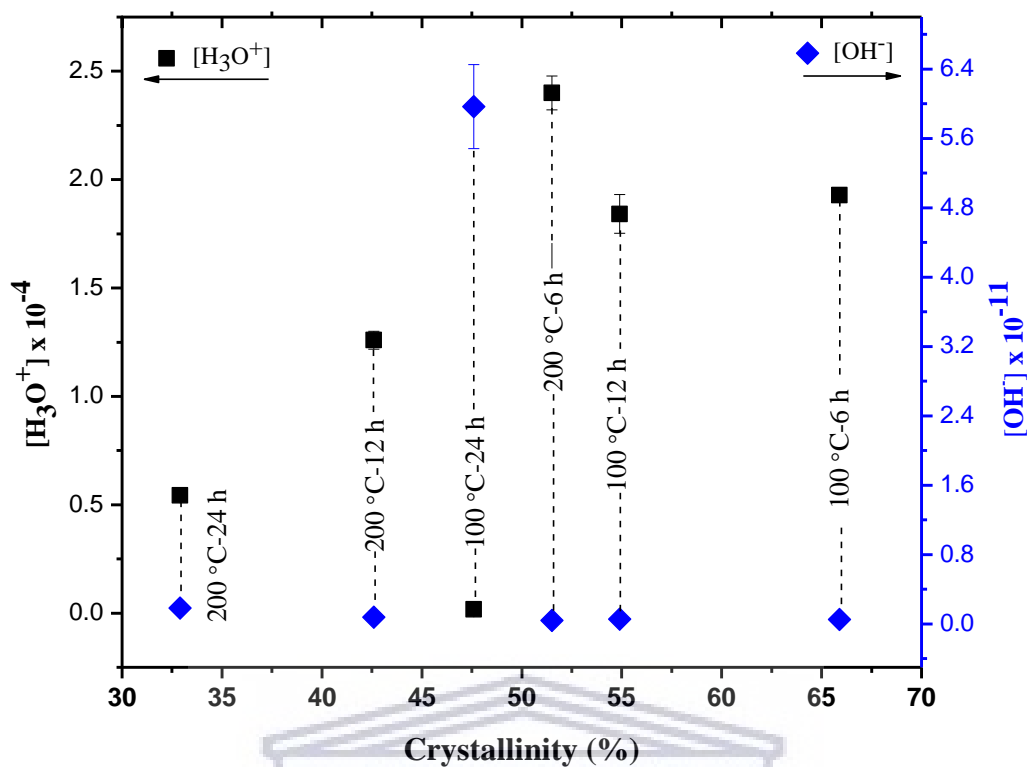


Figure 5.4: pH behaviour of NaBEA zeolite in the interactive environment of hot liquid reaction set at 100 °C for 6, 12 and 24 h (NaBEA16, NaBEA112 and NaBEA124) and 200 °C for 6, 12 and 24 h (NaBEA26, NaBEA212 and NaBEA224).

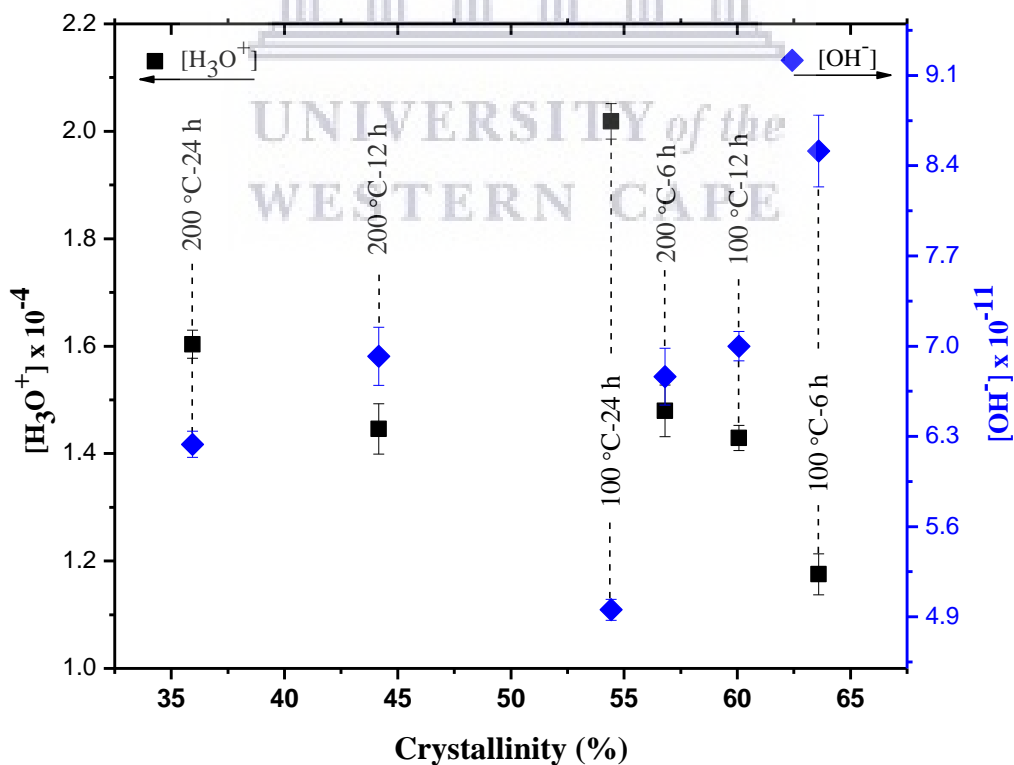


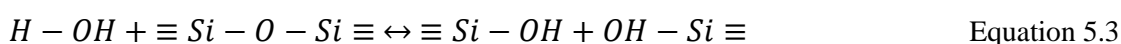
Figure 5.5: pH behaviour of AlBEA zeolite in the interactive environment of hot liquid reaction set at 100 °C for 6, 12 and 24 h (AlBEA16, AlBEA112 and AlBEA124) and 200 °C for 6, 12 and 24 h (AlBEA26, AlBEA212 and AlBEA224).

The treatment of NaBEA and AlBEA zeolite in hot liquid reaction as presented in Figure 5.4 and 5.5 show the behaviour of the zeolite in the environment of H_3O^+ and OH^- species in hot liquid water as described in Equation 5.2.



In this environment, it was observed that the crystallinity of NaBEA zeolite gradually reduced as the amount of (H_3O^+) species decreased (from 1.93×10^{-4} to 1.68×10^{-7} and 2.40×10^{-4} to 5.43×10^{-5} at a treatment temperature of 150 and 200 °C, respectively). While, the associated OH^- species increased in amount (5.19×10^{-11} to 5.96×10^{-9} and 4.17×10^{-11} to 1.84×10^{-10} at 150 and 200 °C, respectively). This observed association can further be linked to the prolonged exposure time of the BEA zeolite in hot liquid phase as presented in Figure 5.2. Similarly, the behaviour of AlBEA zeolite can also be associated with exposure time as in the case of NaBEA zeolite in hot liquid phase. However, the amount of H_3O^+ and OH^- species available for interaction ranged between 10^{-4} or 10^{-11} , respectively (see Figure 5.5). Since the surface nature of BEA zeolites is hydrophilic, the surface functional groups such as protons and hydroxyl groups are exposed to attack by H_3O^+ and OH^- ions in the hot liquid phase reaction. This, in turn, was found to compromise the integrity of the NaBEA and AlBEA crystal structure by directly affecting the crystallinity as indicated in Figure 5.2, 5.4 and 5.5. This suggests that the durability of the NaBEA and AlBEA zeolite in hot liquid phase is best achieved at lower temperatures and shorter exposure times. High temperature and long exposure time (≥ 200 °C and ≥ 24 h) may induce changes in the zeolite framework structure but XRD showed phase purity was maintained.

Xiong et al. (2014) related the degradation of the zeolite structure to the attack of H_3O^+ and OH^- ions through the hydrolysis of Si-O-Al and Si-O-Si bonds by H_3O^+ and OH^- ions respectively. The mechanism of structural change of the zeolite in hot liquid reaction mainly resembles the alkaline pathway through the direct attack of Si-O-Si by hydroxide ions as illustrated in Equation 5.3 (Jamil et al., 2016; Ennaert et al., 2016).



These authors further suggested that the degradation mechanism via the attack of Si-O-Al bonds by hydronium ions is mostly related to the behaviour of zeolite in steam environments. The crystallinity of fly ash based NaBEA and AlBEA zeolites in a hot liquid environment is thus greatly influenced by OH⁻ ion attack as a function of prolonged exposure time in hot liquid at elevated temperatures. To this end, the structural analysis of the treated BEA zeolite using FT-IR was carried out to probe the effect of the hot liquid on the functional groups of the framework structure of the synthesised zeolite.

5.2.2 Structural probe of O-T-O bonds

The functional groups located within the framework structure of NaBEA and AlBEA zeolite before and after hot liquid treatment was probed using FT-IR analysis. Figure 5.6 and 5.7 present the structural analyses of the NaBEA and AlBEA zeolites treated in hot liquid phase.

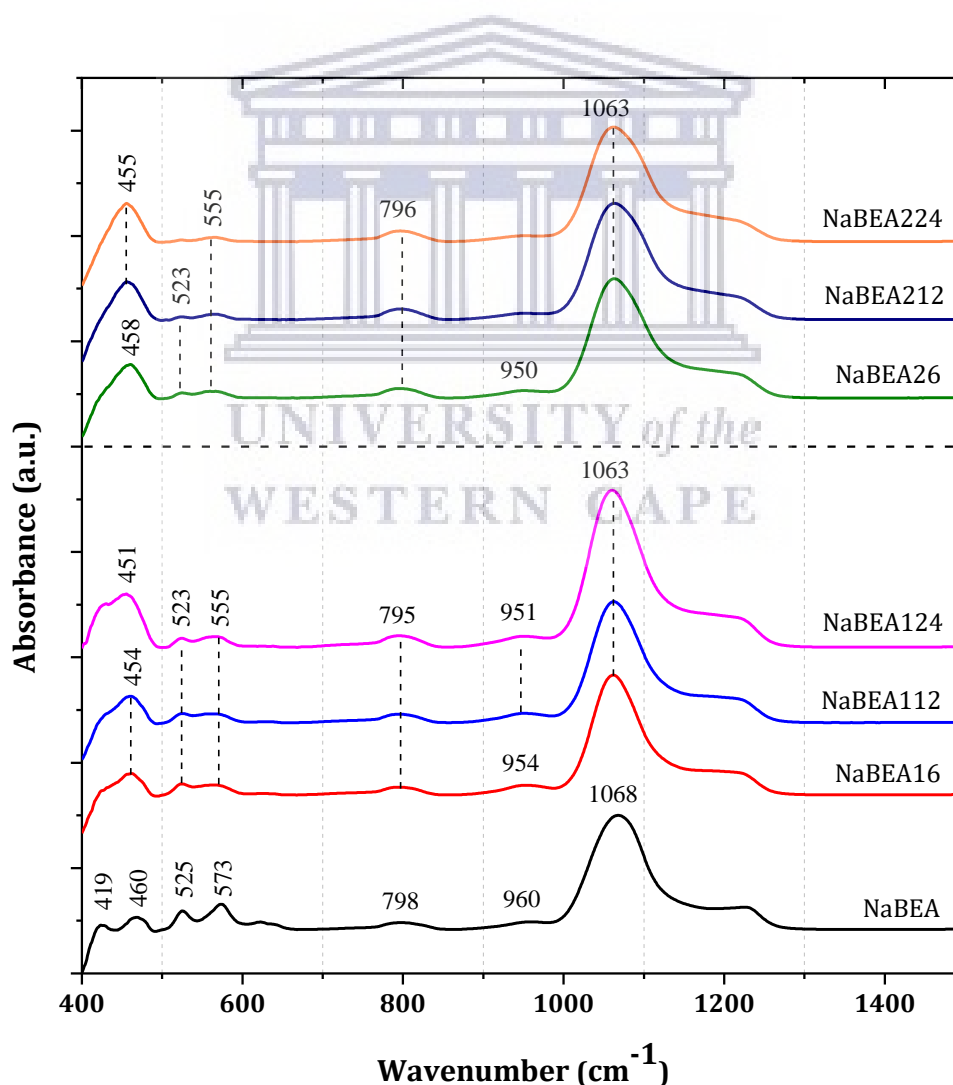


Figure 5.6: FT-IR spectra of parent and hot liquid treated NaBEA zeolites at different temperature: 150 °C for 6, 12 and 24 h (NaBEA16, NaBEA112 and NaBEA124) and 200 °C for 6, 12 and 24 h (NaBEA26, NaBEA212 and NaBEA224).

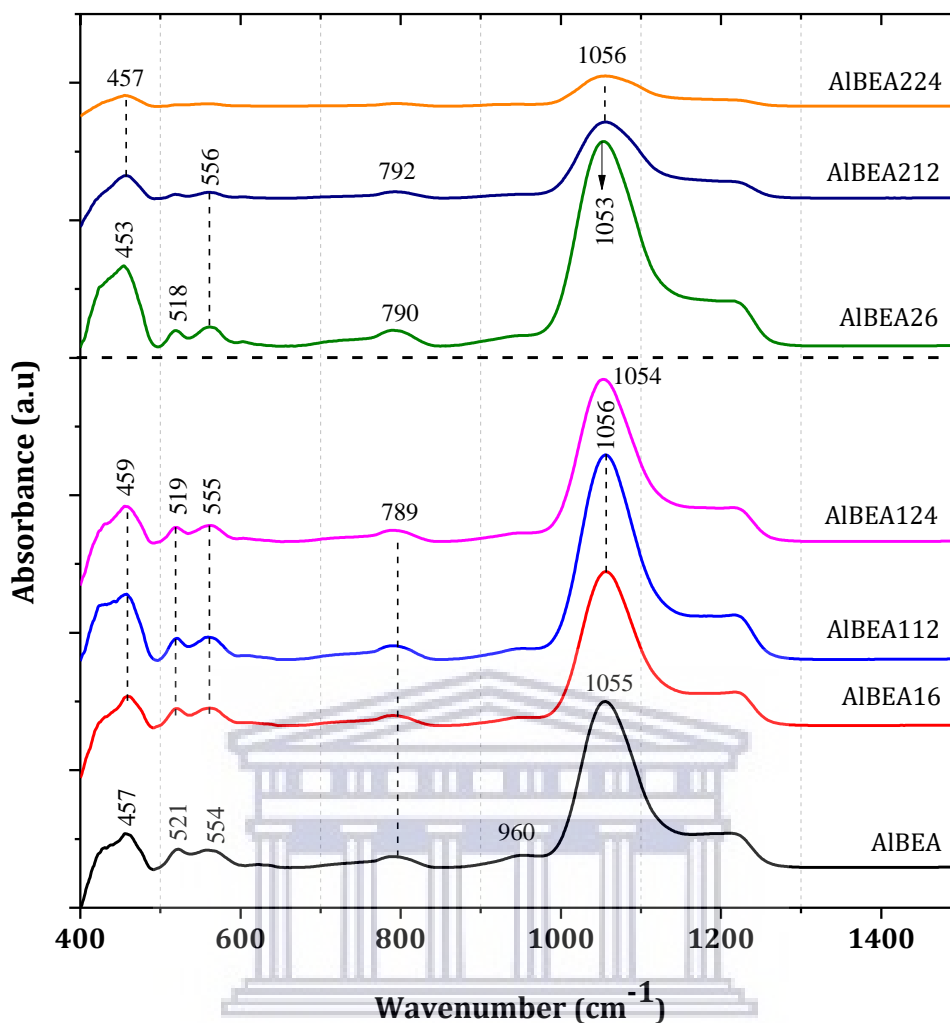


Figure 5.7: FT-IR spectra of parent and hot liquid treated AIBEA zeolites at different temperature: 150 ° for 6, 12 and 24 h (AIBEA16, AIBEA112 and AIBEA124) and 200 °C for 6, 12 and 24 h (AIBEA26, AIBEA212 and AIBEA224).

The structural vibration IR spectra of the parent and treated NaBEA-AIBEA zeolite are shown in Figure 5.6 and 5.7. In these figures, the effect of hot liquid on the BEA zeolite was observed within three main structural characteristic bonds: symmetric, asymmetric and bending vibrations. The vibrational band at 789, 795, 796, 798, 790 and 792 cm^{-1} can be associated with the O-T-O (T = Si or Al) symmetric stretching vibration and internal tetrahedral symmetrical stretching of the external linkage (see Figure 5.6 and 5.7) (Zhang et al., 2017). Upon exposure of parent NaBEA and AIBEA zeolite, the symmetric band gradually shifts to lower and higher wavenumbers. The peak at 798 cm^{-1} observed in the parent NaBEA zeolite shifted to a lower wavenumber of 795 cm^{-1} (NaBEA16, NaBEA112 and NaBEA124) at the treatment temperature of 150 °C which then increased to 796 cm^{-1} (NaBEA26, NaBEA212 and NaBEA224) in hot liquid at elevated temperature of 200 °C

(Figure 5.6). In the case of parent AIBEA zeolite, a gradual peak shift from 789 cm^{-1} to a higher wavenumber at 790 and 792 cm^{-1} was observed upon treatment at a temperature of $200\text{ }^{\circ}\text{C}$ for 6 and 12 h (AIBEA26 and AIBEA212) which peak eventually disappears following prolonged treatment time for 24 h (AIBEA224) (Figure 5.7). Tian et al. (2013) related the increase in peak shift to the removal of the Al content from $-\text{O}-\text{Al}-\text{O}-$ bonds within the framework structure of BEA zeolite. A shift to lower wavenumber, on the other hand, could be associated with the desilication of the $-\text{O}-\text{Si}-\text{O}-$ (O-T-O) (Tian et al., 2013). This, in turn, is also reflected in the shift of the asymmetric O-T-O stretch around 1068 and 1055 cm^{-1} (NaBEA and AIBEA respectively) to: i) a lower wavenumber at 1063 cm^{-1} (Figure 5.6) and ii) a higher wavenumber at 1056 cm^{-1} (Figure 5.7). The asymmetrical vibrational bands are attributed to the external and internal tetrahedral atoms (Zhang et al., 2017) which are sensitive to the respective change of silicon or aluminium content in the framework structure of BEA zeolite (Kantam et al., 2006). Similarly, Fernandez et al. (2018) observed that the wavenumber of the broad asymmetric stretch increases with a decrease in the content of the framework aluminium.

According to Kantam et al. (2006), the minor vibration band at around 960 cm^{-1} which shifted upon treatment (to 954 , 951 and 950 cm^{-1}) (see Figure 5.6-5.7) is attributed to the terminal SiO^- groups on the large external surface of the zeolite due to the formation of small crystallites. The absorption peaks of the parent NaBEA and AIBEA at 525 , and 573 cm^{-1} and 521 and 554 cm^{-1} , respectively, are the characteristic bands associated with the crystalline BEA zeolite framework (Zhang et al., 2017). After the exposure of the parent NaBEA zeolite to hot liquid, the characteristic T-O-T (T = Si or Al) peak shifted to 523 and 555 cm^{-1} and 518 and 556 cm^{-1} (See Figure 5.6 and 5.7) as the intensity of the peak gradually reduced with increased treatment time and temperature. It was noted that the peaks at 525 cm^{-1} (NaBEA224), 521 and 554 cm^{-1} (AIBEA212 and AIBEA224) disappeared, this is consistent with the XRD results (see Figure 5.1 and 5.2) indicating that the integrity of the parent BEA zeolite had been compromised resulting in a crystallinity $\leq 40\%$. The decrease in the T-O-T bands suggested the gradual increase of amorphous material as a consequence of structural collapse as the exposure time and temperature increased as confirmed by the XRD data (Figure 5.1 and 5.2). This is in agreement with the observation of Tian et al. (2013), who related the decrease in wavenumber and intensity of the characteristic peak to the decreased crystallinity.

The pore opening vibration at 419 and 457 cm^{-1} of the parent NaBEA and AlBEA zeolite respectively are attributed to the bending vibration (T-O) (Modhera et al., 2009). It is worth noting, that the T-O vibration became broader and gradually shifted to the left (451, 454, 455 and 458 cm^{-1} , see Figure 5.6) and to the right (453 cm^{-1} , see Figure 5.7) with an increased intensity after the exposure to hot liquid phase. The broadening of the bands suggest a gradual stretch of the Si-O-Si bending which may have affected the pore opening and dimensions, as treatment time and temperature increased, thereby impacting on the relative crystallinity of the treated NaBEA and AlBEA zeolite.

5.2.3 Si-OH content within the BEA zeolite structure using thermogravimetric analysis

The thermal stability of detemplated parent and treated NaBEA and AlBEA zeolite after a hot liquid phase reaction at 150 and 200 $^{\circ}\text{C}$ for 6, 12 and 24h respectively, is described in this section. The TGA curve of the untreated (NaBEA/AlBEA) and treated (NaBEA16, NaBEA112, NaBEA124, NaBEA26, NaBEA212, NaBEA224, AlBEA16, AlBEA112, AlBEA124, AlBEA26, AlBEA212 and AlBEA224) BEA zeolites are presented in Figures 5.8 and 5.9.

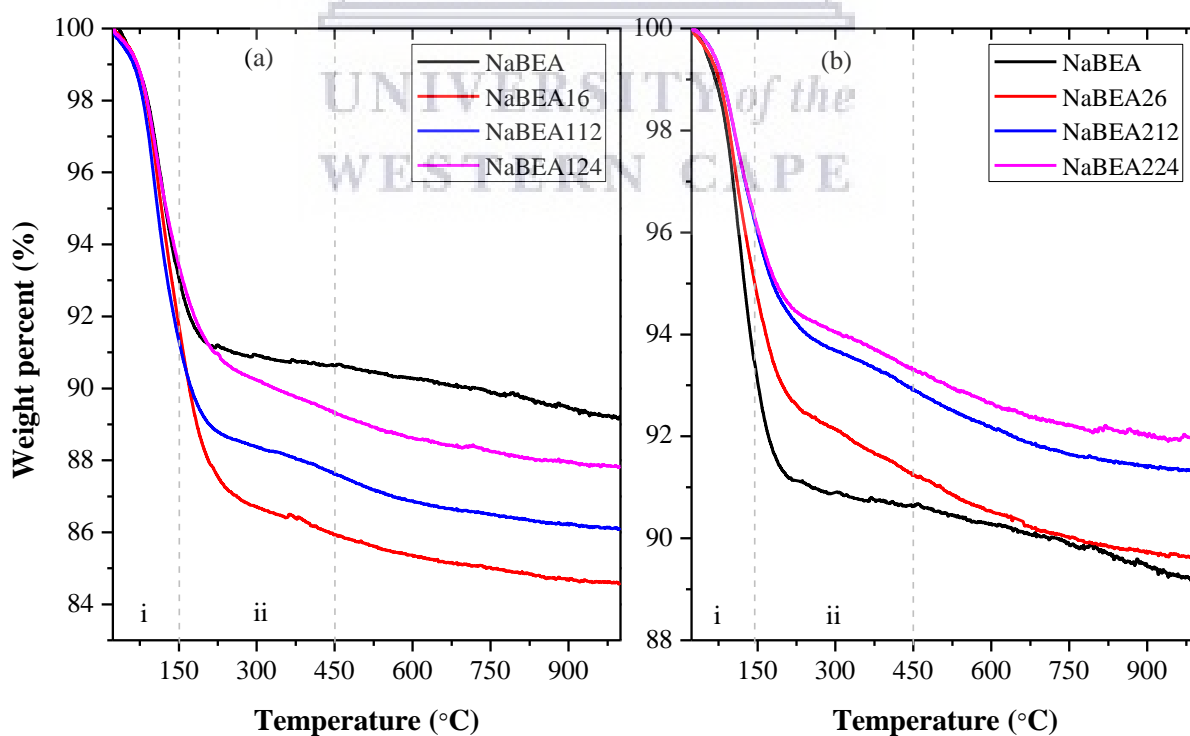


Figure 5.8: TGA of the untreated (NaBEA) and treated zeolite in hot liquid phase reaction at (a) 150 $^{\circ}\text{C}$ (NaBEA16, NaBEA112, NaBEA124) and (b) 200 $^{\circ}\text{C}$ (NaBEA26, NaBEA212, NaBEA224) for 6, 12 and 24 h respectively.

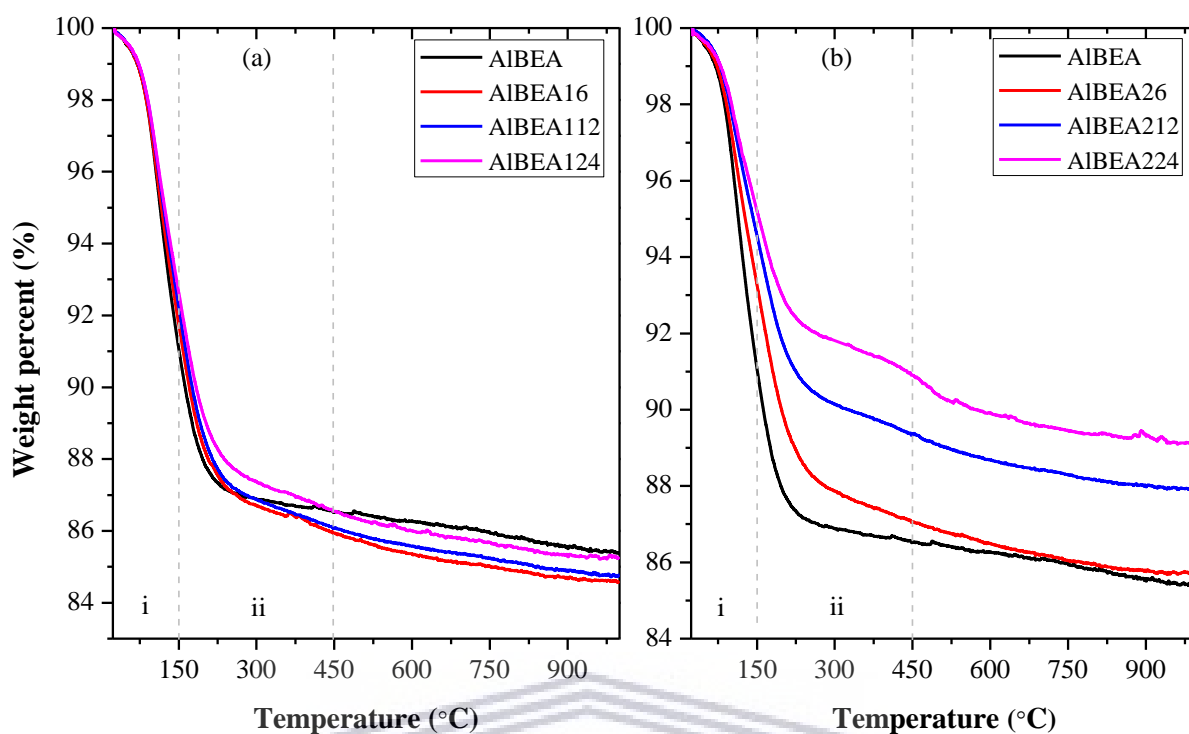


Figure 5.9: TGA of the untreated (AIBEA) and treated zeolite in hot liquid phase reaction at (a) 150 °C (AIBEA16, AIBEA112, AIBEA124) and (b) 200 °C (AIBEA26, AIBEA212, AIBEA224) for 6, 12 and 24 h respectively.

Figure 5.8 and 5.9 show the thermogravimetric curves of the parent and treated (NaBEA and AIBEA) zeolite after exposure to hot liquid reaction. Two major weight loss steps were recorded in the following temperature ranges: i) 25-150 °C and ii) 150-450 °C (Figure 5.8 and 5.9). The first weight loss, step i), can be associated with the physisorbed surface water while the second stage (step ii) is linked to the $H^+ - OH^-$ species bonded to $\sim Si-O-Si\sim$ or $\sim Si-O-Al\sim$ in the framework structure of the BEA zeolite (Zhang et al., 2017). To further confirm this, correlation between the surface water and bonded framework water of the treated (NaBEA and AIBEA) zeolite was drawn alongside the calculated terminal OH group (silanol) using equation 5.4 (Li, et al., 2014).

$$N_{OH} = \frac{2(W_1 - W_2)}{M_{H_2O}} \times 1000 \quad \text{Equation 5.4}$$

Where W_1 and W_2 are the weight of BEA zeolite samples (wt %) at temperature 200 and 1000 °C respectively, M_{H_2O} is the molecular weight of water. Table 5.2, presents the adsorbed surface and bonded framework water as well as the silanol content of the parent and treated NaBEA-AIBEA zeolite.

Table 5.2: Relation between adsorbed surface water, bonded framework water and silanol content.

Sample	Weight loss (%)				N_{OH} (mmol/g)
	Adsorbed water	Dehydroxylation		Total	
	25 - 200 °C	200 - 600 °C	600 - 1000 °C		
NaBEA	8.70	1.01	1.07	10.78	2.31
NaBEA16	11.75	2.89	0.76	15.40	4.06
NaBEA112	10.83	2.29	0.76	13.88	3.39
NaBEA124	8.61	2.76	0.79	12.16	3.94
NaBEA26	7.03	2.43	0.90	10.37	3.70
NaBEA212	5.43	2.39	0.83	8.65	3.57
NaBEA224	5.27	2.08	0.70	8.04	3.08
AlBEA	12.64	1.08	0.88	14.60	2.17
AlBEA16	11.75	2.89	0.76	15.40	4.06
AlBEA112	11.42	3.00	0.82	15.24	4.24
AlBEA124	10.88	3.10	0.74	14.73	4.26
AlBEA26	10.14	3.37	0.79	14.29	4.61
AlBEA212	8.26	3.05	0.75	12.05	4.21
AlBEA224	7.04	3.04	0.76	10.84	4.23

Note: N_{OH} = silanol content.

Table 5.2 presents the calculated results of the adsorbed surface and framework water, as well as the relationship of the water environment to silanol content of BEA zeolite. The first stage of the TGA results between 35 and 200 °C was endothermic which is associated with the mass loss by dehydration or desorption of physically adsorbed water (Bourgeat-Lami et al., 1992). As the parent NaBEA and AlBEA zeolite (1.01 and 1.07%, respectively) is exposed to hot liquid phase, the second stage mass loss between 200-600 °C initially increased to 2.89% (NaBEA16 and AlBEA16). With prolonged treatment time and exposure temperature as in the case of NaBEA zeolite, the mass loss within the second stage environment gradually decreased (2.08% for 24 h at 200 °C). Whereas, the second stage mass loss of AlBEA zeolite increased to 3-3.1% (AlBEA112 and AlBEA124) and 3.37% (AlBEA26) but decreased to 3% (AlBEA212 and AlBEA224) (see Table 5.2). It was worth noting, that the decrease or increase in mass loss within the second stage due to prolonged exposure time and temperature can be associated with dehydroxylation of framework siloxane (Si-O-Si) bonds which results in the formation of terminal silanol (Si-OH) defect sites in the framework (Ek et al., 2001). The calculated silanol content (N_{OH}), indicates that during dehydroxylation some of the siloxane bonds in the BEA framework are degraded and result in the formation of terminal silanol bonds in the zeolite framework.

According to Zhang et al. (2013) the weight loss at 250-450 °C suggested the formation of terminal OH (silanol) structural defects in the framework of the treated BEA zeolite. These consequently increase the framework silanol bonds which reduces framework stability and eventually results in a loss of framework crystallinity. One possible effect is the degradation of the open framework structure of the NaBEA and AlBEA zeolite which is consistent with XRD results (Figure 5.1-5.2). To further confirm the formation of defects in the silanol species within the framework structure of the BEA zeolite, ^{27}Al and ^{29}Si MAS NMR analysis was carried out as presented in the next section.

5.2.4 Framework changes of hot liquid treated BEA zeolite

This section presents analyses of the NMR results of the parent NaBEA and AlBEA zeolite before and after being exposed to hot liquid at 150 or 200 °C at 6, 12 and 24 h respectively. Also, to demonstrate and enable elucidation of the framework structure of treated zeolite, ^{29}Si and ^{27}Al MAS NMR analysed with 8 kHz spinning speed at a magnetic field strength of 11.4 T as described in section 3.10 was carried out. Figure 5.10 and 5.11 present the ^{29}Si MAS NMR of the parent and treated NaBEA/AlBEA zeolite at different temperatures and times.

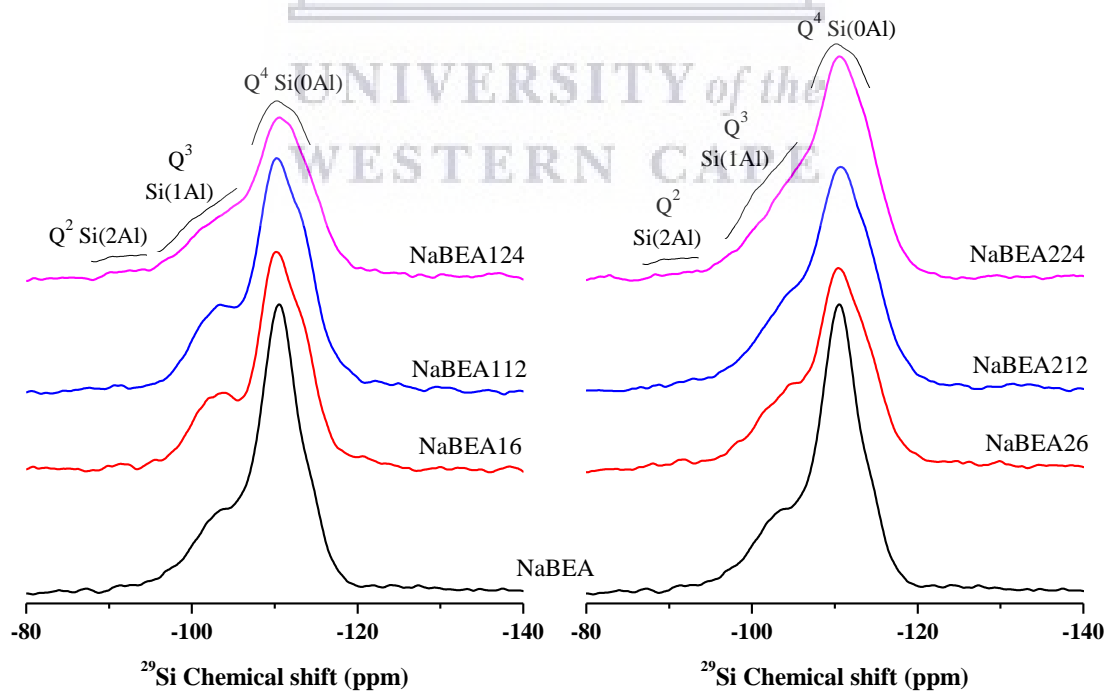


Figure 5.10: ^{29}Si MAS NMR of the parent and treated NaBEA zeolite at 150 °C (NaBEA16, NaBEA112 and NaBEA124) or 200 °C (NaBEA26, NaBEA212 and NaBEA224) at 6, 12 and 24 h, respectively.

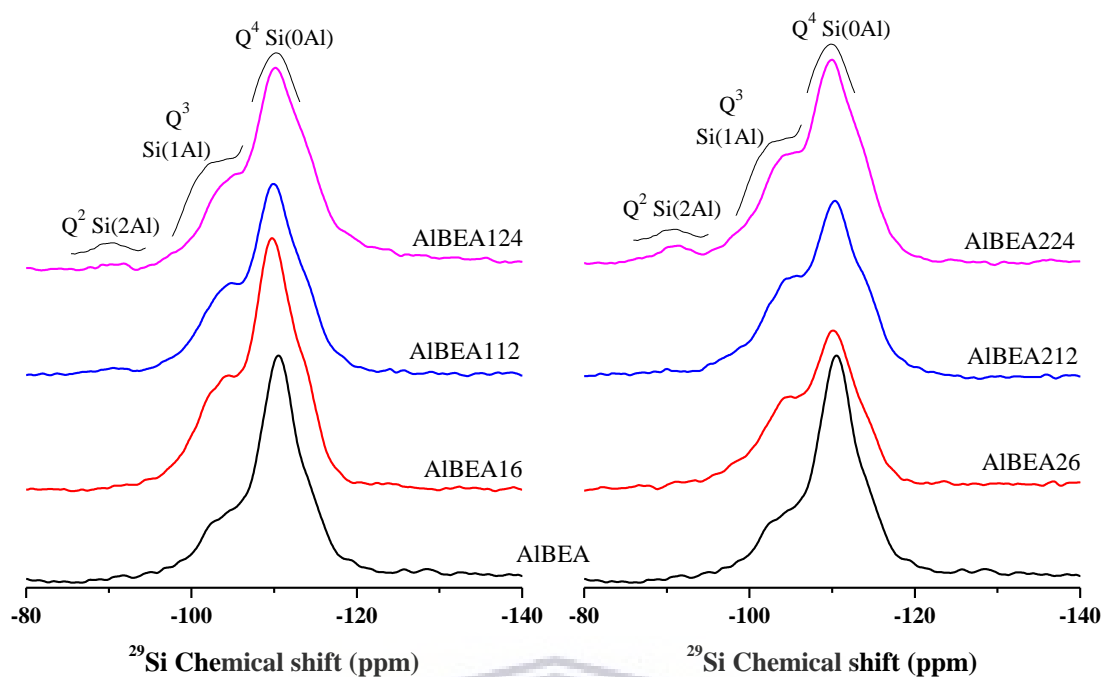


Figure 5.11: ^{29}Si MAS NMR of the parent and treated AIBEA zeolite at 150 °C (AIBEA16, AIBEA112 and AIBEA124) or 200 °C (AIBEA26, AIBEA212 and AIBEA224) at 6, 12 and 24 h, respectively.

The ^{29}Si MAS NMR spectra presented in Figures 5.10 and 5.11 elucidated the framework structural coordination of the parent NaBEA and AIBEA zeolite after the hot liquid phase reaction. In Figure 5.10 and 5.11, two main broad signals assigned to the $\text{Q}^3 \text{Si} (1\text{Al})$ and $\text{Q}^4 \text{Si} (0\text{Al})$ environment were observed around $\delta = -104$ to -107 ppm and $\delta = -110$ to -111 ppm, respectively (Zhang et al., 2013). Other weak peaks were observed at around $\delta = -98$ and $\delta = -114$ ppm which can be attributed to $\text{Q}^2 \text{Si} (2\text{Al})$ and $\text{Q}^4 \text{Si} (0\text{Al})$ coordination respectively (Zhang et al., 2013; Engelhardt, 2001). It is worth noting that the difference in the $\text{Q}^4 \text{Si} (0\text{Al})$ peaks at $-\delta = -110/-111$ ppm and at $\delta = -114$ ppm is related to the degree of Si substituted by Al in the lattice structure. Moreover, the signal of the parent $\text{Q}^3 \text{Si} (0\text{Al})$ and $\text{Q}^4 \text{Si} (1\text{Al})$ species showed a gradual chemical shift associated with changes in the peak intensity and area after exposure to hot liquid phase reaction. The chemical shift, peak intensity and peak area was derived by deconvolution using mixed Lorentzian and Gaussian line shape (see Table 5.3). Afterwards, the change in intensity was used to calculate the framework Si/Al ratio in the treated samples according to equation 4.7 (Holzinger et al., 2018).

Table 5.3: Comparison of chemical shift, Si/Al ratio, intensity and area of deconvoluted Q³ and Q⁴ peak.

	Q ³ Si(1Al)		Q ⁴ Si(0Al)		Si/Al _{FW}
	δ_{decon} (ppm)	Intensity %	δ_{decon} (ppm)	Area %	
NaBEA	-105.53	10.35	-111.05	11.29	23
NaBEA16	-105.51	11.98	-111.12	11.80	22
NaBEA112	-105.75	12.97	-111.19	13.34	20
NaBEA124	-107.00	17.15	-110.93	16.46	16
NaBEA26	-107.01	15.49	-110.81	14.28	18
NaBEA212	-107.00	17.15	-110.93	16.46	16
NaBEA224	-104.92	14.92	-110.87	16.38	18
AlBEA	-105.63	9.33	-111.04	12.18	22
AlBEA16	-105.77	13.67	-110.52	13.65	17
AlBEA112	-106.65	14.62	-110.71	14.05	16
AlBEA124	-106.92	14.17	-111.01	15.13	16
AlBEA26	-106.33	16.75	-110.30	14.99	14
AlBEA212	-106.03	16.50	-110.45	15.36	14
AlBEA224	-106.01	14.96	-110.66	14.64	15

Note: δ_{decon} is the chemical shifts, Si/Al_{FW} is the framework silica and aluminium ratio

Table 5.3 presents the values of the chemical shift obtained by deconvolution of Q⁴ Si (0Al) and Q³ Si (1Al) species of the parent and treated NaBEA and AlBEA. The Q³ Si (1Al) spectra of the parent zeolite (NaBEA and AlBEA) showed a signal around $\delta = -105$ ppm which gradually shifted to a stronger signal at around $\delta = -107$ and -106 ppm respectively, as the treatment time and temperature increased. The Q⁴ Si (0Al) peak at $\delta = -111$ ppm, however, decreased to a weaker signal around $\delta = -110$ ppm with an increased treatment time and temperature. According to Zhang et al. (2017) the upfield shifts are directly influenced by the increased amount of Al content in the framework structure of the treated zeolite due to desilication.

The calculated ²⁹Si MAS NMR Si/Al ratio clearly validated that the relative amount of Al content in the framework structure increased as the Si/Al ratio decreased with prolonged exposure conditions (see Table 5.3). The reactive environment around the Si coordinates allows desilication of the Q³ Si (1Al) species and this corresponds to the observed lower framework Si/Al ratio. Thus, the Q³ Si (1Al) peak shift implies the formation of Q³ Si (1OH)

or Q^3 Si (1O⁻) environments which are indicative of the structural defects of silanol sites (SiOH) (Mintova et al., 2006; Zhang et al., 2017).

The impact of the prolonged exposure time and increased treatment temperatures was observed with the gradual increase in the signal intensities of Q^3 Si (1Al) and peak area of the Q^4 Si (0Al) (see Table 5.3). This is probably due to the increased formation of structural defects which hydrolytically prompt the desilication of the BEA zeolite framework. Furthermore, the increased peak intensity can be linked to the gradual formation of Si-OH defects within the treated zeolite structure (Vjunov et al., 2015). Also, the prolonged exposure time and increased treatment temperature gave rise to the presence of Q^2 Si (2Al) coordination (Figure 5.10 and 5.11) and this indicated the gradual alteration of the framework structure by desilication. The gradual formation of Q^2 Si (2Al) with prolonged exposure time is confirmation of the presence of Si-OH defects in the treated samples (NaBEA224 and AlBEA224) (Prodinger et al., 2018).

As the Si/Al ratio of the framework structure decreased, the resolved Q^3 Si (1Al) peak intensity increased with a gradual shift upfield with an expanded Q^4 Si (0Al) peak area. Considering the flexibility of the zeolite cavities, the broadening of the bands suggest a gradual stretch of the Si-O-Si bending (see Figure 5.6-5.7), increased peak intensity and area indicates the pore opening and dimensions of the parent NaBEA/AlBEA zeolite expand as treatment time and temperature increased. These directly impacted on the crystal structure (crystallinity), framework structure and eventually may lead to the collapse of the crystalline BEA framework into amorphous material or perhaps the transformation of the material into other zeolite phases which was not observed in either case as no uncoordinated Si was formed.

To validate the structural stability of the NaBEA and AlBEA zeolite in hot liquid phase, the relationship between the relative crystallinity (■) and the integrated peak area (▲) of Q^4 Si (0Al) and peak intensity (●) of Q^3 Si (1Al) was evaluated (see Figure 5.12 and 5.13).

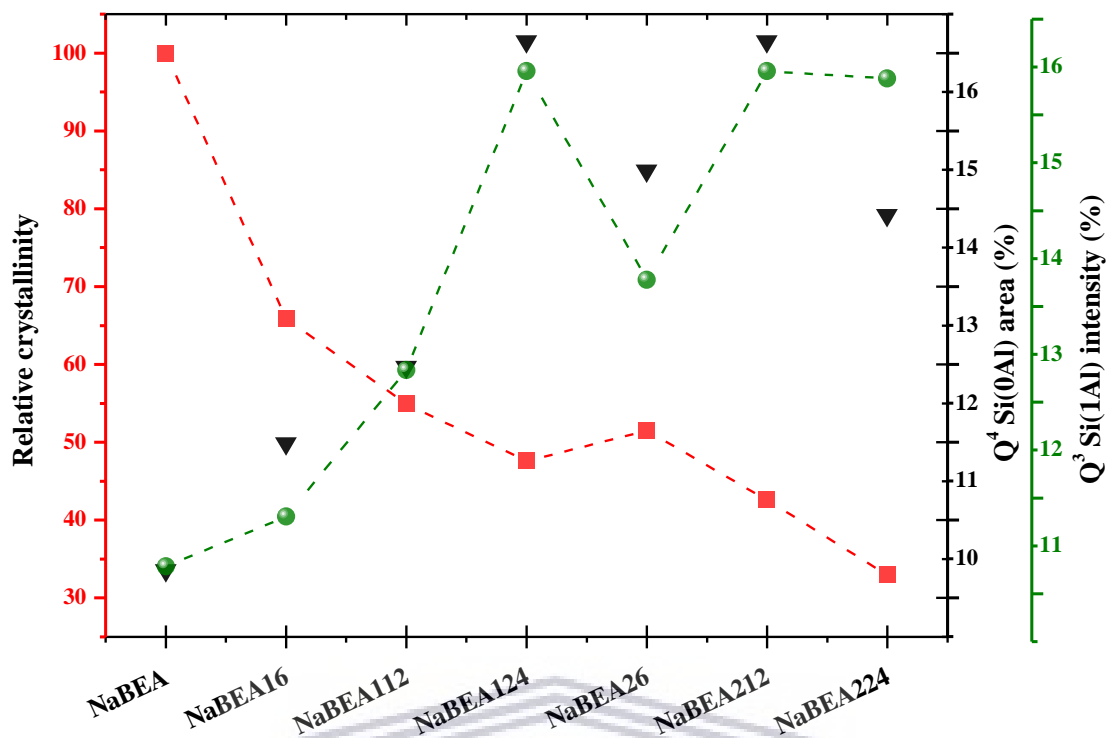


Figure 5.12: Relationship between the relative crystallinity (■) and the ²⁹Si MAS NMR peak intensity (●) and peak area (▼) of the parent and treated NaBEA zeolite at 150 °C (NaBEA16, NaBEA112 and NaBEA124) or 200 °C (NaBEA26, NaBEA212 and NaBEA224) at 6, 12 and 24 h.

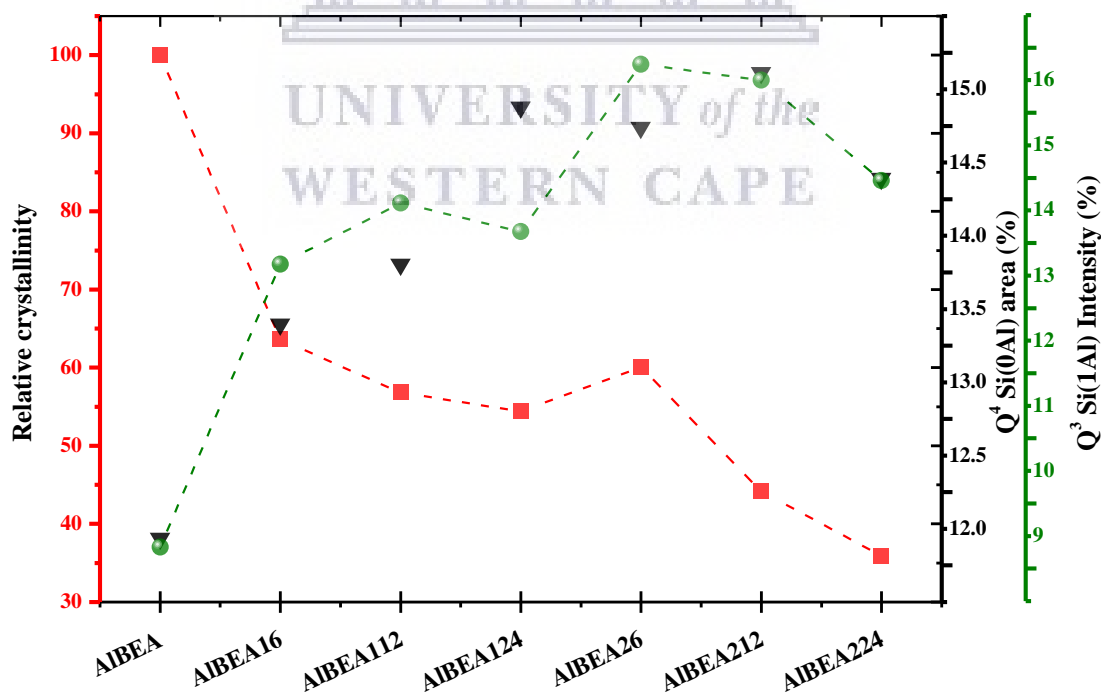


Figure 5.13: Relationship between the relative crystallinity (■) and the ²⁹Si MAS NMR peak intensity (●) and peak area (▼) of the parent and treated AlBEA zeolite at 150 °C (AlBEA16, AlBEA112 and AlBEA124) or 200 °C (AlBEA26, AlBEA212 and AlBEA224) at 6, 12 and 24 h.

Figure 5.12 and 5.13 show that the proportion of peak area and intensity of Q⁴ Si (0Al) and Q³ Si (1Al) in the parent samples (NaBEA and AlBEA) had an impact on the relative crystal structure after exposure to hot liquid treatment. The decrease in relative crystallinity correlated to the increased exposure time and temperature (see Figures 5.1 and 5.2) with an increase in the peak intensity of Q³ Si (1Al) and peak area of Q⁴ Si (0Al) coordination. These results imply that the proportion of Q⁴ Si (0Al) and Q³ Si (1Al) in the framework structure is a major factor affecting the relative stability of the synthesised zeolite in hot liquid phase, as changes in Si coordination species directly influence the Si/Al ratio of the zeolite framework.

²⁷Al MAS NMR spectra of parent NaBEA and AlBEA, as well as the hot liquid treatment of the samples, are shown in Figure 5.14 and 5.15.

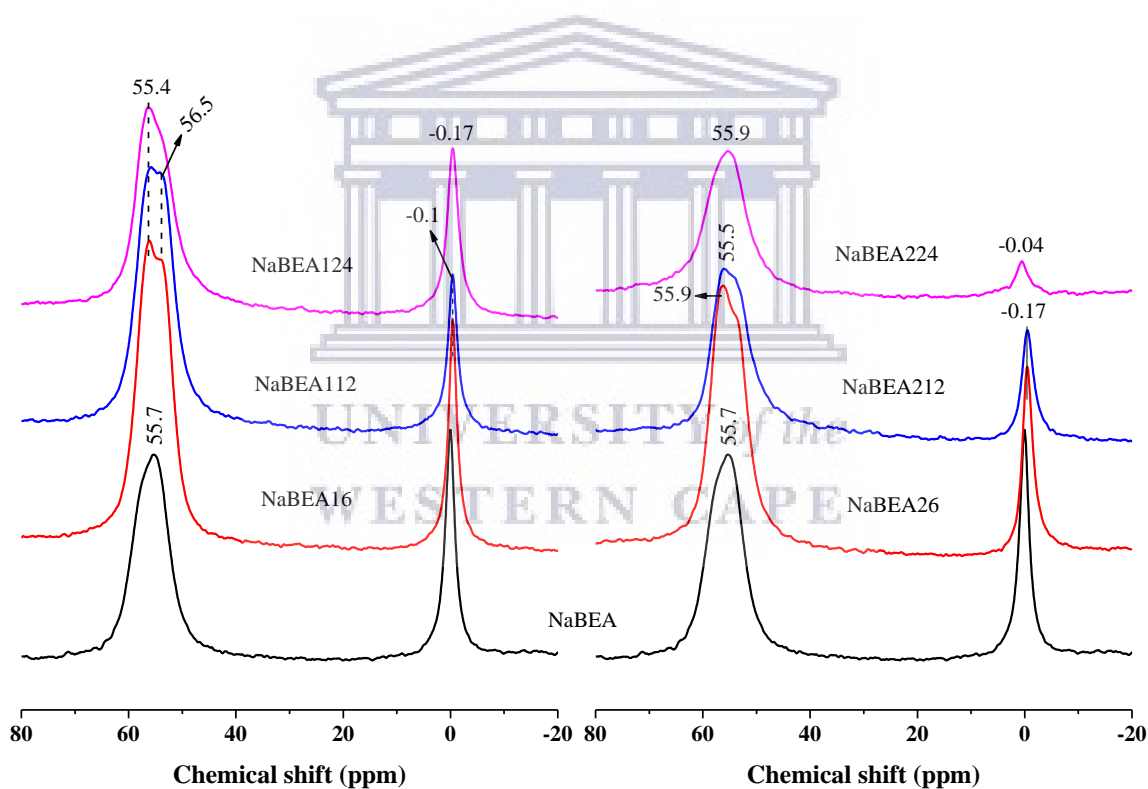


Figure 5.14: ²⁷Al MAS NMR analyses of parent and treated NaBEA zeolite at 150 °C (NaBEA16, NaBEA112 and NaBEA124) or 200 °C (NaBEA26, NaBEA212 and NaBEA224) at 6, 12 and 24 h respectively.

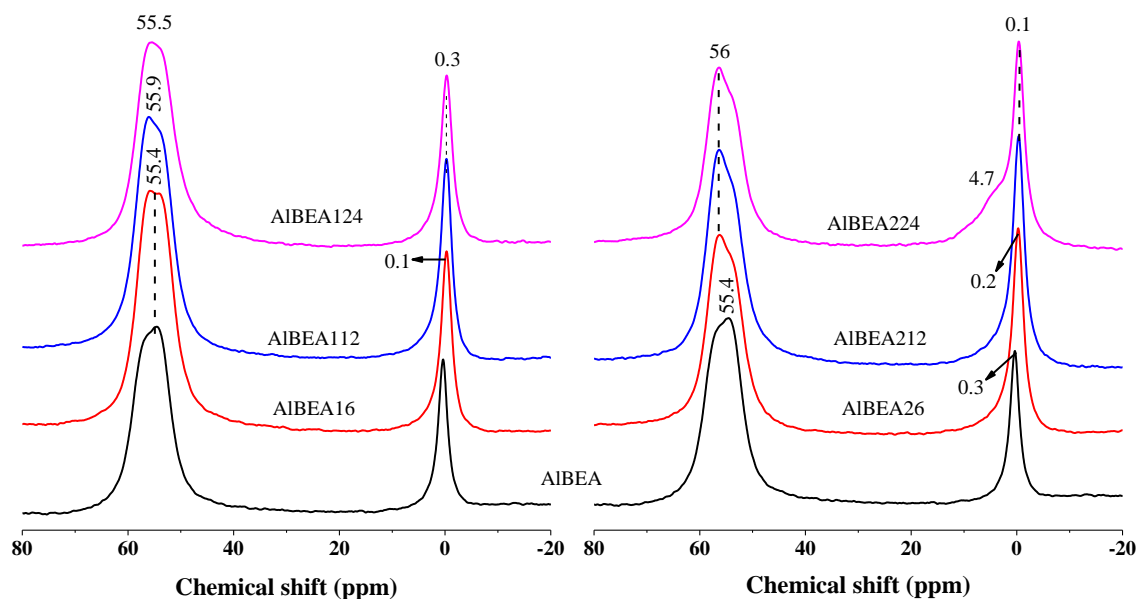


Figure 5.15: ^{27}Al MAS NMR analyses of the parent and treated AIBEA zeolite at 150 °C (AIBEA16, AIBEA112 and AIBEA124) or 200 °C (AIBEA26, AIBEA212 and AIBEA224) at 6, 12 and 24 h respectively.

^{27}Al MAS NMR spectra of the parent and treated samples of NaBEA and AIBEA are shown in Figures 5.14 and 5.15, respectively. Both parent zeolites, NaBEA and AIBEA, show two distinctive Al signals that can be attributed to tetrahedrally coordinated framework aluminium (FAI) or octahedrally coordinated extra framework aluminium (EFAl) located at $\delta = 55.7$ ppm or 0 ppm (see Figure 5.14) and 55.4 ppm or 0.3 ppm (see Figure 5.15), respectively. After the hot liquid treatment, the broad FAI peak at $\delta = 55.7$ and 55.4 ppm of the parent samples shifts downfield to $55.9 \geq \delta \leq 55.9$ ppm (see Figure 5.14 and 5.15). Also, the associated sharp EFAl peak at 0 and 0.3 ppm of the parent samples (NaBEA and AIBEA, respectively) gradually shifted to lower intensity to $0.1 \geq \delta \leq 0.2$ ppm and $-0.04 \geq \delta \leq -0.17$ ppm (see Figure 5.14 and 5.15) upon treatment with hot liquid solution. It is known that the chemical shift is sensitive to Al-O-Si bond and the downfield shift in peak position can be attributed to distortions induced by the hydrolysis of Si-O-Si linkage (Vjunov et al., 2015). This confirmed that the shift in Q^4 Si (0Al) (see Table 5.3) environment is affected by the amount of Al content in the framework structure during water attack.

The calculated fractions of FAI and EFAl of the parent and hot liquid treated NaBEA and AIBEA zeolite was resolved from the integration of ^{27}Al MAS NMR spectra and presented in Table 5.4.

Table 5.4: Detailed ^{27}Al MAS NMR spectra after integration of FAI and EFAl in the parent and hot liquid treated NaBEA and AlBEA zeolite.

	% FAI	% intensity	% EFAl	% intensity
NaBEA	73.03	49.10	26.97	50.90
NaBEA16	79.53	59.84	20.47	40.16
NaBEA112	82.87	50.42	17.13	49.58
NaBEA124	75.86	56.49	24.14	43.51
NaBEA26	79.63	60.44	20.37	39.56
NaBEA212	80.46	62.30	19.54	37.70
NaBEA224	93.47	85.64	6.53	14.36
AlBEA	79.50	57.39	20.50	42.61
AlBEA16	78.84	59.47	21.16	40.53
AlBEA112	76.36	56.57	23.64	43.43
AlBEA124	77.08	56.61	22.92	43.39
AlBEA26	69.41	50.62	30.59	49.38
AlBEA212	66.83	49.75	33.17	50.25
AlBEA224	57.78	50.05	42.22	49.95

^aThe peak intensity was determined from the deconvolution of the respective ^{27}Al MAS NMR

Table 5.4 shows the percentage of FAI and EFAl coordination in relation to their deconvoluted percentage peak intensity. The parent NaBEA and AlBEA zeolite consisted of 73 and 79.5% and 27 and 20.5% of FAI and EFAl coordination, respectively. As exposure time progressed, the FAI of the parent NaBEA zeolite gradually increased while EFAl decreased. At the end of 6 h exposure to hot liquid (150 °C), FAI was 78.5% and EFAl was 20.5%. With prolonged exposure of 12 h, FAI further increases to 83% and EFAl decreased to 17.13%, however, at 24 h it was observed that the FAI coordination decreased to 76% as EFAl coordination increased to 24%. This might be a result of possible desilication (in the case of NaBEA) and realumination (both in the case of AlBEA) taking place at the extra-framework Al coordination. At hot liquid phase conditions of 200 °C, a constant increasing and decreasing trend of FAI coordination: 79.6<80.5<93.5% and EFAl coordination: 20.4>19.5>6.5% was maintained at 6, 12 and 24 h, respectively. At the same time, the intensities of the tetrahedral framework Al increased with decreased intensities in octahedral extraframework Al. The impact can be seen by the framework Si/Al ratio which decreased as a function of hot liquid exposure time and temperature (sample NaBEA).

Sample AlBEA on the other hand, experienced a consistent reduction in tetrahedral coordinated Al from 79.5% AlBEA to 78.8>76.4>77.1% and 69.4>66.8>57.8% for samples

treated at 150 °C (AIBEA16, AIBEA112 and AIBEA124) and 200 °C (AIBEA26, AIBEA212 and AIBEA224) for 6, 12 and 24 h, respectively (see Table 5.4). Consequently, these enhanced the integral fraction of octahedral extra framework Al³⁺ to increase directly in relation to reduced tetrahedral framework Al with prolonged exposure to hot liquid attack (see Table 5.4). Also, the intensities of tetrahedral framework Al decreased as the intensities of the octahedral extraframework Al increased with a decrease in framework Si/Al ratio in the case of treated AIBEA samples (see Table 5.3 and 5.4). Gil et al. (2018), also noticed the increase in the octahedral coordination of BEA zeolite with exposure to hot liquid phase.

The difference in behaviour between NaBEA and AIBEA samples in hot liquid phase can be linked to: i) interactive Al environment, ii) desilication, iii) framework Si/Al ratio. In the case of NaBEA zeolite, as the fraction of octahedral domains decreased, the Al coordination became structurally disordered, thereby exposing Si-O-Si domains to OH attack with prolonged treatment times and increased temperatures (NaBEA224) (Proding et al., 2016; Xiong et al., 2014). In contrast, the integrated tetrahedral Al of the treated AIBEA samples showed a systematic decrease with increased time and temperature (see Table 5.4) and this can be associated with the desilication of the framework Al. This explains the extent of OH attack (hydrolysis) on Si-O-Si sites since Al species form a protective repulsive shield around the neighbouring Si (Al-O-Si) (Groen et al., 2005).

In both cases, the decrease in framework Si/Al ratio (Table 5.3) with prolonged exposure conditions confirm the gradual removal of Si through the attack of Si-O-Si coordination. At the same time, the coherent decrease in tetrahedral Al implies that some tetrahedral framework species are converted to octahedral coordination which then induced the formation of a new resonance around 4.7 ppm. This suggests that the octahedral Al environment enabled the formation of silanol defects in the framework structure of the zeolite by enhancing OH⁻ attack of siloxane bonds (Si-O-Si). Also, the protective layer of Al-O-Si around the Si environments are resistant to hydrolysis but may enhance the OH attack on siloxane bonds (Ravenelle et al., 2010; Jamil et al., 2016).

The formation of defects in the structure of the treated NaBEA and AIBEA zeolite clearly shows that the integrity of the treated samples was compromised at an extended exposure time of 24 h and at high temperatures such as at 200 °C or above. However, there was no structural transformation or total structural collapse under the applied treatment conditions.

5.2.5 Lifetime activity of fly ash based BEA zeolite in hot liquid phase

In this section, the weight loss percentage (see Table 5.3) in relation to the area of the Q⁴ Si(0Al) (see Table 5.4) environment was used to correlate the durability of the treated NaBEA and AlBEA zeolite at different exposure times and temperatures. Figure 5.16 depicts the relationship of weight loss (TGA) and the area of the Q⁴ environment to the stability of NaBEA zeolite in the liquid phase.

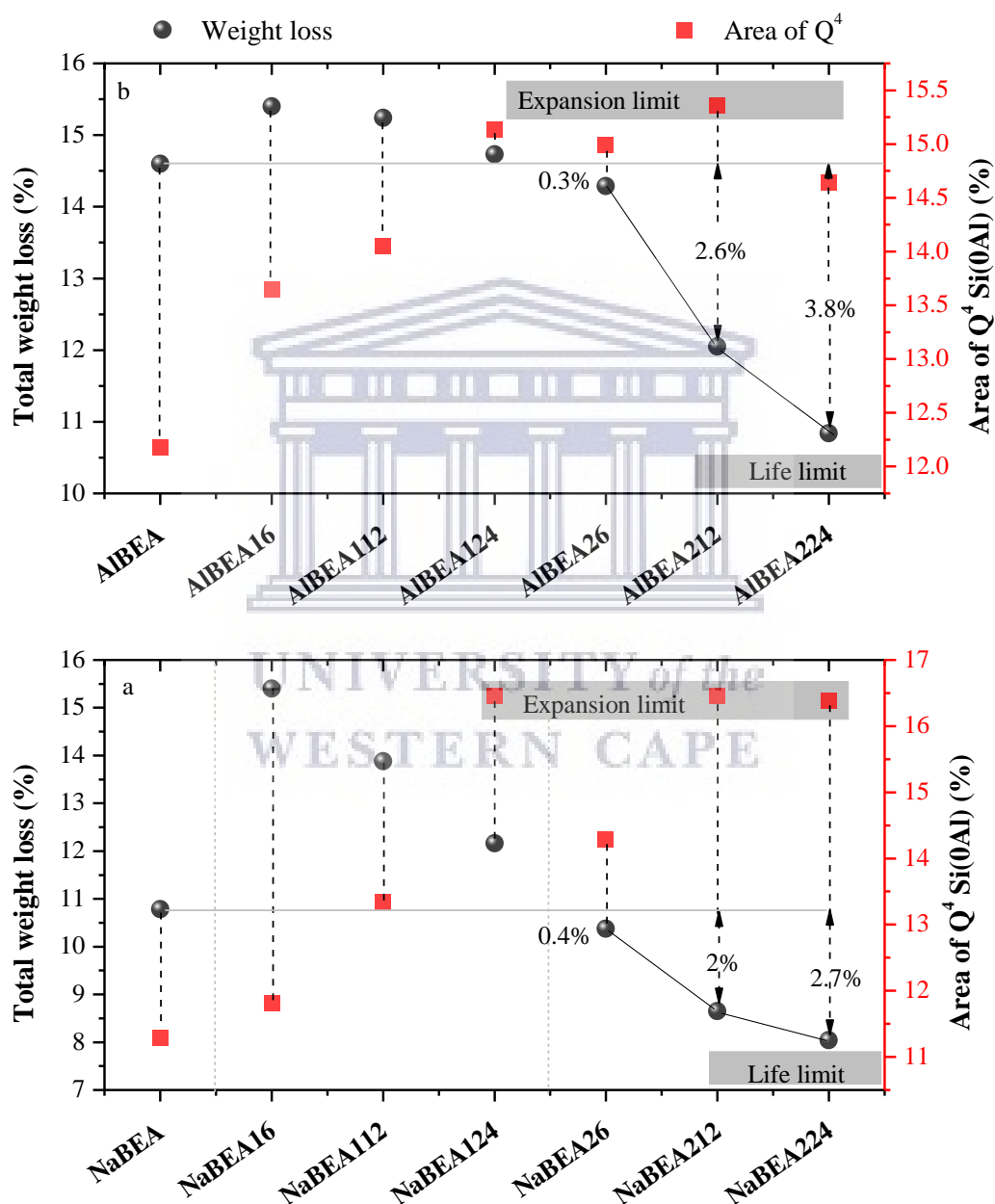


Figure 5.16: Lifetime activity of parent BEA zeolite (a – NaBEA and b - AlBEA) treated in hot liquid phase at different exposure time (6, 12 and 24 h) and temperature (150 and 200 °C).

The stability and area enlargement of the framework structure of the parent NaBEA and AIBEA zeolite treated in hot liquid phase at different treatment times and temperatures is presented in Figure 5.16. Parent NaBEA and AIBEA zeolite exhibited a total weight loss of 10.78 and 14.60% which can be associated with water molecules within the porous structure with a Q^4 Si(OAl) area of 11.29 and 12.18%, respectively. Upon treatment of the parent zeolite, it was observed that the Q^4 Si(OAl) area gradual enlarged to an expansion limit of 16.46 (NaBEA212) and 15.36% (AIBEA212) (Figure 5.16a-b). These can be attributed to the sharp increase in weight loss noticed between the treatment time of 6 and 24 h at 150 °C which then reduced to 10.37 and 14.29% below that of the parent NaBEA and AIBEA zeolite at a treatment time of 6 h at 200 °C, respectively. At this stage, the difference of 0.4 and 0.3% (NaBEA26 and AIBEA26) in the total weight loss after treatment (6 h at 200 °C) of the parent zeolite suggests that the porous structure of the zeolite was under attack. With further increase in treatment time and temperature, the difference in the weight loss increased (2→2.7%, NaBEA212 and NaBEA224; 2.6→3.8%, AIBEA212 and AIBEA224) causing the Q^4 Si(OAl) area to enlarge reaching the highest limit (Figure 5.16a-b). Thus, this challenged the structural stability of the zeolite, thereby exposing the framework to attack in the liquid phase beyond the life limit of 200 °C for 24 h. Hence, the treated BEA zeolites can perform effectively in the liquid phase below this temperature and time which also indicated that regeneration is possible.

5.2.6 Textural properties of the fly ash BEA zeolite in hot liquid phase

The exposure of fly ash based BEA zeolite in hot liquid phase was carried out at 150 and 200 °C for 6, 12 and 24 h, respectively. Different analytical techniques such as XRD, FT-IR, TGA and NMR were used to characterise the treated zeolite. The aforementioned results observed similar behaviour and trends on the treated NaBEA and AIBEA zeolites. Based on this, the present section investigate the surface area, mesopores area, pore volume and pore size distribution of only NaBEA zeolite since their behaviour in hot liquid phase with AIBEA is similar. Figure 5.17 depict the N_2 adsorption-desorption isotherm of the parent and hot treated NaBEA zeolites at different temperature (150 and 200 °C) and time (6, 12 and 24 h).

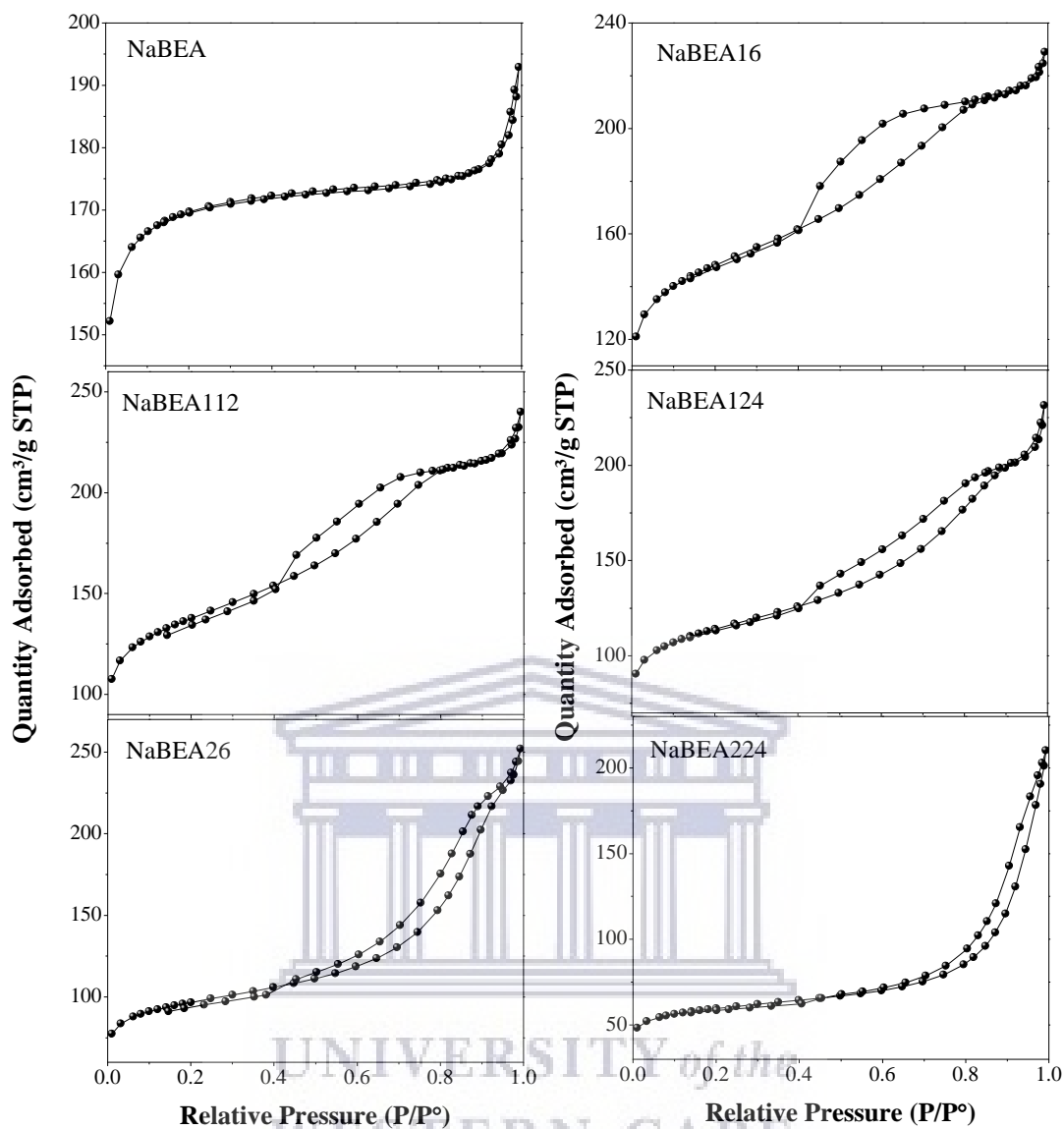


Figure 5.17: N₂ adsorption-desorption isotherms of the parent and treated BEA zeolite at 150 °C (NaBEA16, NaBEA112 and NaBEA124) and 200 °C (NaBEA26 and NaBEA224) at 6 and 24 h, respectively.

Figure 5.17 shows the N₂ adsorption-desorption isotherm of the parent and hot treated NaBEA zeolites. Herein, both the parent and treated NaBEA samples exhibited a type 1 and IV isotherm of the Langmuir adsorption due to the micropore filling in the region of P/P_0 below 0.1 and a capillary condensation in the mesopores within the relative pressure of $0.2 < P/P_0 < 0.4$. The hysteresis loop in the range of $P/P_0 > 0.4$ indicates a well-interconnected mesopores, which enhanced capillary evaporation of adsorbed nitrogen (Thommes et al., 2015; Kim et al., 2014). Moreover, the slit-shaped pores found in the parent BEA zeolite characterise a type H4 hysteresis loop according to IUPAC classification. This is indicative of micropores filling associated with a characteristic type I and II isotherm. After the

treatment of samples NaBEA16, NaBEA112, NaBEA124 and NaBEA26, the hysteresis loop demonstrated type H2b or H3 which shows the creation of large mesopore and pore size distribution (see Figure 5.17). With prolonged treatment, sample BEA224 shows a type H3 or H4 hysteresis loop. This suggest an uptake at the low P/P_0 of micropores filling or large (Thommes et al., 2015). This can be associated to the steady decrease in BET surface area observed after the treatment of NaBEA zeolite in hot liquid. Table 5.5 present the textural properties of the NaBEA zeolite before and after treatment in hot liquid phase at 150 and 200 °C for 6, 12 and 24 h.

Table 5.5: Textural properties of parent and hot liquid treated NaBEA zeolite under different temperature and time.

Sample	S_{BET} (m^2/g)	S_{micro} (m^2/g)	S_{meso} (m^2/g)	V_{tot} (cm^3/g)	V_{micro} (cm^3/g)	V_{meso} (cm^3/g)
NaBEA	670	543	127	0.30	0.20	0.10
NaBEA16	557	385	172	0.35	0.13	0.22
NaBEA112	512	324	187	0.37	0.11	0.26
NaBEA124	425	283	143	0.36	0.09	0.26
NaBEA26	362	242	120	0.39	0.08	0.31
NaBEA224	224	154	71	0.33	0.05	0.27

Not: S_{BET} : BET surface area; S_{micro} : and S_{meso} : micropore and mesopore surface area, V_{tot} : total pore volume, V_{micro} and V_{meso} : micropore and mesopore volume

Table 5.5 present the specific surface area, micropores and mesopores area, micropores and mesopores volume and total pore volume of the parent and treated NaBEA zeolites. The parent NaBEA zeolite shows a surface area of 670 m^2/g and under 150 °C, the treated samples lost 17, 24 and 37% of the BET surface area with exposure time of 6, 12 and 24 h, respectively. Similarly, as the treatment temperature increased to 200 °C the trend was maintained until NaBEA24 sample lost 67% of the total BET surface area after 24 h. It was also observed that the liquid phase treatment led to a decrease in micropores volume. The parent NaBEA zeolite had a micropores volume of 0.20 cm^3/g but after 6 h treatment, the volume reduced to 0.13 cm^3/g which further decreased to 0.11 and 0.09 cm^3/g after 12 and 24 h treatment time, respectively. Moreso, it was observed that with the treatment temperature of 200 °C, the micropores volume of samples NaBEA26 and NaBEA224 significantly reduced to 0.08 and 0.05 cm^3/g . This implies that large mesopores area and pore diameter are generated during the hot liquid treatment of NaBEA zeolite. This is in agreement with the observation as presented in Table 5.5 showing increasing mesopores

area (NaBEA < NaBEA26 < NaBEA112 < NaBEA124) with prolonged treatment time. However, a gradual decrease in mesopores area was noticed under the treatment temperature of 200 °C. Sample NaBEA26 lost about 6 % of the mesopores area after treated for 6 h and a further loss of 44% was observed on NaBEA224 due to prolonged exposure time of 24 h. The impact of hot liquid treated NaBEA zeolite was also found in the gradual increase of the mesopore volume with prolonged exposure time (Table 5.5).

Figure 5.18 depicts the pore size distribution of the parent and treated NaBEA zeolite at different temperature (150 and 200) for 6, 12 and 24 h was obtained using the density functional theory (DFT) method.

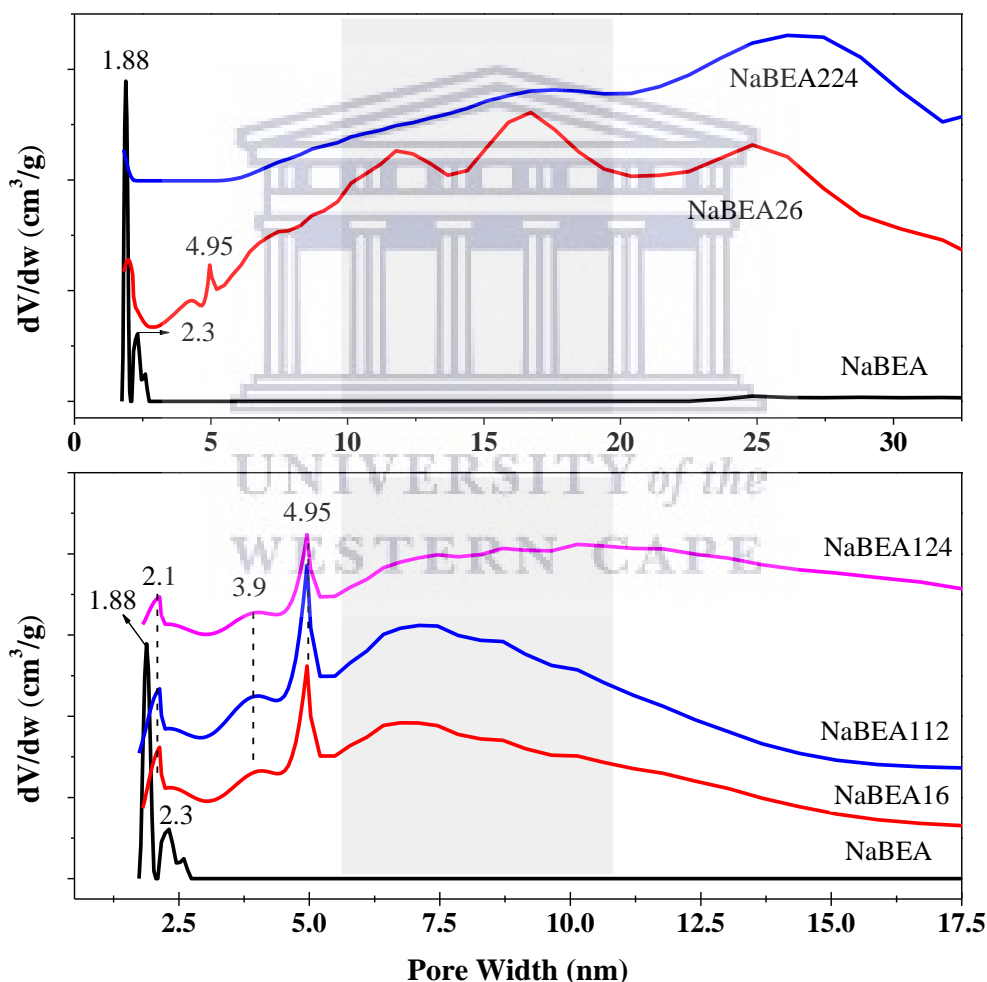


Figure 5.18: DFT pore size distribution plot of the parent and treated NaBEA zeolite at a) 150 °C (NaBEA16, NaBEA112 and NaBEA124) and b) 200 °C (NaBEA26 and NaBEA224) at 6 and 24 h, respectively.

Figure 5.18 presents the pore size distribution of the parent and treated NaBEA zeolite, which was obtained using the DFT method. The parent NaBEA sample showed a major peak at 1.9 and minor at 2.3 nm which corresponds to a typical BEA zeolite (Escola et al., 2018). After 6, 12 and 24 h treatment at 150 °C, a significant change in the pore size distribution was observed (Figure 5.18a). This led to the peak shift to 2.1 nm and the generation of two more peaks centered at 4 and 5 nm as well as a broad distribution between 6 and 12 nm. This observation suggests a shift of the micropores existing in the parent NaBEA zeolite into a larger distribution of mesopores structure in the treated NaBEA zeolites. With increased treatment temperature to 200 °C, the peak at 5 nm was maintained and three broad peaks located between 10 and 30 nm was observed after 6 h (NaBEA26). Under similar condition but different treatment time, 24 h, only a broad distribution between 20 and 35 nm was found in sample NaBEA224.

The pore size distribution clearly proves the gradual disorder of the micropore BEA structure with prolong treatment temperature and time. It is consistent with XRD results showing only less than 35% NaBEA224 zeolite crystallinity was retained after extended exposure (Figure 5.3). The aforementioned observations clearly indicates that as the micropores area of the BEA zeolite gradual shifts into large mesopore area, the mesopore volume increased which enhance structural expansion and eventually led to structural degradation. The enlargement of the Q^4 Si(0Al) area by desilication and the expanded mesopore area, enforced a stretch on the framework structure, thus challenged the crystalline framework integrity and limited lifetime activity of the BEA zeolites.

5.3 Chapter summary

The treatment of NaBEA and AlBEA zeolite in hot liquid reaction demonstrated the potential structural stability of the synthesised fly ash based BEA zeolite in liquid phase applications. As the treatment time and temperature was elevated to 24 h at 200 °C the structural integrity of the zeolite was significantly affected. In this study, it was found that prolong treatment time led to a decrease in surface area and micropore volume while the mesopore volume increased. The desilication of the framework structure elucidated by the various techniques showed the attack of OH causing the hydrolysis of Si-O-Si bonds and the formation of terminal Si-OH group. With these, the tetrahedral framework Al coordination or octahedral extraframework species were directly influenced by the presence

of defects in the BEA structures. In view of this, the crystal structure was susceptible to desilication under the more extreme conditions investigated and the crystal structure was distorted with no evidence of phase transformations observed. It was further noted that prolonged treatment at higher temperature had some effects on the BET surface area, pore volume and pore size distribution which could impact on the zeolite performance. Therefore, under controlled aqueous conditions, coal fly ash-based BEA zeolites offer a stable opportunity for different liquid phase applications at considered reaction conditions not greater than 200 °C for a duration ≤ 24 h.

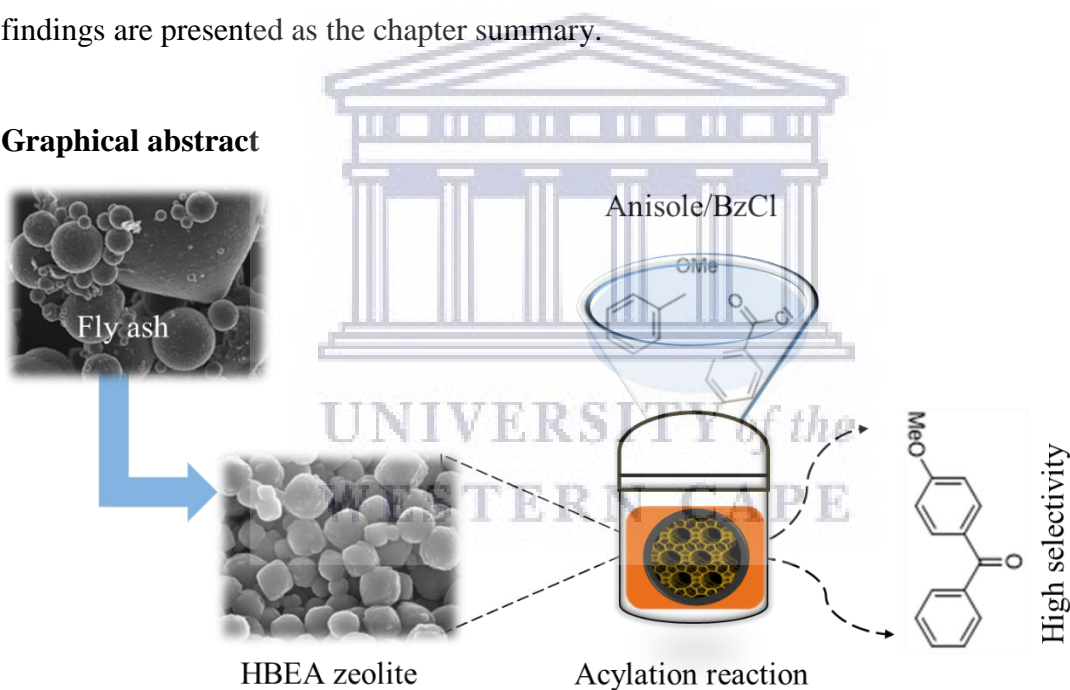


Chapter 6

Acylation of anisole with benzoyl chloride over rapidly synthesised H-BEA zeolite catalyst

In chapter 6, the relationship between the water content in the molar composition and the hydrothermal crystallisation time needed for the rapid production of HBEA zeolite is further explored. The performance of the long and short time order crystallised HBEA zeolite with different crystal size, framework structure, surface area, pore volume and acid site is then investigated through an acylation reaction using anisole with benzoyl chloride over the catalyst. Furthermore, the regeneration and efficiency of the reused catalyst after repeated cycles of reaction runs was also investigated. The outcome was measured using various analytical techniques which are presented and discussed in this chapter. Finally, the major findings are presented as the chapter summary.

Graphical abstract



Highlights

- Shorter hydrothermal crystallisation of HBEA zeolite from fly ash was achieved by reduced molar water fraction
- Rapidly crystallised fly ash HBEA zeolite possesses small particle size, high surface area, high external area and high acid sites.
- Fly ash based HBEA zeolite was highly active in the acylation reaction of anisole with benzoyl chloride

- Large mesopores area, framework Al, large Q⁴ area and strong acid sites of HBEA zeolite enhanced catalytic performance with high conversion rate and selectivity
- High percentage conversion, selectivity and yield is influenced by increased molar ratio of anisole/benzoyl chloride
- The regenerated HBEA zeolites were stable and still possessed high catalytic performance

Abstract

Stable HBEA zeolite with varying crystal size, high surface area and strong acid sites was synthesised from coal fly ash based silica extract via indirect hydrothermal synthesis. The rapid HBEA hydrothermal crystallisation time of 8, 10 and 12 h was a function of reduced molar water fraction in the synthesis composition. The HBEA zeolite prepared from fly ash silica extract had a well-defined spheroidal-shaped morphology contain uniform micro crystallites having different particle sizes of 191.9, 189.7 and 239.2 nm for 8, 10 and 12 h, respectively as found by SEM microscopy. High surface area and microporous area of 702.4 and 632.9 m²/g was a function of shorter hydrothermal time compared to 48 or 72 h synthesised HBEA zeolite with surface areas of 537.5 and 582.2 m²/g. Likewise, the TPD measurement of the fly ash based HBEA zeolites indicate the presence of weak and strong acid sites in the framework structure. The sub-micron crystal sizes with well-defined porosity of HBEA zeolite enhanced diffusion for molecules to access the active acid sites and showed better catalytic conversion and selectivity in acylation reaction of anisole. Also, high conversion, selectivity and yield over HBEA zeolite is associated with framework Al, Q⁴ species, high surface area, high mesoporous area and strong acid sites. It was also observed that with increased anisole/BzCl ratio the conversion of anisole reached 99% with a 98% selectivity of 4-methoxyacetophenone and percentage yield of 97%. Acylation of anisole with benzyl chloride over regenerated HBEA zeolite maintained high conversion and selectivity of 4-methoxyacetophenone after three cycles.

Keywords: HBEA zeolite, crystal size, anisole, benzyl chloride, framework, acylation, conversion, selectivity, yield,

6.0 Introduction

Liquid-phase reactions producing aromatic ketones as one of the prominent intermediates or final products are used to prepare these molecules for their applications as fine chemicals in pharmaceuticals, perfumes, agrochemical (insecticides and plasticisers), textile and food (flavours and dyes) industries. Conventionally, the aromatic ketones have been produced using the Friedel-Crafts acylation, carried out over homogeneous catalysts of Lewis acids (such as AlCl_3 , FeCl_3 , InCl_3 and BF_3) and strong protonic acids (such as concentrated H_2SO_4 , H_3PO_4 , HCl and HNO_3) (Mu et al., 2015; Wang et al., 2017). However, the generation of environmentally corrosive and highly toxic wastes in the process is a major challenge, which makes the recovering and regeneration process of the catalyst difficult (Chen & Ko, 2012). To overcome these challenges, extensive research has been focused on the synthesis of eco-friendly heterogeneous catalysts that have the capacity to be reusable. Such heterogeneous catalysts include: zeolites (or metal based zeolite), clay, Nafion-H and superacids, as well as mesoporous silica-alumina (Mu et al., 2015; Vinu et al., 2005).

Interestingly, the shape selectivity of micro and mesoporous zeolite catalysts significantly prevents the generation of undesired by-products, which is an advantage over other solid catalysts in the Friedel-Crafts process (Salavati-Niasari et al., 2004; Wang et al., 2017). Besides, the characteristic properties of zeolites allow the design of framework structures with efficient performance through the ability to tailor micron to nano sized crystals with Å sized porosity. These changes promote the reduction of the diffusion path due to the microporosity and larger surface area of the zeolite (Ding et al., 2009; Tosheva & Valtchev, 2005). Also, structural tailoring of zeolites can enhance pore size and distribution, thereby inducing hierarchical structure with both micro and mesoporous pore size within the framework. A combination of large surface area, appropriate pore size and pore cavity facilitates easy accessibility of molecules within the framework structure of zeolites (Al-Eid et al., 2019; Verboekend et al., 2016; Zhang & Ostraat, 2016).

More than 235 different structural-types of zeolite have been reported by the International Zeolite Association (<http://www.iza-online.org/>). Among these zeolite-types, significant research has been directed particularly on HBEA, ZSM-5 and HY. Due to the open pore structure of three dimensional 12 membered ring channels and interconnected channels, HBEA zeolite exhibits good catalytic performance in the acylation reaction (Chen et al., 2015; Derouane et al., 2000). The high catalytic activities of HBEA zeolite can also be

attributed to the presence of a high number of defects within the framework structure (Gabrienko et al., 2010). Unfortunately, the preparation of HBEA zeolites using pure synthetic Si and Al precursors involves high manufacturing cost of Si and Al as well as templating agents (Vichaphund et al., 2019). Therefore, there is a need for an alternative, cheap and sustainable source of Si and Al source. Researchers have proposed coal fly ash (CFA) as an inexpensive and recyclable feedstock for the production of both low (A, X, NaP and sodalite) and high silica (ZSM-5 and MOR) zeolites (Missengue et al., 2018; Missengue et al., 2017; Chandrasekar et al., 2008; Halina et al., 2007).

CFA is a by-product of the combustion of coal at coal-fired power plants. South Africa depends majorly on coal for electricity, but generates 36.2 Mt of CFA per annum, with only 5.5% which has been put to use while the rest (94.5%) is disposed in dams and dumpsites (Eskom, 2011). Interestingly, CFA constituents, which are mainly silicon and aluminium are similar to the components forming the framework structures of zeolites (Ameh et al., 2016; Boycheva et al., 2013; Musyoka et al., 2011a). In this regard, the utilisation of CFA as a valuable feedstock material for the synthesis of high silica zeolites such as HBEA zeolite will further enhance the existing remediation techniques that aim at reducing the negative impacts of disposal of coal fly ash in the environment. In this chapter, the influence of reduced water content in the molar composition of the synthesis precursor regime during the synthesis of nano-sized HBEA zeolite at short hydrothermal time was investigated. Also, the relationship between physicochemical properties and catalytic performance of the synthesised HBEA zeolites in Friedel-Crafts acylation was evaluated in relation to the percentage conversion, selectivity and product yield.

6.1 Experimental

The comprehensive experimental protocol for the synthesis and characterised of BEA zeolite products from fly ash-based extracted silica was described and discussed in chapter 3 and 4. In chapter 4, the synthesis of BEA zeolite was optimised and two molar composition (1 Si : 0.017 Al : 0.241 Na : 0.399 TEAOH : 8.980 H₂O or 1 Si : 0.060 Al : 0.241 Na : 0.399 TEAOH : 8.980 H₂O) with Si/Al ratio of 58.8 and 16.7 were achieved as a baseline to study the effect of hydrothermal time on the quality of BEA zeolite. It was apparent in chapter 4 that the hydrothermal time required to obtain high quality BEA zeolite product was achieved in 24 h using the molar composition 1 Si : 0.017 Al : 0.241 Na : 0.399 TEAOH : 8.980 H₂O

(Si/Al ratio = 58.8). Thus, using the best optimised molar composition (Si/Al ratio = 58.8) as the baseline, this chapter presents the influence of reducing the molar water fraction to further reduce the hydrothermal synthesis time for the crystallisation of BEA zeolites. Table 3.5 (chapter 3, section 3.2.4) presents the synthesis conditions and their assigned code names. After screening the synthesised BEA zeolites, the performance of the obtained high quality catalyst (optimised HBEA zeolite) was tested for its activity towards the Friedel-Crafts acylation of anisole with benzoyl chloride as presented in Table 3.7 and described in section 3.2.5.2 (chapter 3).

6.2 Results and discussion

6.2.1 Rapid synthesis of HBEA zeolite: effect of low water content on hydrothermal time

This section discusses the findings that relate to the effect of reduced molar water fraction and the shortest hydrothermal time needed for the complete crystallisation of BEA zeolites. While keeping the synthesis temperature (140 °C) the same, the molar water fraction in the composition: 1 Si : 0.017 Al : 0.241 Na : 0.399 TEAOH : x H₂O, was varied where x is 5.99, 3.99, 2.66 and 1.78 (NaBEA3, NaBEA2, NaBEA1 and NaBEA0, respectively) was investigated under a hydrothermal time of 12 h. After basic characterisation, the condition of $x = 3.99, 2.66$ and 1.78 was kept the same for a hydrothermal time of 8 h (NaBEA84, NaBEA82 and NaBEA80) and 10 h (NaBEA12, NaBEA11 and NaBEA10) at 140 °C (Table 3.5, chapter 3). The following subsections present and discuss the results obtained from the characterisation techniques: XRD, SEM-EDS, FT-IR, TGA, NMR, BET and TPD.

6.2.2 Mineralogical, morphological and structural features

The characterisation of the synthesised products using XRD, SEM-EDS and FT-IR is discussed in this section. Each of the synthesised products were characterised after the removal of the organic template through a calcination process and the resultant products were thus in the detemplated Na-form. Figure 6.1, 6.2 and 6.3 demonstrates the mineralogical phase, structural and morphological features of the synthesised products. Whilst, Table 6.1 and 6.2 present the % crystallinity, % yield, elemental composition, Si/Al_{ex} ratio and crystal size of the products. The crystallinity and percentage yield was estimated using equation 4.5 and 4.4, respectively.

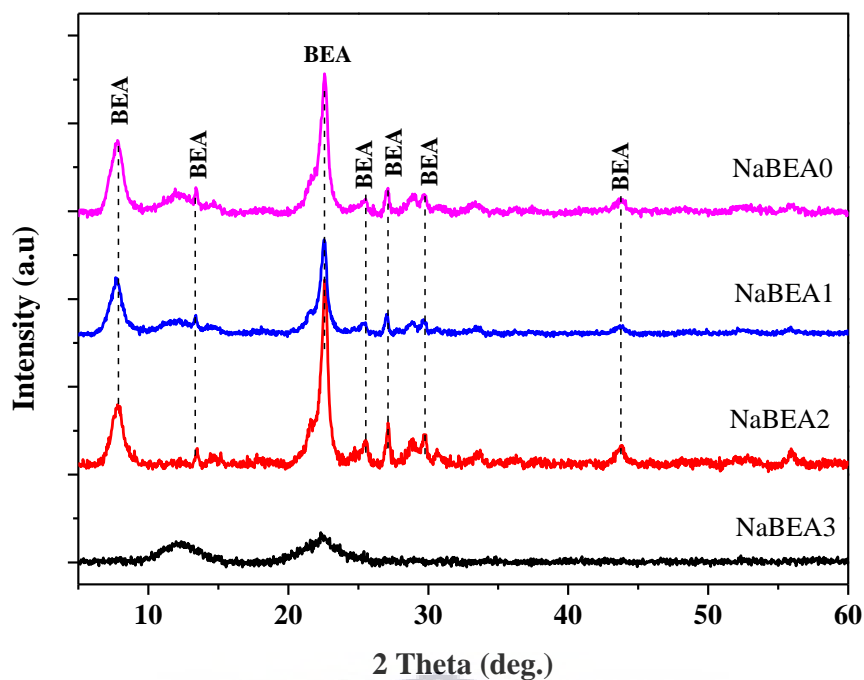


Figure 6.1: XRD patterns showing the effect of molar fraction of water on the crystallisation of BEA zeolites over 12 h using the molar composition (1 Si : 0.017 Al : 0.241 Na : 0.399 TEAOH : x H₂O) with varying water content, $x = 5.99, 3.99, 2.66$ and 1.78 (NaBEA3, NaBEA2, NaBEA1 and NaBEA0, respectively).

Figure 6.1 shows the XRD patterns of the synthesised products from different molar fractions of water under the hydrothermal condition of $140\text{ }^{\circ}\text{C}$ for 12 h. According to the XRD spectra, the two main BEA diffraction peaks were observed when the molar water fraction was 5.99 (NaBEA3). In this case, the broad diffraction peak between 10 and $11^{\circ} 2\theta$ can be associated with the presence of amorphous material while the second peak at $22.5^{\circ} 2\theta$ indicates the initiation of the BEA zeolite phase. As the molar water fraction reduces (from $x = 3.99, 2.66$ and 1.78) in the synthesis composition, the diffraction peaks of a fully crystalline BEA zeolite was noticed (NaBEA2, NaBEA1 and NaBEA0). This further confirmed that low molar water fraction (between 3.99 and 1.78) enhanced the complete formation of pure phase BEA zeolite under the applied conditions and limited the incorporation of amorphous material into the crystalline phase. This is in agreement with the findings in chapter 4 (section 4.4.1) and the studies conducted by Manrique et al. (2016) and Gabrienko et al., (2010) to prepare BEA zeolite produced from pure chemicals.

The intensity of the characteristic diffraction peak at 7.7 and $22.5\text{ }2\theta$ of the NaBEA3 zeolites structures increased with reduced molar water fraction to 3.99 (NaBEA2). However, as the molar water fraction decreased further to 2.66 (NaBEA1) the peak intensity decreased while

at 1.78 molar water fraction (NaBEA0), the diffraction peak intensity increased (Figure 6.1). The diffraction peak intensity at 7.7 and $22.5^\circ 2\theta$ can be related to the relative percentage crystallinity. Using equation 4.5 and 4.6 (see chapter 4, section 4.4), the crystallinity and yield of the synthesised products was estimated as presented in Table 6.1.

Table 6.1: Comparison of the crystallinity, crystal size and yield of the synthesised products.

Samples	Crystallinity (%)	Yield (%)
NaBEA0	99.4	20.8
NaBEA1	66.3	27.0
NaBEA2	100	27.1
NaBEA3	37.4	29.9

In Table 6.1, it was observed that the sample NaBEA2 (higher peak intensity) with 100% relative crystallinity was achieved using 3.99 molar water fraction. Interestingly, with the 1.78 molar water fraction, the relative percentage crystallinity of sample NaBEA0 was 99.4%. The slight reduction in crystallinity could be associated with the presence of some amorphous phase as indicated by the hump between 10 and $11^\circ 2\theta$ in NaBEA1 and NaBEA0 as shown in Figure 6.1. To further study the effect of molar water fraction on the synthesis of fly ash based BEA zeolite, FTIR analysis was carried out as presented in Figure 6.2.

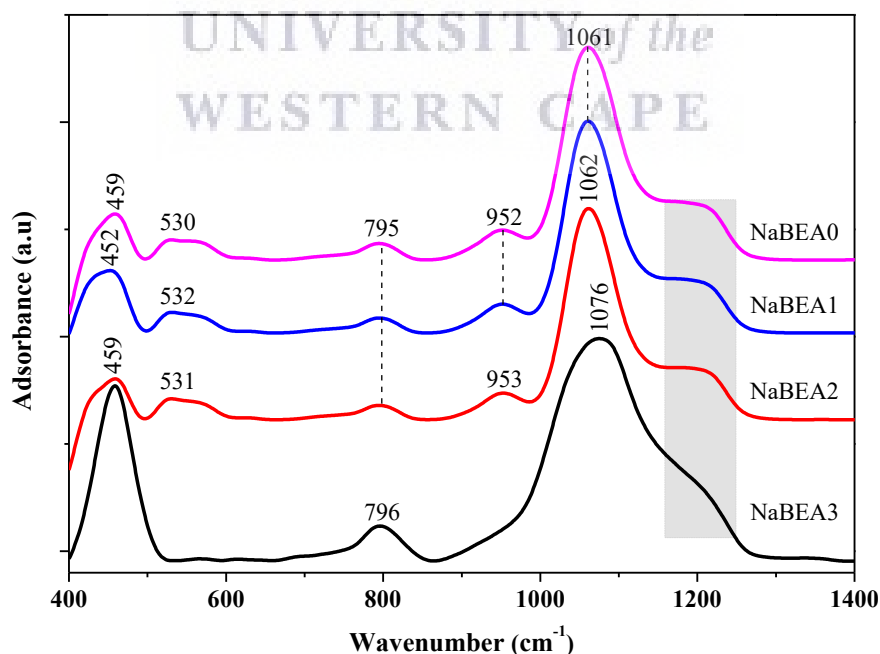


Figure 6.2: FTIR patterns showing the effect of molar fraction of water on the BEA zeolites structure over 12 h using the molar composition (1 Si : 0.017 Al : 0.241 Na : 0.399 TEOH : x H₂O) with varying water content, $x = 5.99, 3.99, 2.66$ and 1.78 (NaBEA3, NaBEA2, NaBEA1 and NaBEA0, respectively).

In the FTIR spectra presented in Figure 6.2, NaBEA3 exhibited three adsorption bands at 459, 796 and 1076 cm^{-1} attributed to bending vibration, symmetrical stretch and asymmetrical stretching vibrations indicating the presence of siloxane structure. The peak at 459 cm^{-1} ascribed to the tetrahedral Si–O bending mode, could indicate the monomeric and dimeric silicate species in a predominant amorphous phase as confirmed by the XRD spectra in Figure 6.1. After decreasing the molar water fraction to 3.99, 2.66 and 1.78 the tetrahedral band at 452 and 459 cm^{-1} was retained. However, a new broad distinct vibration band between 530 and 563 cm^{-1} assigned to the asymmetric stretching vibration of the double-five or six ring was observed (Figure 6.2). Furthermore, the vibrational band at 796 cm^{-1} that was attributed to the O-T-O (T = Si or Al) symmetric stretching vibration and internal tetrahedral symmetrical stretching of the external linkage, shifted to 795 cm^{-1} (Zhang et al., 2017). Moreover, a new vibrational band at 952 and 953 cm^{-1} that is associated with terminal SiO^- groups was formed. According to Zhang et al. (2017) the absorption bands of NaBEA2, NaBEA1 and NaBEA0 at 530 and 563 cm^{-1} are the characteristic peaks belonging to the BEA zeolite structure. Kantam et al. (2006), reported that the minor vibration band at around 952 and 953 cm^{-1} can be attributed to the terminal SiO^- groups on the external surface of the zeolite due to the formation of small crystallites. Lastly, the absence of the asymmetric stretching vibration of the double-five or six ring confirm that NaBEA3 sample is mainly an amorphous material as observed by the XRD spectra in Figure 6.1.

Overall, the bands at 1076 cm^{-1} related to the asymmetric vibrating of T–O–T (T = Si, Al) group, shifted to a lower wavenumber of 1062 and 1063 cm^{-1} as the molar water fraction decreased. Also, the intensity of the shoulder peak that appears at around 1173 cm^{-1} (NaBEA3) became more prominent with an increased molar water fraction (NaBEA2, NaBEA1 and NaBEA0) (Figure 6.2). Tao and Kanoh, (2006) reported that the peak between 1062 and 1063 cm^{-1} and their shoulder bands are associated with the internal and external asymmetric stretch of the zeolite structure. Since the major finger print of a typical BEA zeolite at 452 to 459, 530 to 563 and 795 cm^{-1} were present and prominent in samples NaBEA2, NaBEA1 and NaBEA0, this complimented the XRD spectra (Figure 6.1) showing high purity BEA zeolite can be synthesised from CFA with reduced molar water fraction. To this end, Figure 6.3 presents the effect of molar water fraction on the morphology of the synthesised products under the hydrothermal treatment of 140 °C for 12 h.

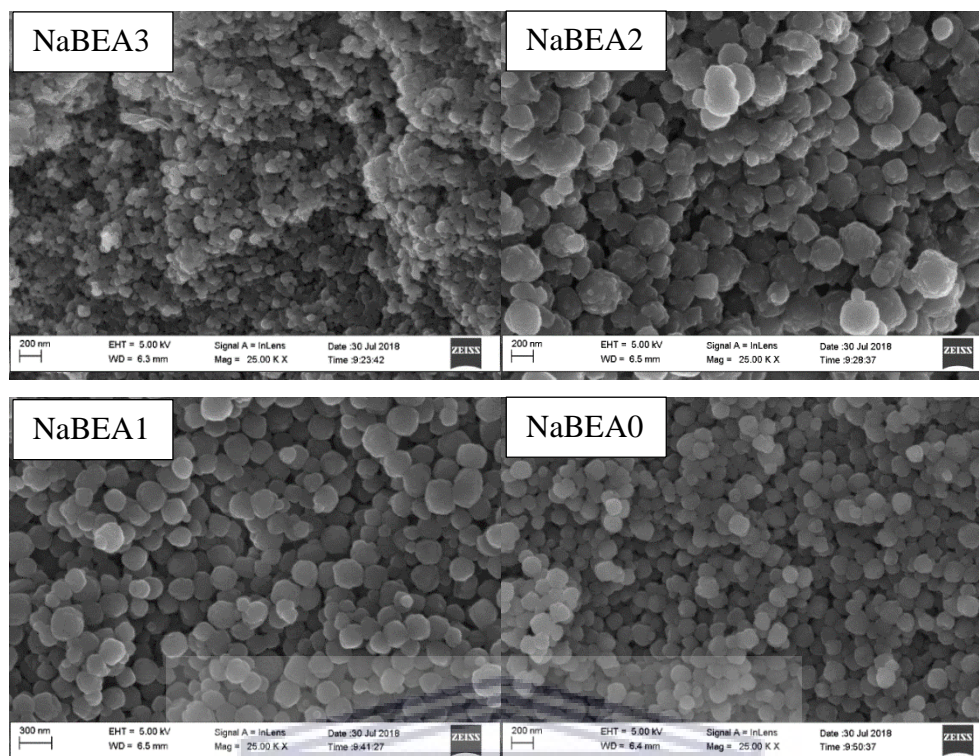


Figure 6.3: SEM morphology showing the effect of molar fraction of water on the crystallisation of BEA zeolites over 12 h using the molar composition composition (1 Si : 0.017 Al : 0.241 Na : 0.399 TEAOH : x H₂O) with varying water content, $x = 5.99, 3.99, 2.66$ and 1.78 (NaBEA3, NaBEA2, NaBEA1 and NaBEA0, respectively).

The SEM images presented in Figure 6.3 clearly show the influence of varied molar water fraction on the morphology of the synthesised BEA zeolite at 140 °C for 12 h. At the molar water fraction of 5.99, a dense small nano crystal morphology with crystal size > 40 nm (NaBEA3) was observed. This can be related to the XRD result in Figure 6.1 which clearly indicated the presence of amorphous material remaining in the synthesised NaBEA3 product. However, as the molar water fraction gradually reduces from 3.99 to 1.78, a well-defined spheroidal-shaped morphology of BEA zeolite structure was formed. High molar water fraction in the synthesis mixture hindered the crystallisation and morphological formation of pure BEA zeolite structure. This is in agreement with the previous observations in chapter 4, section 4.4.1. To further understand the resultant morphological changes in the prepared samples, ImageJ software was used to estimate the crystal sizes.

Table 6.2 shows the elemental composition quantification, Si/Al ratio and crystal size of the synthesised products using SEM-EDS analysis.

Table 6.2: Elemental composition and Si/Al ratio of the synthesised products using SEM-EDS.

Element	O	Na	Al	Si	K	Si/Al _{ex} Ratio	Crystal size (nm)
NaBEA0	56.4	3.7	1.4	38.1	0.4	26	200.2
NaBEA1	58.2		1.4	40.4		30	160.7
NaBEA2	63.4	0.9	1.5	34.1	0.2	23	216.9
NaBEA3	67.8	0.9	1.3	29.9	0.1	23	39.0

Note: Si/Al_{ex} were calculated from the elemental quantification by the SEM-EDS analysis on 7 different spot.

The elemental composition as presented in Table 6.2 noticeably indicates that oxygen, silicon and aluminium together with charge balancing cations of sodium or potassium are the main constituents as is usual in a typical framework structure of the synthesised zeolites. These results further corroborate that other metals from the fly ash were not incorporated into the structure of the BEA zeolites (see Table 4.3). Herein, the Si/Al ratio of the well-crystalline BEA zeolites fell within the range of 23 and 30 with crystal size ranging from 160 to 217 nm (Table 6.2). The Si/Al ratio of the crystalline BEA zeolite obtained was in agreement with previous studies using commercial chemical feedstock that were conducted by Martínez-Franco et al. (2016) and Mintova et al. (2006). Figure 6.4 compared percentage crystallinity, crystal size and percentage yield of the synthesised products.

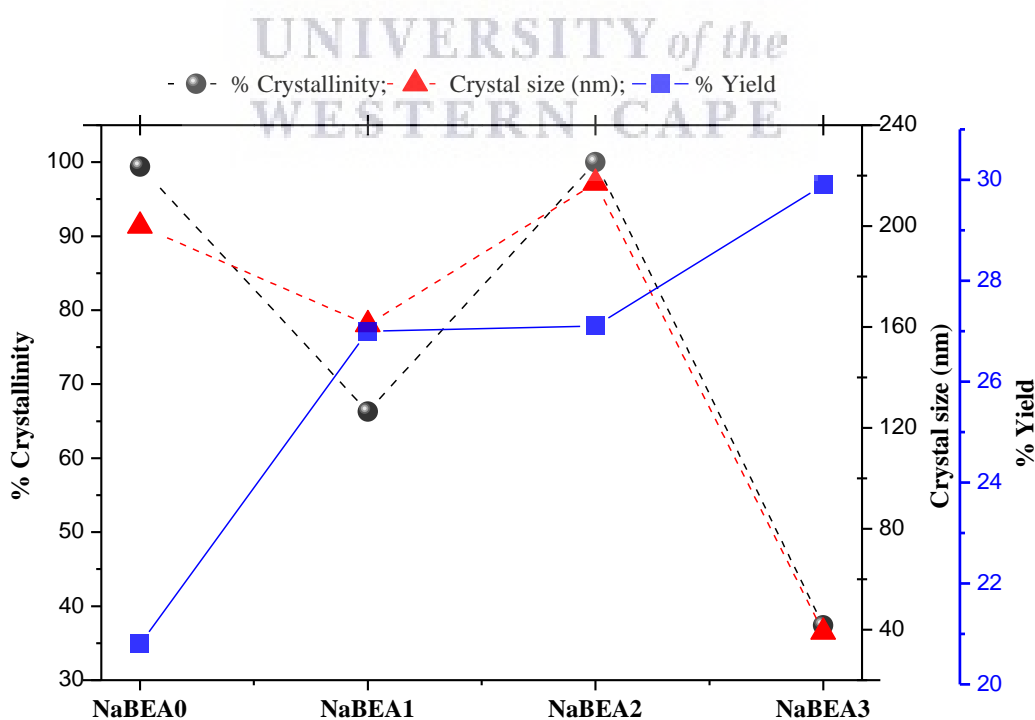


Figure 6.4: Relationship between crystallinity, crystal size and percentage yield of the synthesised products at 140 °C for 12 h.

Figure 6.4 relates the percentage crystallinity, crystal size and percentage yield of the zeolite products. The increasing percentage crystallinity of the synthesised BEA zeolite: 37.4<66.3<99.4<100% can be linked to the continued growth of the zeolite crystal size from 39<160<200<216 nm (NaBEA3, NaBEA1, NaBEA0 and NaBEA2, respectively). It was noticed that the percentage yield decreased with reduced molar water fraction of the synthesis mixtures (Figure 6.4 and Table 6.1). However, the highest recovered yield for sample NaBEA3 contained amorphous materials as confirmed by XRD, FTIR and SEM in Figure 6.1, 6.2 and 6.3. Hence, the generally low percentage yield may be due to the amount of unreacted silica and alumina species removed in the supernatant solution after the crystallisation process. Thus, the lower yield could be related to the reassembling process of the monomers and dimers species which may be due to the dissolution of grown crystals (Al-Eid et al., 2019). In the high water environment, the resultant product was mixed with unreacted amorphous materials which could not be separated, thereby increasing the yield. It has been previously reported in chapter 4 that higher H₂O/SiO₂ ratio resulted in the co-crystallisation of amorphous materials rather than a pure phase BEA zeolite. Moreover, the increase in molar water fraction diluted the concentration of primary aluminium and silicon species and this might hinder the processes of induction and cause slow nucleation (Manrique et al., 2016; Gabrienko et al., 2010).

The sample NaBEA2 with high crystallinity and yield was considered to be the best product BEA zeolite under the synthesis condition of H₂O/Si ratio 3.99, at 140 °C for 12 h. Hence, this molar composition was used further whilst varying H₂O/Si ratio composition, 3.99, 2.66 and 1.78 to study the effect of reduced time (8 and 10 h) on the synthesis of BEA zeolite as described in chapter 3, Table 3.5.

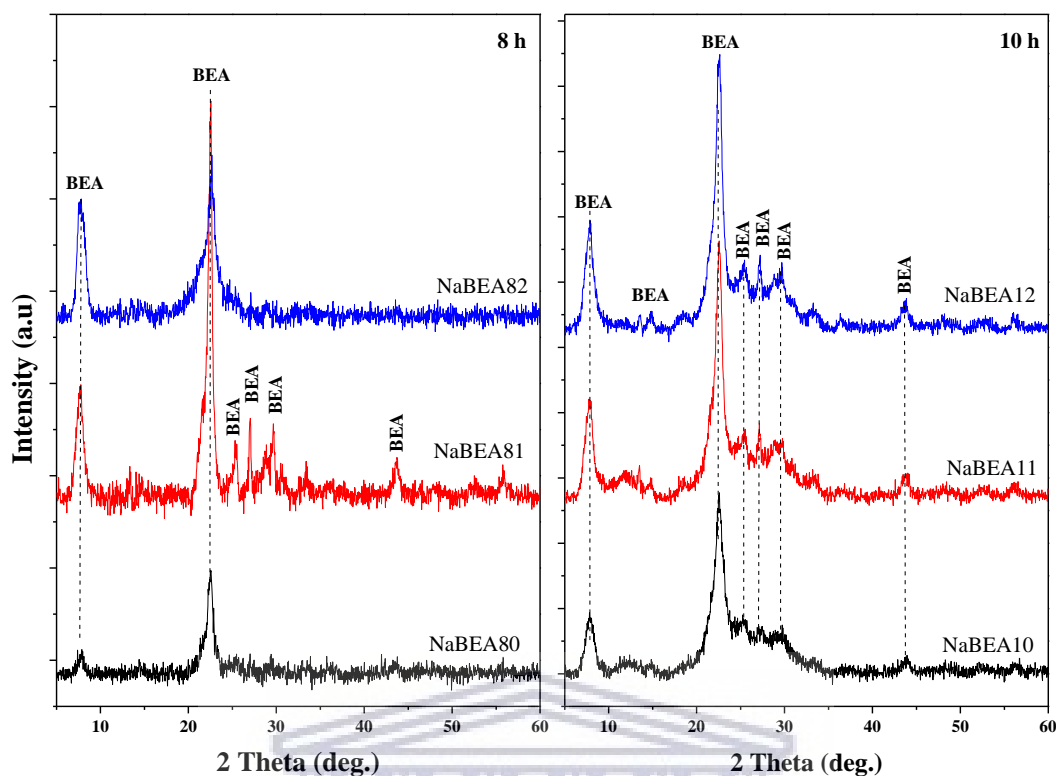


Figure 6.5: XRD patterns showing the effect of molar fraction of water on the crystallisation of BEA zeolites using the molar composition (1 Si : 0.017 Al : 0.241 Na : 0.399 TEAOH : x H₂O) with varying water content, $x = 3.99, 2.66$ and 1.78 for 8 h (NaBEA1², NaBEA11 and NaBEA10) and 10 h (NaBEA82, NaBEA81 and NaBEA80) at 140 °C, respectively.

The XRD diffractogram in Figure 6.5 shows the influence of molar water fraction on the BEA zeolite structures at different synthesis times of 8 and 10 h at 140 °C, respectively. After 8 h hydrothermal synthesis only the sample with molar water fraction of 2.66 (NaBEA81) showed all the characteristic diffraction peaks of BEA zeolite at 7.7, 13.4, 22.4, 27.1, 28.7, 29.6 and 43.4°. It was found that the peak intensity at 7.7 and 22.4° decreased with molar water fraction of 3.99 and 1.78. The associated BEA zeolite peaks at 13.4, 27.1, 28.7 and 43.4° thus gradually disappeared with a decrease or increase in the molar water fraction (NaBEA80 and NaBEA82, respectively) (Figure 6.5-8 h). This indicated that the molar water fraction at 2.66 is the boundary condition for the synthesis of BEA zeolite at 140 °C for 8 h. On the other hand, the diffraction patterns of 10 h samples, NaBEA10, NaBEA11 and NaBEA12 corresponded perfectly to a typical BEA zeolite structure (see Figure 6.5-10 h) as reported in the Database of Zeolite Structure, (<http://www.iza-structure.org/databases/>). The results of the collected diffraction peaks indicate that a pure phase BEA zeolite can be synthesised from low molar water fraction of 1.78 at a reduced synthesis time of 8 or 10 h with some residual amorphous phase. According to Manrique et

al. (2016) and Gabrienko et al. (2010), the reduction in molar water fraction promotes the supersaturation of the reaction species in the synthesis mixture which enhances nuclei formation and allows quick crystal growth.

Interestingly, upon changing the molar water fraction, the diffraction intensity of the characteristic XRD peaks for Na-form BEA zeolite either increased or decreased which affected the crystalline structure of the BEA zeolites (Figure 6.5). In order to validate the results, the relative crystallinity and percentage yield (see equation 4.6) were determined as presented in Table 6.3.

Table 6.3: Comparison of the crystallinity, crystal size and yield of the synthesised products.

Synthesis time	Samples	Crystallinity (%)	Yield (%)
8 h	NaBEA80	13	36.4
	NaBEA81	60	31.7
	NaBEA82	58	32.5
10 h	NaBEA10	86	36.0
	NaBEA11	96	32.6
	NaBEA12	100	32.9

The increased percentage crystallinity of the BEA zeolites as presented in Table 6.3, can be related to the increased diffraction peak area at 7.7 and 22.4° (Figure 6.5). In the case of 8 h hydrothermal treatment, as the molar water fraction decreased, the relative crystallinity also increased from 58 to 60% (NaBEA82<NaBEA81) but then reduced by 47% with a further decreased in the water fraction NaBEA80. Whereas, at 10 h hydrothermal treatment the percentage crystallinity decreased with a reduced molar water fraction from 100 to 86% (NaBEA10<NaBEA11<NaBEA12) (see Table 6.3). When the molar water fraction decreased from 3.99 to 2.66, the percentage yield remained almost the same 32≈33% while the lowest molar water fraction (1.78) had high recovered yield of 36% (NaBEA80 and NaBEA10). This may be due to the presence of some residual amorphous phase and the disappearance of the characteristic peaks of BEA zeolite in samples (see Figure 6.5). Zhu et al. (2017) observed that the percentage yield decreased gradually with increased H₂O/SiO₂ ratio of the synthesis mixture. This clearly supported the observation that at the molar water fraction of 2.66 and 3.99, most reacting species of silicon and alumina are directly incorporated into the framework structure of the zeolite which promotes higher formation and yield of BEA zeolites. Also, the crystallinity decreased gradually with the decreased

molar water fraction, indicating that water in the synthesis composition affected the crystallisation of BEA zeolite but trends were not consistent. The structure of the synthesised products were further characterised using the FTIR analysis and presented in Figure 6.6.

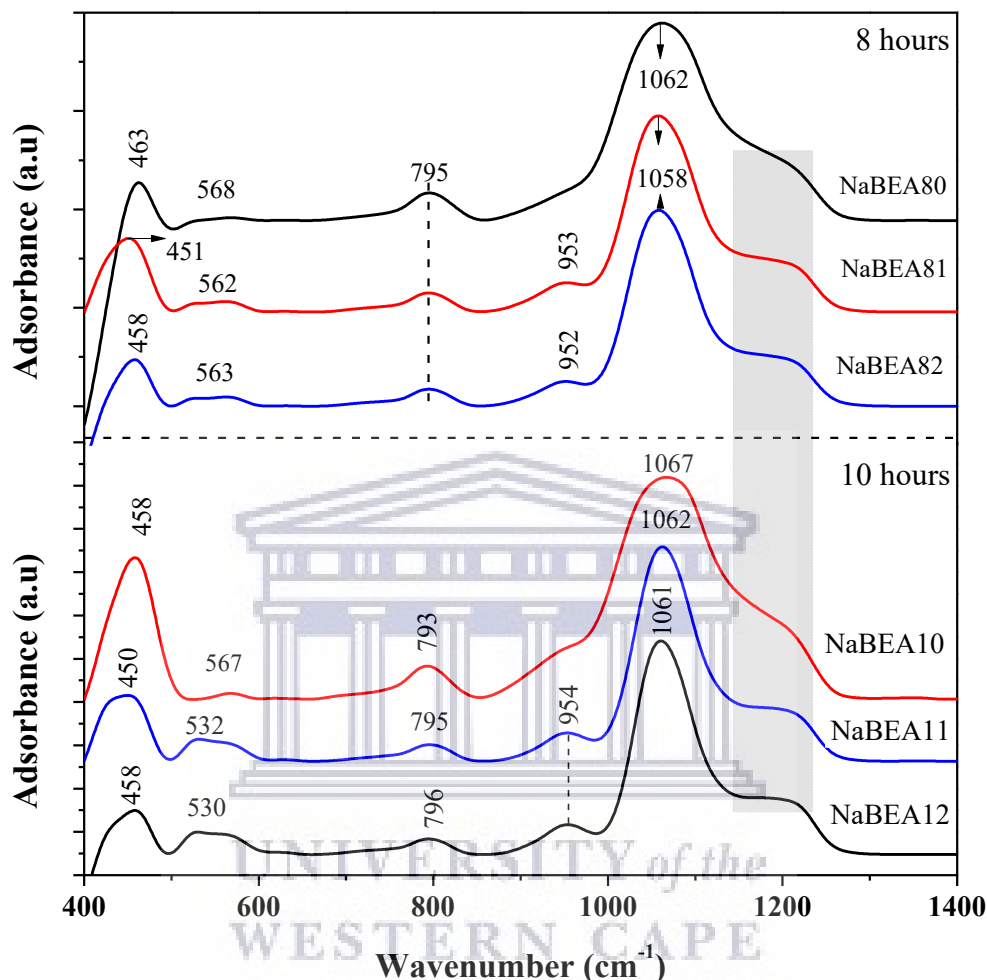


Figure 6.6: FTIR patterns showing the effect of molar fraction water on the crystallisation of BEA zeolites using the molar composition (1 Si : 0.017 Al : 0.241 Na : 0.399 TEAOH : x H₂O) with varying water content, $x = 3.99, 2.66$ and 1.78 for 8 (NaBEA12, NaBEA11 and NaBEA10) and 10 h (NaBEA82, NaBEA81 and NaBEA80) at 140 °C, respectively.

The FTIR spectra of the synthesised zeolitic products were presented in Figure 6.6. Most of the prepared products exhibited the major BEA zeolite characteristic peaks of bending, symmetrical stretch and asymmetrical stretching vibrations. Some of the peaks experienced a gradual shift to either higher or lower wavenumber due to decreased molar water fraction or as the synthesis time changed. Under the hydrothermal treatment of the synthesis mixture with molar water fraction of 1.78 (NaBEA80), only four bands at 463, 568, 795 and 1062 cm^{-1} were observed. As the molar water fraction decreased to 2.66 and 3.99, all the related peaks belonging to a typical BEA zeolite structure were observed in sample NaBEA81 and

NaBEA82, respectively (Figure 6.6-8 h). At 10 h hydrothermal synthesis time the five bands of the bending vibration ($450 - 458 \text{ cm}^{-1}$ and 954 cm^{-1}), the asymmetric stretching ($530 - 567 \text{ cm}^{-1}$ and $1061 - 1067 \text{ cm}^{-1}$) and the symmetric stretching ($793 - 796 \text{ cm}^{-1}$) were the distinct peaks present in the synthesised NaBEA10, NaBEA11 and NaBEA12 zeolite (Figure 6.6-10 h). Although, as the molar water fraction reduced to 1.78, the peak intensity at 954 cm^{-1} significantly decreased (NaBEA10). This clearly confirmed that at the molar water fraction of 2.66 and 3.99 the synthesised NaBEA81 and NaBEA2 predominantly maintain the characteristic peaks belonging to BEA zeolite with high intensity. This is in agreement with the observation of the XRD spectra as presented in Figure 6.5. Also, the presence of band between 952 and 954 cm^{-1} indicates the formation of small monomeric or dimeric crystallites of a crystalline material. Prolonging the hydrothermal time to 10 h, shows that the intensity of the BEA zeolite peaks increased, but since the characteristic peaks were visible in 8 h crystallised samples (NaBEA80, NaBEA81 and NaBEA82) this indicated that the crystallisation process of BEA zeolite can be completed within a shorter time. Tian et al. (2013), related the decrease in wavenumber and intensity of the characteristic peak of BEA zeolite to its decreased crystallinity. The asymmetric vibrating of T–O–T (T = Si, Al) group between 1058 and 1067 cm^{-1} and the shoulder peaks were observed in the BEA zeolite.

The morphological structure of the synthesised BEA zeolite was characterised using SEM analysis as described in chapter 3. Figure 6.7 presents the morphology of the synthesised products under varied molar water fraction of the synthesis mixture at hydrothermal temperature of $140 \text{ }^\circ\text{C}$ for 8 or 10 h as detailed in section 3.2.4.

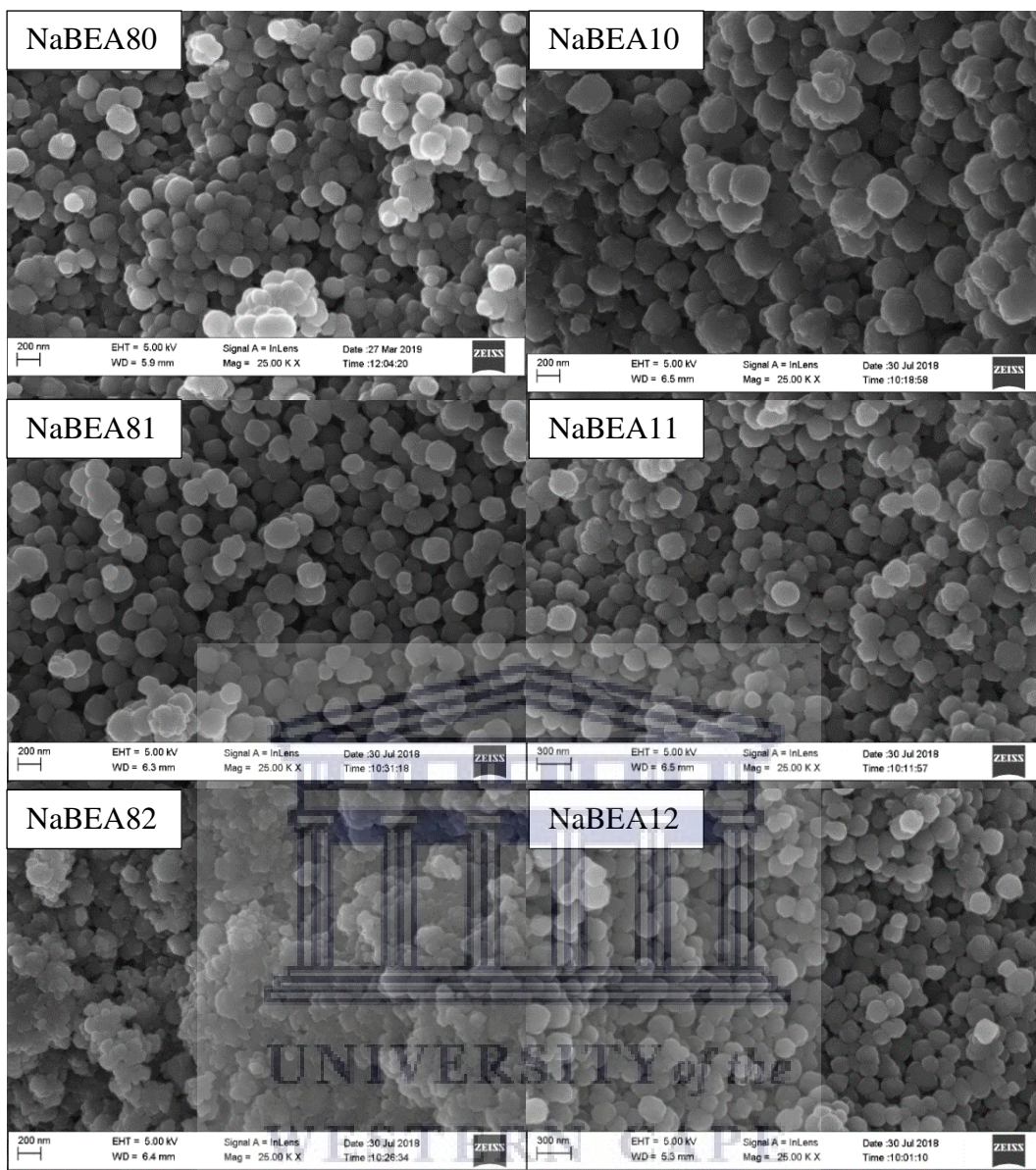


Figure 6.7: SEM morphology showing the effect of molar fraction of water on the crystallisation of BEA zeolites using the molar composition (1 Si : 0.017 Al : 0.241 Na : 0.399 TEOH : x H₂O) with varying water content, $x = 3.99, 2.66$ and 1.78 for 8 (NaBEA12, NaBEA11 and NaBEA82) and 10 h (NaBEA82, NaBEA81 and NaBEA80) at 140 °C, respectively.

The SEM micrographs in Figure 6.7 show the morphological features of the synthesised zeolites obtained from different molar composition with varied molar water fraction at 8 or 10 h. It was observed that most of the synthesised crystals showed a spheroidal-shape associated with BEA zeolite structure. On the contrary, a smaller amorphous particle was observed in sample NaBEA82. Such morphology of BEA zeolite was also observed by Huang et al. (2017). These micrographs confirmed that fully crystalline BEA zeolite was achieved in the synthesis mixture with H₂O/Si ratio between 1.78, 2.66 and 3.99. Thus, low molar water fraction of the precursor gel allowed mobility and rapid interaction between

reacting species resulting in faster crystallisation of BEA zeolite crystal within a shorter hydrothermal time. Table 6.4 present the elemental composition, Si/Al ratio and crystal size of the synthesised BEA zeolites.

Table 6.4: Elemental composition and crystal size of the synthesised products using SEM-EDS.

Synthesis time	Element	O	Na	Al	Si	K	Si/Al _{ex} Ratio	Crystal size (nm)
8 h	NaBEA80	59.7	1.1	1.5	37.6	0.2	26	137.6
	NaBEA81	63.6	-	1.4	35	-	24	166.3
	NaBEA82	62.6	2.2	1.5	33.2	0.6	22	51.3
10 h	NaBEA10	61	2.6	1.3	34.8	0.3	27	211.5
	NaBEA11	55.5	-	1.6	43	-	27	165.7
	NaBEA12	63.1	1	1.5	34.3	0.2	23	134.5

Note: Si/Al_{ex} were calculated from the elemental quantification by the SEM-EDS analysis

The elemental composition as shown in Table 6.4, indicates that the BEA zeolites are mainly composed of oxygen, silicon, aluminium and sodium or potassium with Si/Al ratio >21 and <28. The fully crystallized spheroidal BEA zeolite exhibited uniform nanosized crystals around 138 and 166 nm (NaBEA80 and NaBEA81) while small nanosized crystal of 51 nm were observed in the case of NaBEA82 zeolite morphology. Under the same conditions but different synthesis time of 10 h, the nanosized crystals experienced a gradual decrease in size: 212, 166 and 135 nm and this can be related to the increase in the molar water fraction (NaBEA10 < NaBEA11 < NaBEA12, respectively). The decrease in size of nanosized crystals as the molar water fraction increased may be due to the fast nucleation rate at an early stage of the crystal growth which prevents further growth of large crystals. Hence, the higher molar water fraction at 10 h favoured nucleation rather than crystal growth.

To this end, the optimal conditions: 2.66 and 3.99 of the molar water fraction and hydrothermal time of 8 and 10/12 h (NaBEA81 and NaBEA12≈NaBEA2, respectively) was chosen as appropriate for further study of BEA zeolites. To corroborate the aforementioned observation, the optimised BEA zeolites of NaBEA81, NaBEA12 and NaBEA2 (current chapter 6), NaBEA24, NaBEA48 and NaBEA72 (as discussed in chapter 4) were compared.

6.2.3 Characterisation of optimised HBEA zeolite products

Herein, the optimal HBEA zeolites at short synthesis time of 8, 10 and 12 h and lower molar water fraction was compared with higher molar water fraction and long synthesis time zeolite of 24, 48 and 72 h. Before the full characterisation, the selected NaBEA zeolites were changed to their respective H-form (HBEA) as described in section 3.2.3. The zeolites were each assigned code names as follow: HBEA81 (8 h synthesis time and molar water fraction is 2.66), HBEA12 and HBEA2 (10 and 12 h synthesis time and molar water fraction 3.99, respectively) (present chapter 6) and HBEA24, HBEA48 and HBEA72 (24, 48 and 72 h synthesis time and molar water fraction of 9.945, respectively) (chapter 4).

The characterisation techniques employed in this chapter include: XRD, SEM-EDS, FT-IR, TGA, NMR, BET and TPD. Afterwards, the catalytic performance of each H-form BEA zeolite obtained at different synthesis time was evaluated. Figure 6.8 presents the mineralogical phase formation of the optimised HBEA zeolite after changing from the Na to the H-form using XRD analysis.

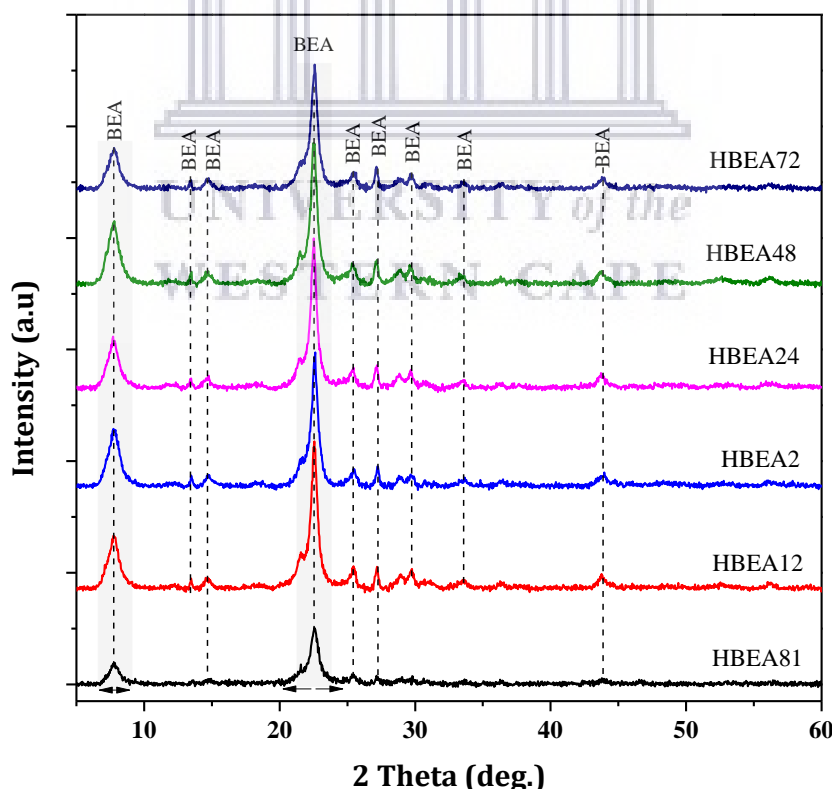


Figure 6.8: XRD patterns of the synthesised HBEA zeolite produced from the molar composition of 1 Si : 0.017 Al : 0.241 Na : 0.399 TEAOH : x H₂O, with varied water content, where x is 2.66, 3.99 and 8.98 and different hydrothermal time of 8, 10, 12, 24, 48 and 72 h. At 8 h, x = 2.66 (HBEA81), 10 and 12 h, x = 3.99 (HBEA12 and HBEA2) and 24, 48 and 72 h, x = 8.98 (HBEA24, HBEA48 and HBEA72, respectively).

The XRD patterns of the six optimised BEA zeolites samples are compared in Figure 6.8. All the diffraction pattern display characteristic peaks at $2\theta = 7.7, 13.4, 22.4, 27.1, 28.7, 29.6$ and 43.4° , which are attributed to the typical BEA zeolite phase. However, sample HBEA81 showed two main peaks at $2\theta = 7.7$, and 22.4° and four minor diffraction peak at $2\theta - 13.4, 27.1, 28.7$ and 29.6° (Figure 6.8). The increasing peak intensity at $2\theta = 7.7$, and 22.4° and reduced background scattering of the BEA zeolites samples as hydrothermal time increased, could be an indication of highly crystalline products. In order to validate the results, the relative crystallinity of each sample was calculated using equation 4.5 as presented in chapter 4.

The relative crystallinity of the H-form samples showed no specific trend but clearly indicated that higher crystalline structure, $>70\%$ BEA zeolites were prepared under the applied conditions except HBEA81 zeolite which is $<45\%$. Besides, the relative crystallinity of short hydrothermal (10 and 12 h) synthesised HBEA12 and HBEA2 was above 90% compared with longer synthesis time of 24 and 72 h (88 and 79%, respectively). Hence, the synthesis of high crystalline BEA zeolite can be maintained when the molar water fraction is kept between 1.77 and 8.98 under a hydrothermal time ≥ 8 and ≤ 72 h. This validated results that the low molar water fraction promoted supersaturation and enhanced the mobility of the reacting species in the synthesis mixture and by close contact promoted a rapid nucleation rate. This enhanced the crystallisation of BEA zeolite structure in a short hydrothermal time.

The morphology of the synthesised samples was compared using SEM-EDS analysis as presented in Figure 6.9.

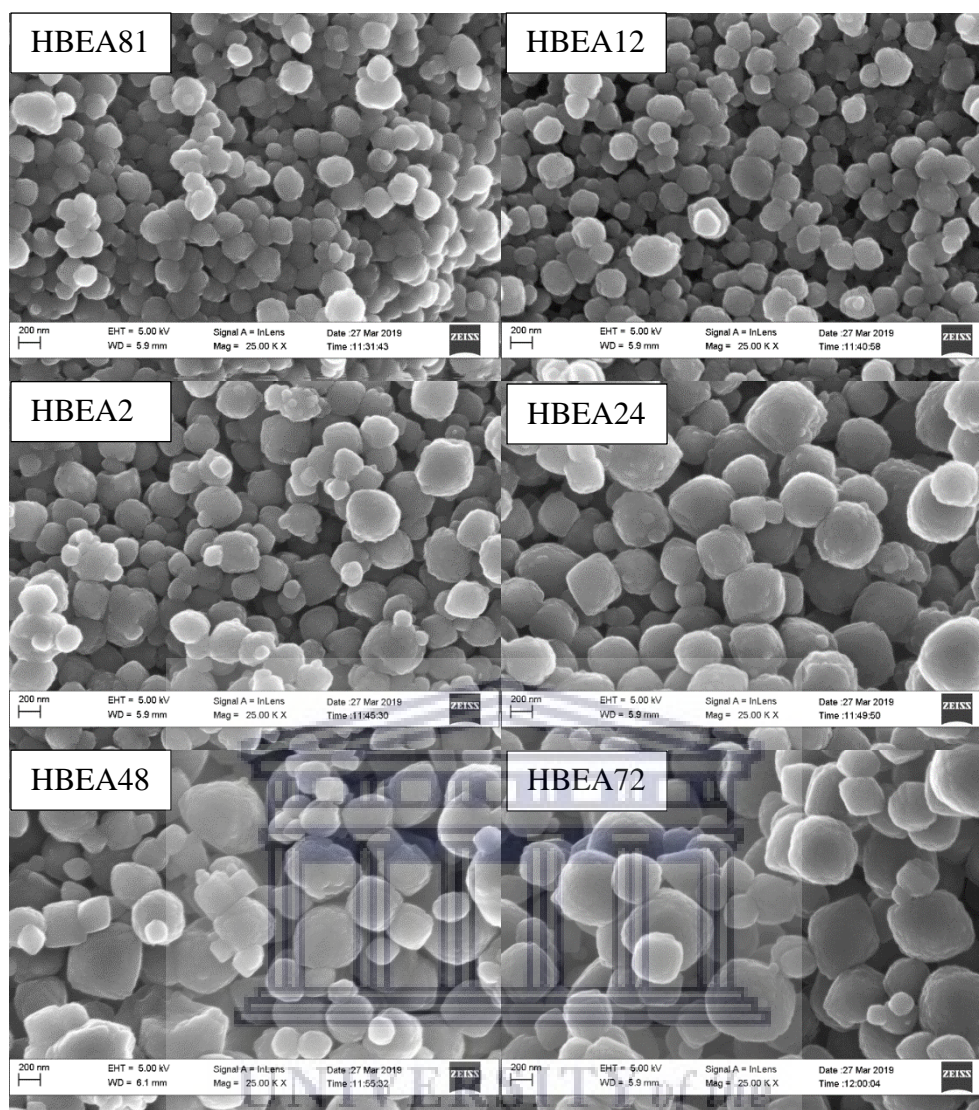


Figure 6.9: SEM micrographs of the synthesised HBEA zeolite produced from the molar composition of: 1 Si : 0.017 Al : 0.241 Na : 0.399 TEAOH : x H₂O, with varied water content, where x is 2.66, 3.99 and 8.98 and different hydrothermal time of 8, 10, 12, 24, 48 and 72 h. At 8 h, $x = 2.66$ (HBEA81), 10 and 12 h, $x = 3.99$ (HBEA12 and HBEA2) and 24, 48 and 72 h, $x = 8.98$ (HBEA24, HBEA48 and HBEA72, respectively).

The SEM micrographs in Figure 6.9, show that HBEA81, HBEA12, HBEA2, HBEA24, HBEA48 and HBEA72 samples have a spheroidal-shaped morphology. Such a spheroidal structure is typical of BEA zeolite (Zhang et al., 2016). Si, O and Al species were the main elemental content of the fly ash derived zeolite framework of the synthesised BEA crystals as presented in Table 6.5.

Table 6.5: Elemental composition and crystal size of the HBEA zeolite using SEM-EDS.

Samples	O	Al	Si	Si/Al_{ex} ratio	Crystal size (nm)
HBEA81	54.2	1.5	44.3	30	191.9
HBEA12	62.0	1.5	36.5	25	189.7
HBEA2	62.5	1.4	36.1	25	239.2
HBEA24	61.3	1.6	37.1	24	369.9
HBEA48	58.6	1.5	39.9	26	321.1
HBEA72	65.5	1.4	33.0	23	379.4

Note: Si/Al_{ex} were determined by SEM-EDS and the crystal size were calculated from SEM micrograph by ImageJ software.

The uptake of the Al in the framework of HBEA zeolite was found to be consistent for all samples as indicated by Si/Al ratios obtained by SEM-EDS analysis hence synthesis time did not alter Si/Al ratios. Most of the synthesised HBEA zeolites have Si/Al ratio ≥ 23 but ≤ 26 except for sample HBEA81 with Si/Al ratio = 30 as seen in Table 6.5. This case could be related to residual silica which was not completely crystalline but remained as amorphous material mixed with the crystalline HBEA zeolite.

Table 6.5 also shows the average crystal size of the fly ash based BEA zeolites as determined by SEM and ImageJ software. The average crystal size increased from 190 to 379 nm as the hydrothermal time increased (HBEA12 < HBEA2 < HBEA24 < HBEA48 < HBEA72). This observation further prove that the more concentrated, supersaturated mixtures promoted rapid formation of nucleation centres which allowed the termination of crystal size growth at low molar water fraction in a short hydrothermal time. These favourable nucleation conditions promoted the rapid transformation of zeolite nuclei into well-ordered, small BEA crystals and limited the crystal growth in low molar water fraction environment. This is in agreement with a study conducted by Möller et al. (2011) using the steam-assisted conversion process to produce BEA zeolite. They further showed that the early stage nucleated zeolite crystallites are restricted from further growth in size due to constant contact of the reacting species in low molar water fraction mixture, allowing rapid incorporation and utilisation of available species in numerous nuclei.

6.2.3.1 Framework stability of HBEA zeolite structure

The framework stability of the synthesis HBEA zeolites after detemplation and ion exchange was probed by thermogravimetric analysis (TGA) and nuclear magnetic resonance spectroscopy (^{29}Si and ^{27}Al MAS NMR) as described in chapter 3. This section presents the results and discussion of the aforementioned analysis. In order to assess the quantity of water and other species, thermogravimetric (TGA) measurements were carried out on the selected HBEA zeolite samples as presented in Figure 6.10.

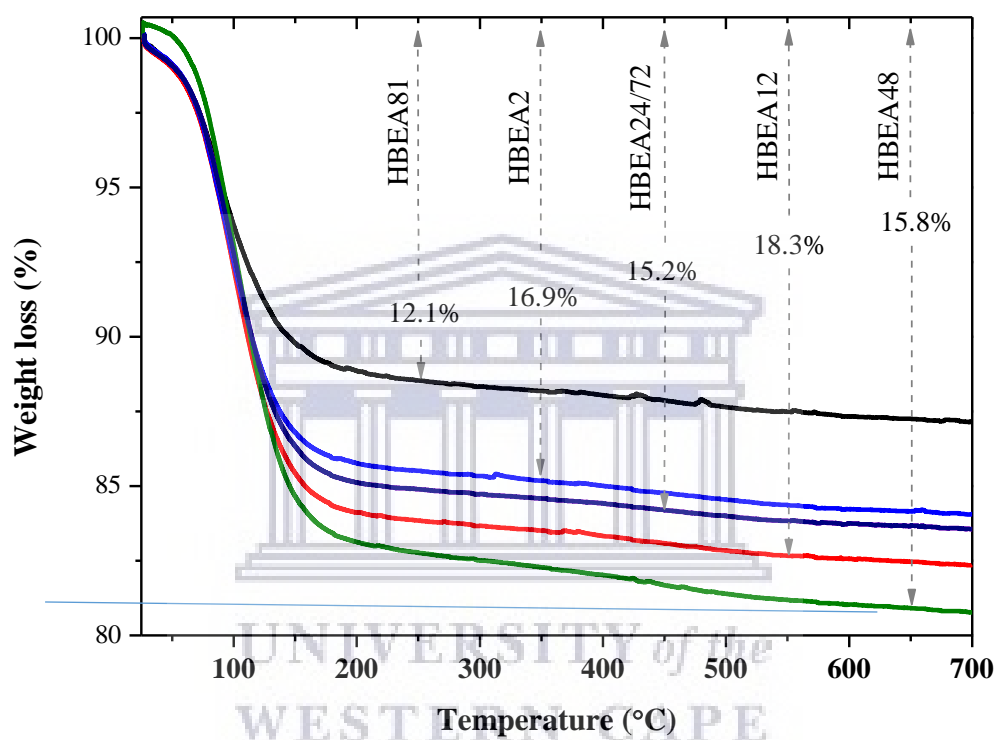


Figure 6.10: TGA analysis of the synthesised HBEA zeolite produced from the molar composition of: 1 Si : 0.017 Al : 0.241 Na : 0.399 TEAOH : x H_2O , with varied water content, where x is 2.66, 3.99 and 8.98 and different hydrothermal time of 8, 10, 12, 24, 48 and 72 h. At 8 h, $x = 2.66$ (HBEA81), 10 and 12 h, $x = 3.99$ (HBEA12 and HBEA2) and 24, 48 and 72 h, $x = 8.98$ (HBEA24, HBEA48 and HBEA72, respectively).

Figure 6.10 shows the thermogravimetric analysis with significant differences observed in the % weight loss of the moisture for both short- (HBEA81, HBEA12 and HBEA2) and long-time hydrothermal synthesized (HBEA24, HBEA48 and HBEA72) zeolite crystals. It was noticed that the thermal induced weight loss showed two stages in the thermal curve (Figure 6.10). The first curve which is attributed to surface moisture content (physisorbed water) was recorded in the temperature range of 25 and 150 °C while the second curve between 150-450 °C can be associated with the loss of $\text{H}^+ - \text{OH}^-$ species bonded to $\sim\text{Si-O}$

Si~ or ~Si-O-Al~ (dehydroxylation) of the framework of the synthesised BEA zeolite structures (Zhang et al., 2017). Table 6.6 shows detailed weight loss between adsorbed surface moisture and bonded framework water.

Table 6.6: The adsorbed surface water (surface moisture content), bonded framework water (dehydroxylation) and total weight loss.

Sample	Weight loss (%)		
	Adsorbed water	Dehydroxylation	Total
	25 - 150 °C	150 - 450 °C	
HBEA81	10.21	1.92	12.13
HBEA12	14.57	2.35	16.92
HBEA2	13.20	2.02	15.23
HBEA24	13.67	2.14	15.80
HBEA48	15.34	2.98	18.32
HBEA72	13.67	2.14	15.80

The weight loss due to surface adsorbed moisture in Table 6.6 can be grouped into three namely: low, medium and high. Sample HBEA81 exhibited a low weight loss of approximately 10.21% while HBEA2, HBEA24 and HBEA72 showed a medium weight loss between 13.20 and 13.67%. Whilst, high moisture related weight loss was observed in sample HBEA12 and HBEA48 at 14.57 and 15.34%, respectively. According to Muriithi et al. (2013), the % weight loss is an indirect measure of microporosity and high void volume being retained in the zeolites. This low weight loss of HBEA81 might suggest low porous structure of the zeolite and further supports the low relative crystallinity (XRD analysis, Figure 6.8) and high Si/Al ratio (SEM-EDS, Table 6.4). Thus, the less Al in the framework structure of the HBEA zeolites can indicate high hydrophobicity. The hydrophilicity of zeolite samples was shown in the sequence of HBEA81 > HBEA48 > HBEA12 > HBEA24~HBEA72 > HBEA2 (see Table 6.5).

The associated dehydroxylation weight loss of <3% in the synthesised HBEA zeolites samples was observed between 150 and 450 °C (Table 6.6). Since dehydroxylation can be associated with framework siloxane (~Si-O-Si~ or ~Si-O-Al~), therefore, the formation of terminal silanol (Si-OH) defects sites in the framework could be high in sample HBEA12 and HBEA48 as the dehydroxylation weight loss is high, 2.35 and 2.98%, respectively.

Further analysis was carried out to validate the framework structure of the synthesised HBEA by nuclear magnetic resonance spectroscopy (^{29}Si and ^{27}Al MAS NMR). The ^{29}Si and ^{27}Al MAS NMR were analysed with 8 kHz spinning speed at a magnetic field strength of 11.4 T as described in section 3.10. Figure 6.11 presented ^{27}Al MAS NMR of HBEA81, HBEA12, HBEA2, HBEA24, HBEA48 and HBEA72 zeolite samples.

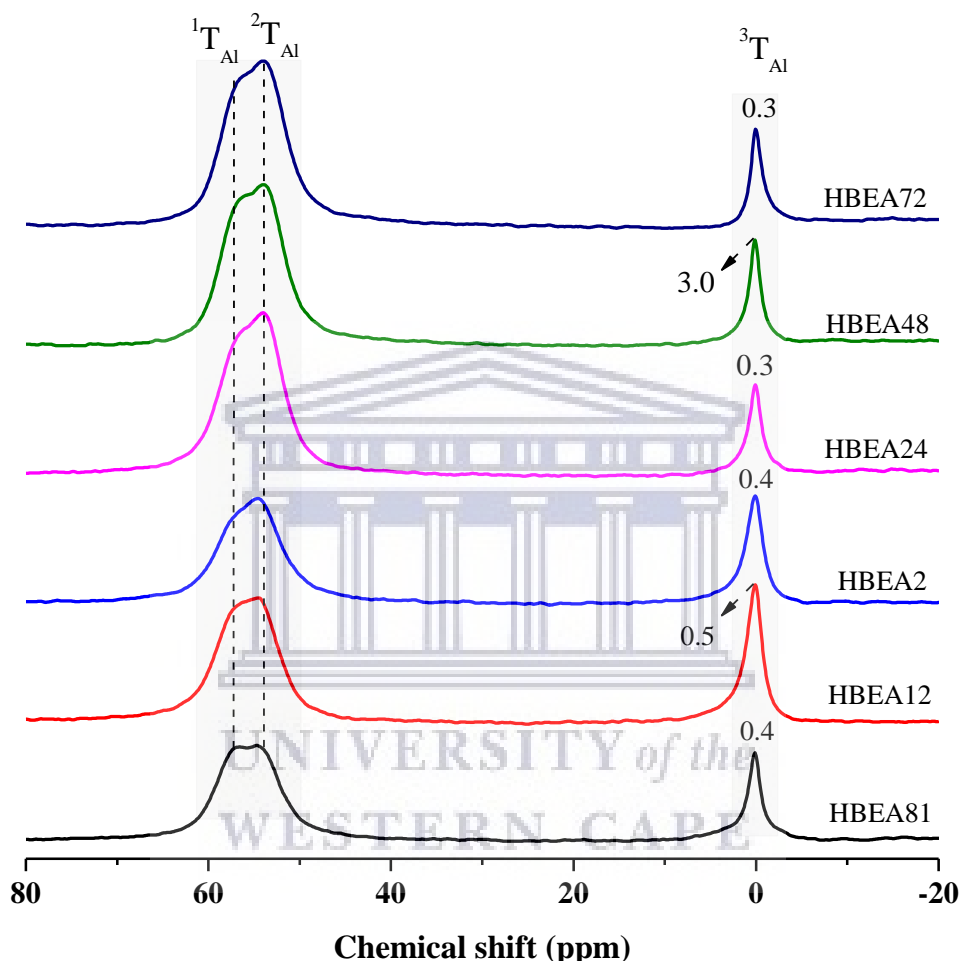


Figure 6.11: ^{27}Al MAS NMR analyses of the synthesised HBEA zeolite produced from the molar composition of: 1 Si : 0.017 Al : 0.241 Na : 0.399 TEAOH : x H₂O, with varied water content, where x is 2.66, 3.99 and 8.98 and different hydrothermal time of 8, 10, 12, 24, 48 and 72 h. At 8 h, $x = 2.66$ (HBEA81), 10 and 12 h, $x = 3.99$ (HBEA12 and HBEA2) and 24, 48 and 72 h, $x = 8.98$ (HBEA24, HBEA48 and HBEA72, respectively).

Figure 6.11 shows the ^{27}Al MAS NMR spectra of HBEA81, HBEA12, HBEA2, HBEA24, HBEA48 and HBEA72 zeolite samples. The ^{27}Al MAS NMR spectroscopy was studied to understand the environment of Al atoms in the synthesised HBEA zeolite samples (Figure 6.11). To further analyse the structure, the peak position of the framework Al (FAL = $^1\text{T}_{\text{Al}}$ and $^2\text{T}_{\text{Al}}$), extra framework Al (EFAI = $^3\text{T}_{\text{Al}}$) and peak width of EFAI was derived by

deconvolution using mixed Lorentzian and Gaussian line shape (Figure 6.11, Table 6.7 and Appendix 2a-f).

Table 6.7: Detailed ^{27}Al MAS NMR spectra after deconvolution FAI and EFAI in the synthesised HBEA zeolite samples.

Sample	Framework Al				Extra-framework Al			
		Integral		Integral	T_{Al}		Integral	Width
	$^1T_{\text{Al}}$	(%)	$^2T_{\text{Al}}$	(%)	total	$^3T_{\text{Al}}$	(%)	(ppm)
HBEA81	57.9	36.6	54.4	42.6	79.2	0.4	20.8	1.8
HBEA12	57.9	42.5	54.5	31.2	73.7	0.5	26.3	1.9
HBEA2	57.9	31.3	54.4	44.6	75.9	0.4	24.1	2.1
HBEA24	57.5	42.4	54.0	44.7	87.1	0.3	12.9	1.7
HBEA48	60.9	51.1	56.6	16.5	67.5	3.0	32.5	1.4
HBEA72	57.5	35.4	53.8	53.9	89.3	0.3	10.7	1.5

Note: $^1T_{\text{Al}}$, $^2T_{\text{Al}}$ and $^3T_{\text{Al}}$ is concentration of the FAI and EFAL peaks in ppm and T_{Al} is total % integral of $^1T_{\text{Al}}$ and $^2T_{\text{Al}}$

It was noticed in Figure 6.11 and Table 6.7 that two major resonance bands were observed, with the first appearing peak between $\delta = 60.9$ and 53.8 ppm, being attributed to tetrahedrally coordinated framework aluminium (FAI) while the second peak occurring between $\delta = 0.3$ and 3.0 ppm was assigned to octahedrally coordinated extra framework aluminium (EFAI) (Prodinger et al., 2018; Zhao et al., 2014). Two contributing FAI peaks of upfield ($^1T_{\text{Al}}$) and downfield ($^2T_{\text{Al}}$) resonance were resolved after the deconvolution of the band (Table 6.7 and Appendix 2a-f). The upfield signal, $^1T_{\text{Al}}$ occurring between 57.5 - 57.9 ppm and the downfield signal, $^2T_{\text{Al}}$ between $\delta = 53.9$ - 54.5 ppm and were both assigned to tetrahedral Al species in HBEA81, HBEA12, HBEA2, HBEA24 and HBEA72 zeolite samples. On the contrary, sample HBEA48 displayed only the upfield signal $^1T_{\text{Al}}$ with a high-field at $\delta = 60.9$ ppm and low-field $\delta = 56.6$ ppm (Figure 6.11, Table 6.7 and Appendix 2). Manrique et al. (2016) have associated the higher upfield signal, >60 and <63 ppm to the presence of distorted tetrahedral Al species within the framework structure of HBEA zeolite. They further assigned the lower upfield to a regular signal of tetrahedral framework Al species. This suggested that the integral percentage of the tetrahedral Al species $^1T_{\text{Al}}$ in Table 6.7 with the descending order: HBEA48 $>$ HBEA12 $>$ HBEA24 $>$ HBEA72 $>$ HBEA2 can be related to the thermal stability of HBEA48 $>$ HBEA12 $>$ HBEA24-HBEA72 $>$ HBEA2, except sample HBEA81 which followed no specific trend (Figure 6.11 and Table 6.6). Hence, showing the

possible presence of terminal $\sim\text{Si-OH}\sim$ defect sites in the framework structure of HBEA48 zeolite.

Table 6.7 clearly shows that the Al species were mostly incorporated into the ${}^2\text{T}_{\text{Al}}$ tetrahedral framework ($\delta = 54$ ppm) with only a small fraction of Al located in the EFAl coordination ($\delta = 0$ ppm). The second major resonance, ${}^3\text{T}_{\text{Al}}$ assigned to six coordinated extra framework aluminium (EFAl) shows peak signals between $\delta = 0.3$ and 0.5 ppm for sample HBEA81, HBEA12, HBEA2, HBEA24 and HBEA72. On the other hand, sample HBEA48 displayed a significant upward peak shift to $\delta = 3.0$ ppm (Figure 6.11, Table 6.7 and Appendix 2a-f). This clearly indicated that the signal was sensitive to the coordination environment of the Al species within the framework structure. The EFAl (${}^3\text{T}_{\text{Al}}$) decreased from 3.0 to 0.3 ppm with decreasing integral intensity (HBEA48 > HBEA12 > HBEA2 > HBEA24 > HBEA72) (Table 6.7) as the Si/Al ratio increased (HBEA48 < HBEA12-HBEA2 < HBEA24 < HBEA72) (Table 6.5).

Wang et al. (2017) reported that during the substitution of Si species by Al species, the negative charge ($\text{SiO}^- \text{Al}$) balanced by protons resulted in the generation of Brønsted acid sites, which can be related to framework Al atoms of tetrahedral coordination. They further reported that the presence of EFAl in the HBEA zeolite can be related to Lewis acid sites in the structure. Also, upfield shifting of the coordinated Al species in the extra framework from 0 ppm to about 4 ppm signified the formation of extra framework aluminium hydroxide species (Zhao et al., 2014). This validated the fact that sample HBEA48 contained distorted tetrahedral Al species due to the presence of terminal $\sim\text{Si-OH}\sim$ or $\sim\text{Al-OH}\sim$ sites in the structure as supported by TGA results (Figure 6.10). Also, the presence of tetrahedrally coordinated Al sites in all the synthesised HBEA zeolites samples could indicate the existence of Brønsted acidity. The results presented herein further suggested that the synthesised HBEA zeolites contained mostly framework with low extra framework Al thus can be active catalysts due to the presence of Brønsted.

${}^{29}\text{Si}$ MAS NMR was carried out as described in chapter 3 to study the incorporation of Al species into the silica framework of the synthesised HBEA zeolites. Figure 6.12 compared the silica environment of the prepared HBEA zeolite samples by nuclear magnetic resonance spectroscopy (${}^{29}\text{Si}$ MAS NMR).

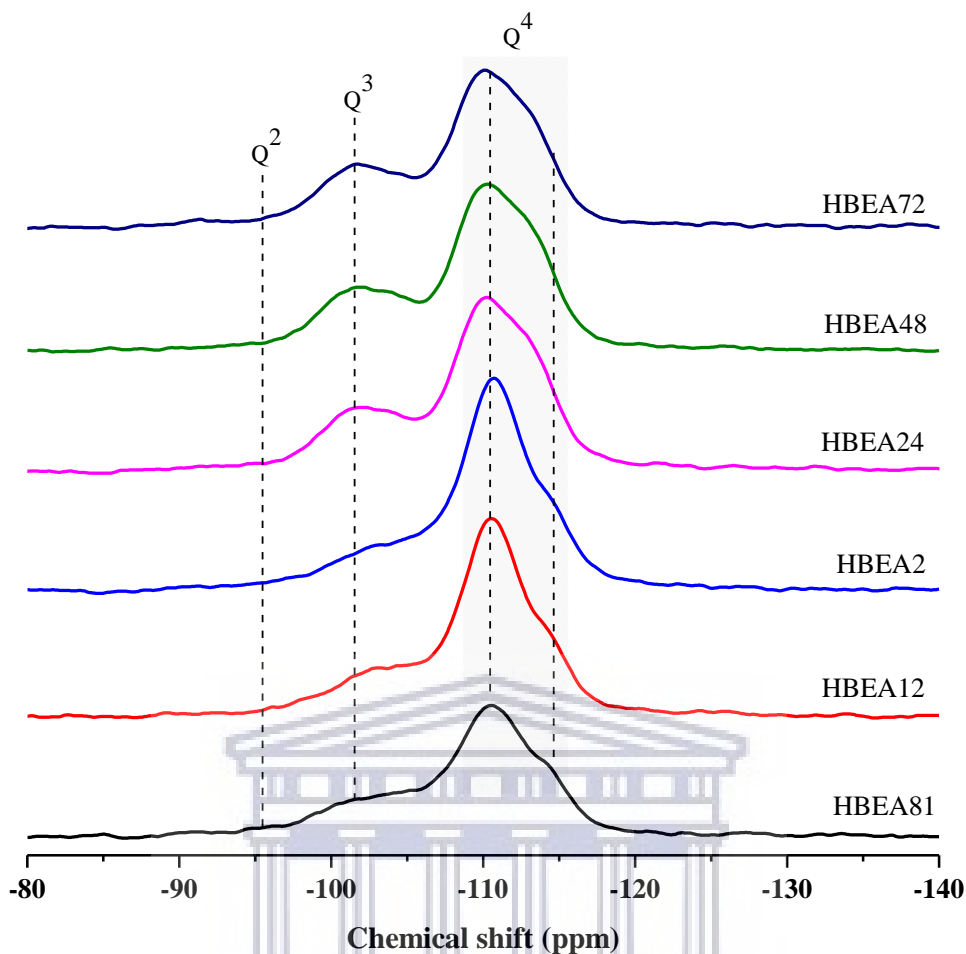


Figure 6.12: ^{29}Si MAS NMR analyses of the synthesised HBEA zeolite produced from the molar composition of: 1 Si : 0.017 Al : 0.241 Na : 0.399 TEAOH : x H_2O , with varied water content, where x is 2.66, 3.99 and 8.98 and different hydrothermal time of 8, 10, 12, 24, 48 and 72 h. At 8 h, $x = 2.66$ (HBEA81), 10 and 12 h, $x = 3.99$ (HBEA12 and HBEA2) and 24, 48 and 72 h, $x = 8.98$ (HBEA24, HBEA48 and HBEA72, respectively).

Figure 6.12 presents the solid-state ^{29}Si MAS NMR spectra of fly ash based HBEA zeolite with different molar water fraction and crystallization time. The spectra presented in Figure 6.12 elucidated two main coordination environments of Q^3 and Q^4 . The chemical shift within these environments was further deconvoluted using mixed Lorentzian and Gaussian line shape. Upon the deconvolution, the framework Si/Al ratio was calculated by applying equation 4.7 (chapter 4) and the influence of hydrothermal time in the peak area of the synthesised HBEA zeolite was evaluated as presented in Table 6.8.

Table 6.8: Chemical shift, Si/Al ratio, intensity and area of deconvoluted Q³ and Q⁴ peak.

Samples	Q ³ Si(1Al)		Q ⁴ Si(0Al)		NMR Si/Al ratio	EDS Si/Al ratio
	δ_{decon} (ppm)	Area %	δ_{decon} (ppm)	Area %		
HBEA81	-102.9	23.7	-111.0	41.1	29.7	30
HBEA12	-104.4	25.1	-111.1	43.4	26.8	25
HBEA2	-104.2	22.8	-111.3	45.5	30.0	25
HBEA24	-103.3	24.6	-110.7	45.8	24.8	24
HBEA48	-103.3	27.1	-110.9	38.9	23.7	26
HBEA72	-103.1	26.3	-110.8	42.9	22.9	23

The resonance bands around $\delta = -102$ to 104.4 ppm are assigned to Q³ Si (1Al) environment and can be related to silicon-bearing OH groups of (SiO)₃Si(OH), whereas the resonances around $\delta = -110$ to -111 ppm are attributed to Q⁴ Si (0Al) of four silicon coordinated atom as shown in Figure 6.12 and as illustrated in Scheme 4.1 (chapter 4). A weak shoulder band at about $\delta = -112$ and -113 ppm, also assigned to four coordinated atoms of related Q⁴ Si (0Al) groups was detected. Similarly, several researchers have located such bands in the structural framework of a typical HBEA zeolite (Zhu et al., 2017; Zhang et al., 2013).

It is worth noting that the Q³ Si (1Al) of sample HBEA12 and HBEA24 at $\delta = -104$ and -111 ppm shifted downward (≥ 0.4 ppm) to $\delta = -103$ and -110 ppm as seen in samples HBEA24, HBEA48 and HBEA72, respectively. The difference in the Q³ Si (1Al) and Q⁴ Si (0Al) can be related to the degree of Si substituted by Al in the lattice structure of the zeolites. This can be confirmed by the decreasing framework Si/Al ratio: $30 < 25 < 24 < 23$ as the hydrothermal time increases from 12-24-48 to -72 h due to the Al substitution processes in the framework structure (HBEA2, HBEA24, HBEA48 and HBEA72, respectively) (Table 6.8). Furthermore, the Q³ area of (SiO)₃Si(OH) of related HBEA72 and HBEA48 samples reached the highest amount of 26 and 27% which then decreased to the lowest percentage of 23% (HBEA2) as the hydrothermal time was reduced to 12 h. Relating the aforementioned observation with the shift in the Q³ environment, this suggested that short hydrothermal time could reduce the amount of ~Si-OH~ defect sites in the framework structure of the fly ash based HBEA zeolites.

6.2.3.2 Textural and acidic properties of HBEA zeolites

The textural and acidity properties of the different zeolites (HBEA81, HBEA12, HBEA2, HBEA24, HBEA48 and HBEA72) was investigated in this section. The difference between

the samples was the synthesis time which was grouped into short and long hydrothermal time. Short hydrothermal time of 8, 10 and 12 h (HBEA81, HBEA12 and HBEA2, respectively) and long hydrothermal time of 24, 48 and 72 h (HBEA24, HBEA48 and HBEA72, respectively) as described in section 6.2.2. Figure 6.13 depict the nitrogen physisorption profile of the synthesised HBEA zeolites.

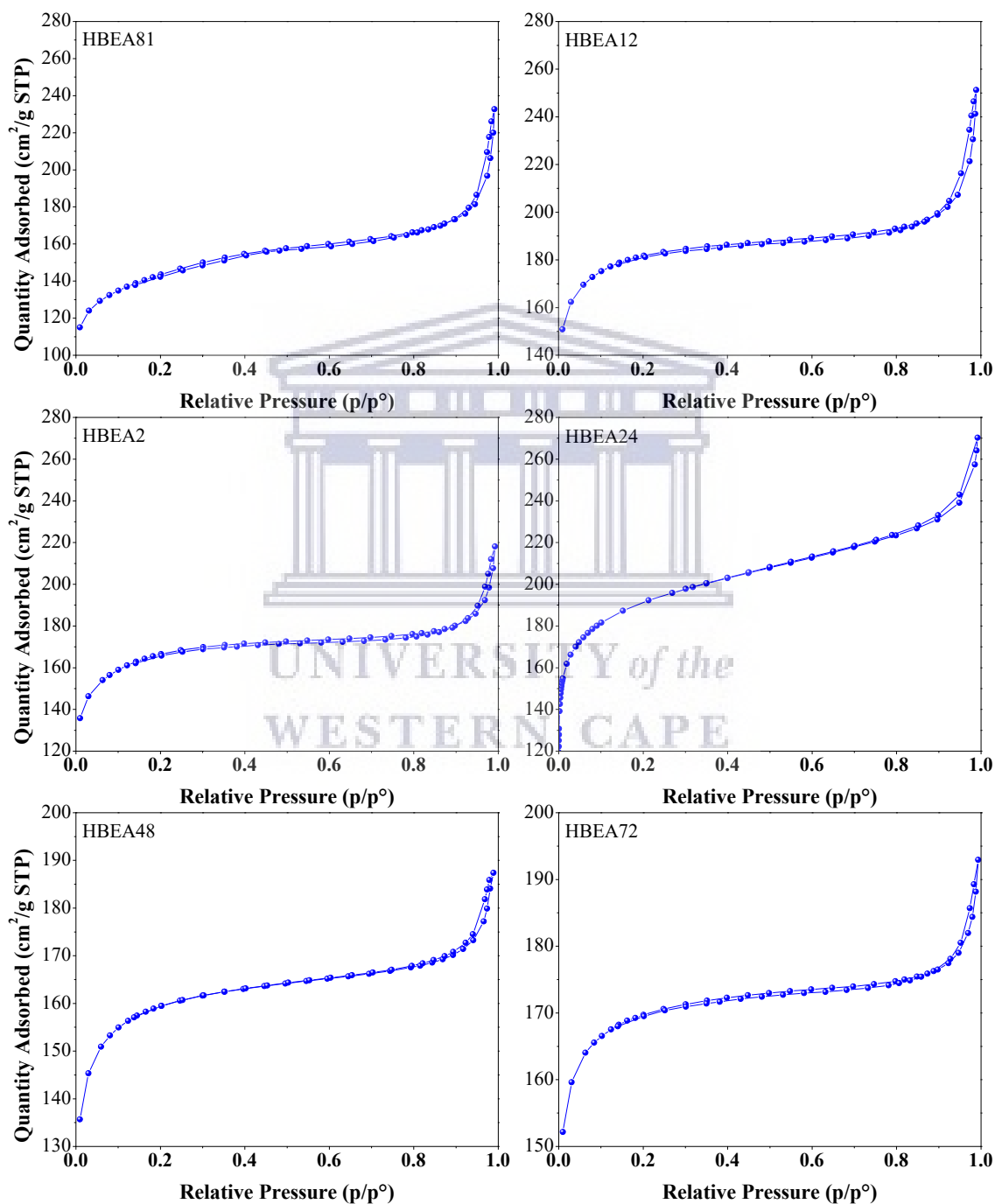


Figure 6.13: N₂ adsorption-desorption isotherms of HBEA zeolite prepared at short crystallisation time of 8, 10 and 12 h (a = HBEA81, HBEA12 and HBEA2, respectively) and long crystallisation time of 24, 48 and 72 h (b = HBEA24, HBEA48 and HBEA72, respectively).

The nitrogen adsorption-desorption isotherms of HBEA zeolite prepared from coal fly ash at different hydrothermal times is presented in Figure 6.13. The isotherms of the samples exhibited both type 1 and type IV with hysteresis loops which indicate the interconnected mesopores, which do not restrict capillary evaporation of adsorbed nitrogen (Thommes et al., 2015). The isotherms curve in Figure 6.13 characterise the Langmuir adsorption of N₂ with corresponding micropore filling at $P/P_0 < 0.17$ while the type IV isotherm within the range $0.2 < P/P_0 < 0.7$ is attributed to the capillary condensation of the mesopores. The combination of both micro and mesoporous structure is a significant advantage of the synthesised HBEA zeolite in catalytic performance. Table 6.9 compares the textural properties of HBEA81, HBEA12, HBEA2, HBEA24, HBEA48 and HBEA72 zeolites.

Table 6.9: Textural properties of the synthesised HBEA zeolite at different hydrothermal time.

Zeolite	S_{BET} [m²/g]	S_{micro} [m²/g]	S_{meso} [m²/g]	V_{micro} [cm³/g]
HBEA81	538	361	177	0.12
HBEA12	702	488	214	0.17
HBEA2	633	425	208	0.15
HBEA24	722	512	210	0.38
HBEA48	538	439	99	0.20
HBEA72	670	543	127	0.20

Note: S_{BET}: BET surface area; S_{micro}: micropore surface area, S_{meso}: mesopore surface area; V_{micro}: micropore volume.

The textural properties of the obtained HBEA zeolites samples at different synthesis time of 8, 10, 12, 24, 48 and 72 h is presented in Table 6.9 (HBEA81, HBEA12, HBEA2, HBEA24, HBEA48 and HBEA72, respectively). The pore size distribution of the interconnected HBEA zeolite at shorter hydrothermal time of 8 h possessed a mesopore area and total surface area of 177 and 538 m²/g, respectively. With increased hydrothermal time, 10 and 12 h the mesopore area increased to 214 and 208 m²/g and due to the high mesoporous surface, the HBEA12 and HBEA2 zeolite exhibited high surface area of 702 and 633 m²/g, respectively. In contrast, as the hydrothermal time increased further to 24, 48 and 72 h (HBEA24, HBEA48 and HBEA72) the mesoporosity of the zeolite decreased from 210 m²/g to 99 and 127 m²/g, respectively. Likewise, the BET surface area showed a significant

variation (722, 538 and 670 m²/g) with prolonged hydrothermal time in no clear chronological order (HBEA24, HBEA48 and HBEA72, respectively).

These results clearly indicate the acceptable degree of microporosity and high degree of mesoporosity of the crystalline HBEA zeolite with high surface area obtained at short (8 to 12 h) synthesis times. The lowest surface area of HBEA81 and HBEA48 of 538 (m²/g) can be directly linked to lower porosity as confirmed by TGA (Figure 6.10). The decrease in FAI and increase in EFAl as shown in Table 6.7 compliments the presence of defects which in turn contributed to the low surface area. This agrees with Al-Eid et al. (2019) observation which relates low surface area and pore volume to the presence of defects within the zeolite framework structure.

Indicatively, with the significant surface area, mesopore area and pore volume of the fly ash based HBEA zeolites, these catalyst could be suitable for different liquid and vapour state applications. Wang et al. (2017) applied HBEA zeolite with surface area between 517 to 556 m²/g for the benzylation of arenes with benzyl chloride. Escola et al. (2018) employed HBEA zeolite with high surface area between 520 to 727 m²/g in a veratrole acylation reaction. This further confirms that the synthesised HBEA zeolite should be suitable for liquid phase reaction such as acylation reactions. Figure 6.14-6.15 illustrates the pore size distribution of the different HBEA zeolite, obtained from fly ash extract at 140 °C for 8, 10, 12, 24, 48 and 72 h using the density functional theory (DFT) method.

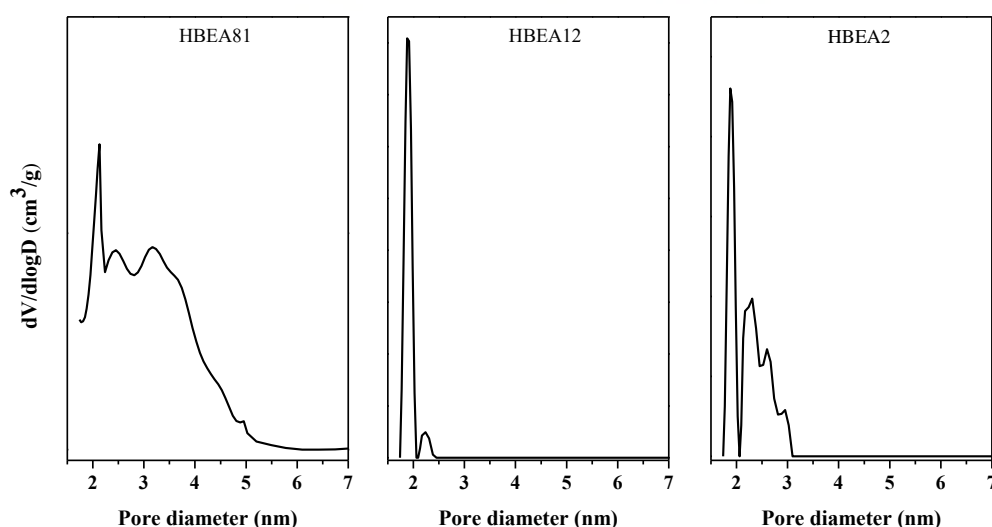


Figure 6.14: Mesopore size distributions of the synthesised HBEA zeolite produced from the molar composition of: 1 Si : 0.017 Al : 0.241 Na : 0.399 TEAOH : x H₂O, with varied water content, where x is 2.66 and 3.99 and different hydrothermal time of 8 and 10-12 h.

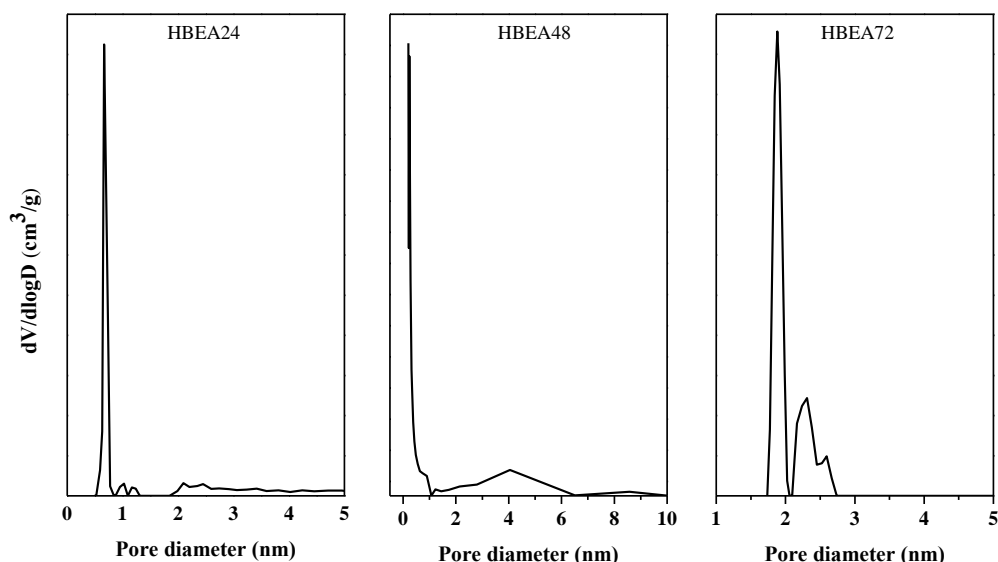


Figure 6.15: Mesopore size distributions of the synthesised HBEA zeolite produced from the molar composition of: 1 Si : 0.017 Al : 0.241 Na : 0.399 TEAOH : 8.98 H₂O, with different hydrothermal time of 24, 48 and 72 h.

The mesopore size distribution curves above 1 nm are presented in Figure 6.14-6.15 were calculated with the DFT method. In the case of HBEA81 sample, a major peak corresponding to a typical zeolitic mesoporous structure (361 m²/g) was observed at about 2.1 nm. The extension of minor and poorly defined peaks observed within the mesopores region of 2.4 and 5 nm indicated the presence of hierarchical pores in the zeolite (Figure 6.14). Also, this may suggest the incomplete condensation of some aggregates which can be linked to the reduced peak intensity as observed by the XRD diffraction pattern (see Figure 6.8-HBEA81). Sample HBEA12 and HBEA2 with the same molar water fraction of 3.99 but different synthesis times of 10 and 12 h, respectively, showed a strong mesopore peak centred around 1.8 nm. It is noteworthy that a well-defined peak around 2.2 nm was found in sample HBEA12 while as the hydrothermal time increased to 12 h (HBEA2) a multimodal pore distribution with several peaks within the range of 2 to 3 nm was found (see Figure 6.14). Hence, the well-defined pore size distribution within 2 to 4 nm can be related to the high mesopores surface area of 488 and 425 m²/g of sample HBEA12 and HBEA2, respectively.

With longer hydrothermal synthesis time as presented in Figure 6.15, mesopores size decreased 0.8 nm with two minor peaks at 1 and 1.25 nm (HBEA24) which was associated with the presence of high microporous structure as validated by the micropore area, 512 m²/g (see Table 6.9). The mesopore size distribution after the hydrothermal crystallisation

for 48 h (HBEA48) also decreased to 0.3 nm with a lower surface area. This could be related to the low textural properties (BET surface area and micro-mesopore area) of HBEA48 sample as described in Table 6.9. Interestingly, a significantly increased mesopores size was observed in the HBEA72 zeolite sample with a major mesopores peak at 1.9 and a minor broad peak at 2.3 nm. This observation complement the increased surface area, micropore area and mesopore area shown in the BET results presented in Table 6.9. This is indicative that aside from the microporosity in the synthesised HBEA zeolite, a secondary porosity has been formed, confirming the hierarchical pore structure. This is in agreement with the observation made by Escola et al. (2018), after modification of BEA zeolite structure in a protozeolitic unit's silanization agent. They reported that i) poorly defined peaks within the micropore and mesopore range indicated the presence of defect alongside porosity, and ii) the broad pore distribution within the range of 2 to 5 nm confirms the mesoporosity of the zeolite and the hierarchical pore distribution. The NH₃ desorption spectra defining the strength and presence of acid sites in HBEA zeolites were investigated using the ammonia temperature-programmed desorption (TPD) as described in section 3.3 and presented in Figure 6.16.

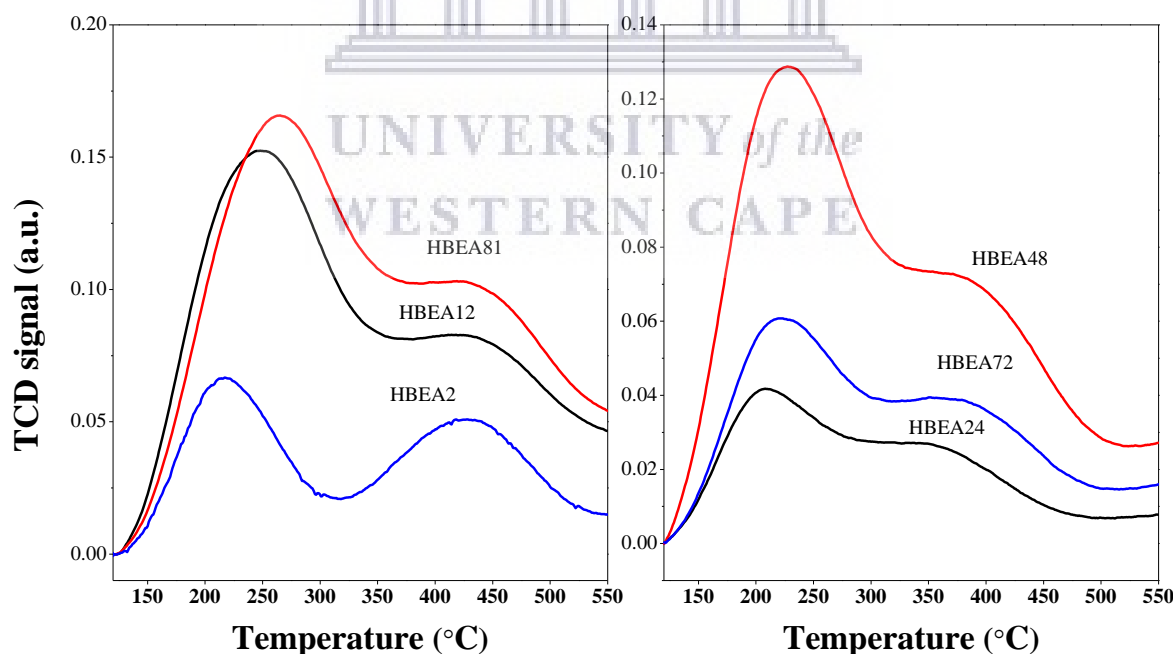


Figure 6.16: TPD profiles of the synthesised HBEA zeolite produced from the molar composition of: 1 Si : 0.017 Al : 0.241 Na : 0.399 TEAOH : x H₂O, with varied water content, where x is 2.66, 3.99 and 8.98 and different hydrothermal time of 8, 10, 12, 24, 48 and 72 h. At 8 h, $x = 2.66$ (HBEA81), 10 and 12 h, $x = 3.99$ (HBEA12 and HBEA2) and 24, 48 and 72 h, $x = 8.98$ (HBEA24, HBEA48 and HBEA72, respectively).

Figure 6.16 shows the temperature-programmed desorption of ammonia (NH₃-TPD) profile of the HBEA zeolites synthesised from different molar water fractions and hydrothermal time. Generally, the NH₃ desorption peaks at relatively low and high temperature can be associated with weak and strong acid sites which is a characteristic of HBEA zeolite (Monama et al., 2019). Herein, the synthesised HBEA samples all exhibited two distinctive desorption peaks at low (212 – 253 °C) and high (365 – 451 °C) temperatures. These peaks signify the temperature desorption of NH₃ which indicates the presence of weak acid sites (hydrogen bonded NH₃ molecules) and strong acid sites that are related to chemisorbed NH₃ molecules on the Bronsted acid sites (Wang et al., 2017). Hence, confirming the presence of weak and strong sites in the synthesised HBEA zeolites at low and high temperature of desorbed NH₃, respectively.

Table 6.10 presents the detailed acidic strength of the zeolites at the different desorption temperature regions.

Table 6.10: Acidity of the synthesised HBEA zeolites.

Samples	Acidic strength				Total acid sites (mmol/g)	NMR Si/Al ratio	EDS Si/Al ratio
	Weak (mmol/g)	T ₁ (°C)	Strong (mmol/g)	T ₂ (°C)			
HBEA81	2.39	236	0.26	447	2.65	29.7	30
HBEA12	2.46	253	0.29	451	2.75	26.8	25
HBEA2	0.90	212	0.66	428	1.56	30.0	25
HBEA24	0.63	203	0.17	365	0.80	24.8	24
HBEA48	1.55	217	0.20	402	1.75	23.7	24
HBEA72	0.58	213	0.14	392	0.72	22.9	23

As shown in Table 6.10, the amounts of NH₃ desorbed at low temperature (212 – 253 °C) were between 0.6 and 2.5 mmol/g NH₃ and thereafter, relatively smaller peaks appeared at higher temperature between 365 and 451 °C. The maximum adsorption of NH₃ due to the weak acid sites (2.39 and 2.46 mmol/g) was seen in samples HBEA81 and HBEA12, and adsorption of NH₃ then declined to a minimum of 0.63 and 0.90 mmol/g (HBEA24 and HBEA72, respectively). Whilst, the strong acid sites of the related Bronsted acid sites can be grouped into high, 0.66 mmol/g (HBEA2), mid-high, 0.17 to 0.29 mmol/g (HBEA24, HBEA48, HBEA12 and HBEA81) and low, 0.14 mmol/g (HBEA72). The shift to lower temperature of the weak acid peak can be related to the HBEA samples prepared for

hydrothermal times of 24, 48 and 72 h. On the other hand, the highest temperature of desorption cannot be related to the increased amount of the strong acid sites in HBEA2 as the NH_3 desorbed at 428 °C. This shows that the more isolated the framework Al, the stronger the acid sites as supported by the Si/Al ratio (see Table 6.10). Thus, the fly ash based HBEA zeolites could be suitable as catalysts for liquid phase acylation or alkylation reactions.

6.2.4 Friedel-Crafts acylation of anisole with benzoyl chloride over HBEA zeolites

In this section, the catalytic performance of the optimised HBEA81, HBEA12, HBEA2, HBEA24, HBEA48 and HBEA72 zeolites is presented. The acylation reaction of anisole with benzoyl chloride (BzCl) was compared among the catalyst as described in chapter 3, section 3.2.5.2. This reaction was chosen as a probe reaction to compare the catalytic performance of the CFA based zeolite samples in order to ensure they are active in the liquid phase. After each experimental run the percentage conversion, selectivity and yield was calculated based on the peak area of the product obtained from GC analysis. The catalytic performance of the zeolites was related to the influence of crystal size and surface area, acid sites and framework aluminium as well as influence of acylation time and anisole/benzoyl chloride ratio.

6.2.4.1 Activity of fly ash-based HBEA zeolite in acylation reaction

The catalytic activity of HBEA81, HBEA12, HBEA2, HBEA24, HBEA48 and HBEA72 zeolite was tested and evaluated based on the rate of conversion, selectivity and yield in the anisole acylation with BzCl as presented in this section. The probe test reaction process was carried out at 120 °C with different reaction time (0, 180, 360, 720 and 1440 min) (detailed in chapter 3). Before each reaction run, the HBEA zeolite were calcined in air at ramping rate of 15 °C/min and held at 450 °C for 3 h to remove moisture. The comparison of the catalytic performance in the probe reaction was grouped into two based on: i) molar water fraction of the synthesis mixture and ii) the synthesis time. The first group, HBEA81, HBEA12 and HBEA2 was obtained from low water fraction of 2.66 and 3.99 at hydrothermal time of 8, 10 and 12 h, respectively (short synthesis). Whereas, the long synthesis time of the samples HBEA24, HBEA48 and HBEA72 was obtained from molar water fraction of 8.98 with synthesis time of 24, 48 and 72 h, respectively (see chapter 3, Table 3.4 and 3.5). The percentage conversion of anisole, selectivity and yield of 4-methoxyacetophenone ($\text{P}_{4\text{Me}}$) are depicted in Figure. 6.17, 6.18 and 6.19.

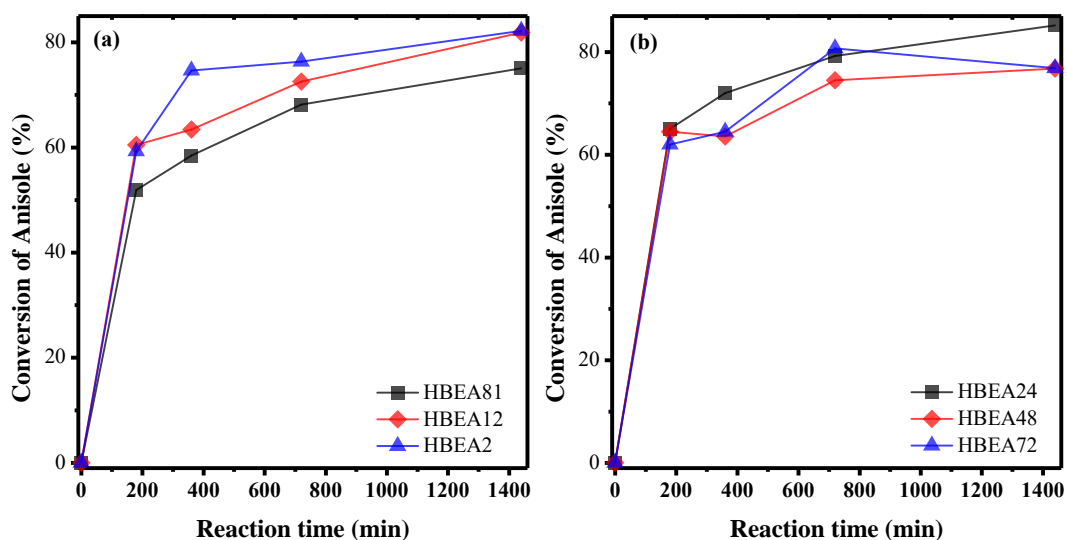


Figure 6.17: Anisole conversion over a) HBEA81, HBEA12 and HBEA2 and b) HBEA24, HBEA48 and HBEA72 zeolites (reaction conditions: temperature = 120 °C, maximum time = 1440 min, anisole/benzoyl chloride ratio = 2.5:1 and catalyst = 0.068 g).

Figure 6.17a-b depicts the conversion of anisole over the different HBEA zeolites catalysts, respectively. Before the experimental runs, a blank reaction test was carried out without the presence of HBEA zeolite catalyst. The blank reaction under the applied conditions revealed that no product was formed in the absence of catalyst in the acylation of anisole with BzCl at the applied conditions. However, when any one of HBEA81, HBEA12, HBEA2, HBEA24, HBEA48 and HBEA72 catalyst was added to the acylation reaction, >50% of the anisole (reactant) was predominantly converted to *p*-position (P_{4Me}) as presented in Figure 6.18 below. While $\geq 40\%$ of the other products were *o*-position (P_{2Me}) and phenyl benzoate. Similarly, Wagholikar et al. (2007) reported that acylation of anisole over MOR and HBEA catalyst synthesised using commercial feedstock chemicals resulted in three conversion products of *p*-, *o*-position and phenyl benzoate. Also, El Berrichi et al. (2005) noticed that the *p*-position of 4-methoxyacetophenone was the major product formed in the conversion of anisole over SBA-15 and HBEA zeolites. Therefore, the fly ash based HBEA zeolites showed a comparable product conversion to conventional synthesised zeolites.

Generally, the conversion curves of P_{4Me} in Figure 6.17a-b show three regions with a steadily increasing conversion rate as reaction time progresses (HBEA81, HBEA12, HBEA2 and HBEA24) except samples HBEA48 and HBEA72 which slightly decreased as the reaction reached 1440 min. This clearly indicated that the steadily increasing conversion rate can be associated with the catalysts with shorter crystallisation times of 8, 10, 12 and 24 h

(HBEA81, HBEA12, HBEA2 and HBEA24, respectively) compared to HBEA48 and HBEA72 with longer crystallisation times (Figure 6.17). This shows that the rapidly synthesised fly ash based HBEA zeolite catalysts are highly active and the conversion of anisole with BzCl increased as a function of reaction time. On the other hand, the decline in conversion rate of anisole over HBEA48 and HBEA72 zeolites made at longer synthesis times might indicate deactivation of the catalyst with increased reaction time which may be due to the low mesoporosity and longer diffusional pathways.

To substantiate the aforementioned results the selectivity of P_{4Me} and product yield over the two groups of HBEA zeolite (short hydrothermal time = HBEA81, HBEA10 and HBAE2 and long hydrothermal time = HBEA24, HBEA48 and HBEA72) were carried out and presented in Figure 6.18 and 6.19, respectively. Figure 6.18 depicts the selectivity of P_{4Me} over the synthesised HBEA zeolites.

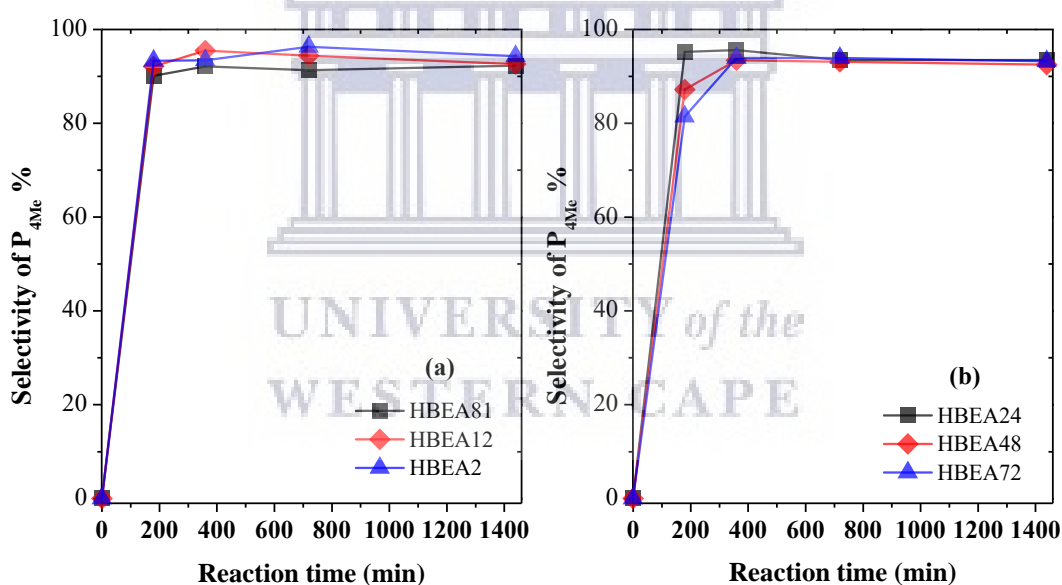


Figure 6.18: Selectivity of P_{4Me} over a) HBEA81, HBEA12 and HBEA2, and b) HBEA24, HBEA48 and HBEA72 zeolites (reaction conditions: temperature = 120 °C, maximum time = 1440 min, anisole/BzCl ratio = 2.5:1 and catalyst = 0.068 g).

Interestingly, it was observed that the conversion and selectivity of HBEA2 > HBEA12 > HBEA81 remained higher compared to HBEA24 > HBEA72 > HBEA48 samples (Figure 6.18a-b). Moreover, in Figure 6.18 the selectivity for P_{4Me} over HBEA zeolites was maintained between $80 > P_{4Me} \leq 96\%$, with the highest selectivity of between 95 and 97% recorded for HBEA2 and HBEA24. After the reaction time of 360 min, the selectivity of sample HBEA24 declined slightly from 96% to 94% which then was maintained as the reaction time was

prolonged to 1440 min (Figure 6.18b). Also, the selectivity of HBEA2 reduced by 2% at the acylation time of 1440 min. This suggested that the catalytic performance of fly ash based HBEA zeolites may be influenced by one or two or a combination of the following factors: crystal size, surface area, pore size distribution (porosity), framework aluminium and weak or strong acid sites.

Notably, among the short hydrothermal synthesised products, it was found that sample HBEA2 with the largest crystal size of 239 nm and high porosity, shows an excellent selectivity towards P_{4Me} compared to HBEA81 and HBEA12 (Table 6.5 and Figure 6.18a). Similarly, HBEA24 with a large crystal size of 370 nm was highly selective towards P_{4Me} compared to other long hydrothermal synthesised HBEA48 and HBEA72 zeolites (Figure 6.18b). This clearly shows that the selectivity of P_{4Me} over HBEA zeolite is probably due to the high mesoporosity of the catalyst which allow easier diffusional pathways of the reactant within the mesopores of a well-distributed hierarchical pore structured zeolites. The well-defined pore structure between 1 to 3.5 nm with high mesopores area of 208 and 210 m^2/g allow better contact with the strong acid sites of 0.66 mmol/g, respectively (see Figure 6.15 and Table 6.9-6.10). Thus, the well-defined hierarchical porosity of HBEA2 and HBEA24 favours better diffusion and limits steric hindrances in the pores of the zeolites. According to Bregolato et al. (2007) the high transformation of anisole to cresols was associated with larger crystal size of the BEA zeolite. This is due to the longer diffusional pathways of anisole within the zeolite porous structure where intramolecular rearrangement favours the formation of the major product, cresol. Arsenova-Härtel et al. (2000) and Ogunbadejo et al. (2015) also reported that in the alkylation of toluene the para-selectivity of the product was higher over a large crystal size of MFI zeolite. They further showed that the selective diffusion over the large crystal sizes eliminate surface diffusion. The percentage yield of P_{4Me} over the different HBEA zeolite samples was compared as presented in Figure 6.19.

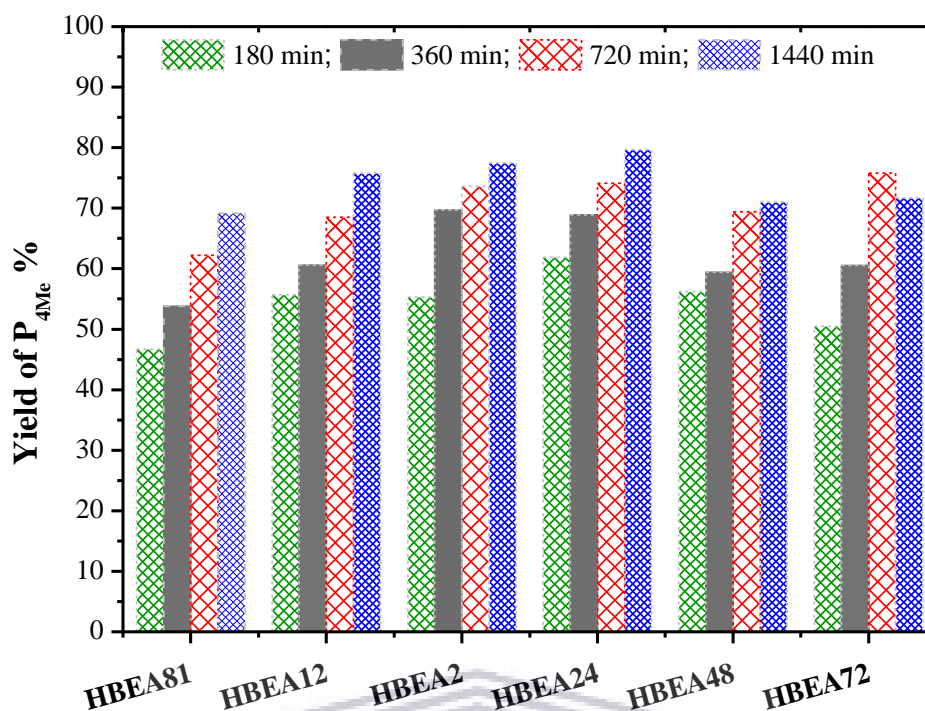


Figure 6.19: Percentage yield of P_{4Me} over HBEA81, HBEA12, HBEA2, HBEA24, HBEA48 and HBEA72 zeolites (reaction conditions: temperature = 120 °C, maximum time = 1440 min, anisole/BzCl ratio = 2.5:1 and catalyst = 0.068 g).

Figure 6.19 depicts the yield of P_{4Me} in the acylation of anisole with BzCl over HBEA zeolites catalyst (over HBEA81, HBEA12, HBEA2, HBEA24, HBEA48 and HBEA72). It was found that the increased yield of P_{4Me} is a function of increased reaction time. Generally, the gradual yield increase of P_{4Me} with reaction time was maintained between 47 and 80% over HBEA2 > HBEA12 > HBEA81 (short hydrothermal synthesis) and HBEA24 > HBEA72 > HBEA48 (long hydrothermal synthesis). Consequently, HBEA12, HBEA48 and HBEA72 achieve similar percentage yield at 0, 180, 360 and 720 min (0, >52, 60 and 69%, respectively) except HBEA72 which showed an increase at 720 h up to 76% yield and then the yield decreased to 72% at 1440 min. The highest P_{4Me} yield mostly achieved at all reaction times was observed over HBEA2 and HBEA24 zeolite both with large crystal sizes and high mesoporosity. Thus this confirms that the *p*-methoxyacetophenone (P_{4Me}) selectivity and yield was enhanced over large crystal size with hierarchical structure and well-distributed mesoporous structure of HBEA zeolites. Hence, it is confirmed that HBEA2 and HBEA24 catalyst are more active among the synthesised HBEA zeolites at all the acylation reaction times.

6.2.4.2 Influence of framework structure in the acylation reaction over HBEA zeolite

The selectivity of *p*-position (P_{4Me}) in the acylation of anisole with BzCl over HBEA81, HBEA12, HBEA2, HBEA24, HBEA48 and HBEA72 zeolites is presented in this section. Herein, the influence of framework Al, extra-framework Al and area of Q^4 Si(0Al) structure on the selectivity of P_{4Me} is presented in Figure 6.20.

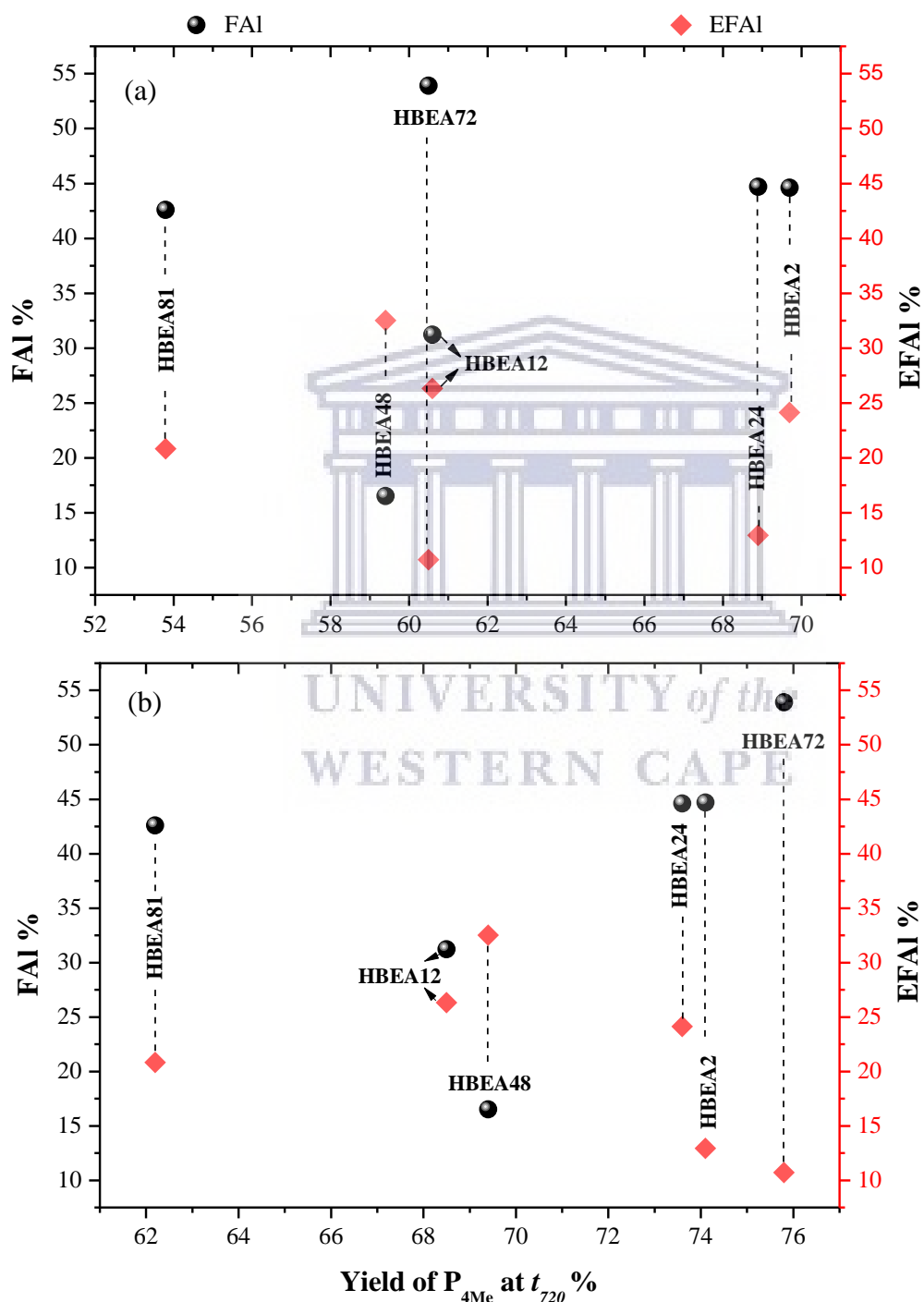


Figure 6.20: Influence of zeolite framework and extra-framework Al (HBEA81, HBEA12, HBEA2, HBEA24, HBEA48 and HBEA72) on the yield of P_{4Me} at a) t_{360} and b) t_{720} acylation time of 360 and 720 min.

Figure 6.20 depicts the correlation between zeolite frameworks Al (FAI), extra-framework Al (EFAI) to the percentage yield of P_{4Me} in the acylation of anisole with BzCl over HBEA81, HBEA12, HBEA2, HBEA24, HBEA48 and HBEA72 zeolites. The two mid reaction times, 360 and 720 min before any noticeable drop in the rate of conversion, selective or percentage yield was used to draw the relationship. From Figure 6.20a it was noticed that at the acylation time, t_{360} of 360 min the percentage yield of P_{4Me} follows the order: HBEA2 > HBEA12 > HBEA81 and HBEA24 > HBEA72 > HBEA48. Whereas, with progressive increase in acylation time, the yield of P_{4Me} constantly increases following the trend: HBEA2 > HBEA12 > HBEA81 and HBEA72 > HBEA24 > HBEA48 at t_{max} of 720 min (see Figure 6.20b). However, as the reaction time progresses to 1440 min, the yield of sample HBEA72 reduced by 15% while HBEA24 increased with 5%. To this end, the high catalytic performance of HBEA2 and HBEA24 with increased acylation time correlated with the presence of strong framework Al as shown in Figure 6.20a-b. The strong FAI of 44.6 and 44.7% associated with HBEA2 and HBEA24 was observed to influence the yield P_{4Me} with a progressive and constant percentage increase of: 55 < 70 < 74 < 78% and 62 < 69 < 74 < 80% with increased acylation time, respectively. Since the FAI can be associated with acid sites, this suggests that the acidity of the zeolite catalyst influenced the rate of conversion. Therefore this shows that Bronsted acid sites associated with framework Al species could enhance the selectivity towards P_{4Me} in a typical acylation reaction of anisole with BzCl over HBEA zeolite.

Aleixo et al. (2017) reported that with a reduced amount of EFAI species the exposed acid site of the framework Al and thus the related Bronsted acid allows high interaction of the reacting molecules thereby shifting the equilibrium towards the designed products. Kim et al. (2015) and Wang et al. (2017) attributed the preferential selectivity of *p*-position to the limitation suffered by *o*-position due to strong steric hindrance in the zeolite pores.

Figure 6.21 presents the relationship of the area of Q^4 Si(OAl) to the percentage yield of P_{4Me} in the acylation of anisole with BzCl at minimum and maximum reaction time.

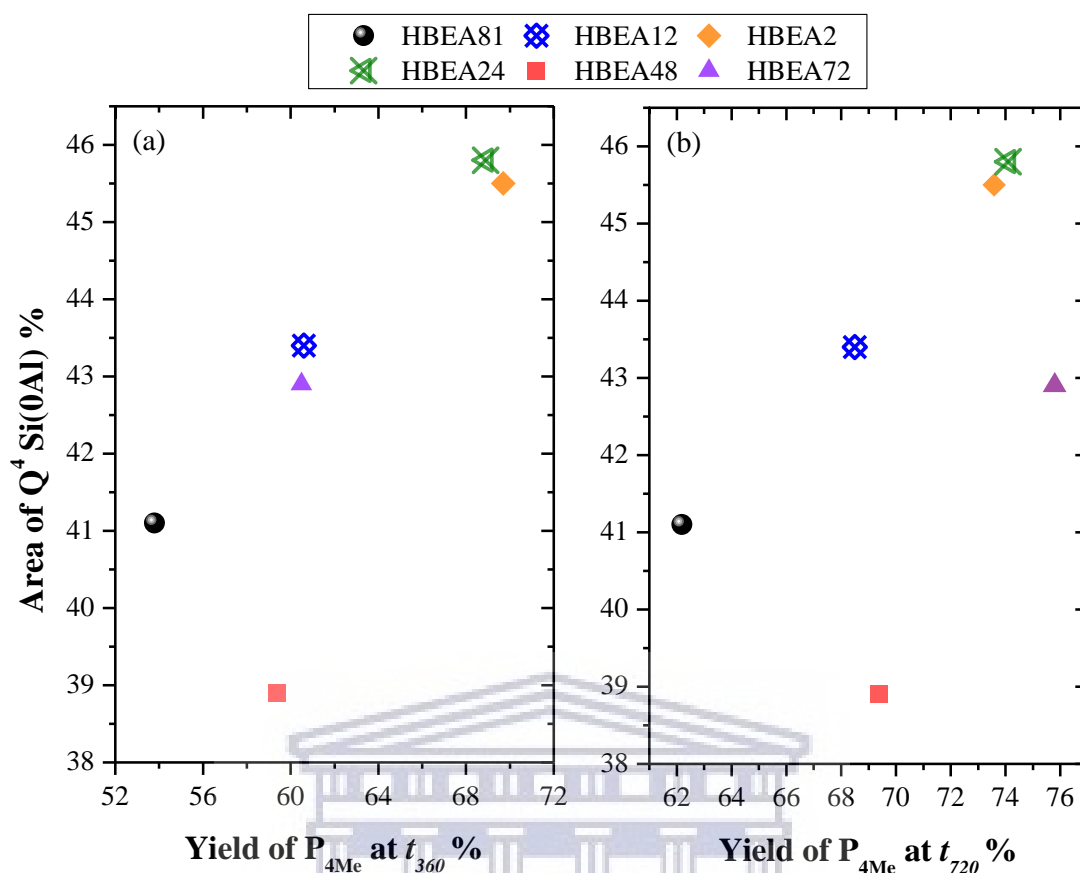


Figure 6.21: Influence of the area, Q⁴ Si(OAl) (HBEA81, HBEA12, HBEA2, HBEA24, HBEA48 and HBEA72) on the yield of P_{4Me} at a) t₃₆₀ and b) t₇₂₀ acylation time of 360 and 720 min.

Figure 6.21 shows the correlation of the Q⁴ Si(OAl) environment to the product yield of P_{4Me} at minimum and maximum acylation time of 360 and 720 min, respectively. The high yield of P_{4Me} at t₃₆₀ = 70 and 69% and t₇₂₀ = 74% was achieved over larger area of Q⁴ Si(OAl) environment (45.5 and 44.8%) HBEA2 and HBEA24, respectively. Interestingly, it is indicative in Figure 6.21 that at 360 and 720 min acylation reaction time the highest obtained percentage yield of P_{4Me} can be directly related to the larger peak area of Q⁴ Si(OAl) environment (HBEA2 and HBEA24). The percentage yield gradual increased by 3 and 6% with increased reaction time of 1440 min (HBEA2 and HBEA24, respectively). Hence, this study proposes that HBEA peak area of the Q⁴ Si(OAl) environment correlated significantly with the high catalytic activity for the acylation reaction of anisole with BzCl. Thus, larger Q⁴ Si(OAl) area indicated the presence of high mesoporous area (see Table 6.9) which allowed easy diffusion of anisole through FAI thereby enhancing better catalytic performance of the synthesised HBEA zeolites (see Figure 6.20a-b).

6.2.4.3 Influence of HBEA textural and acidic properties in the acylation reaction

This section elucidated the behaviour of the surface area, micropore area, micropore volume and acid sites to the catalytic performance of short (HBEA81, HBEA12 and HBEA2) and long (HBEA24, HBEA48 and HBEA72) hydrothermally synthesised zeolites in the acylation reaction of anisole with BzCl. Table 6.11 shows the influence of surface area, microporous area and strong acid sites of the HBEA zeolites in the acylation reaction of anisole and BzCl at 360 min (t_{360}) and 720 min (t_{720}), the time before any decline in conversion rate was noticed.

Table 6.11: Correlation of the catalytic performance to the textural and acid sites properties of HBEA zeolites.

Zeolite	S_{BET} [m ² /g]	S_{micro} [m ² /g]	S_{meso} [m ² /g]	Strong acid [mmol/g] NH ₃	Conversion %		Selectivity %	
					T_{360}	t_{720}	T_{360}	t_{720}
					HBEA81	538	361	177
HBEA12	702	488	214	0.29	63	73	96	94
HBEA2	633	425	208	0.66	75	76	94	96
HBEA24	722	512	210	0.17	72	79	96	94
HBEA48	538	439	99	0.20	64	75	93	93
HBEA72	670	543	127	0.14	65	81	94	94

Note: S_{BET} : BET surface area; S_{micro} : micropore area, S_{meso} : mesopore area, t_{360} and t_{720} : reaction time 360 and 720 min before any decline in conversion rate.

Table 6.11 shows the conversion of anisole and selectivity of P_{4Me} in the acylation of anisole with BzCl over HBEA zeolite at 360 and 720 min reaction time. The materials are grouped (HBEA zeolites) according to short hydrothermal time synthesis of 8, 10 and 12 h (HBEA81, HBEA12 and HBEA2) and long hydrothermal time synthesis of 24, 48 and 72 h (HBEA24, HBEA48 and HBEA72). The association between surface area, micropore area, mesopore area and strong acid sites to the conversion rate, selectivity and yield was established.

The conversion of anisole and selectivity of P_{4Me} over the surface area of 538 m²/g HBEA81 at t_{360} was 59 and 92% which gradually increased to 68 and 91% at t_{720} as presented in Table 6.11. As the surface area increased to 702 m²/g in HBEA12 the rate of anisole conversion and selectivity of P_{4Me} increased to 63 and 96% at t_{360} , respectively. Moreover, as the acylation reaction reaches t_{720} , the rate of conversion and selectivity over HBEA12 increased to 73 and

94%, respectively. Also, the acylation of anisole with BzCl over HBEA2 zeolite ($S_{\text{BET}} = 633 \text{ m}^2/\text{g}$) showed a conversion rate of 75% and selectivity of 94% at t_{360} which increased both in conversion and selectivity with time, t_{720} to 76 and 96%, respectively. This shows that HBEA2 achieved the best catalytic performance compared to HBEA81 and HBEA12 in the acylation reaction of anisole with BzCl due to the high mesoporous area and strong acid sites of $208 \text{ m}^2/\text{g}$ and $0.66 \text{ mmol}/\text{g}$, respectively (see Table 6.9 and 6.10).

Based on the long hydrothermal synthesised HBEA zeolite (HBEA24, HBEA48 and HBEA72), the conversion of anisole and selectivity of $\text{P}_{4\text{Me}}$ over the surface area of $538 \text{ m}^2/\text{g}$ of HBEA48 at t_{360} was 64 and 93% which increased to 75 and 93% at t_{720} , respectively (Table 6.11). With increasing surface area ($670 \text{ m}^2/\text{g}$ HBEA72) a gradual increase in the rate of conversion (65 and 81%) and selectivity (94%) was observed at t_{360} and t_{720} , respectively. After a further increase in surface area, $722 \text{ m}^2/\text{g}$ for HBEA24, the rate of conversion and selectivity increased to 72 and 96% at t_{360} . As the acylation time increased, t_{720} the rate of conversion increased to 79% as the selectivity of $\text{P}_{4\text{Me}}$ was maintained at 94%. On the other hand, a slight reduction occurred in the conversion of anisole at t_{720} by 2% over the highest surface area HBEA24 ($722 \text{ m}^2/\text{g}$) compared to $670 \text{ m}^2/\text{g}$ of HBEA72 zeolite. Interestingly, when the acylation reaction reached 1440 min, the conversion of anisole over sample HBEA24 maintained a consistent increase compared to sample HBEA72 which showed a significant decline in the rate of conversion, selectivity and yield (see Figure 6.17, 6.18 and 6.19). This is indicative that the rate of conversion and selectivity correlate directly with the high surface area of HBEA2 and HBEA24 zeolite (Table 6.11).

In order to further understand the textural properties that influence better catalytic performance, correlation between the mesopores area and the rate of conversion and selectivity was investigated as presented in Table 6.11 and Figure 6.22.

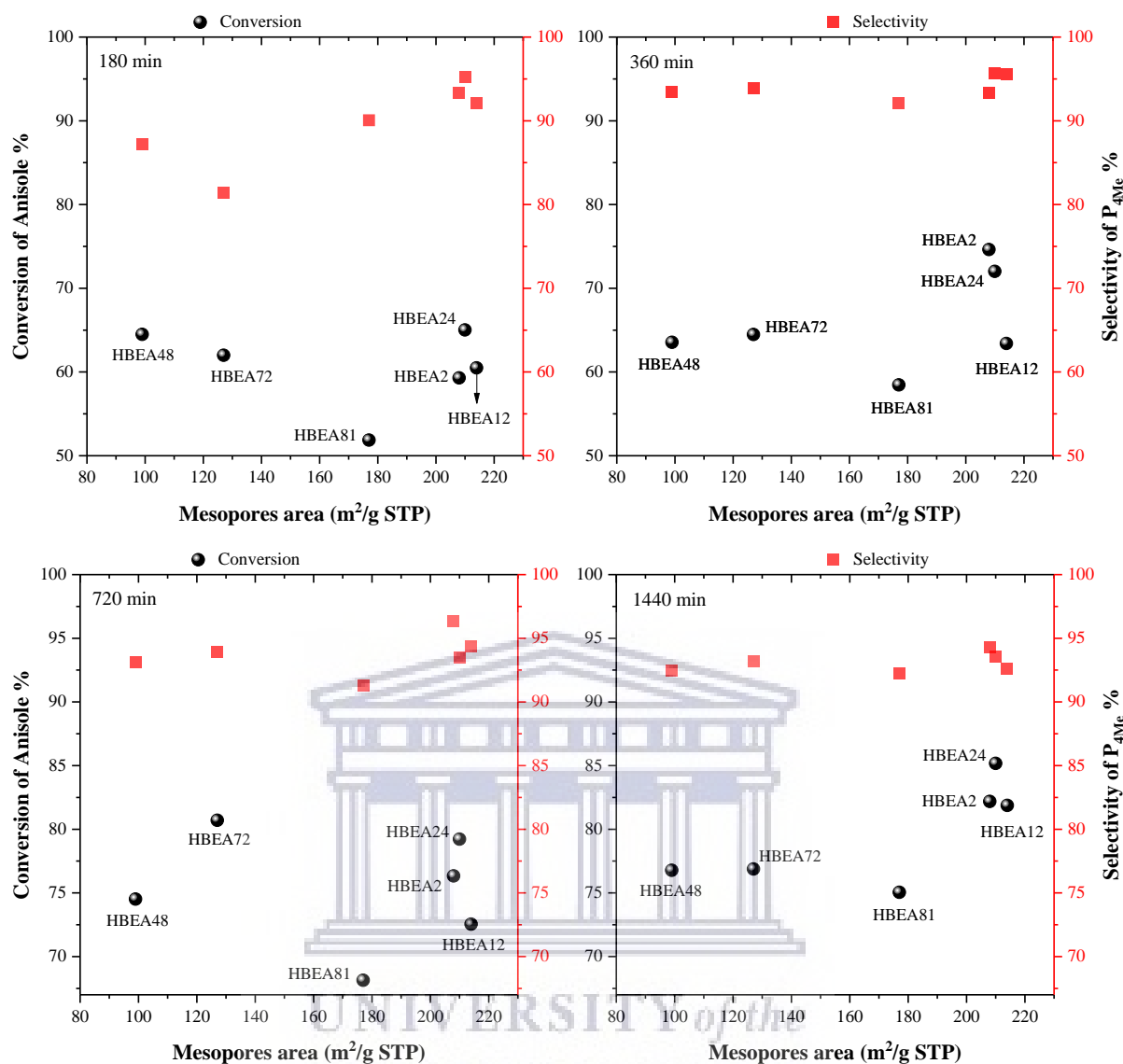


Figure 6.22: Conversion of anisole as a function of mesoporosity of HBEA zeolite (HBEA81, HBEA12, HBEA2, HBEA24, HBEA48 and HBEA72) in acylation reaction.

Figure 6.22 shows the relationship between the rate of anisole conversion, selectivity and the mesopores area of the HBEA zeolite in the acylation reaction of anisole with BzCl. It was observed that among the short hydrothermal synthesised zeolite (HBEA81, HBEA12 and HBEA2), the conversion of anisole and selectivity over HBEA2 constantly shows most of the highest catalytic performances as the reaction time progressed from 180 to 1440 min (see Figure 6.22). This could be ascribed to the significantly high mesoporosity (208 m²/g) which allowed easy accessibility of the reactant to the strong acid sites (0.66 mmol/g) within the pore structure of the HBEA2 zeolite (see Table 6.11). On the contrary, HBEA12 with the highest mesoporous surface area of 214 m²/g but low strong acid sites (0.29 mmol/g) showed reduced catalytic performance. This indicated that since HBEA2 possesses both

high mesoporous area and strong acid sites (0.66 mmol/g), anisole could diffuse through the well-defined hierarchical pore structure (above 2 nm) of the zeolite to the active acid sites which promoted the rate of conversion and selectivity. Also, the limited conversion of the reactant despite the high mesopore area of HBEA12 can be attributed to few strong acid sites in the framework which in turn lowered the conversion of anisole and the selective formation of P_{4Me}.

Similarly, the 24, 48 and 72 h hydrothermal synthesised HBEA zeolites showed active catalytic performance in the acylation of anisole with BzCl (see Table 6.11 and Figure 6.22). The reduced catalytic performance correlated with decreased mesoporous area: 210>127>99 m²/g (HBEA24, HBEA72 and HBEA48, respectively). Thus, the existence of small mesoporous surface area and few strong acid sites slows the conversion of anisole, thereby reducing the acylation reaction with BzCl within the zeolite. This further supports that large mesoporous area allows accessibility of the diffused reactants to interact with sufficient active acid sites which then facilitates the selective formation of products. Serrano et al. (2009) reported that the catalytic performance of MCM-41 and ZSM-5 can be enhanced by mesoporous structure and active acid sites within the framework structure of zeolite in an acylation reaction. Kim et al. (2015) also showed that MFI zeolite structures with well-defined mesoporous structure allows the rapid diffusion of the reacting molecules to exhibit better conversion and selectivity.

The efficiency of the catalytic conversion of anisole and the selectivity of P_{4Me} over HBEA2 and HBEA24 have shown to be the highest as a function of reaction time, framework Al, area of Q⁴ species, large mesopore area and active acid sites. Hence, this study clearly demonstrated that the catalytic performance of CFA based BEA zeolite is equivalent to pure chemical based synthesised BEA zeolites. Also, it was shown that the combination of strong FAI and the peak area of the Q⁴ Si(0Al) species can influence better catalytic performance. Therefore HBEA2 and HBEA24 were chosen for further study which included the influence of anisole/benzoyl chloride ratio and the kinetics of the reaction and deactivation of the catalyst.

6.2.4.4 Influence of anisole/benzoyl chloride ratio in acylation reaction

The comparison of 5:1 and 9.5:1 anisole/BzCl ratio in the acylation reaction over HBEA2 and HBEA24 zeolites is presented in this section (detailed in Table 3.7). Also, the percentage

selectivity and yield of P_{4Me} (4-methoxyacetophenone) and P_{2Me} (2-methoxyacetophenone) and phenyl benzoate are presented herein. Figure 6.23 and 6.24 depicts the conversion of anisole and selectivity of P_{4Me} (anisole/BzCl ratio = 5:1 and 9.5:1, respectively).

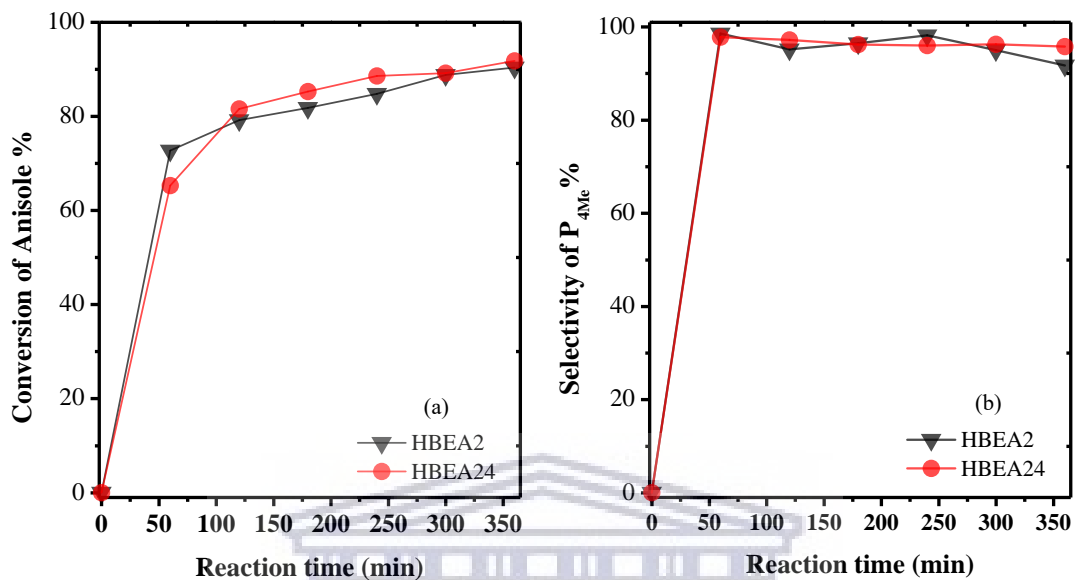


Figure 6.23: Anisole conversion and selectivity of P_{4Me} over HBEA2 and HBEA24 zeolites (reaction conditions: temperature = 120 °C, maximum time = 350 min, anisole/BzCl ratio = 5:1 and catalyst = 0.068 g).

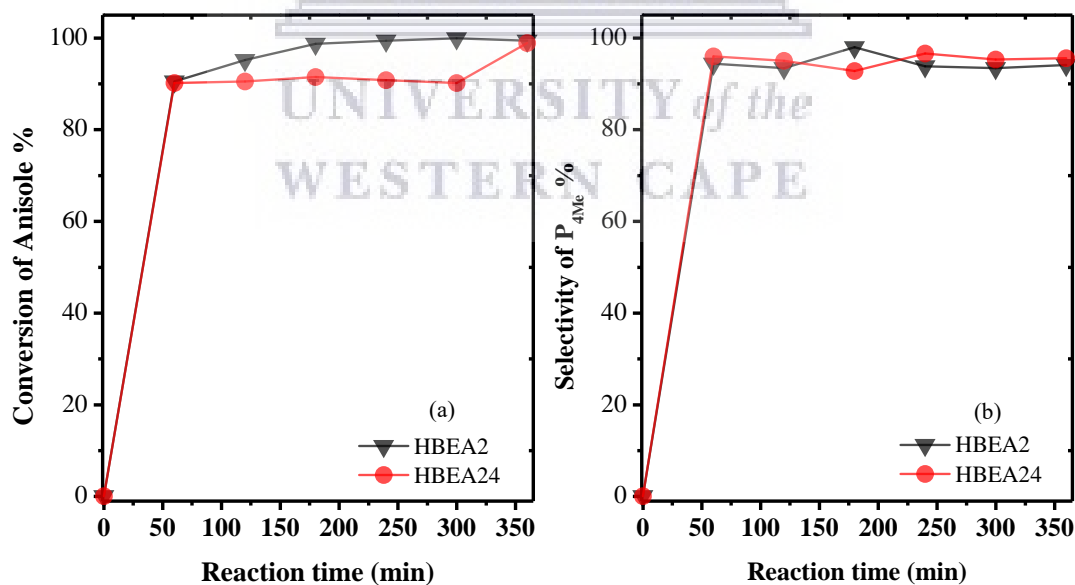


Figure 6.24: Anisole conversion and selectivity of P_{4Me} over HBEA2 and HBEA24 zeolites (reaction conditions: temperature = 120 °C, maximum time = 350 min, anisole/BzCl ratio = 9.5:1 and catalyst = 0.068 g).

Figure 6.23 and 6.24 depict the conversion of anisole and the selectivity towards P_{4Me} in the acylation of anisole with BzCl ratio (ratio = 5:1 and 9.5:1) over HBEA2 and HBEA24

zeolites. When the molar fraction of anisole/BzCl was 5:1 (Figure 6.23a), 72 or 70% conversion over HBEA2 or HBEA24 zeolite was obtained after 60 min of reaction, respectively. As the reaction time progressed from 60 to 360 min the conversion of BzCl continually increased with the highest conversion of 90% recorded after 360 min. Under similar conditions, with increased anisole/BzCl ratio to 9.5:1, the conversion rate increased to about 91% over HBEA2 and HBEA24 at an acylation time of 60 min, respectively (Figure 6.24a). It was confirmed that the conversion and selectivity of the acylation of anisole with BzCl reaction is a function of time. The acylation over HBEA24 maintained almost $\leq 91\%$ conversion of P_{4Me} at reaction time between 60 and 300 min (Figure 6.24a) with anisole/BzCl ratio of 9.5:1. On the other hand, HBEA2 showed a consistent increase in the conversion of anisole over time with a maximum of 99% conversion achieved after 240 min. This shows that at high anisole/benzoyl chloride ratio the rate anisole of conversion reached the maximum of 99% compared to 59 or 65% conversion at a lower anisole/benzoyl chloride ratio (Figure 6.17).

Thus, the performance of the fly ash based HBEA zeolite can be influenced by the molar ratio fraction of the reactant (anisole/BzCl) and increased anisole/BzCl ratio led to higher conversion of anisole. The selectivity and yield of the acylation of anisole for different ratios of benzoyl chloride over HBEA2 and HBEA24 zeolite was compared as shown in Figure 6.23-6.24 and Table 6.12-6.13.

Table 6.12: Selectivity and yield of P_{2Me} , P_{4Me} and phenyl benzoate (P_{Bz}) over HBEA2 and HBEA24 zeolite in a reaction mix of anisole/BzCl ratio 5:1.

Product	Samples	Selectivity %	Yield %					
			Reaction time (min)					
			60	120	180	240	300	360
P_{4Me}	HBEA2	91.7 - 98.6	71.7	75.4	83.2	78.9	84.4	82.9
	HBEA24	95.8 - 97.8	63.9	79.4	82.1	85.1	85.9	87.9
P_{2Me}	HBEA2	0.1 - 4.9	-	2.6	0.1	1.7	2.7	4.4
	HBEA24	1.4 - 2.3	-	1.4	1.8	2.3	2	2
P_{Bz}	HBEA2	1.4 - 3.5	1.0	1.2	1.4	1.1	1.7	3.1
	HBEA24	0.8 - 1.9	1.4	0.8	1.5	1.2	1.3	1.9

Table 6.13: Selectivity and yield of P_{2Me}, P_{4Me} and phenyl benzoate (P_{Bz}) over HBEA2 and HBEA24 zeolite in a reaction mix of anisole/BzCl ratio 9.5:1.

Product	Samples	Selectivity %	Yield %					
			Reaction time (min)					
			60	120	180	240	300	360
P _{4Me}	HBEA2	93.4 - 98.0	85.4	88.9	96.8	93.2	93.4	93.6
	HBEA24	92.8 - 96.6	85.7	86.0	84.9	85.8	86	94.5
P _{2Me}	HBEA2	2.7 - 4.0	3.2	-	-	3.5	4.0	2.7
	HBEA24	1.7 - 2.7	2.4	3.0	3.1	1.7	1.7	1.8
PBz	HBEA2	1.8 - 6.7	1.9	6.2	1.9	2.6	2.6	3.2
	HBEA24	1.3 - 3.8	2.1	2.3	3.5	1.3	2.5	2.5

Note: the products P_{4Me}, P_{2Me} and PBz = 4-methoxyacetophenone, 2-methoxyacetophenone and phenyl benzoate.

Table 6.12 and 6.13 show the product selectivity and their percentage yield in the probe acylation reaction of anisole with BzCl over HBEA2 and HBEA24 zeolites. The identified products over HBEA2 and HBEA24 zeolites included P_{2Me}, P_{4Me} and phenyl benzoate. Both catalysts showed that P_{4Me} is the main product in all the acylation reactions. When an anisole/BzCl ratio of 5:1, was applied the highest selectivity of 99 and 98% P_{4Me} with a yield of 72 and 64% was observed over HBEA2 and HBEA24 after the acylation reaction of 60 min, respectively (Figure 6.23 and Table 6.12). After the acylation time of 120 min, there was a slight decline in selectivity over HBEA2 and HBEA24 (from 99 and 98% to 95 and 97%, respectively). As the acylation reaction was further prolonged in the 5:1 anisole/BzCl ratio, the selectivity gradually decreased (Figure 6.23). However, the percentage yield maintained a consistent increase from 72 to 83% and 64 to 88% (HBEA2 and HBEA24, respectively) with increased reaction time (Table 6.12).

When the molar ratio of anisole/BzCl was 9.5:1, the selectivity and yield was between 93 and 98% and 85 and 98% over HBEA2 and HBEA24 (Figure 6.24 and Table 6.12-6.13). Moreover, a steady increase in the yield of P_{4Me} was observed for the 9.5:1 anisole/BzCl ratio (Table 6.13). At 180 min, HBEA2 showed the highest selectivity and yield of 98 and 97%, respectively. Only a small amount of about 1 to 4% P_{2Me} (isomer) and phenyl benzoate was observed in the acylation reaction. After 180 min, equilibrium was attained from 240 to 360 min by maintaining 93 and 86% yield of P_{4Me} (HBEA2 and HBEA24, respectively). Expect for HBEA24 which increased in yield by 8% after 360 min acylation reaction.

It can be deduced from this study that the acylation reaction of anisole with BzCl over fly ash based HBEA zeolites shows that: i) selectivity and yield increased with increased molar fraction of anisole/BzCl reactants, ii) with anisole/BzCl ratio of 9.5:1 selectivity decreased while yield increases, iii) the best acylation reaction time with highest selectivity and yield was at 180 min and iv) HBEA2 zeolite is highly active in conversion of anisole with the highest selectivity and yield of P_{4Me} compared to HBEA24 sample. Suggesting that the preferential selectivity of para-position (P_{4Me}) over ortho-position (P_{2Me}) could be due to stronger steric hindrance.

Calleja et al. (2014) reported that the relative yield of 4-methoxyacetophenone increased with a reduced concentration of the acylating agent in a typical acylation reaction of anisole with acetyl chloride over ZSM-5 zeolites. They further observed that the formation of 2-methoxyacetophenone is likely favoured by the presence of benzoic acid due to the anhydride nature of the acylating agent (benzoyl chloride). Also, the side product of phenyl benzoate might have resulted from the benzoylation or demethylation of anisole to form phenol (Wagholikar et al., 2007; Patil et al., 2002). Wagholikar et al. (2007) further observed that the presence of phenol compounds as a side product could be due to the bimolecular disproportionation of anisole on the acid sites. This elucidates the fact that the indirect hydrothermal synthesised BEA from CFA possesses the textural properties and acidic centres suitable for selective reaction (shape selectivity) in a typical liquid phase reactions.

6.2.4.5 Reaction kinetics

This section presents the reaction kinetics obtained from the experimental results in the aforementioned subsection 6.2.3.2. The kinetic study was performed based on acylation time, temperature and percentage conversion following the Langmuir-Hinshelwood mechanism. Theoretically, the acylation reaction is influenced by the concentration of anisole and benzoyl chloride. Since anisole is the excess reactant (mole ratio 5:1 and 9.5:1 anisole/BzCl), the acylation of anisole was considered as a pseudo-first-order reaction with respect to BzCl. Hence, the reaction rate equation can be said to follow the standard first-order reaction rate expression as shown in equation 6.1.

$$-\ln(1 - X) = kt$$

Equation 6.1

where k is the reaction rate constant, t is the reaction time and X is the conversion of anisole. Figure 6.25 (regression plot) illustrates the plots of $-\ln(1 - X)$ against reaction time, t (min) over HBEA2 and HBEA24 zeolites at 120 °C.

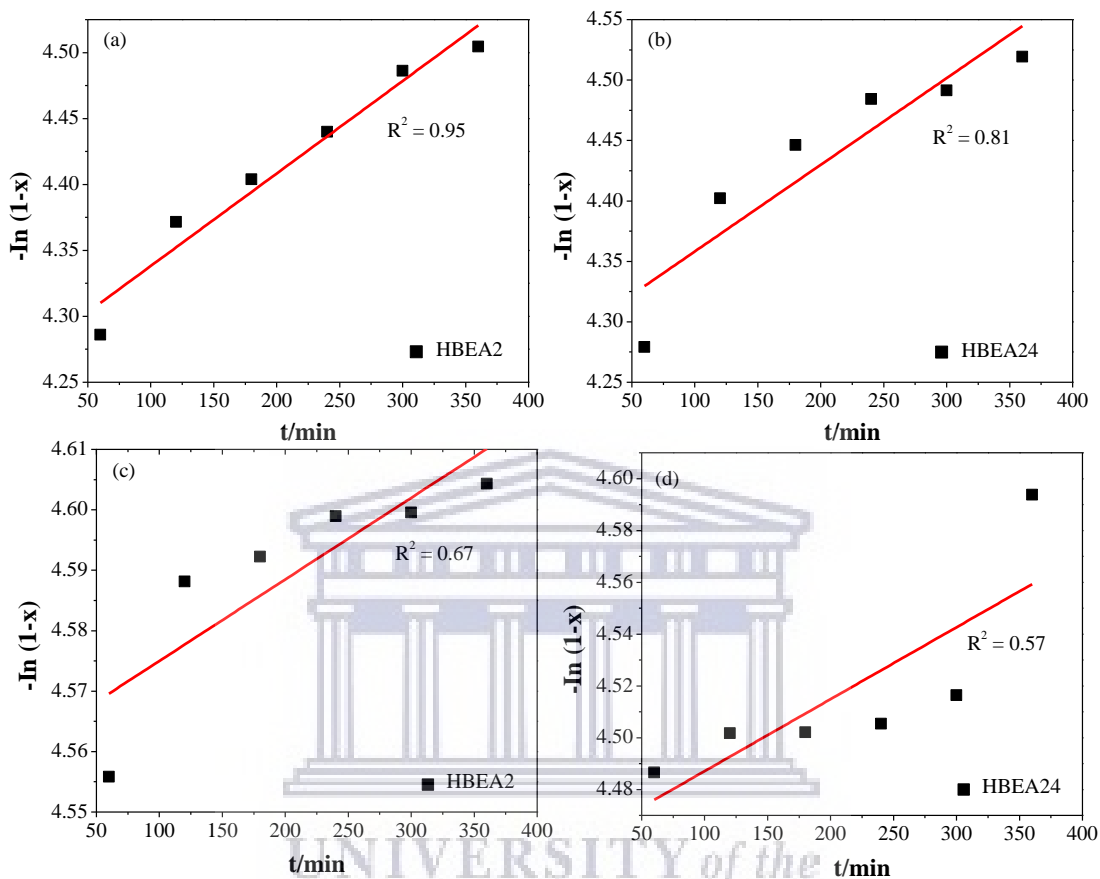


Figure 6.25: Regression plot illustrate the pseudo-first-order reaction of excess anisole reacting BzCl in molar ratio of a-b) 5:1 and c-d) 9.5:1 anisole/BzCl.

The plot in Figure 6.25 confirms that the acylation of anisole with benzoyl chloride over HBEA2 and HBEA24 zeolite is a function of time. Also, the acylation reaction follows a first-order reaction rate over HBEA2 and HBEA24 in respect to BzCl as the limiting reagent. It was observed that the regression value, R^2 was 0.95 and 0.81 when anisole/BzCl ratio was 5:1 for HBEA2 and HBEA24, respectively. With increased anisole/BzCl ratio to 9.5:1 the R^2 value reduced to 0.67 and 0.57 for HBEA2 and HBEA24, respectively. This suggests a better catalytic performance of HBEA2 and HBEA24 zeolite at 5:1 anisole/BzCl ratio since the regression shows a relatively good correlation of $R^2 = 0.95$ and 0.81 with selectivity of P_{4Me} . Whereas, the declined selectivity observed at anisole/BzCl ratio of 9.5:1 elucidated the poor correlation value of $R^2 = 0.67$ and 0.57 as presented in Figure 6.25 and Table 6.14.

Table 6.14: Kinetics showing the rate of reaction of anisole with BzCl over HBEA zeolite.

Zeolite	Anisole/BzCl ratio	Kinetics value	
		R ²	k (10 ⁻¹ min)
HBEA2	5:1	0.95	7.0
	9:1	0.67	3.0
HBEA24	5:1	0.81	7.8
	9:1	0.51	2.0

In Table 6.14 a high reaction rate, k of 7.0 and 7.8 (10^{-4} min^{-1}) was noticed with the acylation of anisole/BzCl ratio of 5:1 over HBEA2 and HBEA24 zeolites, respectively. However, the deviation of k , 3.0 and 2.0 (10^{-4} min^{-1}) is lower with an increased anisole/BzCl ratio to 9.5:1 for HBEA2 and HBEA24, respectively. This indicated that due to the increment of the forward reaction, k , the rate of $P_{4\text{Me}}$ selectivity would increase at anisole/BzCl ratio of 5:1. However, the highest anisole conversion and yield was mostly achieved using the acylation of anisole/BzCl ratio of 9.5:1 over HBEA2 and HBEA24 zeolite. With the increase of the molar ratio of anisole/BzCl ratio from 5:1 to 9.5:1, the equilibrium of the reaction for the conversion of anisole increased from 73 to 90.5% and 73 to 90.1% (reaction time = 60 min) (HBEA2 and HBEA24, respectively) which further increased to 99.89% as a function of reaction time.

6.2.4.6 Regeneration of HBEA zeolite in acylation reaction

The reuse of HBEA2 and HBEA24 zeolite in the acylation of anisole with benzoyl chloride was investigated. The deactivation tests were carried under the following conditions of 9.5:1 anisole/BzCl ratio at 120 °C for 60 min with the fresh catalyst (recycled and recalcined) subjected to three reaction runs and regeneration cycles. After each cycle, the zeolites were filtered-off and washed with dichloromethane several times as described in section 3.2.5.3. Afterwards, the HBEA zeolite were calcined in air at a ramping rate of 15 °C/min and held at 450 °C for 3 h to remove moisture and organics. The aforementioned parameters were chosen because i) the highest conversion rate was achieved within the shortest reaction time of 60 min under 9.5:1 anisole/BzCl ratio, ii) both HBEA2 and HBEA24 catalysis have similar anisole conversion rates after 60 min acylation reaction and iii) since the conversion is higher at high molar ratio of anisole/BzCl, the adsorption of the product was achieved in short reaction time. Figure 6.26 and 6.27 depicts the conversion and yield of $P_{4\text{Me}}$ over regenerated HBEA2 and HBEA24 zeolites.

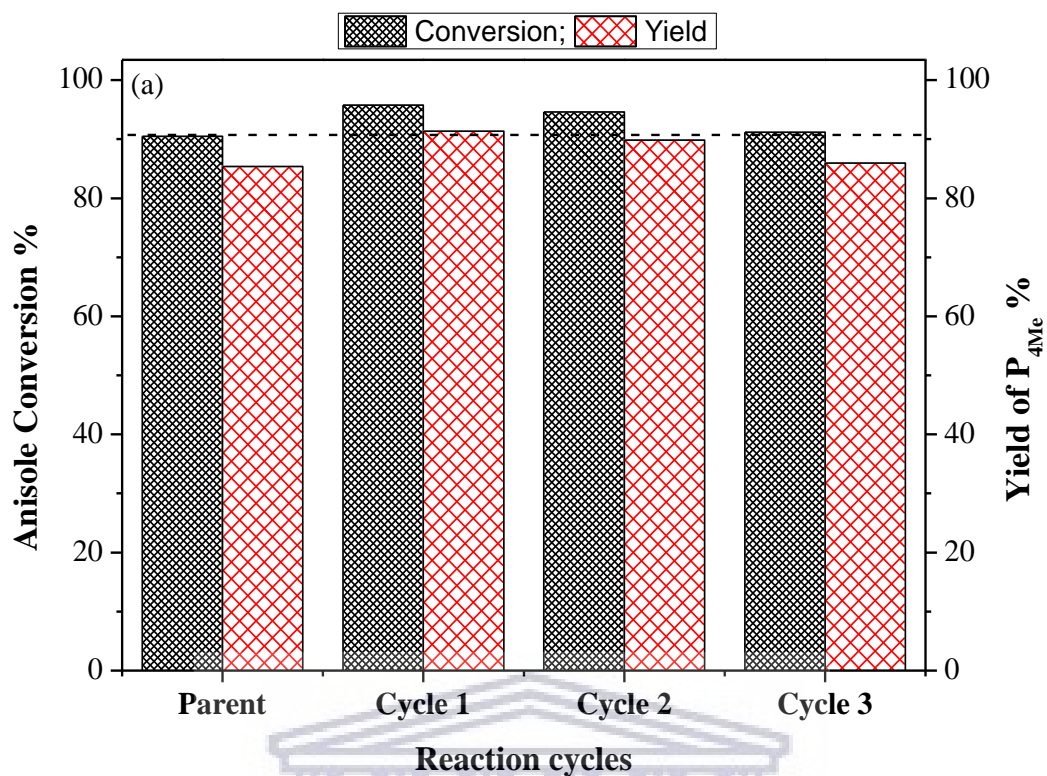


Figure 6.26: Conversion of anisole and percentage yield of P_{4Me} over recycled HBEA2 in the acylation reaction based on 9.5:1 anisole/BzCl ratio for 60 min.

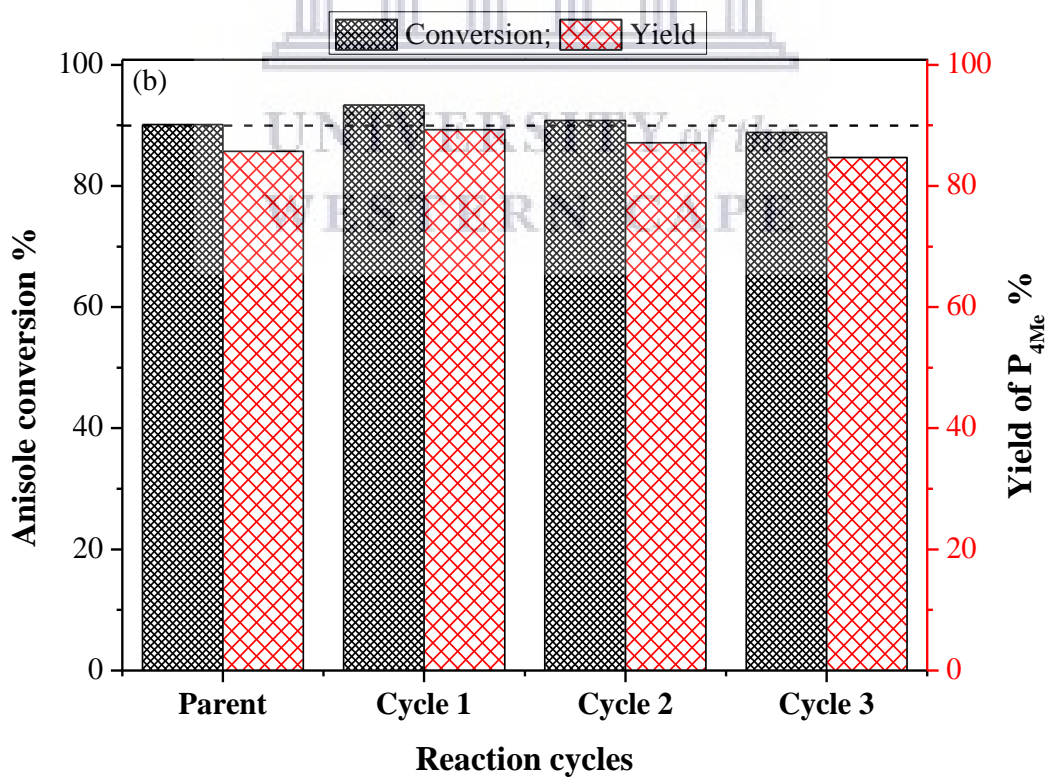


Figure 6.27: Conversion of anisole and percentage yield of P_{4Me} over recycled HBEA24 in the acylation reaction based on 9.5:1 anisole/BzCl ratio for 60 min.

Figure 6.26 and 6.27 depicts the reuse of HBEA2 and HBEA24 catalyst over three reaction cycles. Comparing the activity of the parent HBEA2 and HBEA24 with each following cycle of regeneration, it was interesting to notice that at the first reuse cycle the conversion of anisole increased from 90% (parent zeolite) to 96 and 93% in the acylation over HBEA2 and HBEA24, respectively. At the second cycle, HBEA2 (Figure 6.26) still showed an increase of 95% above the threshold while HBEA24 reached 91.1% conversion rate (Figure 6.27) which was close to the threshold. In the third cycle, the catalytic performance of HBEA2 reduced to 91% which is slightly above the parent conversion of 90.5% (threshold). On the other hand, the conversion of anisole over HBEA24 further declined to 89% which was slightly below the 90.5% of the parent conversion rate. Hence, these results showed that the fly ash based HBEA zeolites can be regenerated for several reaction cycles. Thus, it could be speculated that the catalytic activity of the reused HBEA zeolite can be associated with the ability to maintain phase purity, structural integrity and framework stability.

Figure 6.28 presents the changes that occurred in the zeolitic phase, structural transformation and framework stability using XRD after the reuse of the catalyst over three cycles.

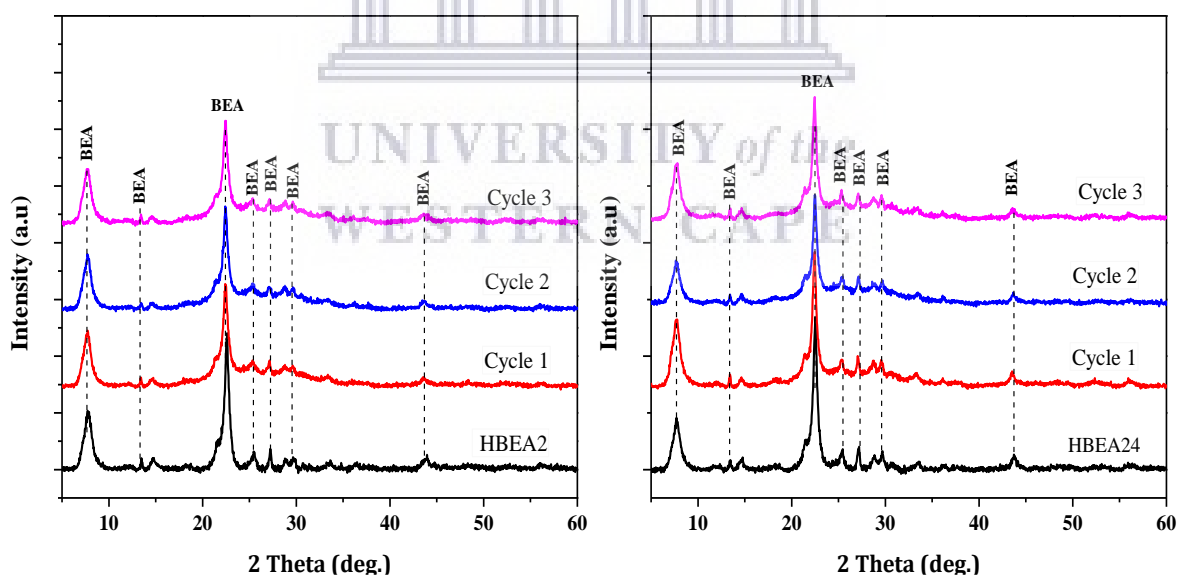


Figure 6.28: XRD spectra of the recycled catalyst a) HBEA2 and b) HBEA24 zeolite in the acylation of anisole with BzCl.

The XRD diffractogram in Figure 6.28 shows the phase purity of the recycled HBEA2 and HBEA24 after three acylation reaction and regenerations cycle. It was observed that the diffraction patterns of the parent zeolites at 7.7, 13.4, 22.4, 27.1, 28.7, 29.6 and 43.4° 2θ was

retained after each recycled process. Although, the peak intensity at $2\theta = 22.4^\circ$ of the zeolite decreased gradually with repeated cycles compared to the parent HBEA zeolites (HBEA2 and HBEA24), however, the phase integrity was still maintained. The decrease in peak intensity is indicative that the repeated regeneration of the HBEA zeolite could lead to a gradual structural degradation after several acylation reactions. Hence, the stability of the regenerated zeolites confirms that the prepared fly ash based HBEA zeolites is suitable for the acylation reaction and can be recycled.

6.3 Chapter summary

The synthesis of HBEA zeolite from coal fly ash at a short hydrothermal time was a function of reduced molar water fraction in the synthesis mixture. High molar water fraction hinders the complete formation of pure phase BEA zeolite within a short synthesis time due to residue of amorphous material remaining in the zeolitic product. The minimum molar water fraction = 1.77 induced rapid crystallisation of HBEA zeolite within the shortest hydrothermal time of 8 h or less. The rapidly grown HBEA crystals were smaller in size and had high surface area as well as high mesopore area and stronger acid sites. Interestingly, the catalytic performance of the HBEA zeolite prepared either in short (8, 10 and 12 h) or long (24, 48 and 72 h) hydrothermal time was above 50% in the conversion of anisole. The gradual increase in the rate of conversion was a function of increasing the reaction time. HBEA2 and HBEA24 zeolite samples were the most promising catalysts for the acylation of anisole with BzCl with percentage conversion of 82 and 85%, respectively. The catalytic performance significantly increased to 99.8% between the reaction time of 60 and 180 min with increased molar ratio of anisole/BzCl (5:1 or 9.5:1) with percentage selectivity and yield of 98 and .97%, respectively. The different factors that influenced the performance of the CFA synthesised HBEA zeolite in the acylation of anisole with BzCl included: reaction time, framework Al, peak area of Q4 Si(0Al) species, large mesopore area and active acid sites. Moreover, the regenerated HBEA zeolite maintained a stable structure with no phase compromise and active catalytic performance >80% conversion rate and percentage yield after three regenerated cycles. Therefore, the fly ash based prepared HBEA zeolite is suitable as a heterogeneous catalyst for the liquid phase conversion of anisole with active performance.

Chapter 7

Conclusions and recommendations

This chapter summarizes the significance of the research findings based on the outlined aims and objectives in chapter 1. Further highlighted herein is the overview elucidating the contribution to knowledge of the research and afterwards, a concluding synopsis was presented. In addition, the chapter outlines recommendations for future research on the synthesis, modification and applications of BEA zeolite.

7.0 Introduction

The laboratory synthesis of high silica BEA zeolite with high industrial values from pure chemical source have been reported by several researchers. However, the cost of the needed feedstock material such as silica and aluminium is high. Hence, since the components of CFA (SiO_2 and Al_2O_3) is similar to that of zeolites, it may be an alternative and cheap feedstock material. Therefore the reuse of CFA will not only solve its environmental impacts, but the development of an innovative process for the production of BEA zeolite will also add industrial value. However, there are challenges associated with the synthesis process. This included low molar Si/Al ratio of CFA, external addition of Si and Al source and impure zeolite phase. Hence, it is important to develop and design an effective synthesis protocol that is void of the aforementioned and will promote the production of pure high silica BEA zeolite with high catalytic activity from CFA. The major focus of the study was to synthesise BEA zeolite by indirect hydrothermal synthesis from South Africa CFA without the addition of an extra silica source. Also, the behaviour and performance of the synthesised HBEA zeolite was evaluated in liquid phase and acylation reaction. In order to achieve this, five major objectives were outlined in the introductory part as follows: i) attain a high molar Si/Al ratio of the feedstock by use of oxalic acid as the chelating agent for the extraction of silica from CFA, ii) Identify and optimise the synthesis conditions such as molar formulation and synthesis time for the production of BEA zeolite from the fly ash based extract using the indirect hydrothermal process, iii) determine the stability of the synthesised BEA zeolite in hot liquid phase reaction, iv) determine the physicochemical properties and catalytic performance of the synthesised BEA zeolite in acylation, v) determine the percentage conversion, selectivity and product yield in the acylation reaction. Conclusions are drawn below based on each of these objectives as achieved in line with the research questions.

7.1 Research findings

7.1.1 Attaining high molar Si/Al ratio of the feedstock

The elemental composition of the CFA was predominantly oxides of silica - 56%, and aluminium - 27%, with about 11% oxides of Fe and Ca content. This indicated the insufficiency of the CFA molar Si/Al ratio = 2 to produce high silica zeolites. In order to overcome this challenge, a multi-step process for the extraction of silica involving fusion, precipitation and reflux was applied. After the acid treatment of the fused fly ash clear solution with H₂SO₄, the Si/Al ratio of the recovered precipitate (FFAE) increased to 11. Furthermore, a complete mineral phase transformation of the CFA into amorphous extract of aluminosilica was obtained after the 1.5 M oxalic acid reflux process at 80 °C for 6 h. Interestingly, the composition of the extract was about 92% silica, 1.5% Al and 7% Na oxides, thus this greatly enhanced the increase in the molar Si/Al ratio to 61 of the feedstock material. It is noteworthy that the silica extract from CFA demonstrated 94% purity and high molar Si/Al ratio that is suitable for the zeolitisation process of high silica BEA zeolite. Therefore, the chelation of Al, Na and other element enhanced the Si/Al ratio of the silica extract necessary for the successful synthesis of BEA zeolite through the indirect hydrothermal process (question 1 and objective 1).

7.1.2 Optimisation of BEA zeolite process from CFA

The synthesis of BEA zeolite from CFA was achieved via an indirect hydrothermal method. This four step process include fusion, precipitation, reflux and hydrothermal treatment. The first three steps called the extraction process of silica from CFA have shown the successful increase of the molar Si/Al ratio needed for the synthesis of high silica zeolites as mentioned above. After the hydrothermal treatment of the new formulated molar composition: 1 Si : 0.017 Al : 0.241 Na : 0.399 TEAOH : 8.980 H₂O, the recovered product was solid crystals with a typical morphology of BEA zeolite. This was set as the baseline for the synthesis of BEA zeolite and afterwards, different parameters such as the effect of sodium (Si/Na ratio), aluminium (Si/Al ratio) and the synthesis time of the molar composition was studied. The change in the molar fraction of Si/Na and Si/Al ratio had a significant effect on the crystalline structure and size, the crystal morphology and the percentage yield of the BEA zeolite. The variation in molar fraction of Na content affected the morphology of the synthesised BEA zeolite. At low molar fraction sodium content of ≤ 0.241 , a spheroidal-shaped structure was exhibited but with increased in molar fraction Na content ≥ 0.317 , the

spherical crystal shape changed to a large cuboidal-shaped crystal structure. Moreover, the crystal size enlarged which is indicative of gradual crystal growth from 0.50 μm to $\geq 0.62 \mu\text{m}$ but increased $\geq 2 \mu\text{m}$ as the morphology changes with increased molar Na content.

Upon the gradual increase in the molar fraction of Al content from 0.017 to 0.060, the crystallinity of the BEA zeolite gradually increased to 100% with crystal growth into the micro-size. With further increase in Al content to 0.172, a significant reduction and growth in crystallinity (45%) and crystal size (1.75 μm) was observed. This elucidated that the quality of CFA based BEA zeolite can either be compromised or greatly improved by merely altering the molar fraction of Na or Al of the synthesis mixture under the hydrothermal synthesis conditions set at 140 °C for 72 h. Under the set hydrothermal condition, the best molar regimes: 1 Si : 0.017 Al : 0.241 Na : 0.399 TEOH : 8.980 H₂O (BEA4) or 1 Si : 0.060 Al : 0.241 Na : 0.399 TEOH : 8.980 H₂O (BEAA1), with Si/Al ratio of 58.8 or 16.7, possessed high percentage crystallinity, small crystal size and improved product yield of the synthesised BEA zeolite, respectively.

The threshold molar regime of BEA4 and BEAA1 were further treated hydrothermally at 140 °C for 12, 24, 48 and 72 h to investigate the influence of crystallisation time on the framework structure of BEA zeolite after calcination process. A complete crystal growth was noticed after subjecting the molar regime 1 Si : 0.060 Al : 0.241 Na : 0.399 TEOH : 8.980 H₂O (BEAA1 Si/Al ratio = 16.7) to 48 h hydrothermal treatment. Interestingly, the study demonstrated that the molar composition of 1 Si : 0.017 Al : 0.241 Na : 0.399 TEOH : 8.980 H₂O (BEA4 Si/Al ratio = 58.8) enhanced a fast nucleation rate and promoted crystallinity and crystal growth within a short crystallisation time of 24 h. The framework structure shows two distinctive Al peaks associated with tetrahedrally coordinated framework aluminium or octahedrally coordinated extra framework aluminium of BEA zeolite framework structure. Thus, aluminium species are mainly located within the framework with a low amount at extra framework of the HBEA zeolite.

This study for the first time clearly designed and developed a new synthesis protocol via the indirect hydrothermal method to produce BEA zeolite from CFA. The innovative process has eliminated the external addition of silica or aluminium sources to the synthesis mixture and formulated a suitable molar regime for the hydrothermal crystallisation of HBEA zeolite from CFA. The HBEA products have demonstrated high structural crystallinity, high

thermal stability, high hydrothermal framework stability, high surface area with micro-mesoporous structure and suitable pore volume (question 2-3 and objective 2).

7.1.3 Influence of molar water on the hydrothermal time

Considering the optimised synthesis conditions (1 Si : 0.017 Al : 0.241 Na : 0.399 TEAOH : 8.980 H₂O) that resulted in the short hydrothermal crystallisation of BEA zeolite in 24 h, the effect of molar H₂O on the hydrothermal time was conducted. To this end, all other synthesis conditions were kept constant: 1 Si : 0.017 Al : 0.241 Na : 0.399 TEAOH : x H₂O at an hydrothermal temperature of 140 °C except the molar water fraction in the composition which was varied (where x is 5.99, 3.99, 2.66 and 1.78). The crystallisation of HBEA zeolite from CFA achieved at a short hydrothermal time of 8, 10 and 12 h, was a function of reduced molar water fraction in the synthesis mixture. High molar water fraction hindered the complete formation of pure phase BEA zeolite within a short synthesis time due to the lowered concentration of TEA⁺ species, thus reducing the supersaturation of the molar regime. Therefore leading to the formation of residue of amorphous material that remained in the zeolite product.

It was found that under different hydrothermal time of 10 and 12 h but similar molar water fraction of 3.99, the crystalline structure of the BEA zeolite increased from 70% to 100% with prolonged synthesis time, respectively. The molar water fraction of 1.78, 2.66 and 3.99 maintained a crystalline structure of $\geq 12\%$ but $\leq 65\%$ after the hydrothermal treatment of 8 h. It was established that the essential formulation of 1 Si : 0.017 Al : 0.241 Na : 0.399 TEAOH : x H₂O had a molar water fraction (x H₂O) of 2.66 and 3.99 for the hydrothermal crystallisation of BEA zeolite at 140 °C for 8 and 10-12 h, respectively. These novel experimental protocols lead to the rapid formation of HBEA crystals from CFA extract within the shortest hydrothermal time of 8 h. The HBEA zeolites possess fine micro-size with high thermal framework stability, high surface area, suitable pore volume, well-defined pore size distribution, maintained both framework and extra framework Al and weak-stronger acid sites (question 4 and objective 2).

7.1.4 Stability of the synthesised BEA zeolite in hot liquid phase reaction

The BEA zeolite produced from the hydrothermal treatment using optimised molar formulation (1 Si : x Al : 0.241 Na : 8.980 H₂O : 0.396 TEAOH, where $x = 0.017$ (NaBEA) and 0.060 (AlBEA)) at 140 °C for 72 h was used to study the framework stability of the

CFA based zeolite in hot liquid phase. The exposure of the synthesised NaBEA and AlBEA zeolite in hot liquid reaction simulated the behaviour of the framework structure in potential real life catalytic applications. It was observed that after the hot liquid treatment of the parent NaBEA and AlBEA zeolite, the crystallinity reduced significantly to about 30% with prolonged exposure time - 24 h and increased temperature - 200 °C. This led to the decrease in surface area and micropore volume, thus exerted a gradual expansion on the framework structure by the filling of water molecules in microporous voids caused the mesopore area and volume to increase. The decreased framework Si/Al ratio indicated the desilication of the BEA zeolite structure.

The desilication of the framework structure demonstrate the attack of OH species by the hydrolysis of Si-O-Si bonds, thereby resulting in the formation of terminal Si-OH group. Hence, the crystalline structure of BEA zeolite is susceptible to desilication under the more extreme hot liquid conditions. Interestingly, with the observed structural distortion, no evidences of phase transformations was found. In conclusion, for the first time this research has shown that the framework structure of the CFA based BEA zeolite under controlled aqueous conditions (not greater than 200 °C for a duration ≤ 24 h) has the potential to be applied in different liquid phase reaction such as Friedel– Crafts acylation and hydrodealkylation reaction (question 5 and objective 3). .

7.1.5 Physicochemical properties and catalytic performance of HBEA zeolite

Friedel-Crafts acylation of anisole with benzoyl chloride over the optimised HBEA81, HBEA12, HBEA2, HBEA24, HBEA48 and HBEA72 (obtained after the hydrothermal time of 8, 10, 12, 24, 48 and 72 h, respectively) was used as a probe reaction to compare the catalytic activity of the CFA based zeolites. Both short and long hydrothermal synthesised HBEA zeolite from CFA showed active properties and good performance. Some of the properties that influenced the catalytic activity include: surface area, mesoporous area, hierarchal pore structure, framework Al, peak area of Q⁴ species and acid sites. The conversion rate of anisole over the HBEA zeolite prepared in short (8, 10 and 12 h) or long (24, 48 and 72 h) hydrothermal time was above 50% with a high selectivity of 4-methoxyacetophenone (>80%). To this end, the efficiency of the catalytic conversion of anisole and the selectivity of 4-methoxyacetophenone over HBEA2 and HBEA24 have demonstrated to be the highest with progressed reaction time. Under similar conditions but increased molar anisole/BzCl ratio of 5:1, the percentage conversion of anisole was 82 or

85% over the zeolite samples. It was found that catalytic performance significantly increased to 99% conversion rate, 99% selectivity and 97% percentage yield with increased molar ratio of anisole/BzCl up to 9.5:1. This study established that CFA based BEA zeolite is highly active in the Friedel-Crafts acylation of anisole with benzoyl chloride. Also, after three regeneration cycles of the HBEA zeolite, a suitable framework structure was maintained with no phase compromise observed and the rate of anisole conversion of all the recycled zeolite remained greater than 80%. The BEA zeolite produced from CFA is thus suitable as a heterogeneous catalyst for the liquid phase conversion and still retains its catalytic properties after regeneration (question 6-7 and objective 4-6).

7.1.6 Significance of the research findings

This research has demonstrated that Class F CFA is a suitable feedstock material for the synthesis of BEA zeolite via indirect hydrothermal process. The designed experimental protocol completely eliminated the need for external addition of silica or aluminium source to the synthesis mixture (Patent Application No. PCT/IB2017/053730). Suitable molar regime that was targeted towards the generation of pure BEA zeolite phase was formulated. Other significant findings from this study include:

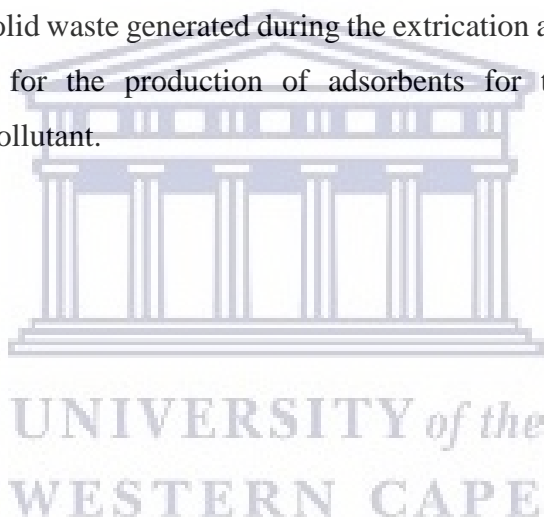
- The framework structure of BEA zeolite is susceptible to desilication but the zeolitic phase was stable after prolonged exposure to hot liquid.
- It was found that the increased weight loss correlate to the enlarged Q⁴ Si(0Al) area species which signifies the tolerance limit of the framework structure with prolonged exposure time in hot liquid reaction.
- The CFA based HBEA zeolite was highly active in the Friedel-Crafts acylation of anisole with benzoyl chloride
- The combination of strong FAI and the peak area of the Q⁴ Si(0Al) species can influence better catalytic performance
- The regenerated HBEA zeolites was stable and still possessed high catalytic performance

7.2 Recommendations for future study

The fundamental research aims, objectives and questions raised in this thesis have been successfully addressed. Yet, there are other interesting aspect, although not within the scope

of the study, which can be further researched. This research, therefore, recommends the following:

- This study has shown that the Si/Al ratio of amorphous aluminosilicate is within the required molar Si/Al ratio for the synthesis of high silica zeolite. It is however important for further research to be conducted on the multi-step process for the extraction of silica in order to replace the fusion step and the use of oxalic acid treatment process.
- The co-crystallisation of metal into the framework structure of BEA zeolite and post-modification processes can be studied.
- The catalytic activity of the CFA based BEA zeolite can further be investigated under various liquid and vapour reaction conditions.
- The liquid and solid waste generated during the extraction and synthesis process can be investigated for the production of adsorbents for the removal of dye or environmental pollutant.



References

- Adriano, D. C., Page, A. L., Elsewi, A. A., Chang, A. C., & Straughan, I. (1980). Utilization and disposal of fly ash and other coal residues in terrestrial ecosystems: A review. *Journal of Environmental Quality*, 9(3), 333-344.
- Ahmad, A. A., & Hameed, B. H. (2010). Fixed-bed adsorption of reactive azo dye onto granular activated carbon prepared from waste. *Journal of Hazardous Materials*, 175(1-3), 298-303.
- Ahmaruzzaman, M. (2010). A review on the utilization of fly ash. *Progress in Energy and Combustion Science*, 36(3), 327-363.
- Akinyemi, S. A., Akinlua, A., Gitari, W. M., Akinyeye, R. O., & Petrik, L. F. (2011). The leachability of major elements at different stages of weathering in dry disposed coal fly ash. *Coal Combustion and Gasification Products*, 3, 28-40.
- Aldahri, T., Behin, J., Kazemian, H., & Rohani, S. (2016). Synthesis of zeolite Na-P from coal fly ash by thermo-sonochemical treatment. *Fuel*, 182, 494-501.
- Al-Eid, M., Ding, L., Saleem, Q., Badairy, H., Sitepu, H., & Al-Malki, A. (2019). A facile method to synthesize hierarchical nano-sized zeolite beta. *Microporous and Mesoporous Materials*, 279, 99-106.
- Aleixo, R., Elvas-Leitao, R., Martins, F., Carvalho, A. P., Brigas, A., Martins, A., & Nunes, N. (2017). Kinetic study of Friedel-Crafts acylation reactions over hierarchical MCM-22 zeolites. *Molecular Catalysis*, 434, 175-183.
- Alothman, Z. A. (2012). A review: fundamental aspects of silicate mesoporous materials. *Materials*, 5(12), 2874-2902.
- Álvarez-Ayuso, E., & Querol, X. (2008). Study of the use of coal fly ash as an additive to minimise fluoride leaching from FGD gypsum for its disposal. *Chemosphere*, 71(1), 140-146.
- Ameh, A. E., Fatoba, O. O., Musyoka, N. M., & Petrik, L. F. (2017). Influence of aluminium source on the crystal structure and framework coordination of Al and Si in fly ash-based zeolite NaA. *Powder Technology*, 306, 17-25.
- Ameh, A. E., Musyoka, N. M., Fatoba, O. O., Syrtsova, D. A., Tplyakov, V. V., & Petrik, L. F. (2016). Synthesis of zeolite NaA membrane from fused fly ash extract. *Journal of Environmental Science and Health, Part A*, 51(4), 348-356.
- American Society for Testing and Materials, (1993). ASTM 618: Standard specification for fly ash and raw or calcined natural pozzolain for uses as a mineral admixture in Portland

- cement concrete. In: Annual book of ASTM Standards. ASTM, Philadelphia, Pennsylvania.
- Andaç, Ö., Tatlıer, M., Sirkecioğlu, A., Ece, I., & Erdem-Şenatalar, A. (2005). Effects of ultrasound on zeolite A synthesis. *Microporous and Mesoporous Materials*, 79(1-3), 225-233.
- Andrade E., Solis C., Aceves J.M., Miranda R., Cruz J., Rocha M.F., & Zavala E.P. (2008). Characterisation of natural and modified zeolite using ion beam analysis techniques. *Nuclear Instruments and Methods in Physics Research B*, 266, 2379-2382.
- Arsenova-Härtel, N., Bludau, H., Schumacher, R., Haag, W. O., Karge, H. G., Brunner, E., & Wild, U. (2000). Catalytic and sorption studies related to the para selectivity in the ethylbenzene disproportionation over H-ZSM-5 catalysts. *Journal of Catalysis*, 191(2), 326-331.
- Asl, S. M. H., Javadian, H., Khavarpour, M., Belviso, C., Taghavi, M., & Maghsudi, M. (2019). Porous adsorbents derived from coal fly ash as cost-effective and environmentally-friendly sources of aluminosilicate for sequestration of aqueous and gaseous pollutants: A review. *Journal of Cleaner Production*, 208, 1131-1147.
- Baerlocher, C., McCusker, L. B., & Olson, D. H. (2007). *Atlas of Zeolite Framework Types (6th ed)*. Elsevier Science, New York, NY, USA.
- Barzetti, T., Selli, E., Moschetti, D., & Forni, L. (1996). Pyridine and ammonia as probes for FTIR analysis of solid acid catalysts. *Journal of the Chemical Society, Faraday Transactions*, 92(8), 1401-1407.
- Bass, J. L., & Turner, G. L. (1997). Anion distributions in sodium silicate solutions. Characterization by ²⁹Si NMR and infrared spectroscopies, and vapor phase osmometry. *The Journal of Physical Chemistry B*, 101(50), 10638-10644.
- Bellussi, G., Pazzuconi, G., Perego, C., Girotti, G., & Terzoni, G. (1995). Liquid-phase alkylation of benzene with light olefins catalyzed by β -zeolites. *Journal of Catalysis*, 157(1), 227-234.
- Belviso, C. (2018). State-of-the-art applications of fly ash from coal and biomass: A focus on zeolite synthesis processes and issues. *Progress in Energy and Combustion Science*, 65, 109-135.
- Belviso, C., Cavalcante, F., & Fiore, S. (2010). Synthesis of zeolite from Italian coal fly ash: differences in crystallization temperature using seawater instead of distilled water. *Waste Management*, 30(5), 839-847.

- Belviso, C., Cavalcante, F., Di Gennaro, S., Lettino, A., Palma, A., Ragone, P., & Fiore, S. (2014). Removal of Mn from aqueous solution using fly ash and its hydrothermal synthetic zeolite. *Journal of Environmental Management*, *137*, 16-22.
- Bhanarkar, A. D., Gavane, A. G., Tajne, D. S., Tamhane, S. M., & Nema, P. (2008). Composition and size distribution of particles emissions from a coal-fired power plant in India. *Fuel*, *87*(10), 2095-2101.
- Blissett, R. S., & Rowson, N. A. (2012). A review of the multi-component utilisation of coal fly ash. *Fuel*, *97*, 1-23.
- Borm, P. J. (1997). Toxicity and occupational health hazards of coal fly ash (CFA). A review of data and comparison to coal mine dust. *The Annals of Occupational Hygiene*, *41*(6), 659-676.
- Bourgeat-Lami, E., Di Renzo, F., Fajula, F., Mutin, P. H., & Des Courieres, T. (1992). Mechanism of the thermal decomposition of tetraethylammonium in zeolite beta. *The Journal of Physical Chemistry*, *96*(9), 3807-3811.
- Boycheva, S., Zgureva, D., & Vassilev, V. (2013). Kinetic and thermodynamic studies on the thermal behaviour of fly ash from lignite coals. *Fuel*, *108*, 639-646.
- Breck, D. W. (1984). *Zeolite Molecular Sieves: Structure, Chemistry and Use*. Krieger.
- Bregolato, M., Bolis, V., Busco, C., Ugliengo, P., Bordiga, S., Cavani, F., Ballarini, N., Maselli, L., Passeri, S., Rossetti, I., & Forni, L. (2007). Methylation of phenol over high-silica beta zeolite: Effect of zeolite acidity and crystal size on catalyst behaviour. *Journal of Catalysis*, *245*(2), 285-300.
- Bukhari, S. S., Behin, J., Kazemian, H., & Rohani, S. (2015). Conversion of coal fly ash to zeolite utilizing microwave and ultrasound energies: a review. *Fuel*, *140*, 250-266.
- Burnard, K., & Bhattacharya, S. (2011). Power generation from coal.
- Byrappa, K., & Yoshimura, M. (2001). *Handbook of Hydrothermal Technology*. Noyes Publications/William Andrew Publishing, LLC, New York.
- Calleja, G., Sanz, R., Orcajo, G., Briones, D., Leo, P., & Martínez, F. (2014). Copper-based MOF-74 material as effective acid catalyst in Friedel–Crafts acylation of anisole. *Catalysis Today*, *227*, 130-137.
- Camblor, M. A., Corma, A., & Valencia, S. (1998b). Synthesis in fluoride media and characterisation of aluminosilicate zeolite beta. *Journal of Materials Chemistry*, *8*(9), 2137-2145.
- Camblor, M. A., Corma, A., Martinez, A., Martinez-Soria, V., & Valencia, S. (1998). Mild hydrocracking of vacuum gas oil over NiMo-Beta zeolite catalysts: the role of the

- location of the NiMo phases and the crystallite size of the zeolite. *Journal of Catalysis*, 179(2), 537-547.
- Cao, F., Wu, Y., Gu, J., & Wang, J. (2011). Hydrothermal synthesis of nanocrystalline zeolite Beta by acid-catalyzed hydrolysis of tetraethylorthosilicate. *Materials Chemistry and Physics*, 130(1-2), 727-732.
- Carr, D. A., Lach-hab, M., Yang, S., Vaisman, I. I., & Blaisten-Barojas, E. (2009). Machine learning approach for structure-based zeolite classification. *Microporous and Mesoporous Materials*, 117(1), 339-349.
- Chandrasekar, G., You, K. S., Ahn, J. W., & Ahn, W. S. (2008). Synthesis of hexagonal and cubic mesoporous silica using power plant bottom ash. *Microporous and Mesoporous Materials*, 111(1), 455-462.
- Chang, H. L., & Shih, W. H. (2000). Synthesis of zeolites A and X from fly ashes and their ion-exchange behavior with cobalt ions. *Industrial & Engineering Chemistry Research*, 39(11), 4185-4191.
- Chatterjee, S., Mondal, S., & De, S. (2018). Design and scaling up of fixed bed adsorption columns for lead removal by treated laterite. *Journal of Cleaner Production*, 177, 760-774.
- Chaves, T. F., Pastore, H. O., Hammer, P., & Cardoso, D. (2015). As-synthesized TEA-BEA zeolite: Effect of Si/Al ratio on the Knoevenagel condensation. *Microporous and Mesoporous Materials*, 202, 198-207.
- Chen, C. W., & Ko, A. N. (2012). Synthesis of Aromatic Ketones from Aromatic Compounds Using Vanadium-Containing Mesoporous Silicates. *Journal of the Chinese Chemical Society*, 59(9), 1104-1110.
- Chen, S., Yang, Y., Zhang, K., & Wang, J. (2006). BETA zeolite made from mesoporous material and its hydrocracking performance. *Catalysis Today*, 116(1), 2-5.
- Chen, Z., Chen, W., Tong, T., & Zeng, A. (2015). Continuous liquid phase acylation of toluene over HBEA zeolite: Solvent effects and origin of the deactivation. *Journal of Molecular Catalysis A: Chemical*, 396, 231-238.
- Chester, A. W., & Derouane, E. G. (2009). *Zeolite Characterization and Catalysis*. Springer Science & Business Media.
- Cho, H., Oh, D., & Kim, K. (2005). A study on removal characteristics of heavy metals from aqueous solution by fly ash. *Journal of Hazardous Materials*, 127(1), 187-195.

- Cioffi, R., Maffucci, L., & Santoro, L. (2003). Optimization of geopolymer synthesis by calcination and polycondensation of a kaolinitic residue. *Resources, Conservation and Recycling*, 40(1), 27-38.
- Colthup, N. B., Daly, L. H., & Wiberley, S. E. (1990). *Introduction to Infrared and Raman Spectroscopy*. Academic Press Ltd, London.
- Costa, D. G., & Capaz, R. B. (2015). Structural analysis of zeolite beta through periodic ab initio simulations of XRD and ²⁹Si and ¹⁷O NMR spectra. *Journal of Molecular Structure*, 1097, 112-116.
- Costa, J. A. S., & Paranhos, C. M. (2018). Systematic evaluation of amorphous silica production from rice husk ashes. *Journal of Cleaner Production*, 192, 688-697.
- Crelling, J. C., Hagemann, H. W., Sauter, D. H., Ramani, R. V., Vogt, W., Leininger, D., Krzack, S., Meyer, B., Orywal, F., Reimert, R., Bonn, B., Bertmann, U., Klose, W. & Dach, G. (2010), *Coal*. Ullmann's Encyclopedia of Industrial Chemistry.
- Criado, M., Fernandez-Jimenez, A., & Palomo, A. (2007). Alkali activation of fly ash: Effect of the SiO₂/Na₂O ratio, Part 1: FTIR study. *Microporous and Mesoporous Materials*, 106: 180-191.
- Cundy, C. S., & Cox, P. A. (2005). The hydrothermal synthesis of zeolites: Precursors, Intermediates and reaction mechanism. *Microporous and Mesoporous Materials*, 82(1-2), 1-78.
- Database of Zeolite Structures. (www.iza-structure.org/databases/)
- de Franco, M. A. E., de Carvalho, C. B., Bonetto, M. M., de Pelegrini Soares, R., & Féris, L. A. (2017). Removal of amoxicillin from water by adsorption onto activated carbon in batch process and fixed bed column: Kinetics, isotherms, experimental design and breakthrough curves modelling. *Journal of Cleaner Production*, 161, 947-956.
- Derouane, E. G., Crehan, G., Dillon, C. J., Bethell, D., He, H., & Hamid, S. D. A. (2000). Zeolite catalysts as solid solvents in fine chemicals synthesis: 2. competitive adsorption of the reactants and products in the Friedel–Crafts acetylations of anisole and toluene. *Journal of Catalysis*, 194(2), 410-423.
- Ding, L., Zheng, Y., Hong, Y., & Ring, Z. (2007). Effect of particle size on the hydrothermal stability of zeolite beta. *Microporous and Mesoporous Materials*, 101(3), 432-439.
- Ding, L., Zheng, Y., Yang, H., & Parviz, R. (2009). LCO hydrotreating with Mo-Ni and W-Ni supported on nano-and micro-sized zeolite beta. *Applied Catalysis A: General*, 353(1), 17-23.

- Ding, L., Zheng, Y., Zhang, Z., Ring, Z., & Chen, J. (2006). Effect of agitation on the synthesis of zeolite beta and its synthesis mechanism in absence of alkali cations. *Microporous and Mesoporous Materials*, 94(1-3), 1-8.
- Doucet, F. J., Mohamed, S., Neyt, N., Castleman, B. A., & van der Merwe, E. M. (2016). Thermochemical processing of a South African ultrafine coal fly ash using ammonium sulphate as extracting agent for aluminium extraction. *Hydrometallurgy*, 166, 174-184.
- Drzaj, B., Hocevar, S., & Pejovnik, S. (Eds.). (1985). *Zeolites: Synthesis, Structure, Technology and Application*. Amsterdam: Elsevier.
- Eary, L. E., Rai, D., Mattigod, S. V., & Ainsworth, C. C. (1990). Geochemical factors controlling the mobilisation of inorganic constituents from fossil fuel combustion residues: II. Review of the minor elements. *Journal of Environmental Quality*, 19(2), 202-214.
- Eisler, R. (2012). *The Fukushima 2011 Disaster*. CRC Press, Taylor & Francis Group, London.
- Ek, S., Root, A., Peussa, M., & Niinistö, L. (2001). Determination of the hydroxyl group content in silica by thermogravimetry and a comparison with ¹H MAS NMR results. *Thermochimica Acta*, 379(1-2), 201-212.
- El Berrichi, Z., Cherif, L., Tessonier, J. P., Louis, B., Fraissard, J., Ledoux, M. J., & Pham-Huu, C. (2005). GaSBA-15: a new and active Friedel-Crafts acylation catalyst. In *Studies in Surface Science and Catalysis* (Vol. 158, pp. 1413-1420). Elsevier.
- Electric Power Research Institute (EPRI) (2009). *Coal ash: characteristics, management and environmental issues*. Technical update.
- Elliot, A. D., & Zhang, D. K. (2005, April). Controlled release zeolite fertilisers: a value added product produced from fly ash. In *International Ash Utilization Symposium (IAUS) and World of Coal Ash (WOCA)* (pp. 1-32).
- El-Mogazi, D., Lisk, D. J., & Weinstein, L. H. (1988). A review of physical, chemical, and biological properties of fly ash and effects on agricultural ecosystems. *Science of the Total Environment*, 74, 1-37.
- El-Naas, M. H., Alhaija, M. A., & Al-Zuhair, S. (2017). Evaluation of an activated carbon packed bed for the adsorption of phenols from petroleum refinery wastewater. *Environmental Science and Pollution Research*, 24(8), 7511-7520.
- Engelhardt, G. (2001). Solid state NMR spectroscopy applied to zeolites. In *Studies in surface science and catalysis* (Vol. 137, pp. 387-418). Elsevier.

- Ennaert, T., Van Aelst, J., Dijkmans, J., De Clercq, R., Schutyser, W., Dusselier, M., Verboekend, D., & Sels, B. F. (2016). Potential and challenges of zeolite chemistry in the catalytic conversion of biomass. *Chemical Society Reviews*, 45(3), 584-611.
- Escola, J. M., Serrano, D. P., Sanz, R., Garcia, R. A., Peral, A., Moreno, I., & Linares, M. (2018). Synthesis of hierarchical Beta zeolite with uniform mesopores: Effect on its catalytic activity for veratrole acylation. *Catalysis Today*, 304, 89-96.
- Eskom, (2011). Electricity Supply Commission, South Africa, annual report. Available at www.eskom.co.za. Accessed on January 31st, 2012.
- Eskom, (2016). *Electricity Supply Commission, South Africa, annual report*. Available at www.eskom.co.za. Saturday, 20 February 2016.
- Eskom, (2018). *Electricity Supply Commission, South Africa, annual report*. Available at www.eskom.co.za. Accessed on July 18th, 2018.
- Farrusseng, D., & Tuel, A. (2016). Perspectives on zeolite-encapsulated metal nanoparticles and their applications in catalysis. *New Journal of Chemistry*, 40(5), 3933-3949.
- Fatoba, O. O. (2010). *Chemical interactions and mobility of species in fly ash-brine co-disposal systems* (Doctoral dissertation, University of the Western Cape).
- Fernandez, S., Ostraat, M. L., Lawrence III, J. A., & Zhang, K. (2018). Tailoring the hierarchical architecture of beta zeolites using base leaching and pore-directing agents. *Microporous and Mesoporous Materials*, 263, 201-209.
- Fernández-Jiménez, A., & Palomo, A. (2005). Composition and microstructure of alkali activated fly ash binder: effect of the activator. *Cement and Concrete Research*, 35(10), 1984-1992.
- Firouzi, A., Atef, F., Oertli, A. G., Stucky, G. D., & Chmelka, B. F. (1997). Alkaline lyotropic silicate–surfactant liquid crystals. *Journal of the American Chemical Society*, 119(15), 3596-3610.
- Fisher, G. L., Prentice, B. A., Silberman, D., Ondov, J. M., Biermann, A. H., Ragaini, R. C., & McFarland, A. R. (1978). Physical and morphological studies of size-classified coal fly ash. *Environmental Science & Technology*, 12(4), 447-451.
- Foner, H., Robl, T., Hower, J., & Graham, U. (1999). Characterization of fly ash from Israel with reference to its possible utilization. *Fuel*, 78(2), 215-223.
- Frost and Sullivan (2010). Zeolites industry trends and worldwide markets in 2010. A report from technical insights. www.frost.com
- Gabrienko, A. A., Danilova, I. G., Arzumanov, S. S., Toktarev, A. V., Freude, D., & Stepanov, A. G. (2010). Strong acidity of silanol groups of zeolite beta: Evidence

- from the studies by IR spectroscopy of adsorbed CO and ¹H MAS NMR. *Microporous and Mesoporous Materials*, 131(1-3), 210-216.
- Gascon, J., Kapteijn, F., Zornoza, B., Sebastian, V., Casado, C., & Coronas, J. (2012). Practical approach to zeolitic membranes and coatings: state of the art, opportunities, barriers, and future perspectives. *Chemistry of Materials*, 24(15), 2829-2844.
- Georgiev, D., Bogdanov, B., Angelova, K., Markovska, I., & Hristov, Y. (2009, June). Synthetic zeolites—Structure, classification, current trends in zeolite synthesis. In *Economics and Society Development on the Base of Knowledge: International Scientific Conference* (Vol. 7).
- Gil, B., Roth, W. J., Grzybek, J., Korzeniowska, A., Olejniczak, Z., Eliáš, M., Opanasenko, M., & Čejka, J. (2018). The effect of hot liquid water treatment on the properties and catalytic activity of MWW zeolites with various layered structures. *Catalysis Today*, 304, 22-29.
- Grand, J., Awala, H., & Mintova, S. (2016). Mechanism of zeolites crystal growth: new findings and open questions. *CrystEngComm*, 18(5), 650-664.
- Grand, J., Awala, H., & Mintova, S. (2016). Mechanism of zeolites crystal growth: new findings and open questions. *CrystEngComm*, 18(5), 650-664.
- Groen, J. C., Peffer, L. A., Moulijn, J. A., & Pérez-Ramírez, J. (2005). Mechanism of hierarchical porosity development in MFI zeolites by desilication: The role of aluminium as a pore-directing agent. *Chemistry-A European Journal*, 11(17), 4983-4994.
- Gross .M, Soulard .M, Caultet .P, Patarin .J, Saude .I (2007). Synthesis of faujasite from coal fly ashes under smooth temperature and pressure conditions: A cost saving process. *Microporous and Mesoporous Materials*, 104, 67-76.
- Guo, P., Yan, N., Wang, L., & Zou, X. (2017). Database mining of zeolite structures. *Crystal Growth & Design*, 17(12), 6821-6835.
- Hahn, M. W., Copeland, J. R., Van Pelt, A. H., & Sievers, C. (2013). Stability of Amorphous Silica–Alumina in Hot Liquid Water. *ChemSusChem*, 6(12), 2304-2315.
- Halina, M., Ramesh, S., Yarmo, M. A., & Kamarudin, R. A. (2007). Non-hydrothermal synthesis of mesoporous materials using sodium silicate from coal fly ash. *Materials chemistry and physics*, 101(2), 344-351.
- Hartmann, M., Machoke, A. G., & Schwieger, W. (2016). Catalytic test reactions for the evaluation of hierarchical zeolites. *Chemical Society Reviews*, 45(12), 3313-3330.

- Heidrich, C., Feuerborn, H. J., & Weir, A. (2013, April). Coal combustion products: a global perspective. In *World of Coal Ash Conference* (pp. 22-25).
- Hethnawi, A., Nassar, N. N., Manasrah, A. D., & Vitale, G. (2017). Polyethylenimine-functionalized pyroxene nanoparticles embedded on Diatomite for adsorptive removal of dye from textile wastewater in a fixed-bed column. *Chemical Engineering Journal*, 320, 389-404.
- Holler, H., & Wirsching, U. (1985). Zeolite formation from fly-ash. *Fortschritte der Mineralogie*, 63(1), 21-43.
- Holzinger, J., Beato, P., Lundegaard, L. F., & Skibsted, J. (2018). Distribution of Aluminum over the Tetrahedral Sites in ZSM-5 Zeolites and Their Evolution after Steam Treatment. *The Journal of Physical Chemistry C*.
- Hould, N. D., Foster, A., & Lobo, R. F. (2011). Zeolite beta mechanisms of nucleation and growth. *Microporous and Mesoporous Materials*, 142(1), 104-115.
- Hould, N. D., Kumar, S., Tsapatsis, M., Nikolakis, V., & Lobo, R. F. (2009). Structure and colloidal stability of nanosized zeolite beta precursors. *Langmuir*, 26(2), 1260-1270.
- Hu, T., Chen, J., Wang, H., Ma, J., & Wei, M. (2006). Influence of shaped and modified H β zeolite on etherification of FCC light gasoline. *Microporous and Mesoporous Materials*, 94(1-3), 283-287.
- Huang, G., Ji, P., Xu, H., Jiang, J. G., Chen, L., & Wu, P. (2017). Fast synthesis of hierarchical Beta zeolites with uniform nanocrystals from layered silicate precursor. *Microporous and Mesoporous Materials*, 248, 30-39.
- Inada, M., Tsujimoto, H., Eguchi, Y., Enomoto, N., & Hojo, J. (2005). Microwave-assisted zeolite synthesis from coal fly ash in hydrothermal process. *Fuel*, 84(12), 1482-1486.
- International Union of Pure and Applied Chemistry (IUPAC), Macromolecular Division Commission on Functional Polymers. *Pure & Applied Chemistry*, 68 (1996) 1479-1489.
- International Zeolite Association. Available at <http://www.iza-online.org/>. Accessed on March 22nd, 2019.
- Iyer, R. S., & Scott, J. A. (2001). Power station fly ash—a review of value-added utilization outside of the construction industry. *Resources, Conservation and Recycling*, 31(3), 217-228.
- Izquierdo, M., & Querol, X. (2012). Leaching behaviour of elements from coal combustion fly ash: an overview. *International Journal of Coal Geology*, 94, 54-66.

- Jala, S., & Goyal, D. (2006). Fly ash as a soil ameliorant for improving crop production - a review. *Bioresource Technology*, 97(9), 1136-1147.
- Jamil, A. K., Muraza, O., Osuga, R., Shafei, E. N., Choi, K. H., Yamani, Z. H., Somali, A., & Yokoi, T. (2016). Hydrothermal stability of one-dimensional pore ZSM-22 zeolite in hot water. *The Journal of Physical Chemistry C*, 120(40), 22918-22926.
- Jankowski, J., Ward, C. R., French, D., & Groves, S. (2006). Mobility of trace elements from selected Australian fly ashes and its potential impact on aquatic ecosystems. *Fuel*, 85(2), 243-256.
- Javaid, A. (2005). Membranes for solubility-based gas separation applications. *Chemical Engineering Journal*, 112(1), 219-226.
- Jegadeesan, G., Al-Abed, S. R., & Pinto, P. (2008). Influence of trace metal distribution on its leachability from coal fly ash. *Fuel*, 87(10-11), 1887-1893.
- Jha, B., & Singh, D. N. (2011). A review on synthesis, characterization and industrial applications of fly ash zeolites. *Journal of Materials Education*, 33(1), 65.
- Jia, X., Khan, W., Wu, Z., Choi, J., & Yip, A. C. (2018). Modern synthesis strategies for hierarchical zeolites: bottom-up versus top-down strategies. *Advanced Powder Technology*.
- Jiang, J., Jorda, J. L., Yu, J., Baumes, L. A., Mugnaioli, E., Diaz-Cabanas, M. J., Kolb, U., & Corma, A. (2011). Synthesis and structure determination of the hierarchical meso-microporous zeolite ITQ-43. *Science*, 333(6046), 1131-1134.
- Kamimura, Y., Itabashi, K., & Okubo, T. (2012). Seed-assisted, OSDA-free synthesis of MTW-type zeolite and “Green MTW” from sodium aluminosilicate gel systems. *Microporous and Mesoporous Materials*, 147(1), 149-156.
- Kantam, M. L., Rao, B. P., Choudary, B. M., Rao, K. K., Sreedhar, B., Iwasawa, Y., & Sasaki, T. (2006). Synthesis of nanocrystalline zeolite beta in supercritical fluids, characterization and catalytic activity. *Journal of Molecular Catalysis A: Chemical*, 252(1-2), 76-84.
- Kazemian, H., Naghdali, Z., Kashani, T. G., & Farhadi, F. (2010). Conversion of high silicon fly ash to Na-P1 zeolite: alkaline fusion followed by hydrothermal crystallization. *Advanced Powder Technology*, 21(3), 279-283.
- Kim, J. C., Cho, K., Lee, S., & Ryoo, R. (2015). Mesopore wall-catalyzed Friedel–Crafts acylation of bulky aromatic compounds in MFI zeolite nanosponge. *Catalysis Today*, 243, 103-108.

- Kim, J., Han, J., Kwon, T. S., Park, Y. K., & Jeon, J. K. (2014). Oligomerization and isomerization of dicyclopentadiene over mesoporous materials produced from zeolite beta. *Catalysis Today*, 232, 69-74.
- Kirschhock, C. E., Feijen, E. J., Jacobs, P. A., & Martens, J. A. (2008). Hydrothermal zeolite synthesis. *Handbook of Heterogeneous Catalysis: Online*, 160-178.
- Kirumakki, S. R., Nagaraju, N., & Chary, K. V. (2006). Esterification of alcohols with acetic acid over zeolites H β , HY and HZSM5. *Applied Catalysis A: General*, 299, 185-192.
- Kong, L., Chen, H., Tai, J., Shen, J., Zhang, S., & Chen, J. (2009). Synthesis of small crystal zeolite beta in a biphasic H₂O–CTAB–alcohol system. *Materials Letters*, 63(2), 343-345.
- Kotova, O. B., Shabalin, I. N., Shushkov, D. A., & Kocheva, L. S. (2016). Hydrothermal synthesis of zeolites from coal fly ash. *Advances in Applied Ceramics*, 115(3), 152-157.
- Koukouzas, N., Ward, C. R., Papanikolaou, D., Li, Z., & Ketikidis, C. (2009). Quantitative evaluation of minerals in fly ashes of biomass, coal and biomass–coal mixture derived from circulating fluidised bed combustion technology. *Journal of Hazardous Materials*, 169(1), 100-107.
- Krüger, J. E. (2003). South African fly ash: A cement extender. *A South African coal Ash Association publication*.
- Kumar, M., Li, R., & Rimer, J. D. (2016). Assembly and evolution of amorphous precursors in zeolite L crystallization. *Chemistry of Materials*, 28(6), 1714-1727.
- Kutchko, B. G., & Kim, A. G. (2006). Fly ash characterization by SEM-EDS. *Fuel*, 85(17), 2537-2544.
- Lai, R., Yan, Y., & Gavalas, G. R. (2000). Growth of ZSM-5 films on alumina and other surfaces. *Microporous and Mesoporous Materials*, 37(1-2), 9-19.
- Larlus, O., Mintova, S., Wilson, S. T., Willis, R. R., Abrevaya, H., & Bein, T. (2011). A powerful structure-directing agent for the synthesis of nanosized Al- and high-silica zeolite Beta in alkaline medium. *Microporous and Mesoporous Materials*, 142(1), 17-25.
- Lechert, H. (2001). The pH-value and its importance for the crystallization of zeolites. In *Verified Syntheses of Zeolitic Materials* (pp. 33-38). Elsevier Science.
- Lee, Y. R., Soe, J. T., Zhang, S., Ahn, J. W., Park, M. B., & Ahn, W. S. (2017). Synthesis of nanoporous materials via recycling coal fly ash and other solid wastes: A mini review. *Chemical Engineering Journal*, 317, 821-843.

- Li, B., Song, G., Wu, Y., Li, F., Xue, J., & Lv, Z. (2017). Synthesis and characterization of mesoporous zeolite Beta templated by a novel organosiloxane. *Journal of Porous Materials*, 24(6), 1673-1678.
- Li, K. M., Jiang, J. G., Tian, S. C., Chen, X. J., & Yan, F. (2014). Influence of Silica Types on Synthesis and Performance of Amine–Silica Hybrid Materials Used for CO₂ Capture. *The Journal of Physical Chemistry C*, 118(5), 2454-2462.
- Li, R., Chawla, A., Linares, N., Sutjipto, J. G., Chapman, K. W., Martínez, J. G., & Rimer, J. D. (2018). Diverse Physical States of Amorphous Precursors in Zeolite Synthesis. *Industrial & Engineering Chemistry Research*, 57(25), 8460-8471.
- Li, Y., & Yu, J. (2014). New stories of zeolite structures: their descriptions, determinations, predictions, and evaluations. *Chemical Reviews*, 114(14), 7268-7316.
- Li, Y., Li, L., & Yu, J. (2017). Applications of zeolites in sustainable chemistry. *Chem*, 3(6), 928-949.
- Lima, P. M., Garetto, T., Cavalcante Jr, C. L., & Cardoso, D. (2011). Isomerization of n-hexane on Pt–Ni catalysts supported on nanocrystalline H-BEA zeolite. *Catalysis Today*, 172(1), 195-202.
- Lin, C. F., & Hsi, H. C. (1995). Resource recovery of waste fly ash: synthesis of zeolite-like materials. *Environmental Science & Technology*, 29(4), 1109-1117.
- Lin, X., Huang, Q., Qi, G., Shi, S., Xiong, L., Huang, C., Chen, X., Li, H., & Chen, X. (2017). Estimation of fixed-bed column parameters and mathematical modelling of breakthrough behaviors for adsorption of levulinic acid from aqueous solution using SY-01 resin. *Separation and Purification Technology*, 174, 222-231.
- Liu, H., Shen, T., Wang, W., Li, T., Yue, Y., & Bao, X. (2015a). From natural aluminosilicate minerals to zeolites: synthesis of ZSM-5 from rectorites activated via different methods. *Applied Clay Science*, 115, 201-211.
- Liu, Z., Dong, X., Zhu, Y., Emwas, A. H., Zhang, D., Tian, Q., & Han, Y. (2015). Investigating the influence of mesoporosity in zeolite Beta on its catalytic performance for the conversion of methanol to hydrocarbons. *ACS Catalysis*, 5(10), 5837-5845.
- Losch, P., Boltz, M., Bernardon, C., Louis, B., Palčić, A., & Valtchev, V. (2016). Impact of external surface passivation of nano-ZSM-5 zeolites in the methanol-to-olefins reaction. *Applied Catalysis A: General*, 509, 30-37.

- Lutz, W., Toufar, H., Kurzhals, R., & Suckow, M. (2005). Investigation and modeling of the hydrothermal stability of technically relevant zeolites. *Adsorption*, 11(3-4), 405-413.
- Lutz, W., Zibrowius, B., & Löffler, E. (1994). Hydrothermal and alkaline stability of high-silica Y-type zeolites in dependence on the dealumination procedure. In *Studies in Surface Science and Catalysis* (Vol. 84, pp. 1005-1012). Elsevier.
- Ma, Y., Yan, C., Alshameri, A., Qiu, X., & Zhou, C. (2014). Synthesis and characterization of 13X zeolite from low-grade natural kaolin. *Advanced Powder Technology*, 25(2), 495-499.
- Madzivire, G., Maleka, R. M., Tekere, M., & Petrik, L. F. (2019). Cradle to cradle solution to problematic waste materials from mine and coal power station: acid mine drainage, coal fly ash and carbon dioxide. *Journal of Water Process Engineering*.
- Madzivire, G., Petrik, L. F., Gitari, W. M., Ojumu, T. V., & Balfour, G. (2010). Application of coal fly ash to circumneutral mine waters for the removal of sulphates as gypsum and ettringite. *Minerals Engineering*, 23(3), 252-257.
- Maia, A. Á. B., Neves, R. F., Angélica, R. S., & Pöllmann, H. (2015). Synthesis, optimisation and characterisation of the zeolite NaA using kaolin waste from the Amazon Region. Production of Zeolites KA, MgA and CaA. *Applied Clay Science*, 108, 55-60.
- Mainganye, D., Ojumu, T., & Petrik, L. (2013). Synthesis of zeolites Na-P1 from South African coal fly ash: effect of impeller design and agitation. *Materials*, 6(5), 2074-2089.
- Majchrzak-Kucęba, I. (2013). A simple thermogravimetric method for the evaluation of the degree of fly ash conversion into zeolite material. *Journal of Porous Materials*, 20(2), 407-415.
- Mallapur, V. P., & Oubagaranadin, J. U. K. (2017). A brief review on the synthesis of zeolites from hazardous wastes. *Transactions of the Indian Ceramic Society*, 76(1), 1-13.
- Manrique, C., Guzmán, A., Pérez-Pariente, J., Márquez-Álvarez, C., & Echavarría, A. (2016). Effect of synthesis conditions on zeolite Beta properties and its performance in vacuum gas oil hydrocracking activity. *Microporous and Mesoporous Materials*, 234, 347-360.

- Martínez, C., & Pérez-Pariente, J. (2011). *Zeolites and ordered porous solids: Fundamentals and applications*. 3rd FEZA School of Zeolite, Valencia, Editorial Universitat Politecnica de Valencia, ISBN 978-84-8303-719-7.
- Martínez-Franco, R., Paris, C., Martínez-Armero, M. E., Martínez, C., Moliner, M., & Corma, A. (2016). High-silica nanocrystalline Beta zeolites: efficient synthesis and catalytic application. *Chemical Science*, 7(1), 102-108.
- Matsukata, M., Osaki, T., Ogura, M., & Kikuchi, E. (2002). Crystallization behavior of zeolite beta during steam-assisted crystallization of dry gel. *Microporous and Mesoporous Materials*, 56(1), 1-10.
- Mehmood, S., Reddy, B. V., & Rosen, M. A. (2012). Energy analysis of a biomass co-firing based pulverized coal power generation system. *Sustainability*, 4(4), 462-490.
- Mintova, S., Reinelt, M., Metzger, T. H., Senker, J., & Bein, T. (2003). Pure silica BETA colloidal zeolite assembled in thin films. *Chemical Communications*, (3), 326-327.
- Mintova, S., Valtchev, V., Onfroy, T., Marichal, C., Knözinger, H., & Bein, T. (2006). Variation of the Si/Al ratio in nanosized zeolite Beta crystals. *Microporous and Mesoporous Materials*, 90(1-3), 237-245.
- Misran, H., Singh, R., Begum, S., & Yarmo, M. A. (2007). Processing of mesoporous silica materials (MCM-41) from coal fly ash. *Journal of Materials Processing Technology*, 186(1), 8-13.
- Missengue, R. N. M., Losch, P., Sedres, G., Musyoka, N. M., Fatoba, O. O., Louis, B., Pale, P., & Petrik, L. F. (2017). Transformation of South African coal fly ash into ZSM-5 zeolite and its application as an MTO catalyst. *Comptes Rendus Chimie*, 20(1), 78-86.
- Missengue, R., Losch, P., Musyoka, N., Louis, B., Pale, P., & Petrik, L. (2018). Conversion of South African coal fly ash into high-purity ZSM-5 zeolite without additional source of silica or alumina and its application as a methanol-to-olefins catalyst. *Catalysts*, 8(4), 124.
- Modhera, B., Chakraborty, M., Parikh, P. A., & Jasra, R. V. (2009). Synthesis of nanocrystalline zeolite β : Effects of crystallization parameters. *Crystal Research and Technology: Journal of Experimental and Industrial Crystallography*, 44(4), 379-385.
- Molina, A., & Poole, C. (2004). A comparative study using two methods to produce zeolites from fly ash. *Minerals Engineering*, 17(2), 167-173.

- Moliner, M. (2011). Basic principles of zeolite synthesis. *Zeolites and Ordered Porous Solids*, 37.
- Moliner, M., Rey, F., & Corma, A. (2013). Towards the Rational Design of Efficient Organic Structure-Directing Agents for Zeolite Synthesis. *Angewandte Chemie International Edition*, 52(52), 13880-13889.
- Möller, K., Yilmaz, B., Jacubinas, R. M., Müller, U., & Bein, T. (2011). One-step synthesis of hierarchical zeolite beta via network formation of uniform nanocrystals. *Journal of the American Chemical Society*, 133(14), 5284-5295.
- Monama, W., Mohiuddin, E., Thangaraj, B., Mdleleni, M. M., & Key, D. (2019). Oligomerization of lower olefins to fuel range hydrocarbons over texturally enhanced ZSM-5 catalyst. *Catalysis Today*.
- Mondragon, F., Rincon, F., Sierra, L., Escobar, J., Ramirez, J., & Fernandez, J. (1990). New perspectives for coal ash utilization: synthesis of zeolitic materials. *Fuel*, 69(2), 263-266.
- Mor, S., Manchanda, C. K., Kansal, S. K., & Ravindra, K. (2017). Nanosilica extraction from processed agricultural residue using green technology. *Journal of Cleaner Production*, 143, 1284-1290.
- Moreno, N., Querol, X., Andrés, J. M., Stanton, K., Towler, M., Nugteren, H., Janssen-Jurkovicova, M., & Jones, R. (2005). Physico-chemical characteristics of European pulverized coal combustion fly ashes. *Fuel*, 84(11), 1351-1363.
- Moriyama, R., Takeda, S., Onozaki, M., Katayama, Y., Shiota, K., Fukuda, T., Sugilara, H., & Tani, Y. (2005). Large-scale synthesis of artificial zeolite from coal fly ash with a small charge of alkaline solution. *Fuel*, 84(12-13), 1455-1461.
- Morris, R. E. (2005). Modular materials from zeolite-like building blocks. *Journal of Materials Chemistry*, 15(9), 931-938.
- Mu, M., Fang, W., Liu, Y., & Chen, L. (2015). Iron (III)-Modified Tungstophosphoric Acid Supported on Titania Catalyst: Synthesis, Characterization, and Friedel–Craft Acylation of m-Xylene. *Industrial & Engineering Chemistry Research*, 54(36), 8893-8899.
- Muniz, J. R., Ramírez, A. M., Robles, J. A., Melo, P. G., Bocardo, J. E., & Martínez, A. M. (2010). Synthesis and characterization of high silica zeolites from coal fly ash (CFA): two cases of zeolite syntheses from the same waste material. *Latin Am. Appl. Res*, 40, 323-328.

- Murayama, N., Yamamoto, H., & Shibata, J. (2002). Mechanism of zeolite synthesis from coal fly ash by alkali hydrothermal reaction. *International Journal of Mineral Processing*, 64(1), 1-17.
- Muriithi, G. N., Gitari, W. M., Doucet, F., & Petrik, L. F. (2013). Re-use of South African fly ash for CO₂ capture and brine remediation. Unpublished PhD thesis, University of the Western Cape, South Africa.
- Musyoka, N. M., Petrik, L. F., & Hums, E. (2011a). Ultrasonic assisted synthesis of zeolite A from coal fly ash using mine waters (acid mine drainage and circumneutral mine water) as a substitute for ultra-pure water. *International Mine Water Association*.
- Musyoka, N. M., Petrik, L. F., Balfour, G., Gitari, W. M., & Hums, E. (2011b). Synthesis of hydroxy sodalite from coal fly ash using waste industrial brine solution. *Journal of Environmental Science and Health, Part A*, 46(14), 1699-1707.
- Musyoka, N. M., Petrik, L. F., Gitari, W. M., Balfour, G., & Hums, E. (2012a). Optimization of hydrothermal synthesis of pure phase zeolite Na-P1 from South African coal fly ashes. *Journal of Environmental Science and Health, Part A*, 47(3), 337-350.
- Musyoka, N. M., Petrik, L., & Hums, E. (2012b). Synthesis of zeolite A, X and P from a South African coal fly ash. In *Advanced Materials Research* (Vol. 512, pp. 1757-1762). Trans Tech Publications.
- Na, K., & Somorjai, G. A. (2015). Hierarchically nanoporous zeolites and their heterogeneous catalysis: current status and future perspectives. *Catalysis Letters*, 145(1), 193-213.
- Nagy, J. B., Bodart, P., Hannus, I., & Kiricsi, I. (1998). Synthesis, characterization and use of zeolitic microporous materials. DecaGen Ltd, Szeged, Hungary.
- Nelson, P. F., Shah, P., Strezov, V., Halliburton, B., & Carras, J. N. (2010). Environmental impacts of coal combustion: A risk approach to assessment of emissions. *Fuel*, 89(4), 810-816.
- Noor-ul-Amin. (2014). A multi-directional utilization of different ashes. *RSC Advances*, 4(107), 62769-62788.
- Nyambura, M. G., Mugeru, G. W., Felicia, P. L., & Gathura, N. P. (2011). Carbonation of brine impacted fractionated coal fly ash: implications for CO₂ sequestration. *Journal of Environmental Management*, 92(3), 655-664.
- Ogunbadejo, B. A., Osman, M. S., Arudra, P., Aitani, A. M., & Al-Khattaf, S. S. (2015). Alkylation of toluene with ethanol to para-ethyltoluene over MFI zeolites: Comparative study and kinetic modeling. *Catalysis Today*, 243, 109-117.

- Ojha, K., Pradhan, N. C., & Samanta, A. N. (2004). Zeolite from fly ash: synthesis and characterization. *Bulletin of Materials Science*, 27(6), 555-564.
- Ojumu, T. V., Du Plessis, P. W., & Petrik, L. F. (2016). Synthesis of zeolite A from coal fly ash using ultrasonic treatment—A replacement for fusion step. *Ultrasonics Sonochemistry*, 31, 342-349.
- Pan, F., Lu, X., Zhu, Q., Zhang, Z., Yan, Y., Wang, T., & Chen, S. (2014). A fast route for synthesizing nano-sized ZSM-5 aggregates. *Journal of Materials Chemistry A*, 2(48), 20667-20675.
- Panagiotopoulou, C., Tsivilis, S., & Kakali, G. (2015). Application of the Taguchi approach for the composition optimization of alkali activated fly ash binders. *Construction and Building Materials*, 91, 17-22.
- Pandey, V. C., Singh, J. S., Singh, R. P., Singh, N., & Yunus, M. (2011). Arsenic hazards in coal fly ash and its fate in Indian scenario. *Resources, Conservation and Recycling*, 55(9-10), 819-835.
- Pathan, S. M., Aylmore, L. A. G., & Colmer, T. D. (2003). Properties of several fly ash materials in relation to use as soil amendments. *Journal of Environmental Quality*, 32(2), 687-693.
- Patil, P. T., Malshe, K. M., Kumar, P., Dongare, M. K., & Kemnitz, E. (2002). Benzoylation of anisole over borate zirconia solid acid catalyst. *Catalysis Communications*, 3(9), 411-416.
- Perez-Ramirez, J., Christensen, C. H., Egeblad, K., Christensen, C. H., & Groen, J. C. (2008). Hierarchical zeolites: enhanced utilisation of microporous crystals in catalysis by advances in materials design. *Chemical Society Reviews*, 37(11), 2530-2542.
- Petrik, F.L, Missengue-Na-Moutoula, R., Ameh, E.A., & Hlatywayo, T. (2017). Process for production of high silica content zeolite from fly ash, WO/2017/221192-Patent.
- Petrik, L., White, R., Klink, M., Somerset, V., Key, D.L., Iwuoha, E., Burgers, C. & Fey, M.V. (2005). *Utilization of Fly Ash for Acid Mine Drainage Remediation*. Water Research Commission Report No. 1242/1/05.
- Petroleum, B. (2017). BP statistical review of world energy. British Petroleum, London.
- Popovic, A., Djordjevic, D., & Polic, P. (2001). Trace and major element pollution originating from coal ash suspension and transport processes. *Environment International*, 26(4), 251-255.

- Prasetyoko, D., Ramli, Z., Endud, S., Hamdan, H., & Sulikowski, B. (2006). Conversion of rice husk ash to zeolite beta. *Waste Management*, 26(10), 1173-1179.
- Primo, A., & Garcia, H. (2014). Zeolites as catalysts in oil refining. *Chemical Society Reviews*, 43(22), 7548-7561.
- Prodinger, S., Derewinski, M. A., Vjunov, A., Burton, S. D., Arslan, I., & Lercher, J. A. (2016). Improving stability of zeolites in aqueous phase via selective removal of structural defects. *Journal of the American Chemical Society*, 138(13), 4408-4415.
- Prodinger, S., Shi, H., Wang, H., Derewinski, M. A., & Lercher, J. A. (2018). Impact of structural defects and hydronium ion concentration on the stability of zeolite BEA in aqueous phase. *Applied Catalysis B: Environmental*, 237, 996-1002.
- Querol, X., Alastuey, A., Fernández-Turiel, J., & López-Soler, A. (1995). Synthesis of zeolites by alkaline activation of ferro-aluminous fly ash. *Fuel*, 74(8), 1226-1231.
- Querol, X., Moreno, N., Umaña, J. T., Alastuey, A., Hernández, E., Lopez-Soler, A., & Plana, F. (2002). Synthesis of zeolites from coal fly ash: an overview. *International Journal of Coal Geology*, 50(1), 413-423.
- Querol, X., Plana, F., Alastuey, A., & López-Soler, A. (1997). Synthesis of Na-zeolites from fly ash. *Fuel*, 76(8), 793-799.
- Querol, X., Umana, J. C., Plana, F., Alastuey, A., Lopez-Soler, A., Medinaceli, A., Valero, A., Domingo, M. J., & Garcia-Rojo, E. (2001). Synthesis of zeolites from fly ash at pilot plant scale. Examples of potential applications. *Fuel*, 80(6), 857-865.
- Quijorna, N., Miguel, G. S., & Andrés, A. (2011). Incorporation of Waelz slag into commercial ceramic bricks: a practical example of industrial ecology. *Industrial & Engineering Chemistry Research*, 50(9), 5806-5814.
- Raclavska, H., Raclavsky, K., & Matysek, D. (2009). Colour measurement as a proxy method for estimation of changes in phase and chemical composition of fly ash formed by combustion of coal. *Fuel*, 88(11), 2247-2254.
- Ramakrishna, S., Ma, Z., & Matsuura, T. (2011). *Polymer membranes in biotechnology: preparation, functionalization and application*. World Scientific, Singapore.
- Ramesh, K., & Reddy, D. D. (2011). Zeolites and their potential uses in agriculture. In *Advances in Agronomy* (Vol. 113, pp. 219-241). Academic Press.
- Rattanasak, U., & Chindaprasirt, P. (2009). Influence of NaOH solution on the synthesis of fly ash geopolymer. *Minerals Engineering*, 22(12), 1073-1078.

- Ravenelle, R. M., Schüßler, F., D'Amico, A., Danilina, N., Van Bokhoven, J. A., Lercher, J. A., Jones, C. W., & Sievers, C. (2010). Stability of zeolites in hot liquid water. *The Journal of Physical Chemistry C*, *114*(46), 19582-19595.
- Rayalu, S. S., Udhoji, J. S., Munshi, K. N., & Hasan, M. Z. (2001). Highly crystalline zeolite-a from fly ash of bituminous and lignite coal combustion. *Journal of Hazardous Materials*, *88*(1), 107-121.
- Rida, M. A., & Harb, F. (2014). Synthesis and characterization of amorphous silica nanoparticles from aqueous silicates using cationic surfactants. *Journal of Metals, Materials and Minerals*, *24*(1).
- Rios, C. A., & Williams, C. D. (2008). Synthesis of zeolitic materials from natural clinker: A new alternative for recycling coal combustion by-products. *Fuel*, *87*(12), 2482-2492.
- Robson, H. (2001). *Verified synthesis of zeolitic materials*. 2nd Edition Gulf Professional Publishing, Amsterdam.
- Rodríguez, E. D., Bernal, S. A., Provis, J. L., Paya, J., Monzo, J. M., & Borrachero, M. V. (2013). Effect of nanosilica-based activators on the performance of an alkali-activated fly ash binder. *Cement and Concrete Composites*, *35*(1), 1-11.
- Saikia, B. J., & Parthasarathy, G. (2010). Fourier transform infrared spectroscopic characterization of kaolinite from Assam and Meghalaya, Northeastern India. *Journal of Modern Physics*, *1*(04), 206.
- Saikia, N., Kato, S., & Kojima, T. (2006). Compositions and leaching behaviours of combustion residues. *Fuel*, *85*(2), 264-271.
- Sakthivel, T., Reid, D. L., Goldstein, I., Hench, L., & Seal, S. (2013). Hydrophobic high surface area zeolites derived from fly ash for oil spill remediation. *Environmental Science & Technology*, *47*(11), 5843-5850.
- Salakhum, S., Yuthalekha, T., Chareonpanich, M., Limtrakul, J., & Wattanakit, C. (2018). Synthesis of hierarchical faujasite nanosheets from corn cob ash-derived nanosilica as efficient catalysts for hydrogenation of lignin-derived alkylphenols. *Microporous and Mesoporous Materials*, *258*, 141-150.
- Salavati-Niasari, M., Hasanalian, J., & Najafian, H. (2004). Alumina-supported FeCl₃, MnCl₂, CoCl₂, NiCl₂, CuCl₂, and ZnCl₂ as catalysts for the benzylation of benzene by benzyl chloride. *Journal of Molecular Catalysis A: Chemical*, *209*(1-2), 209-214.
- Scheetz, B. E., & Earle, R. (1998). Utilization of fly ash. *Current Opinion in Solid State and Materials Science*, *3*(5), 510-520.

- Serrano, D. P., & van Grieken, R. (2001a). Heterogenous events in the crystallization of zeolites. *Journal of Materials Chemistry*, *11*(10), 2391-2407.
- Serrano, D. P., García, R. A., & Otero, D. (2009). Friedel–Crafts acylation of anisole over hybrid zeolitic-mesostructured materials. *Applied Catalysis A: General*, *359*(1-2), 69-78.
- Serrano, D. P., Van Grieken, R., Sanchez, P., Sanz, R., & Rodriguez, L. (2001). Crystallization mechanism of all-silica zeolite beta in fluoride medium. *Microporous and Mesoporous Materials*, *46*(1), 35-46.
- Shaheen, S. M., Hooda, P. S., & Tsadilas, C. D. (2014). Opportunities and challenges in the use of coal fly ash for soil improvements—a review. *Journal of Environmental Management*, *145*, 249-267.
- Sheng, C., & Li, Y. (2008). Experimental study of ash formation during pulverized coal combustion in O₂/CO₂ mixtures. *Fuel*, *87*(7), 1297-1305.
- Shigemoto, N., Hayashi, H., & Miyaura, K. (1993). Selective formation of Na-X zeolite from coal fly ash by fusion with sodium hydroxide prior to hydrothermal reaction. *Journal of Materials Science*, *28*(17), 4781-4786.
- Siddique, R. (2004). Performance characteristics of high-volume Class F fly ash concrete. *Cement and Concrete Research*, *34*(3), 487-493.
- Simon-Masseron, A., Marques, J. P., Lopes, J. M., Ribeiro, F. R., Gener, I., & Guisnet, M. (2007). Influence of the Si/Al ratio and crystal size on the acidity and activity of HBEA zeolites. *Applied Catalysis A: General*, *316*(1), 75-82.
- Soe, J. T., Kim, S. S., Lee, Y. R., Ahn, J. W., & Ahn, W. S. (2016). CO₂ Capture and Ca²⁺ Exchange Using Zeolite A and 13X Prepared from Power Plant Fly Ash. *Bulletin of the Korean Chemical Society*, *37*(4), 490-493.
- Somerset, V., Petrik, L. F., White, R. A., Klink, M. J., Key, D., & Iwuoha, E. (2004). The use of X-ray fluorescence (XRF) analysis in predicting the alkaline hydrothermal conversion of fly ash precipitates into zeolites. *Talanta*, *64*(1), 109-114.
- Somerset, V., Petrik, L., & Iwuoha, E. (2008). Alkaline hydrothermal conversion of fly ash precipitates into zeolites 3: the removal of mercury and lead ions from wastewater. *Journal of Environmental Management*, *87*(1), 125-131.
- Speight, J. G. (2005). *Handbook of coal analysis* (Vol. 166). John Wiley & Sons, NJ, USA.
- Sun, H., Wu, D., Guo, X., & Navrotsky, A. (2015). Energetics and structural evolution of Na–Ca exchanged zeolite A during heating. *Physical Chemistry Chemical Physics*, *17*(14), 9241-9247.

- Sun, J., Bonneau, C., Cantín, Á., Corma, A., Díaz-Cabañas, M. J., Moliner, M., Zhang, D., Li, M., & Zou, X. (2009). The ITQ-37 mesoporous chiral zeolite. *Nature*, *458*(7242), 1154.
- Tanabe, K., & Hölderich, W. F. (1999). Industrial application of solid acid-base catalysts. *Applied Catalysis A: General*, *181*(2), 399-434.
- Tanaka, H., Eguchi, H., Fujimoto, S., & Hino, R. (2006). Two-step process for synthesis of a single phase Na-A zeolite from coal fly ash by dialysis. *Fuel*, *85*(10), 1329-1334.
- Tauanov, Z., Shah, D., Inglezakis, V., & Jamwal, P. K. (2018). Hydrothermal synthesis of zeolite production from coal fly ash: A heuristic approach and its optimization for system identification of conversion. *Journal of Cleaner Production*, *182*, 616-623.
- Thommes, M., Kaneko, K., Neimark, A. V., Olivier, J. P., Rodriguez-Reinoso, F., Rouquerol, J., & Sing, K. S. (2015). Physisorption of gases, with special reference to the evaluation of surface area and pore size distribution (IUPAC Technical Report). *Pure and Applied Chemistry*, *87*(9-10), 1051-1069.
- Tian, F., Wu, Y., Shen, Q., Li, X., Chen, Y., & Meng, C. (2013). Effect of Si/Al ratio on mesopore formation for zeolite beta via NaOH treatment and the catalytic performance in α -pinene isomerization and benzylation of naphthalene. *Microporous and Mesoporous Materials*, *173*, 129-138.
- Tishmack, J. K., & Burns, P. E. (2004). The chemistry and mineralogy of coal and coal combustion products. *Energy, Waste and the Environmental: a Geochemical Perspective. Geological Society*, *236*, 223-46.
- Tong, M., Zhang, D., Zhu, L., Xu, J., Deng, F., Xu, R., & Yan, W. (2016). An elaborate structure investigation of the chiral polymorph A-enriched zeolite beta. *CrystEngComm*, *18*(10), 1782-1789.
- Tosheva, L., & Valtchev, V. P. (2005). Nanozeolites: synthesis, crystallization mechanism, and applications. *Chemistry of Materials*, *17*(10), 2494-2513.
- van Bekkum, H., & Kouwenhoven, H. W. (2009). Progress in the use of zeolites in organic synthesis. *ChemInform*, *40*(23), no-no.
- Vassilev, S. V., & Vassileva, C. G. (2005). Methods for characterization of composition of fly ashes from coal-fired power stations: a critical overview. *Energy & Fuels*, *19*(3), 1084-1098.
- Vaudry, F., Di Renzo, F., Espiau, P., Fajula, F., & Schulz, P. (1997). Aluminum-rich zeolite beta. *Zeolites*, *19*(4), 253-258.

- Verboekend, D., Nuttens, N., Locus, R., Van Aelst, J., Verolme, P., Groen, J. C., Pérez-Ramírez, J., & Sels, B. F. (2016). Synthesis, characterisation, and catalytic evaluation of hierarchical faujasite zeolites: milestones, challenges, and future directions. *Chemical Society Reviews*, 45(12), 3331-3352.
- Vereshchagina, T. A., Kutikhina, E. A., Solovyov, L. A., Vereshchagin, S. N., Mazurova, E. V., Chernykh, Y. Y., & Anshits, A. G. (2018). Synthesis and structure of analcime and analcime-zirconia composite derived from coal fly ash cenospheres. *Microporous and Mesoporous Materials*, 258, 228-235.
- Vichaphund, S., Wimuktiwan, P., Sricharoenchaikul, V., & Atong, D. (2019). In situ catalytic pyrolysis of Jatropha wastes using ZSM-5 from hydrothermal alkaline fusion of fly ash. *Journal of Analytical and Applied Pyrolysis*.
- Vinai, R., Lawane, A., Minane, J. R., & Amadou, A. (2013). Coal combustion residues valorisation: Research and development on compressed brick production. *Construction and Building Materials*, 40, 1088-1096.
- Vinu, A., Sawant, D. P., Ariga, K., Hossain, K. Z., Halligudi, S. B., Hartmann, M., & Nomura, M. (2005). Direct synthesis of well-ordered and unusually reactive FeSBA-15 mesoporous molecular sieves. *Chemistry of Materials*, 17(21), 5339-5345.
- Vjunov, A., Fulton, J. L., Camaioni, D. M., Hu, J. Z., Burton, S. D., Arslan, I., & Lercher, J. A. (2015). Impact of aqueous medium on zeolite framework integrity. *Chemistry of Materials*, 27(9), 3533-3545.
- Vogt, E. T. C., & Weckhuysen, B. M. (2015). Fluid catalytic cracking: recent developments on the grand old lady of zeolite catalysis. *Chemical Society Reviews*, 44(20), 7342-7370.
- Wadlinger, R. L., Kerr, G. T., & Rosinski, E. J. (1975). US Patent 3,308,069, 1967.
- Wagholikar, S. G., Niphadkar, P. S., Mayadevi, S., & Sivasanker, S. (2007). Acylation of anisole with long-chain carboxylic acids over wide pore zeolites. *Applied Catalysis A: General*, 317(2), 250-257.
- Wang, C. F., Li, J. S., Wang, L. J., & Sun, X. Y. (2008). Influence of NaOH concentrations on synthesis of pure-form zeolite A from fly ash using two-stage method. *Journal of Hazardous Materials*, 155(1), 58-64.
- Wang, S., & Wu, H. (2006). Environmental-benign utilisation of fly ash as low-cost adsorbents. *Journal of Hazardous Materials*, 136(3), 482-501.
- Wang, S., Wu, D., Sun, Y., & Zhong, B. (2001). The synthesis of MCM-48 with high yields. *Materials Research Bulletin*, 36(9), 1717-1720.

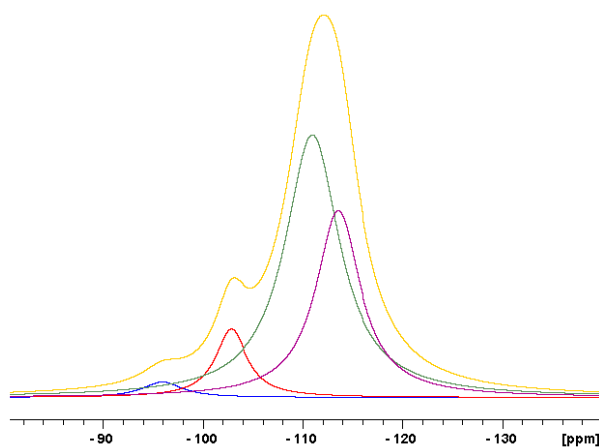
- Wang, W., Li, M., & Zeng, Q. (2015). Adsorption of chromium (VI) by strong alkaline anion exchange fiber in a fixed-bed column: experiments and models fitting and evaluating. *Separation and Purification Technology*, *149*, 16-23.
- Wang, Z., Wang, L., Zhou, Z., Zhang, Y., Li, H., Stampfl, C., Liang, C., & Huang, J. (2017). Benzoylation of arenes with benzyl chloride over H-beta zeolite: effects from acidity and shape-selectivity. *The Journal of Physical Chemistry C*, *121*(28), 15248-15255.
- Wdowin, M., Franus, M., Panek, R., Badura, L., & Franus, W. (2014). The conversion technology of fly ash into zeolites. *Clean Technologies and Environmental Policy*, *16*(6), 1217-1223.
- Wei, Y., Parmentier, T. E., de Jong, K. P., & Zečević, J. (2015). Tailoring and visualizing the pore architecture of hierarchical zeolites. *Chemical Society Reviews*, *44*(20), 7234-7261.
- Weitkamp, J. (2000). Zeolites and catalysis. *Solid State Ionics*, *131*(1-2), 175-188.
- White, S. C., & Case, E. D. (1990). Characterization of fly ash from coal-fired power plants. *Journal of Materials Science*, *25*(12), 5215-5219
- World Coal Association (WCA). (2013). Coal facts 2013.
- Wright, P. A., & Lozinska, M. (2011). Structural Chemistry and Properties of zeolites. *Zeolites and Ordered Porous Solids*, 5th International FEZA Conference, 3rd FEZA School on zeolites, Valencia, Spain.
- Wu, Y., Tian, F., Liu, J., Song, D., Jia, C., & Chen, Y. (2012). Enhanced catalytic isomerization of α -pinene over mesoporous zeolite beta of low Si/Al ratio by NaOH treatment. *Microporous and Mesoporous Materials*, *162*, 168-174.
- Xia, X. H., Chen, B., Wu, X. D., Hu, Y., Liu, D. H., & Hu, C. Y. (2017). Coal use for world economy: Provision and transfer network by multi-region input-output analysis. *Journal of Cleaner Production*, *143*, 125-144.
- Xiong, G., Liu, X., Zhao, R., Liu, J., Yin, J., Meng, Q., Guo, Z., & Liu, L. (2017). Synthesis and crystallization mechanism of nano-sized zeolite beta aggregates via aerosol-assisted method. *Microporous and Mesoporous Materials*, *249*, 97-104.
- Xiong, H., Pham, H. N., & Datye, A. K. (2014). Hydrothermally stable heterogeneous catalysts for conversion of biorenewables. *Green Chemistry*, *16*(11), 4627-4643.
- Yan, F., Jiang, J., Li, K., Liu, N., Chen, X., Gao, Y., & Tian, S. (2017). Green synthesis of nanosilica from coal fly ash and its stabilizing effect on CaO sorbents for CO₂ capture. *Environmental Science & Technology*, *51*(13), 7606-7615.

- Yan, F., Jiang, J., Tian, S., Liu, Z., Shi, J., Li, K., Chen, X., & Xu, Y. (2016). A green and facile synthesis of ordered mesoporous nanosilica using coal fly ash. *ACS Sustainable Chemistry & Engineering*, 4(9), 4654-4661.
- Yan, H., Xue-min, C., Liu, L. P., Liu, X. D., & Chen, J. Y. (2012). The hydrothermal transformation of solid geopolymers into zeolites. *Microporous and Mesoporous Materials*, 161, 187-192.
- Yang, S., & Navrotsky, A. (2002). In situ calorimetric study of the growth of silica TPA-MFI crystals from an initially clear solution. *Chemistry of Materials*, 14(6), 2803-2811.
- Yao, Z. T., Ji, X. S., Sarker, P. K., Tang, J. H., Ge, L. Q., Xia, M. S., & Xi, Y. Q. (2015). A comprehensive review on the applications of coal fly ash. *Earth-Science Reviews*, 141, 105-121.
- Yilmaz, B., Trukhan, N., & Mueller, U. (2012). Industrial outlook on zeolites and metal organic frameworks. *Chin. J. Catal*, 33(1), 3-10.
- Yin, C., Tian, D., Xu, M., Wei, Y., Bao, X., Chen, Y., & Wang, F. (2013). One-step synthesis of hierarchical mesoporous zeolite Beta microspheres from assembly of nanocrystals. *Journal of Colloid and Interface Science*, 397, 108-113.
- Yoon, Y. H., & Nelson, J. H. (1984). Application of gas adsorption kinetics I. A theoretical model for respirator cartridge service life. *American Industrial Hygiene Association Journal*, 45(8), 509-516.
- Yu, Y., Chen, N., Wang, D., Tian, C., Li, M., & Feng, C. (2017). Adsorption of phosphorus based on Hangjin clay granular ceramic from aqueous solution and sewage: Fixed-bed column study. *Environmental Progress & Sustainable Energy*, 36(5), 1323-1332.
- Yuvakkumar, R., Elango, V., Rajendran, V., & Kannan, N. (2014). High-purity nano silica powder from rice husk using a simple chemical method. *Journal of Experimental Nanoscience*, 9(3), 272-281.
- Zacco, A., Borgese, L., Gianoncelli, A., Struis, R. P., Depero, L. E., & Bontempi, E. (2014). Review of fly ash inertisation treatments and recycling. *Environmental Chemistry Letters*, 12(1), 153-175.
- Zhang, H., Xie, B., Meng, X., Müller, U., Yilmaz, B., Feyen, M., Maurer, S., Gies, H., Tatsumi, T., Bao, X., Zhang, W., De Vos, D., & Xiao, F. (2013). Rational synthesis of Beta zeolite with improved quality by decreasing crystallization temperature in organotemplate-free route. *Microporous and Mesoporous Materials*, 180, 123-129.

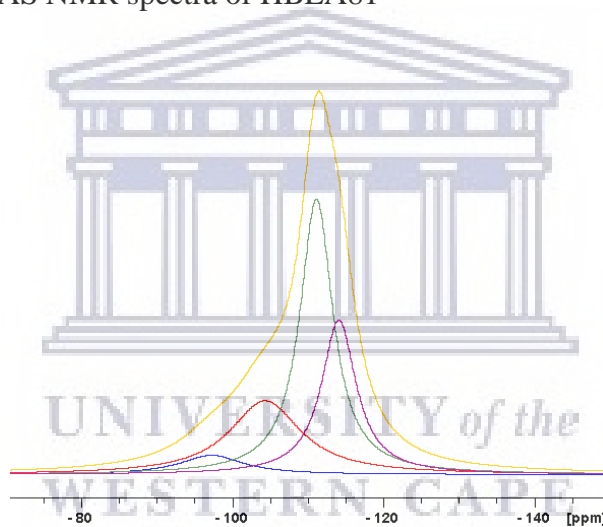
- Zhang, J., Cao, P., Yan, H., Wu, Z., & Dou, T. (2016). Synthesis of hierarchical zeolite Beta with low organic template content via the steam-assisted conversion method. *Chemical Engineering Journal*, 291, 82-93.
- Zhang, K., & Ostraat, M. L. (2016). Innovations in hierarchical zeolite synthesis. *Catalysis Today*, 264, 3-15.
- Zhang, K., Liu, Z., Yan, X., Hao, X., Wang, M., Li, C., & Xi, H. (2017). In situ assembly of nanoparticles into hierarchical Beta zeolite with tailored simple organic molecule. *Langmuir*, 33(50), 14396-14404.
- Zhang, L., Chen, K., Chen, B., White, J. L., & Resasco, D. E. (2015). Factors that determine zeolite stability in hot liquid water. *Journal of the American Chemical Society*, 137(36), 11810-11819.
- Zhao, X. S., Lu, G. Q., & Zhu, H. Y. (1997). Effects of ageing and seeding on the formation of zeolite Y from coal fly ash. *Journal of Porous Materials*, 4(4), 245-251.
- Zhao, Z., Xu, S., Hu, M. Y., Bao, X., Peden, C. H., & Hu, J. (2014). Investigation of aluminium site changes of dehydrated zeolite h-beta during a rehydration process by high-field solid-state NMR. *The Journal of Physical Chemistry C*, 119(3), 1410-1417.
- Zhu, G., Li, Y., Chen, H., Liu, J., & Yang, W. (2008). An in situ approach to synthesize pure phase FAU-type zeolite membranes: effect of aging and formation mechanism. *Journal of Materials Science*, 43(9), 3279-3288.
- Zhu, Z., Xu, H., Jiang, J., Wu, H., & Wu, P. (2017). Hydrophobic Nanosized All-Silica Beta Zeolite: Efficient Synthesis and Adsorption Application. *ACS Applied Materials & Interfaces*, 9(32), 27273-27283.

Appendix

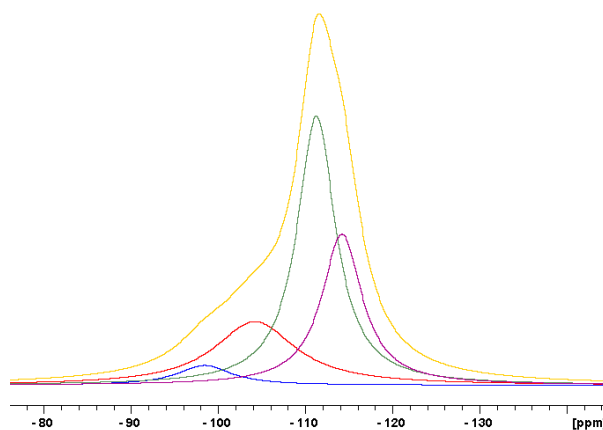
Appendix 1: Deconvoluted ^{29}Si MAS NMR spectra



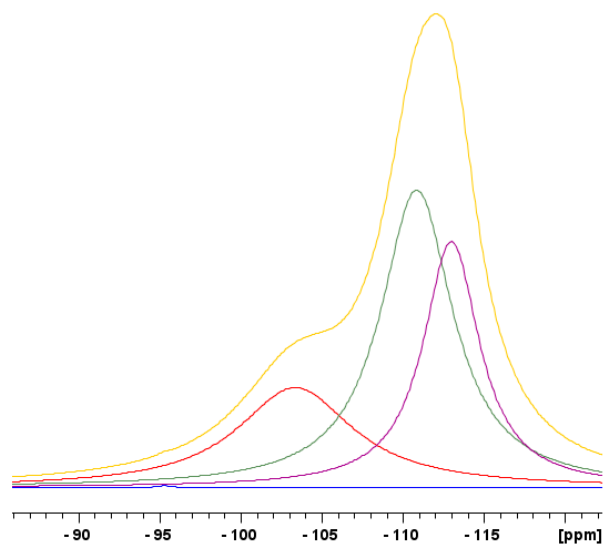
Deconvoluted ^{29}Si MAS NMR spectra of HBEA81



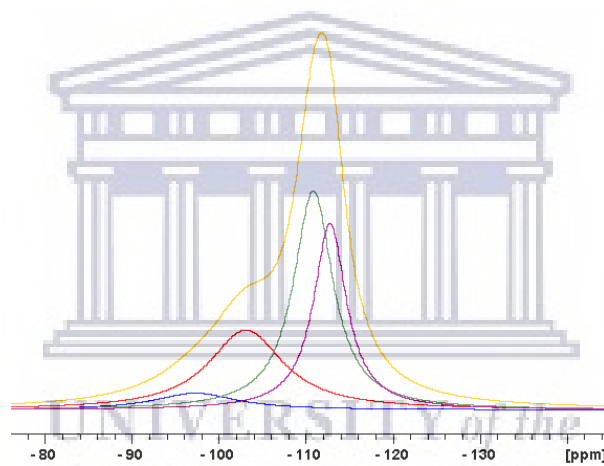
Deconvoluted ^{29}Si MAS NMR spectra of HBEA12



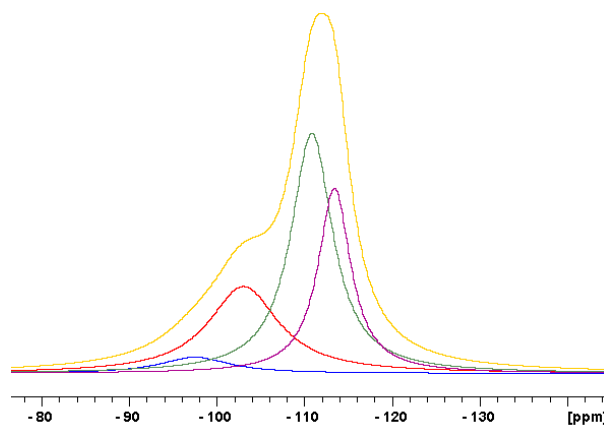
Deconvoluted ^{29}Si MAS NMR spectra of HBEA2



Deconvoluted ^{29}Si MAS NMR spectra of HBEA24

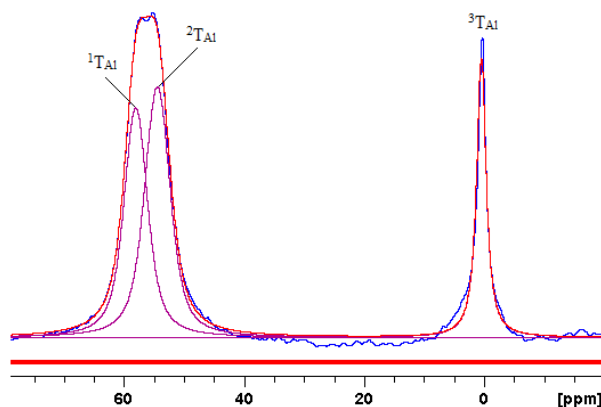


Deconvoluted ^{29}Si MAS NMR spectra of HBEA48

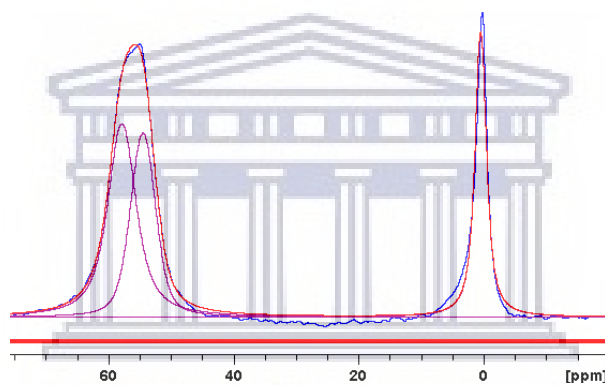


Deconvoluted ^{29}Si MAS NMR spectra of HBEA72

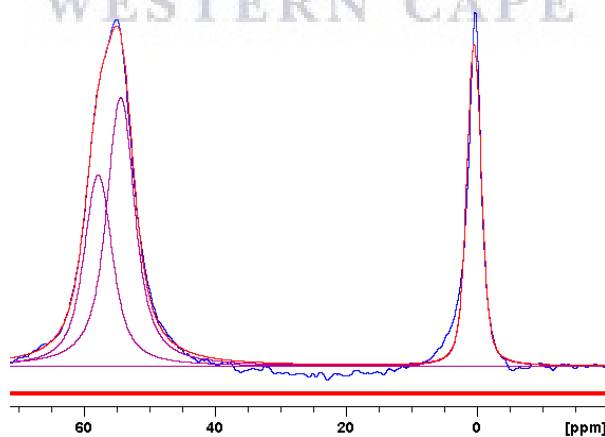
Appendix 2: Deconvoluted ^{27}Al MAS NMR spectra



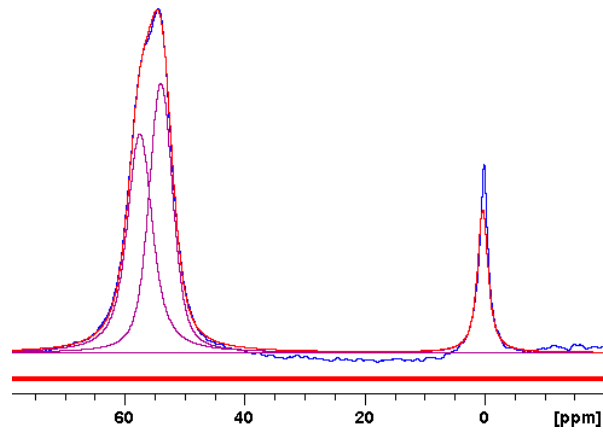
Deconvoluted ^{27}Al MAS NMR spectra of HBEA81



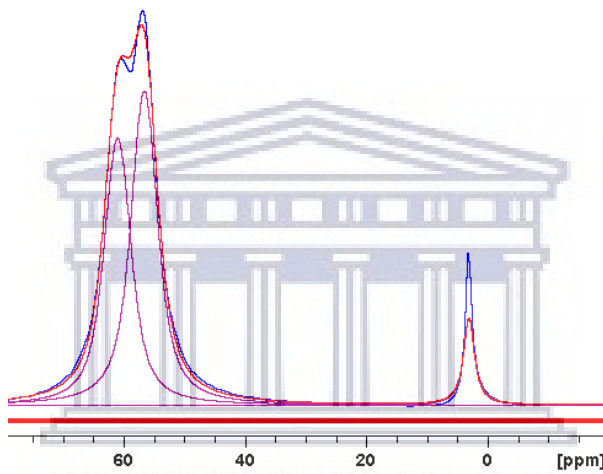
Deconvoluted ^{27}Al MAS NMR spectra of HBEA12



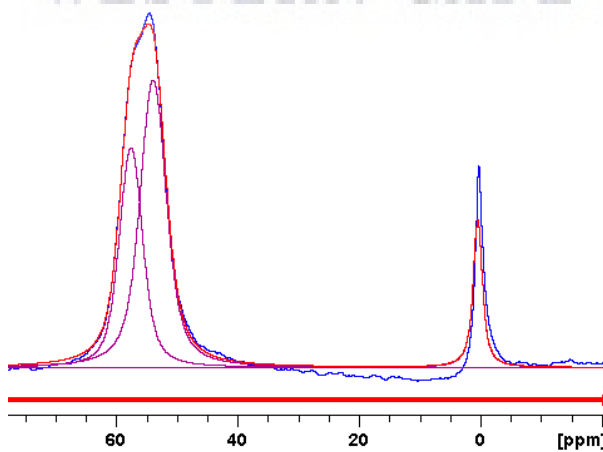
Deconvoluted ^{27}Al MAS NMR spectra of HBEA2



Deconvoluted ^{27}Al MAS NMR spectra of HBEA24

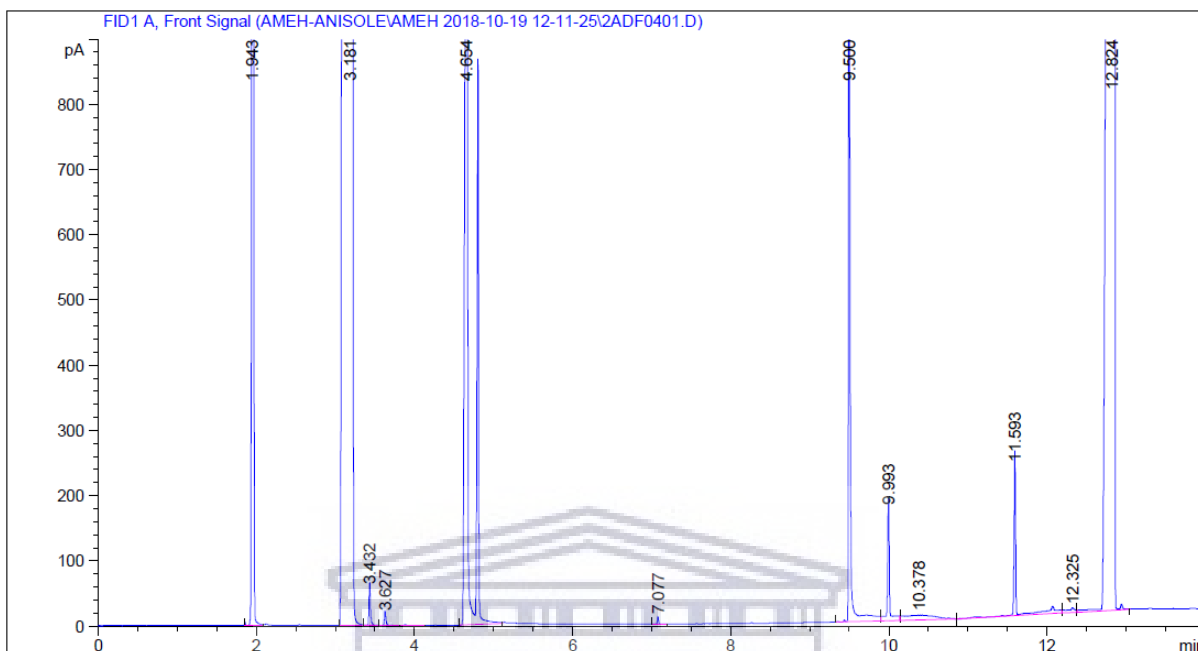


Deconvoluted ^{27}Al MAS NMR spectra of HBEA48

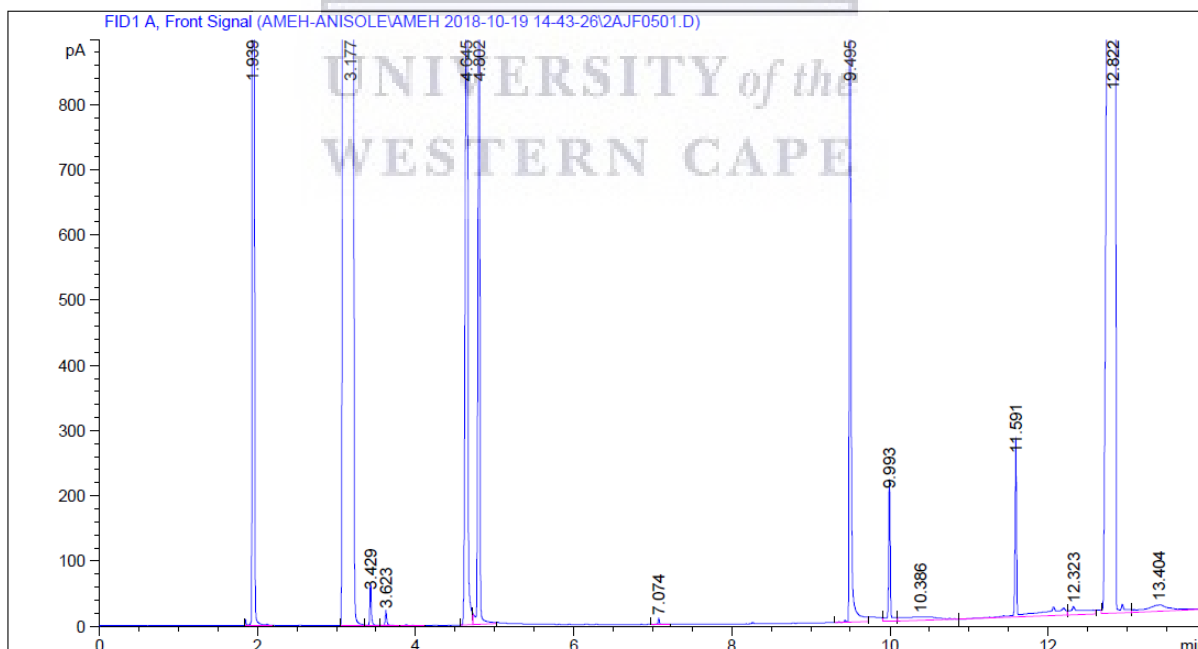


Deconvoluted ^{27}Al MAS NMR spectra of HBEA72

Appendix 3: GC spectra of the acylation of anisole with benzoyl chloride over HBEA zeolites



GC spectra of the acylation of anisole with benzoyl chloride over HBEA2 zeolite at reaction time of 4 hours



GC spectra of the acylation of anisole with benzoyl chloride over HBEA24 zeolite at reaction time of 4 hours